11th Numerical Towing Tank Symposium

7-9 September 2008

Brest/France

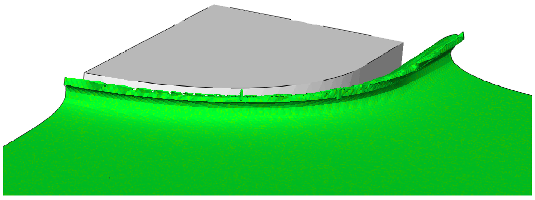

ENSIETA
ÉCOLE NATIONALE SUPÉRIEURE D'INGÉNIEURS
FORMATION INITIALE - FORMATION CONTINUE - RECHERCHE

TuTech
TUHH Technologie GmbH

Sponsored by

Brest Métropole Océane

NUMECA
www.numeca.com

CD-Adapco
www.cd-adapco.com

Germanischer Lloyd
www.gl-group.org

SUNDAY, 7.9.2008

SESSION CHAIRMAN Volker BERTRAM

13:30 Satu HÄNNINEN, Tommi MIKKOLA
Wave excitation on a ship bow in short waves.
13:55 P. QUEUTEY, M. VISONNEAU, A. LEROYER, G. DENG, E.GUILMINEAU
RANSE simulations of a Naval Combatant in Head Waves
14:20 G. GRECO ,T. BAZZI, M. MASIA, G. COLICCHIO, C. LUGNI
Violent seakeeping problem: an application to a patrol ship
14:45 Marek KRASKOWSKI
Simulation of the hull dynamics with RANSE method

SESSION CHAIRMAN Patrick QUEUTEY

15:40 Anna-Maria TOCU, Adrian LUNGU
Numerical Analysis of the Three-Dimensional Viscous Flow around a Propeller Ship.
16:05 Adrian LUNGU, Anna-Maria TOCU
Wave Resistance Minimization for Ships Running under the Restricted Water Condition.
16:30 Carlos A. PEREZ-GUTIERREZ, M. TAN, P.A. WILSON
Validation and Verification of Hull Resistance Components Using a Commercial CFD Code.
16 :55 Keun Woo SHIN, H. B. BINGHAM, P. ANDERSEN
Numerical Analysis of Ship-ship interaction by a high order potential flow code with ship motions.
17:20 Claus SIMONSEN, Rasmus CARSTENS
RANS Simulation of the flow around a ship appended with rudder, ice fins and rotating propeller

MONDAY, 8.9.2008

SESSION CHAIRMAN François DENISET

09:00 Jeroen WACKERS, Michel VISONNEAU
Adaptive grid refinement for ISIS-CFD
09:25 G. COLICCHIO, Claudio LUGNI
Preliminary LBM study of hydrodynamic problems
09:50 Kunihide OASHI, Takanori HINO
A Comparative Study of DDES and URANS by an Unstructured Grid based NS Solver
10:15 Andreas KARLSSON, R. BENSOW, C. FUREBY
Numerical simulations of the flow around a 6:1 prolate spheroid.

SESSION CHAIRMAN Claudio LUGNI

11:10 France FLOC'H, JM LAURENS, S. KERAMPRAN, JB LEROUX
Trajectory prediction by coupling Euler-Newton equations and flow models
11:35 Francis HUEBER, Mario CAPONETTO
CFD for the 33rd America's cup
12:00 Ruijun FAN, ZHOU ZHOU
Numerical predictions and experimental verifications for the hydrodynamic performance of horizontal axis marine current turbine

SESSION CHAIRMAN Jan SZANTYR

13:30 Lars GREITSCH
Prognosis of Rudder Cavitation Risk in Ship Operation
13:55 Nai-Xian LU, N. BERCHICHE, R.E. BENSOW
Numerical simulations of cavitating flow around a 2D hydrofoil using opeFOAM and Fluent
14:20 Andrea CALIFANO
Influence of the near wall treatment on the flow features around a two-dimensional hydrofoil close to the free surface
14:45 Antoine DUCOIN, François DENISET, André ASTOLFI, JF SIGRIST
Numerical and experimental study of a submerged foil

SESSION CHAIRMAN Jean-Marc LAURENS

15:40 Tadeusz KORONOWICZ, Zbigniew KRZEMIANOWSKI, Jan A. SZANTYR
Numerical Determination of the Propeller Design Velocity Field Including Scale Effect and Rudder Influence
16:05 Pawel DYMARSKI, P. FLASZYNSKI, M. KRASKOWSKI, R. BIERNACKI
Modelling of Tip Vortex behind a Blade Using Different Turbulence Models and Different RANSE Solvers. Comparison with LDA measurements
16:30 Daniel SCHMODE
RANS computations for wake improving vortex generators
16:55 Hendrik VORHOELTER, Stefan KRUEGER
Wake Field Analysis of a Drifting Ship with RANS-CFD-Methods

TUESDAY, 9.9.2008

SESSION CHAIRMAN Stefan KYULEVCHELIEV

09:00 Thomas SPENKUCH, S. TURNOCK, S. WRIGHT, A. SHENOI
The use of CFD in modelling Covering and Blanketing Effects in Yacht Race Simulations

09:50 S.G. LEWIS, D.A. HUDSON, S.R. TURNOCK
Improvement to body impact predictions using CFD through analysis of an unsteady boundary layer.

10:15 A. TASSIN, N. JACQUES, A. NEME, JM LAURENS
Simplified models for the estimation of slamming loads on bulbous bows

11:00 J. OBERHAGEMANN, O. EL MOCTAR, M. HOLTMANN, T. SCHELLIN, V. BERTRAM, K. DAEWOONG
Numerical Simulation of Stern Slamming and Whipping

WAVE EXCITATION ON A SHIP BOW IN SHORT WAVES

Satu Hänninen and Tommi Mikkola
Marine technology, Department of Applied Mechanics, TKK Helsinki University of Technology[1]

1 INTRODUCTION

This study focuses on the numerical simulation of the wave excitation on a passenger ship in short head waves. The aim has been to consider, whether it is possible to assess the reliability of the frequency content of the wave loads - also in local areas of the hull.

The motivation of the study originates from springing. Springing has been studied for decades already, see for instance the references in *Storhaug et al. (2003)*. Nevertheless, the physics of the non-linear springing excitation is not yet fully understood. Studying springing excitation by model tests or full-scale measurements is challenging, sometimes even impossible, because the critical wave loads are very weak. That is why the common trend has been to focus on the vibratory responses instead of analysing the excitation. Marine Technology of TKK has done recently model tests to measure springing-type excitation, *Manderbacka et al. (2008)*, *Linnas (2008)*. Those model-test results have shown that when non-linear springing occurs, the ship-wave interaction includes severe wave breaking. This indicates that if springing is analysed numerically, a fully non-linear behaviour of the free-surface deformation should be allowed by the numerical method. A RANS-solver combined with an interface capturing method is one option. One advantage of studying springing with this type of method is the high pressure resolution on the hull. In model tests the resolution is limited by the scale of the model as well as the size and the number of the pressure sensors. On the other hand, the computational expenses of springing simulations are significant. The spatial scale related to nonlinear springing excitation is significantly smaller than the global scale of the problem. For instance *Vidic-Perunovic (2005)* and *Storhaug et al. (2003)* have recently compared the numerical predictions given by the state-of-the-art seakeeping methods to full-scale measurements. The conclusion has been that the numerical prediction is challenging and that the potential flow theories are not necessarily reliable in the case of springing. The most encouraging results have been obtained with a strip theory which takes into account the bi-directionality of the wave field. According to the knowledge of the authors of this abstract, field methods have not been applied for the study of springing before.

2 NUMERICAL METHOD

The flow-solver ISIS-CFD has been used, *Queutey and Visonneau (2007)*. ISIS-CFD is an unsteady RANS-solver, but in the present study it has been used as an Euler-solver. The solver uses an interface capturing method to solve free-surface flows. The blended interface capturing scheme BICS (*FINE/Marine, 2007)* has been applied for the discretization of the transport of the mass fraction. However, in practical terms, in the present study it reduces into the Inter-Gamma differencing scheme (*Jasak and Weller (1995)*) due to the very small time steps used.

3 ON THE COMPUTATIONS

Results for one of the simulated cases in regular head-waves are presented in the following. The information of the wave and ship is given in Table 3. As the wave length is small in comparison to the ship length, the ship motions can be neglected and the grid has been kept fixed during the simulations. The simulations were performed in model

---

[1] Marine Technology, TKK Helsinki University of Technology, Tietotie 1, FIN-02015 Espoo, Finland. E-mail: Satu.Hanninen@hut.fi

scale and the parameters and the results are given in model scale. The scale of the model is 1:49.

Table 1: Information on the ship and the wave

Ship model		Wave	
Length L_{pp}	7.0m	Wave period T_w	0.82s
Breadth B	1.10m	Height H_w	0.08m
Draught T	0.18m	Wave steepness H_w/L_w	0.08
Speed V	1.47m/s	encounter frequency ω_e	16.5rad/s

The grids were generated with the hexahedral grid generator Hexpress. The computation was repeated with three different grid densities while keeping the Courant number fixed. The refinement ratios of the grids and time steps were 1.25 for the grids coarse / medium and 1.20 for the grids medium / fine. The number of cells and the cell sizes in the refinement box to transport the wave are given in Table 2. L_c denotes cell length and H_c cell height. A refinement box was used also on the bow area. The simulation domain contained only one half of the hull as a head-waves case is symmetric. The wave boundary was located 3 wave lengths in front of the ship fore perpendicular FPP (the distance from the FPP is $0.45L_{pp}$) and the grid outflow boundary $1.2\times L_{pp}$ behind the ship aft perpendicular APP. The grid breadth was $1\times L_{pp}$ and height $1.46\times L_{pp}$. The vertical location of the grid bottom and top boundaries are different depending on the grid density. This difference between the grids had to be accepted to ensure the same location of the free-surface level in each case. This detail is related to the way, in which Hexpress generates grids. Nevertheless, the bottom and top boundaries in each grid are too far from the computational zone of interest to affect the results.

Table 2: Information on grids.

	Number of cells	L_w/L_c	H_w/H_c	T_e/dt
Coarse	2126208	58.32	8.00	245.16
Medium	3783100	72.90	10.00	306.45
Fine	6592542	87.49	11.94	367.86

Besides of the three dimensional grids, 2D grids were generated to test the transportation of the waves first. The 2D grids were generated in an identical way to the 3D grids except that the bow refinement box and y-direction were omitted.

The computations were performed on a high-performance supercluster called Murska (CSC the Finnish IT center for science). In 3D, 10 processors were used for the coarse-grid, 18 for the medium-grid and 32 for the fine-grid computation. The simulated time was 10.8 seconds in model scale. This means that the computation with the coarse, medium and fine grids included 7000, 8700 and 10500 time steps respectively.

4 APPLYING THE NUMERICAL WAVE BOUNDARY CONDITION

The wave was generated with the numerical boundary condition, which defines the velocity distribution and the mass distribution on the boundary according to the Airy wave theory. Due to the fact that the time steps were very small but the vertical cell sizes still rather large, the wave profile on the boundary was not smooth, (see the left figure in Fig. 1). Additionally, the wave on the boundary was not fully physical as a consequence of the significant wave steepness and the applied linear theory. Therefore it is normal that the wave transforms, while it travels further from the boundary. To get an idea of the transformation, the wave signal was analysed at two observation points. The point one is located at the ship fore perpendicular three wave lengths away from the wave boundary and the point two 1.5 wave lengths further downstream. The actual wave heights are compared to the given input wave height in Table 3. The proportion of the 2. and 3. harmonic order components divided by the first order component are also given. The conclusion is that the wave height and the frequency content depend on the observation point. The wave is roughly 10 percent larger than the given input value on the fine grid and it increases the coarser the grid is. The grid density also affects the frequency content of the wave. Besides, the non-linear components are larger at the observation point two than at the point one. At point one, the higher-order components increase with finer grids, but at point two the trend is not that clear.

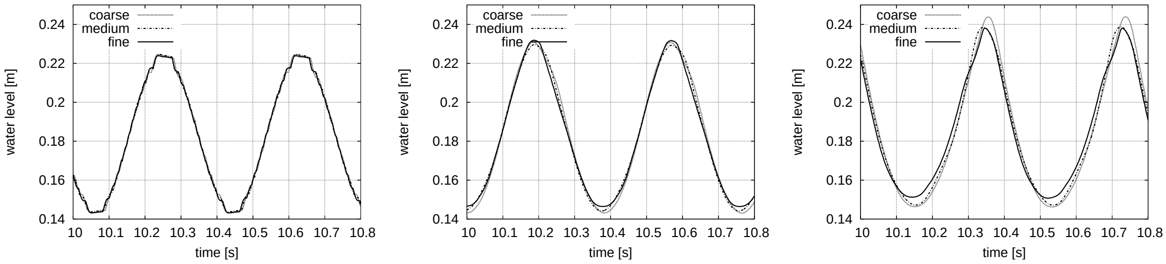

Figure 1: Signals of the wave heights in 2D simulations. Left: wave maker, middle: 3 wave lengths from the wave boundary, right: 4.5 wave lengths from the wave boundary.

Table 3: Wave on the 2D grid

	$3L_w$ from the wave bc				$4.5L_w$ from the wave bc			
	H/H_{input}	1. comp	2./1. comp.	3./1. comp.	H/H_{input}	1. comp.	2./1. comp.	3./1. comp.
coarse	1.10	0.0543	0.08	0.03	1.22	0.0568	0.26	0.11
medium	1.06	0.0521	0.11	0.02	1.14	0.0539	0.24	0.08
fine	1.07	0.0515	0.13	0.05	1.09	0.0493	0.27	0.12

These results indicates that the present grids affect the wave. Besides of the grid density, the location of the outflow boundary and the length of the refinement box may also affect the results. Despite of these facts, the respective grid densities were used for the 3D simulations to get a first estimate of the wave excitation.

5 RESULTS ON THE WAVE LOADS

The results on the bow area are analysed, because the main non-linearities are likely to appear there and the validation data from the model tests is also from that area.

5.1 Solution accuracy of the vertical excitation

The vertical excitation is considered on the two areas shown in Fig. 2. The vertical force acting on the larger area is called Fz1 and the vertical force acting on the smaller area is called Fz2. In the analysis, a further restriction is followed: only the area of the hull surface (cell faces) on which the mass fraction c gets a value larger or equal to 0.5 is considered, i.e. the part of the hull surface approximated to be below the free surface.

The raw signals Fz1 and Fz2 on the fine grid are plotted in Fig. 3. Both signals include noise, especially the force Fz1. The fact that the noise is more significant on Fz1 than Fz2 indicates that it originates further from the free-surface level towards the ship bottom. The grid is coarser close to the bottom hull than around the free-surface, which is probably the reason for the noise.

The filtered force signals obtained with the different grid densities are compared in Fig. 4. The filtered signal

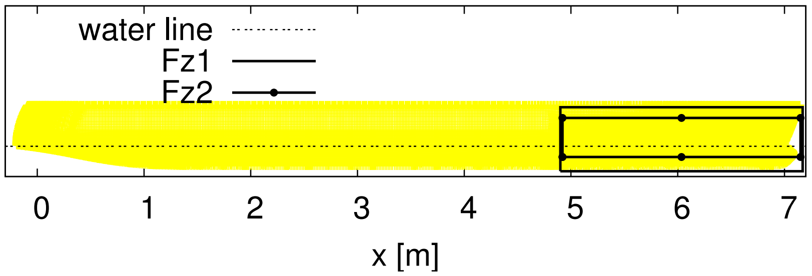

Figure 2: The surface areas of the hull on which the forces Fz1 and Fz2 are calculated.

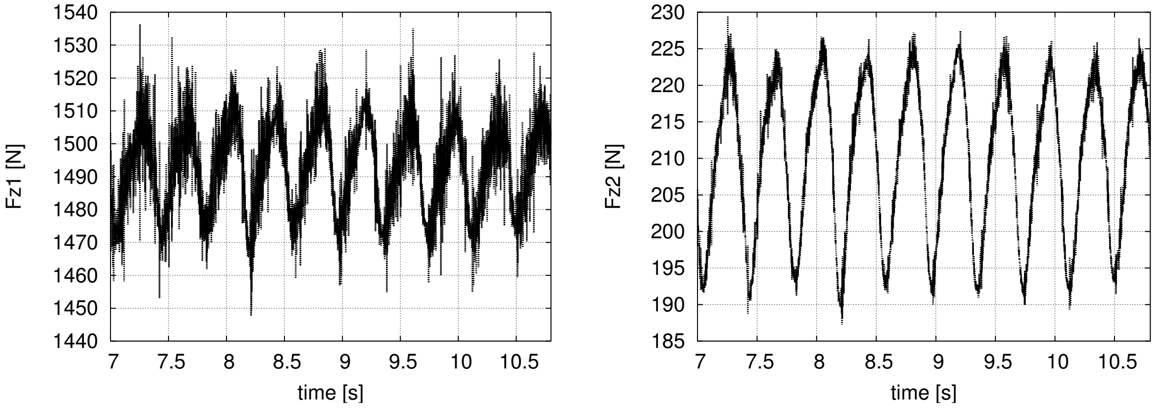

Figure 3: On the left the signal of Fz1 and on the right that of Fz2.

includes the harmonic components from zero angular frequency up to the frequency 58 rad/s. The signals look quite different, and based on them it cannot be concluded that the solution is converging towards a specific result with grid refinement. The first-, second- and third-order harmonic components were calculated from the power spectra of the signals. The results divided by the respective result of the fine grid are presented in Table 4. The first order components on the different grids show reasonable behaviour. The second order components of both Fz1 and Fz2 are oscillating, but the oscillation amplitude is possibly getting smaller with grid refinements. More computations with different grid densities would be required to confirm this. The third order component, on the other hand, is diverging and the results for it are the least reliable.

Table 5 compares the second and third order components to the first order component of the result. It can be seen that the proportion of those components are almost the same on the coarse and fine grids, whereas the results on the medium grid deviate clearly from these.

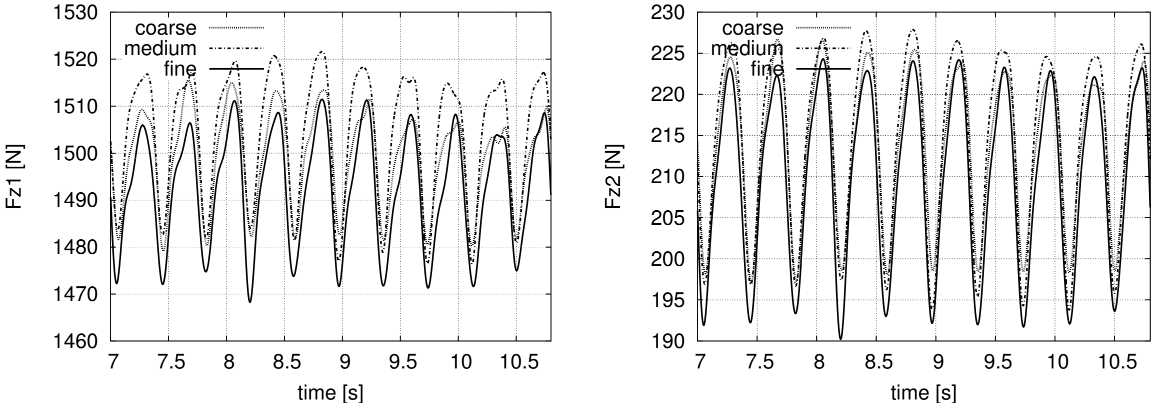

Figure 4: Left: filtered signal Fz1. Right: filtered signal Fz2.

Table 4: The 1., 2. and 3. order components of Fz divided by the respective result on the fine grid.

	Components of Fz on area 1			Components of Fz on area 2		
	1. order	2. order	3. order	1. order	2. order	3. order
coarse	0.79	0.77	0.86	0.82	0.86	0.89
medium	1.00	1.06	0.79	0.94	1.06	0.80

Table 5: The proportion of the 2. and 3. order components of 1. order component of Fz.

	Fz on area 1		Fz on area 2	
	2./1. order	3./1. order	2./1. order	3./1. order
coarse	0.41	0.18	0.33	0.12
medium	0.45	0.13	0.36	0.10
fine	0.42	0.17	0.32	0.12

5.2 On the validation

This test case was part of a model-test set, *Manderbacka et al. (2008)*, *Linnas (2008)*. The model-test results consists of the local pressures measured by 32 pressure sensors on the bow area. Figure 5 shows an example on the comparison of the measured local pressures and the pressures computed on the fine grid in three locations (p1, p2 and p3). Despite the differences between the measurements and the simulations, these first results are encouraging.

6 DISCUSSION AND CONCLUSIONS

The grid dependency study of the vertical force results shows that the first-order harmonic terms are converging towards a certain result with finer grids. The trend obtained for the second- and third-order terms was not that obvious.

The grid dependency of the wave field was first analysed in 2D. The increase of the wave force with grid refinement seems to be contradictory to the decrease of the wave height with grid refinement. This may indicate that the coarser grids do not capture accurately enough the interaction of the waves and the hull.

The comparison of the measured and computed pressure signals looks encouraging. Before drawing further conclusions on the agreement between the local pressures in the model test and in the computations, the grid dependency of the local pressures should be analysed as well. It is also necessary that an analysis on the differences of the model-test and computational wave is included to the validation.

The aim of the study was to find out whether this kind of numerical method could be applied to get further knowledge on the non-linear springing loads. The results show that it could and that the strong non-linearity of the excitation is revealed. Based on these results it is not possible to determine yet the accuracy of the obtained non-linear terms. More computations are required with finer grids.

7 ACKNOWLEDGEMENT

This study has been done within a research project funded by Tekes, Finnish Funding Agency for Technology and Innovation, and Aker Yards. The financial support is gratefully acknowledged. The authors are thankful to Prof. Michel Visonneau and the CFD-team of ECN-CNRS for discussions on ISIS-CFD.

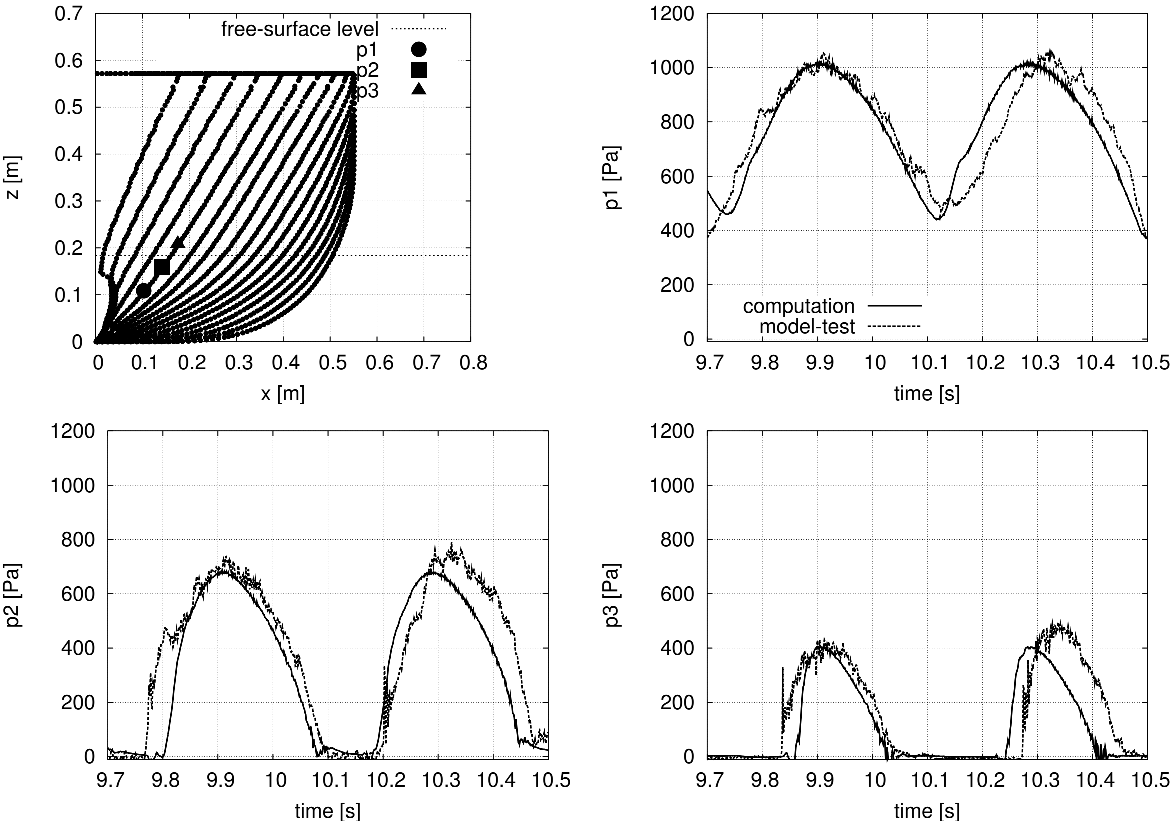

Figure 5: Above left: the locations of the presented pressure signals p1, p2 and p3.

REFERENCES

Fine/Marine v2.0. Fine/Marine v2.0 Tutorial, Comprehensive description of the input data file for ISIS-CFD v2.0. 2007.

Jasak H, Weller HG. Interface tracking capabilities of the Inter-Gamma differencing scheme. Internal report, Mechanical Engineering department, Imperial College of Science, London, 1995.

Linnas R. Model tests of springing type wave loads on a bow of a cruise vessel. Master's thesis being prepared. Marine Technology, Department of Applied Mechanics, Helsinki University of Technology, 2008.

Manderbacka, Tenovuo K, Matusiak J. Model Experiments of springing-type wave loads on a cruise vessel. 8th International Conference on Hydrodynamics. 30. Sept. -3. Oct. 2008.

Queutey P, Visonneau M. An interface capturing method for free-surface hydrodynamic flows. Comput Fluids 36: 1481-1510, 2007.

Storhaug G, Vidic-Perunovic J, Rüdinger F, Holtsmark G, Helmers JB, Gu X. Springing/whipping response of a larger ocean going vessel - A comparison between numerical simulations and full-scale measurements. 3rd International Conference on Hydroelasticity in Marine Technology, Oxford, UK, September, 2003.

Vidic-Perunovic J. Springing response due to bi-directional wave excitation. PhD thesis, Department of Mechanical Engineering, Technical University of Denmark, 2005.

RANSE Simulations of a Naval Combatant in Head Waves

Patrick Queutey, Michel Visonneau, Alban Leroyer, Ganbo Deng and Emmanuel Guilmineau.
Laboratoire de Mécanique des Fluides, Ecole Centrale de Nantes
CNRS-UMR 6598, 44321 Nantes Cedex 3, France
Patrick.Queutey@ec-nantes.fr

1 Introduction

This article addresses the computation of a frigate advancing in regular head waves: both restrained from motions and free to trim and sink. Simulation are performed with the free-surface capturing viscous solver ISIS-CFD included in the computational suite FINE^{TM}/Marine, recently extended to account for six degrees of freedom motions (6DOF) for solid and deformable bodies and 1st to 3rd order Stokes waves generation. These new characteristics make possible the simulation of complex physical phenomena like manoeuvring, dynamic stability and sea-keeping within a unique mathematical and physical framework, the Reynolds Averaged Navier-Stokes Equations for multi-fluid flows.

The ship forward speed diffraction and radiation problem is a formidable mathematical challenge. However, once treated in the fully non-linear environment of multi fluid RANSE Equations, it becomes no more complex than the ship resistance problem in calm water. The validation study focuses on the US Navy combatant (DTMB 5512) at model scale in conditions ranging from moderate speed in long and smooth waves to high speed in short and steep waves. These test cases are retained to correspond as much as possible to the experiments published by IIHR during the last two years (see [1] and [2] for more details on the experimental configurations and computations performed in IIHR).

2 The computational procedure

Computations are performed with the ISIS-CFD flow solver developed by EMN (Equipe Modélisation Numérique, i.e. CFD Department of the Fluid Mechanics Laboratory). Turbulent flow is simulated by solving the incompressible unsteady Reynolds-averaged Navier-Stokes equations (RANSE). The solver is based on the finite volume method to build the spatial discretization of the transport equations. The face-based method is generalized to two-dimensional, rotationally-symmetric, or three-dimensional unstructured meshes for which non-overlapping control volumes are bounded by an arbitrary number of constitutive faces. The velocity field is obtained from the momentum conservation equations and the pressure field is extracted from the mass conservation constraint, or continuity equation, transformed into a pressure-equation. In the case of turbulent flows, additional transport equations for modeled variables are discretized and solved using the same principles. Free-surface flow is simulated with a multi-phase flow approach. Incompressible and non-miscible flow phases are modelized through the use of conservation equations for each volume fraction of phase/fluid discretized with specific compressive discretization schemes detailed in [4]. Several turbulence models ranging from one-equation model to Reynolds stress transport model are implemented in ISIS-CFD. Most of the classical linear eddy-viscosity based closures like the two-equation $k-\omega$ SST model by Menter [5] are implemented. Two more sophisticated turbulence closures are also implemented in the ISIS-CFD solver, an explicit algebraic stress model (EASM) [6] and a Reynolds stress transport model [7]. Recently, a module coupling the flow and the equations of motion for 6 degrees of freedom has been incorporated in ISIS-CFD, together with several mesh deformation algorithms developed for fully unstructured grids. These developments are based on methodologies which are described in [8] and not recalled here for the sake of brevity.

3 Description of the test case characteristics

The DTMB model is L=3.048m long with 0.132m draft. Two speed and wave conditions have been selected according to the experimental data sets described in the afore-mentioned articles. The first experimental data is for a medium speed condition (Fr=0.28, $Re = 4.86 \times 10^6$) with a linear incident wave, wavelength $\lambda = 1.5L$, and amplitude $A = 0.006L$, leading to $A_k = 2\pi A/\lambda = 0.025$. The second experimental data is for a high speed condition (Fr=0.41, $Re = 7.12 \times 10^6$) with steeper incoming waves ($\lambda = 0.5L$, and $A_k = 0.075$), for which a complex non-linear breaking wave phenomena is observed.

4 Fixed and free ship in long waves at moderate speed

4.1 Solution strategy and grid design

The computational domain extends from $-2.0L < x < +3.5L$, $0.0 < y < 2.0L$ and $-1.50L < z < 0.5L$, where the symmetry condition is taken into account at $y = 0$. The ship axis is located along the x-axis with the bow located at x=0 and the stern at x=L. The free-surface at rest lies at $z = 0$. The incident wave is generated at the inlet according to the first order Stokes theory, wall function is used at the ship wall and various far-field and symmetry boundary conditions are used at the other boundaries of the computational domain. The grid generated with HEXPRESS^{TM}, is composed of several generations of hexahedrons. A unique lofted surface covers the entire domain is used to create a local zone of refinement near the free-surface, and a second lofted surface with increased refinement parameters is added at the vicinity of the body to properly capture details of the free surface. Correct propagation of waves is assumed by the use of a refinement box starting from the inlet and ending after the ship. The grid is composed of 2.0 million control volumes with about 40,000 CVs located on the hull. The first point close to the hull is located at $y^+ = 30$, approximately. About 20 to 25 points are located vertically in the layer where the free-surface is supposed to move and a wave length is described with 40 to 50 control volumes.

4.2 Fixed ship

For this first configuration, the ship is fixed at its dynamic equilibrium position (FP=-0.0031Lpp, AP=-0.0007Lpp). Fig. 1 provides a comparison between the temporal evolution of experimental and computed forces coefficients (5.6% error on resistance). The experiments are rebuilt with their mean and first harmonic. The signals exhibit a good periodicity and linearity in satisfactory agreement with the reconstructed experimental signals.

Agreement with rebuilt experimental signals is good even if the the maximum of the heave force is slightly over-estimated. For this case of moderate Froude number and wave amplitude but long wave length, the periodic behaviour is rapidly captured after four wave interactions. No phase analysis has been performed and the rebuilt experimental signals are simply time adjusted to match the maximum of the computed force coefficients. It should be noticed that the ship starts at rest with an acceleration to reach its nominal speed at time $t = 2s$ following a sinusoidal law to prevent a too high response of the free-surface to high acceleration.

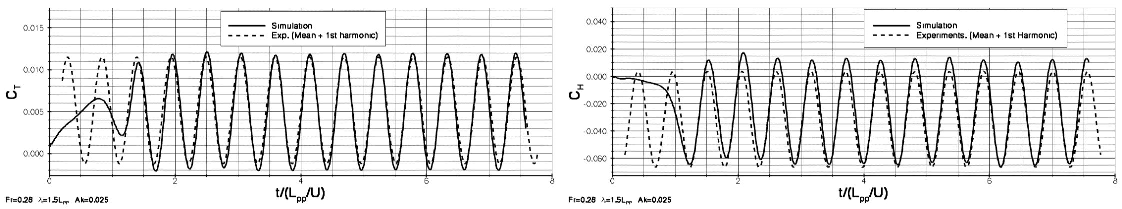

(a) Resistance

(b) Heave

Figure 1: DTMB5512 - Fr=0.28 - Time evolution of the resistance and heave to experiments

Four selected times are retained during one encounter period: time $t/T = 0$ corresponds to the time when the wave crest reaches $x/Lpp = 0$, and time $t/T = 1/2$ when the wave trough is at $x/Lpp = 0$. Fig. 2 compare the unsteady wave pattern obtained by numerical simulation with results from experiments at $t/T = 0$ only. The signals exhibit a good periodicity and linearity in satisfactory agreement with the reconstructed experimental signals. Quantitative agreement is achieved at any of the four specific times for both the locations, and the amplitudes of the waves. Compressive scheme property is also put in evidence when looking at the shape of the very crisp bow and stern waves even if the combination of the time step of $0.01s$ with grid size yields a maximum Courant number of about 20.

4.3 Influence of free trim and sinkage on flow characteristics

Effect of free trim and sinkage motion is to increase by about 12% the resistance coefficient from 0.00492 for the fixed case, to 0.00554 when the two degrees of freedom are solved. Figs 3 provide a comparison between the predicted (solid line) and experimental (symbols) pitch and heave motions. The experiments were performed at IIHR and described in [2]. The predicted pitch and heave appear to be in good agreement with the experiments, with a slight over-prediction of the computed pitch.

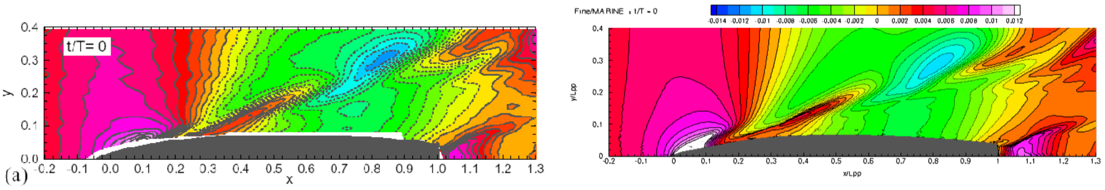

(a) Experiments (b) Computations

Figure 2: DTMB5512 - Fr=0.28 - Phase-averaged free-surface elevation at t=0.

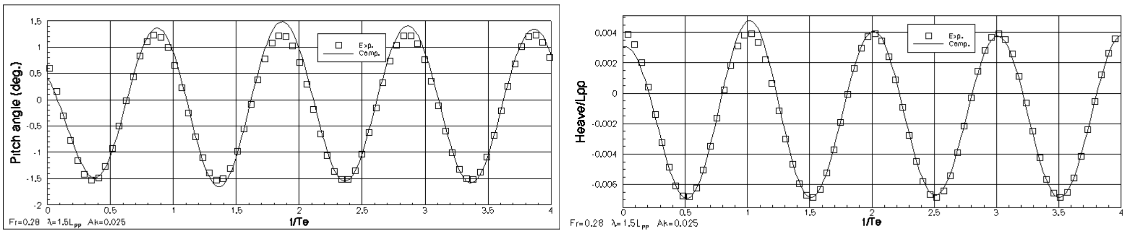

(a) Pitch (b) Heave

Figure 3: DTMB5512 - Fr=0.28 - Time evolution of the pitch and heave. Predictions (solid line) and experiments (symbols).

Fig. 4 compare the unsteady wave pattern at $t/T = 0$ only. obtained by numerical simulation with and without motion for trim and sinkage. The same selected four times used previously where selected. Even if this case could be considered as a moderate case with linear interaction from the point of view of the Froude number and the wave parameters, noticeable differences arise from these comparisons.

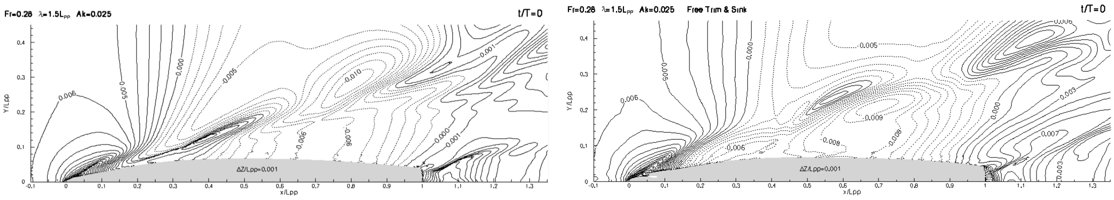

(a) Fixed (b) Free

Figure 4: DTMB5512 - Fr=0.28 - Phase-averaged free-surface elevation at t=0.. Influence of the the ship motion.

One of the easiest difference to detect concerns the bow region where it is expected that the ship radiates as the bow moves up and down. This is numerically observed at time $T0 = t/T = 0$ and $T1 = t/T = 1/4$ where the sharp diffraction line of the fixed case is attenuated. Since the free surface is not a boundary but results from the interpolation of the mass fraction 0.5, a direct comparison between the two cases is not straightforward. A possible solution consists in using a same structured Cartesian intermediate grid support on which the free surface is interpolated for each case, then in computing the difference between the wave elevations observed with and without motion. This has been done in the bow region only and shown in Fig. 5 that represents the contours of the afore-mentioned wave elevation difference between the fixed and free configuration at time T1 with a step size of $0.0005Lpp$ for the iso-contours plot. If the fixed case is taken as a reference, then the ship motion induces a reduction up to 40% of the sharp bow wave elevation at that time, indicating that the effect of motion is not negligible at all.

5 Fixed ship in short waves at high speed

5.1 Solution strategy and grid design

The extension of the computational domain remains identical, compared to the previous medium speed case but additional refinement boxes have been included in order to improve the simulation of bow and stern breaking waves. This grid is composed of 4.0 million control volumes with about 75,000 CVs located on

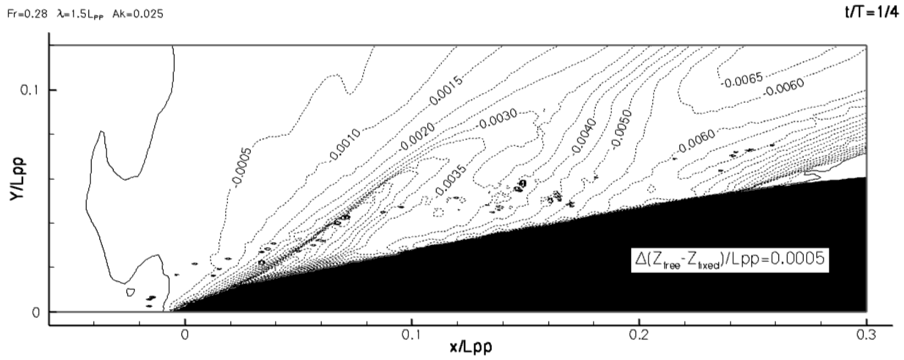

Figure 5: DTMB5512 - Fr=0.28 - Wave elevation differences at the bow at $T1 = t/T = 1/4$

the hull. The first point close to the hull is located at $y^+ = 30$, approximately. The same criteria as before is used to generate a background grid able to capture and convect these steeper and shorter waves.

5.2 Forces coefficients

A first interesting and unexpected results is the time needed to get a perfect periodic signal for the resistance and 12 wave periods are needed to get a signal of good periodicity (computed mean=0.0699, exp.=0.0737). The FFT analysis of the resistance is shown in Fig. 6. One observes, on one hand, a very good agreement between the computed and experimental signals, and on the other hand, the very rich content of the computed signals in terms of frequency. The first harmonic is of course equal to the encounter frequency but the second harmonic, in excellent agreement with the measurements, is quite strong (about 23% in terms of amplitude) and clearly associated with the breaking wave phenomena, as this will be explained in the next subsections. Even the third and fourth harmonics are clearly visible on the computed signal. The agreement on the amplitudes is very satisfactory on the heave and pitch and one notices a slight overestimation of the amplitude of the first harmonic of the resistance force.

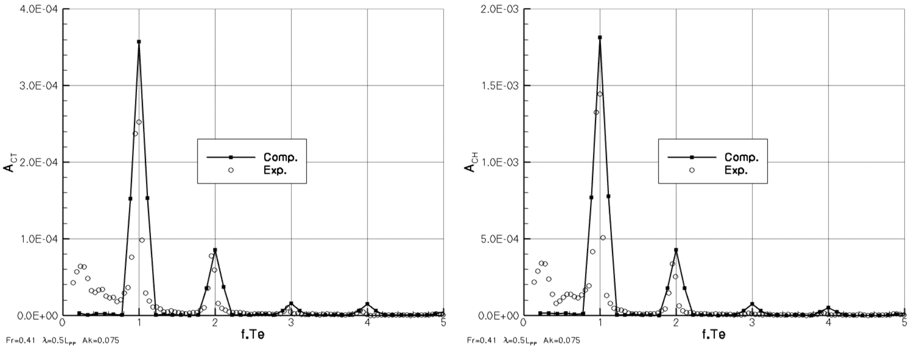

(a) Resistance

(b) Heave

Figure 6: FFT analysis of the resistance and heave for the fixed ship - Fr=0.41, Ak=0.075 case.

5.3 Unsteady free-surface elevations

In order to relate the evolution of the forces to the instantaneous topology of the free-surface elevation, one defines as previously times corresponding to the four quarter periods and Tb, Tmin and Tmax where Tb is the time at which breaking of the main bow wave occurs, Tmin and Tmax are the instants corresponding to the minimum and maximum resistance force, respectively. Fig. 7 shows the evolution of the resistance and heave with the location of the afore-mentioned specific times.

Figs. 8 and 9 provide perspective views of the computed wave profile at three specific times, Tmin, Tmax and Tb, previously defined. The inflexion point observed in the temporal evolution of the resistance which occurs at T=Tb=0.7T is clearly due to the splash of the main bow breaking wave. The main breaking phenomena is clearly illustrated and one can see the secondary shoulder breaking wave occurring at Tmin.

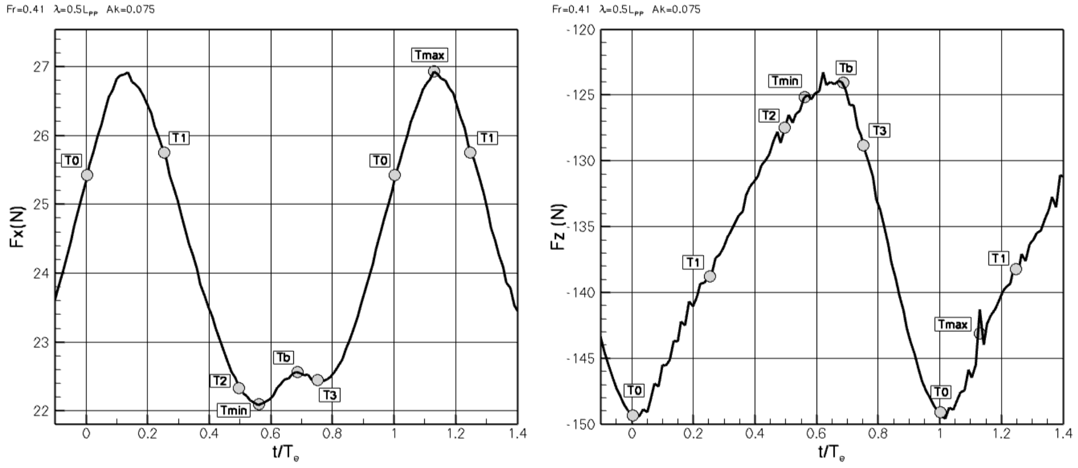

(a) Resistance

(b) Heave

Figure 7: Forces evolution over one period for the fixed ship - Fr=0.41, Ak=0.075 case.

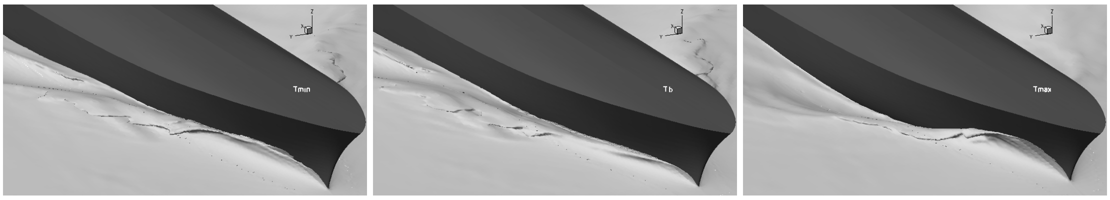

(a) Tmin

(b) Tb

(c) Tmax

Figure 8: Phase-averaged free-surface elevations close to the bow at times Tmin, Tmax and Tb for the fixed ship - Fr=0.41, Ak=0.075 case.

Near the stern, the rooster-tail breaking wave is also well defined behind an almost entirely dry transom since only a very small portion of the bottom of the transom appears to be periodically wetted. Let us recall that the flow in water and air is modelled with the same accuracy, which is a first good point in favour of the physical reliability of this simulation. To go beyond this level of accuracy, it would be necessary to automatically improve the local size of the grid by employing local and parallelised local grid adaptation according to the instantaneous location of the free-surface. And then, the free-surface tension effects will have to be also included to remain physically consistent. All these developments are currently underway and will be proposed in the next versions of this flow solver.

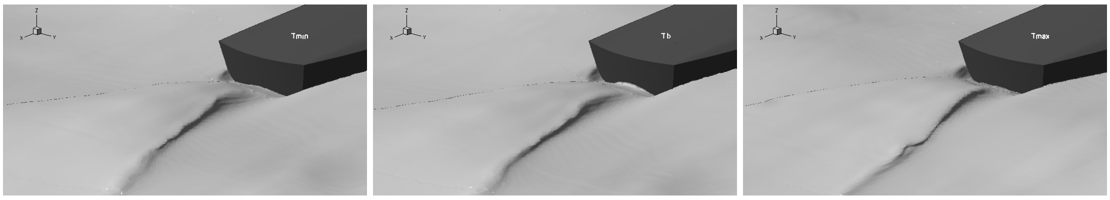

(a) Tmin

(b) Tb

(c) Tmax

Figure 9: Phase-averaged free-surface elevations close to the stern at times Tmin, Tmax and Tb for the fixed ship - Fr=0.41, Ak=0.075 case.

Figs. 10 show the evolution of the free-surface elevation at four equi-distributed phases precised in Fig. 7. The accumulation of iso-lines indicating the occurrence of breaking waves, one can observe a first large bow breaking wave followed by a smaller breaking shoulder wave observed at t/T=0.25 and t/T=0.50 extending from x=0.25 to x=0.45. One can also notice the occurrence of a well-defined rooster-tail breaking wave animated with an ondulatory motion in time.

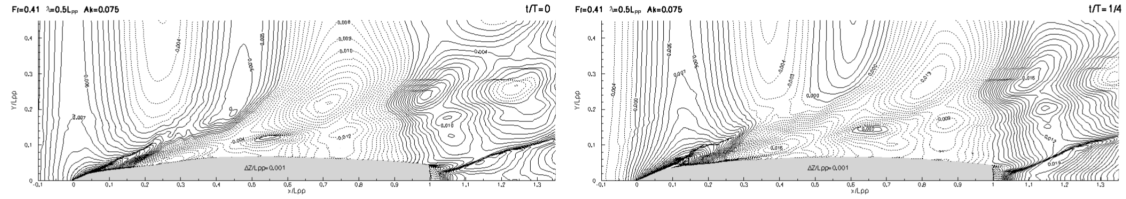

(a) t/T=0.00

(b) t/T=0.25

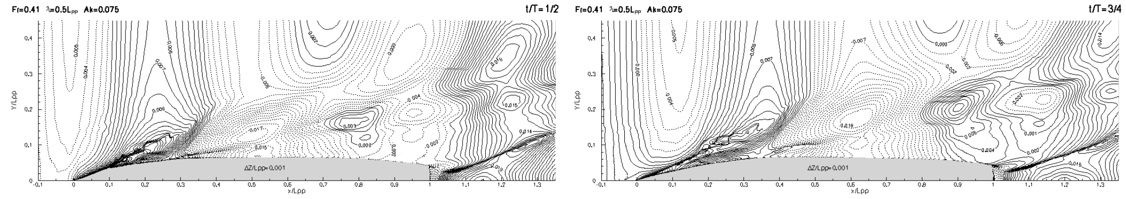

(c) t/T=0.50

(d) t/T=0.75

Figure 10: Phase-averaged free-surface elevations at the four quarter periods t/T=0, 0.25, 0.50 and 0.75 for the fixed ship - Fr=0.41, Ak=0.075 case.

6 Conclusions

This article has presented a set of viscous computations for a fixed or free pitch and heave surface combatant David-Taylor model basin (DTMB 5512) advancing in head waves. A detailed comparison on the forces coefficients, the phase-averaged free-surface elevations when available, between simulation and experiments has been shown for the fixed ship at moderate (Fr=0.28) and high (Fr=0.41) Froude number, demonstrating an excellent agreement. With a unique viscous computational tool, it has been demonstrated that it is possible to compute implicitly radiated and diffracted waves. Even for the medium speed test case (Fr=0.28), the computational results demonstrate that the radiated bow and stern waves associated with the heave and pitch of the ship can not be neglected.

References

[1] Carrica, P.; Wilson, R.; Stern, F. *Unsteady RANSE simulation of the ship forward speed diffraction problem. Computers & Fluids*, **35/6**, 545–570, (2006).

[2] Carrica, P.; Wilson, R.; Noack, R.; Stern, F *Ship motions using single-phase level set with dynamic overset grids. Computers & Fluids*, **35/9**, 1415–14330, (2007).

[3] Hay, A.; Leroyer, A.; Visonneau, M. *H-adaptive Navier-Stokes simulations of free-surface flows around moving bodies. Journal of Marine Science and Technology*, **11/1**, 1–18, (2006).

[4] Queutey, P; Visonneau, M. *An interface capturing method for free-surface hydrodynamic flows. Computers & Fluid*, **36/9**, 1481–1510 (2007).

[5] Menter, F. *Zonal two-equations $k-\omega$ turbulence models for aerodynamic flows*, *AIAA Paper*, **93-2906**, (1993).

[6] Deng, G.; Queutey, P; Visonneau, M. *Three-dimensional flow computation with Reynolds stress and algebraic stress models. Engineering Turbulence Modeling and Experiments, 6*, 389–398, (2005).

[7] Duvigneau, R.; Visonneau, M.; Deng, G. *On the role played by turbulence closures for hull shape optimization at model and full scale. Journal of Marine Science and Technology*, **153**, 1–25, (2003).

[8] Leroyer, A.; Visonneau, M. *Numerical methods for RANSE simulations of a self-propelled fish-like body. J. Fluid & Structures*, **20/3**, 975–991, (2005).

Violent seakeeping problem: an application to a patrol ship

G. Greco, T. Bazzi, M. Masia, G. Colicchio, C. Lugni
INSEAN, Rome/Italy, c.lugni@insean.it

This work is part of an ongoing experimental and numerical research activity on water-on-deck phenomena. Previous steps of the investigation have been documented in Greco *et al.* (2007) and Greco *et al.* (2008).

Experimentally, the interactions between regular incoming waves and a patrol ship model, without forward motion and free in heave and pitch, have been studied (see figure 1). The incoming wavelength and steepness were systematically varied and the occurrence of water-on-deck phenomena was recorded. Rigid ship motions, pressure on the deck, pressure and force on the deck superstructure, were measured. The flow evolution along the deck was recorded with a digital video camera.

Figure 1: 3D experiments on a patrol ship model: global view of the model and deck set-up.

Numerically, the adopted strategy couples the rigid-ship motions with the water flow along the deck. The seakeeping problem is studied with a 3D weakly-nonlinear potential flow solver based on the weak-scatter hypothesis. It implies that the free-surface conditions are linearized while the body impermeability condition is satisfied along the instantaneous wetted surface of the vessel defined by the incoming waves and the rigid body motions. Further, nonlinear contributions are retained in the Froude-Krylov and hydrostatic loads. The evolution of the shipped water is investigated by assuming shallow-water conditions onto the deck. The 2D (in the deck plane) in-deck problem is split in series of 1D coupled problems each one solved adopting a Godunov method for the main flux variables (see *i.e.* Toro 2001). The boundary conditions are enforced by means of a Level-Set technique (see *i.e.* Colicchio *et al.* 2005). Local and global induced green-water loads are estimated on the deck using an available empirical formula for the pressure (Buchner 1995). Forces and moments induced by water-shipping events are introduced as additional loads ,$\vec{F}_{wod}$, in the rigid body motions so that the seakeeping and in-deck problems can be studied as coupled. All elements of the coupled A-B solver have been verified and validated.

In the following, the model tests and the numerical results are compared and discussed within a combined analysis of the water-on-deck problem.

Model-test matrix and water-on-deck occurrence The cases studied experimentally are given in table 1 in terms of the wavelength-to-ship length ratio, λ/L, and the incoming-wave steepness, kA, with k the wave number and A the wave amplitude. The high freeboard and the relative slenderness of the ship model prevented the water shipping for $kA \leq 0.15$ and any

λ/L. Water on deck occurred for $kA \geq 0.2$ and wavelengths comparable or larger than the ship length. Because of this and due to the presence of a bulwark on the vessel, in all cases with water shipping the deck remained wet between successive events.

Table 1: Experimental test matrix. λ/L is the wavelength-to-ship length ratio and kA is the incoming-wave steepness kA, with k the wave number and A the wave amplitude. Occurrence of water on deck is indicated through the boolean variables.

kA λ/L	0.5	0.75	1.0	1.25	1.5
0.1		NO	NO	NO	NO
0.15	NO	NO	NO	NO	NO
0.2	NO	NO	YES	YES	YES
0.25	NO	NO	YES	YES	YES

Analysis: cases with water on deck Here the cases with the largest incoming wave steepness ($kA = 0.25$) are discussed in terms of water-on-deck flow and rigid ship motions.

Figure 2 shows the top view of the water-on-deck event caused by incoming waves with $\lambda = L$ as predicted experimentally (in the carriage reference frame) and numerically (in the deck reference frame). The water shipping appears globally as a Dam-Breaking type event: the liquid enters the deck from the bow (placed at the top of each plot) and bow sides and the interaction among the different water masses leads to a flow mainly along the ship centerplane (top-left plot, see *i.e.* Barcellona *et al.* 2003). As it propagates, the inner flow enlarges and becomes shallower. Experimentally the water 'flies' on the deck and eventually hits the liquid left on the deck, under the gravity action. This can not be predicted by the shallow-water theory but the flow features appear consistent with the model tests (top right plot). The jump of the water is connected with the presence of the bulwark but it could also occur without bulwark, as discussed by Barcellona *et al.* (2003) and by Greco *et al.* (2007) in the framework of Plunging *plus* Dam-Breaking type of water on deck.

At the beginning of the water shipping, the thickest layer of liquid already on the deck is near the superstructure (placed at the bottom of each plot) and is leaving it, moving mostly toward the bow and in minor quantity toward the deck sides. Eventually this liquid impacts against the water newly shipped (left-center plot). The latter is more energetic, so the resulting water front (right-center plot) moves basically toward the wall. Behind the front, the partial reflection of the water from the bulwark causes a sloshing of the water. This is symmetric in the numerical case, while small lateral disturbances destroyed such property in the model tests.

The liquid-liquid interaction causes spray in the physical case which can not be handled by the numerical solver. Both numerical and experimental solutions show a water-off-deck phase from the sides of the propagating water front (see right-center and left-bottom plots) and a later impact of the water against the superstructure (right-bottom plot). The features described repeat periodically in time as a new event is caused.

Globally the agreement is quite promising and is confirmed when longer incoming waves are examined (see figure 3 for $\lambda = 1.5L$). In this case the water-on-deck phenomena keep the same general behavior discussed, but the events become less severe: the water front moves more slowly and the interaction with the wall appears less strong.

Figure 4 provides the heave and pitch time histories for $\lambda = L$. Despite in the resonance regime, the motions are limited. This could be the result of cancellation effects. The experimental results are compared with linear and weakly-nonlinear solutions accounting for or less the green-water

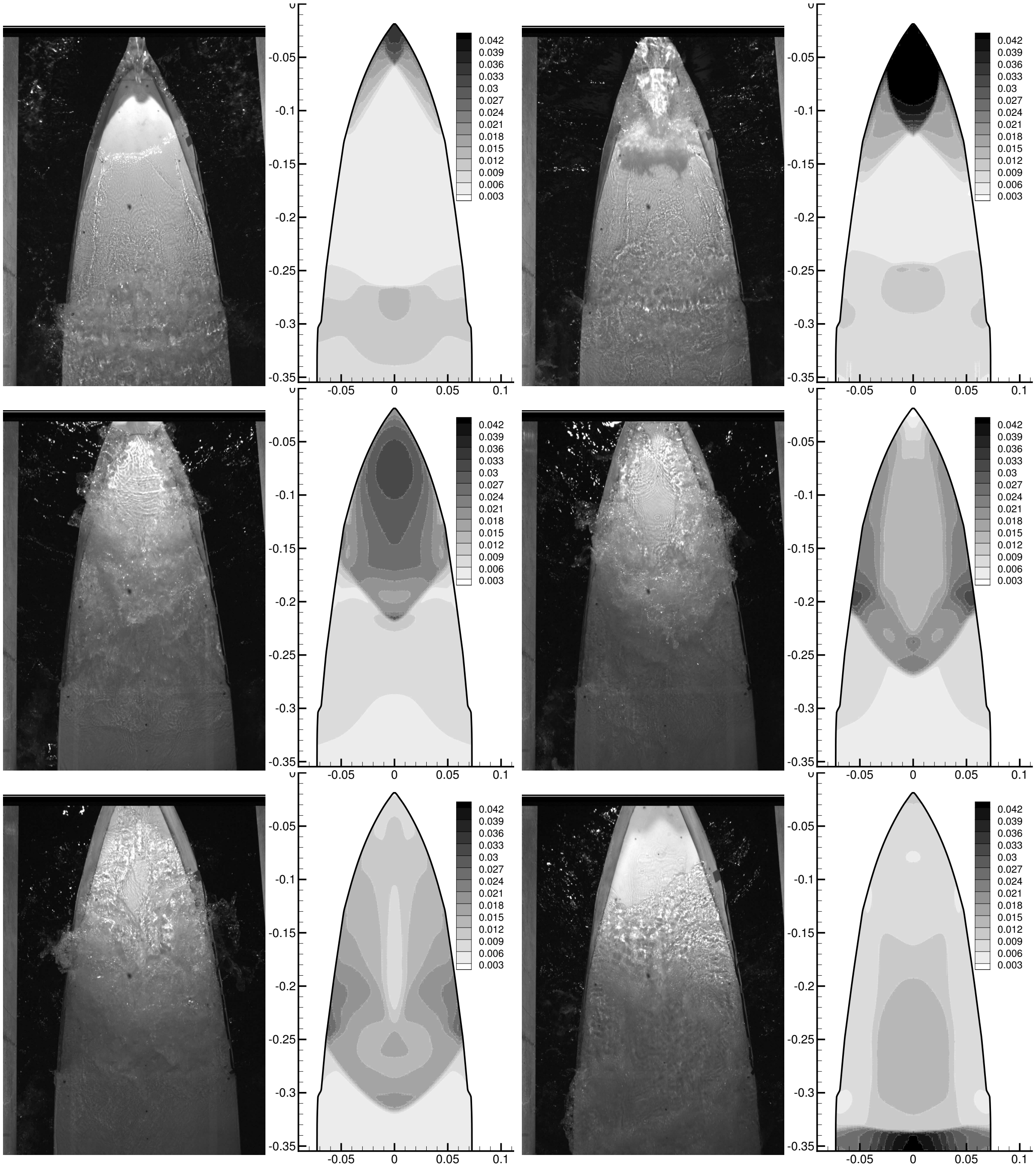

Figure 2: Water-on-deck event: top view. In each plot, experiments (left) and numerics (right). Time increases from left to right and from top to bottom with time intervals: $0.04T$, $0.08T$, $0.29T$, $0.37T$, $0.46T$ and $0.67T$. $\lambda = L$ and $kA = 0.25$. Numerical simulations with $\Delta x = \Delta y \simeq 0.0015L$ for the in-deck problem and with $\Delta t = 0.01T$ for the rigid-motion time integration. T is the incoming-wave period.

loads, $\vec{F}_{wod}$.

Examining the heave motion, the linear solution overestimates both peak and trough and the results are practically not improved when the water-on-deck action is included. The weakly-nonlinear effects allow to recover the trough of the motion but unphysical higher harmonics appear when $\vec{F}_{wod}$ is neglected. The inclusion of such loads provides a satisfactory agreement with the model tests, though the nonlinearities in the trough are not predicted correctly.

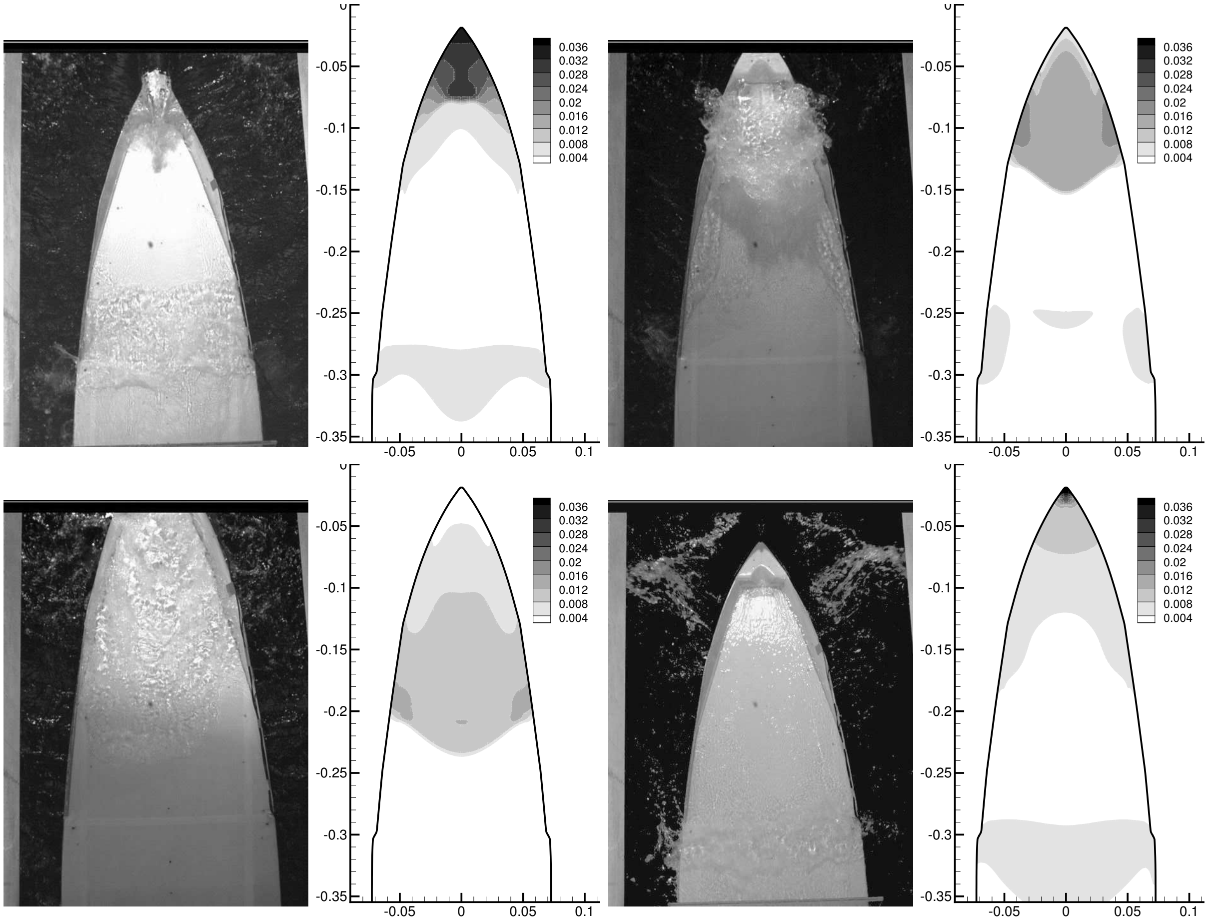

Figure 3: Water-on-deck event: top view. In each plot, experiments (left) and numerics (right). Time increases from left to right and from top to bottom with time intervals: $0.1T$, $0.24T$, $0.48T$ and T. $\lambda = 1.5L$ and $kA = 0.25$. Numerical simulations with $\Delta x = \Delta y \simeq 0.0015L$ for the in-deck problem and with $\Delta t = 0.01T$ for the rigid-motion time integration. T is the incoming-wave period.

Once phased the heave motion, the linear pitch solution shows a clear phase shift which is not avoided when the green-water loads are considered, while it is reduced by the weakly nonlinear effects. The peaks and troughs are better handled when $\vec{F}_{wod}$ is included, but some discrepancies with the experiments are present.

As λ increases (see figure 5 for $\lambda = 1.5L$) the motions enlarge but the nonlinear and local effects reduce, together with the water-on-deck severity. As a result, the improvement using a weakly-nonlinear solution is more limited and still connected with a peak-trough prediction and a phase-shift correction. It is also evident a more peaked behavior in the measurements and the weakly-nonlinear solution with respect to the linear results.

The present analysis suggests that, close to $\lambda = L$, the interaction between the water-on-deck events and the weakly-nonlinear contributions in the Froude-Krylov and hydrostatic terms plays an important role and affects the rigid motions. Unlike, the green-water loads by themselves are not relevant for the motions. As λ increases, both the mentioned nonlinear interaction and the water-shipping severity become limited.

Figure 6 examines the effect of radiation and scattering effects on the rigid motions for $\lambda = L$ and $1.5L$. This is made by avoiding the corresponding wave-elevation contribution from the boundary conditions along the deck profile, within the shallow-water simulation. For this vessel, in the examined conditions the wave radiation is very limited. So there is no visible effect of the radiation waves on the motions, while the scattering phenomena are important for all the incoming wavelength-to-ship length ratios considered.

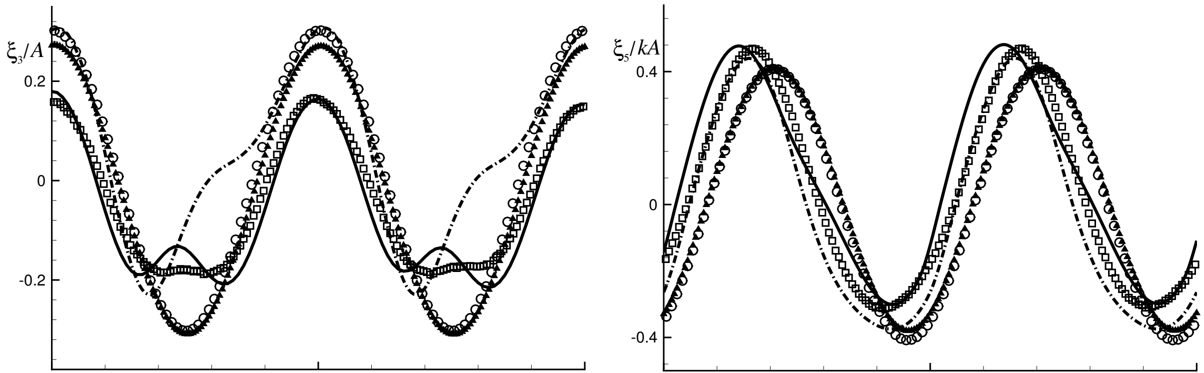

Figure 4: Heave (left) and pitch (right) time histories. Empty Squares: experiments; empty circles and full triangles: linear without and with water on deck, respectively; dash-dotted and solid lines: weakly nonlinear without and with water on deck, respectively. $\lambda = L$ and $kA = 0.25$. T is the incoming-wave period.

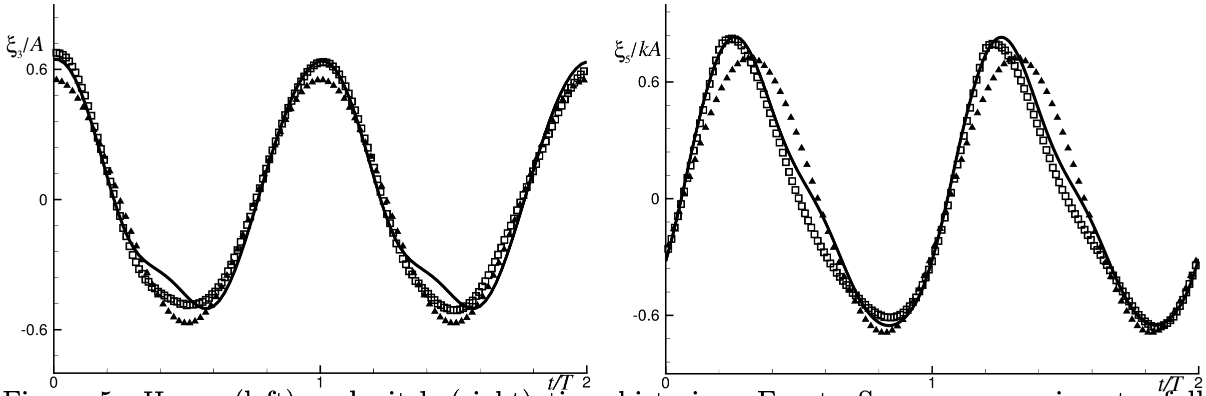

Figure 5: Heave (left) and pitch (right) time histories. Empty Squares: experiments; full triangles: linear with water on deck; solid lines: weakly nonlinear with water on deck. $\lambda = 1.5L$ and $kA = 0.25$. T is the incoming-wave period.

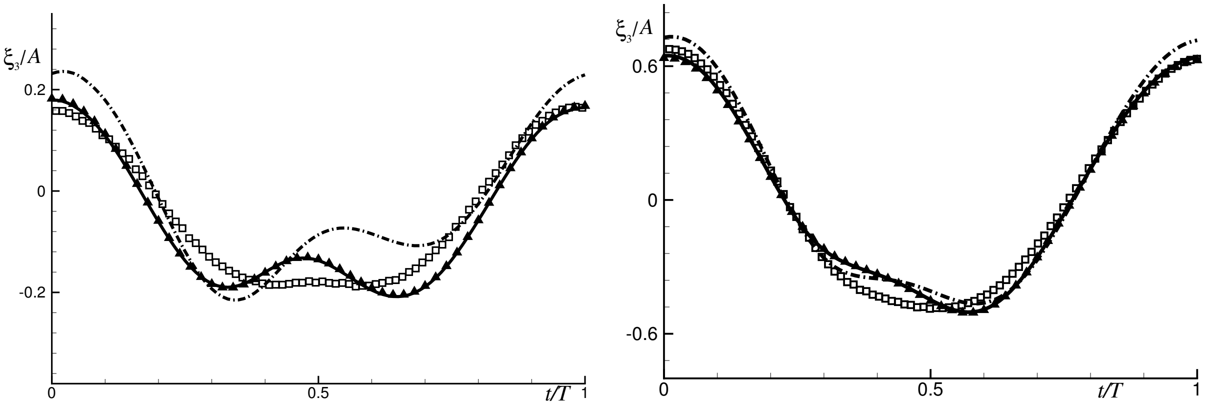

Figure 6: Heave time history: $\lambda = L$ (left) and $\lambda = 1.5L$ (right). Empty Squares: experiments; solid lines: weakly nonlinear; full triangles: weakly nonlinear without radiating effects; dash-dotted lines: weakly nonlinear without scattering effects. $kA = 0.25$ and T is the incoming-wave period.

Conclusions The occurrence of 3D water-on-deck events is studied experimentally and numerically. In the model tests, regular incoming waves have been generated and their interaction with a patrol ship model, free in heave and pitch and without forward motion, were studied. In the numerical simulations, a 3D weakly-nonlinear potential flow solver for the seakeeping problem is combined with a nonlinear shallow-water solver for the water flow onto the deck caused by water-shipping events. The model tests and the numerical results have been used to analyze the water-on-deck phenomena and their influence on the heave and pitch motions.

For the examined conditions and geometry, the analysis highlighted the importance of weakly-nonlinear effects and the role played by the interaction of the water-on-deck phenomena with the Froude-Krylov and hydrostatic loads, in particular near $\lambda = L$. The studied vessel is characterized by a fine bow, in the framework of platforms it is interesting to investigate if similar conclusions apply also to a blunt bow. This aspect is left to a future research.

The present research activity is partially supported by the Centre for Ships and Ocean Structures (CeSOS), NTNU, Trondheim, within the 'Violent Water-Vessel Interactions and Related Structural Loads' project, partially supported by the Italian Navy within the '6-dof RANSE' project and partially done within the framework of the 'Programma di Ricerca di Idrodinamica Navale 2007-2009' funded by *Ministero Infrastrutture e Trasporti.*

References

BARCELLONA, M., M. LANDRINI, M. GRECO, AND O. FALTINSEN (2003). An Experimental Investigation on Bow Water Shipping. *to appear on Journal Ship Research 47*(4), 327–346.

COLICCHIO, G., M. LANDRINI, AND J. CHAPLIN (2005). Level-set Computations of Free Surface Rotational Flows. *Journal of Fluids Engineering, Transactions of the ASME 127*(6), 1111–1121.

GRECO, M., T. BAZZI, G. COLICCHIO, AND C. LUGNI (2008). 3D ship-seakeeping problem: weak-scatterer theory *plus* shallow-water on deck. In *Proc. of* 23th *Int. Workshop of Water Waves and Floating Bodies*, Jeju, Korea, pp. 1–4.

GRECO, M., G. COLICCHIO, T. BAZZI, AND C. LUGNI (2007). Numerical and Experimental Investigation of Violent Seakeeping Flows. In *Proc. of Int. Comference of Violent Flows VF-2007*, Fukuoka, Japan.

GRECO, M., G. COLICCHIO, AND O. M. FALTINSEN (2007). Shipping of Water on a Two-dimensional Structure. Part 2. *J. of Fluid Mech. 581*, 371–399.

TORO, E. (2001). *Godunov Methods: Theory and Applications.* Kluwer Academic/Plenum Publishers.

Simulation of the hull dynamics with RANSE method.

Marek Kraskowski

Ship Design and Research Centre S.A., Poland
marek.kraskowski@cto.gda.pl

The paper presents the mathematical model of the 6-DOF motion module, developed lately by CTO S.A. as an extension of RANSE solver COMET, as well as first results obtained with it. Although the RANSE method is considered inefficient for the simulations of rigid body dynamics due to high computational effort, and alternative methods like strip theory or panel methods are preferably used whenever possible, developing the rigid body motion solvers based on RANSE is still worth taking into account. Unlike the models based on strip theory or potential flow, RANSE model (using the VOF method for multiphase flows) has no limitations of the shape complexity, free surface deformation or motion amplitudes.

Coupling the COMET solver with simple 2D motion module is successfully used in CTO S.A. since 2005 for evaluating the dynamic trim and sinkage of the ship hull. Some experience gained from using this module was used in developing the 6DOF module, however, coding itself was done from scratch in order to obtain better legibility of the code and the structure of files.

It was intended to keep the mathematical model as simple as possible, taking advantage of the feasibility of numerical methods. Description of the mathematical model requires defining the coordinate systems first – they are defined as follows:

- Global coordinate system (GCS) – $0, x, y, z$ – non-rotating, non-accelerating, fixed in space or moving with constant ship speed
- Body coordinate system (BCS) – $0, x_0, y_0, z_0$ – fixed to the body centre of gravity, axes aligned with the body's principal axes of inertia, moving and rotating together with the body
- Temporary coordinate system (TCS) – $0, x_\omega, y_\omega, z_\omega$ – "Z" axis aligned with the immediate angular velocity vector, "X" and "Y" axes defined arbitrarily so as to create the right-handed coordinate system

The basic motion equations in the following form were used:

$$\begin{aligned} m \cdot \ddot{x}_C &= \sum_i F_{Xi} \\ m \cdot \ddot{y}_C &= \sum_i F_{Yi} \\ m \cdot \ddot{z}_C &= \sum_i F_{Zi} \end{aligned} \qquad (*)$$

$$\begin{aligned} I_{X0} \cdot \ddot{\varphi}_{X0} - \left(I_{Y0} - I_{Z0}\right) \dot{\varphi}_{Y0} \dot{\varphi}_{Z0} &= \sum_i M_{X0i} \\ I_{Y0} \cdot \ddot{\varphi}_{Y0} - \left(I_{Z0} - I_{X0}\right) \dot{\varphi}_{Z0} \dot{\varphi}_{X0} &= \sum_i M_{Y0i} \\ I_{Z0} \cdot \ddot{\varphi}_{Z0} - \left(I_{X0} - I_{Y0}\right) \dot{\varphi}_{X0} \dot{\varphi}_{Y0} &= \sum_i M_{Z0i} \end{aligned} \qquad (**)$$

where x_C, y_C, z_C – coordinates of the body centre of gravity in GCS, m is the body mass, I_{X0}, I_{Y0}, I_{Z0} - moments of inertia in BCS, $\ddot{\varphi}, \dot{\varphi}$ - angular accelerations and velocities in BCS, F and M are forces and moments in BCS.

An advantage of this approach is that the moments of inertia remain constant when the body moves, however, the angular velocity and moments must me transformed from GCS to BCS and vice versa in each time step.
Using the additional, temporary coordinate system following the angular velocity requires calculating it in each time step, but greatly simplifies the procedure of rotating the body.

The algorithm of the computations in 6 DOF can be then described as follows (only the procedure for computing the angular motion is described, for the translational motion the procedure is quite simple) :

- Initialize the body motion solver: set the initial location of gravity centre in GCS, initial angular velocity and acceleration in BCS
- Compute the moments in GCS (COMET)
- Transform the moment vector to BCS
- Compute the angular acceleration in BCS for current time step. Equations (**) are nonlinear, so the values of angular velocity are taken from previous time step (marked with OLD), e.g.:

$$\ddot{\varphi}_{X0} = \frac{M_{X0} + \left(I_{Y0} - I_{Z0}\right)\dot{\varphi}_{Y0}^{OLD} \cdot \dot{\varphi}_{Z0}^{OLD}}{I_{X0}}$$

- Compute the angular velocity in BCS, e.g. $\dot{\varphi} = \dot{\varphi}_{X0}^{OLD} + \ddot{\varphi}_{X0} \cdot \Delta t$ (Δt is the time step)
- Transform the angular velocity vector to GCS
- Define the TCS
- Compute the angle of rotation for current time step: $\Delta\varphi = |\omega| \cdot \Delta t$
- Rotate the BCS in TCS by $\Delta\varphi$ - new BCS obtained (at this step, the computational mesh is being rotated in TCS by $\Delta\varphi$)
- Transform the current angular velocity to new BCS
- Go to next time step.

To increase the stability of the motion computations, in each time step the acceleration value used in integrating the body motion is computed as follows:

$\ddot{\varphi} = 0.5\left(\ddot{\varphi} + \ddot{\varphi}_{OLD}\right)$ where $\ddot{\varphi}_{OLD}$ is the value from previous time step.

The procedure described above is appropriate for computing the motion of free floating body. Such problem, however, hardly ever appears in evaluating the ship hull quality in respect of hydrodynamics. In manoeuvring or seakeeping tests, the motion in some degrees of freedom is usually fixed. Including the constraint conditions in the presented mathematical model is quite difficult, as the equations are formulated for body coordinate system and the constraints are defined in global coordinate system. This problem has not been solved yet, but one of the ideas to be exercised is to introduce the artificial springs of large, but finite stiffness and strong numerical damping on chosen degrees of freedom.

First test of the 6-DOF module was done for the cube, dropped freely into the water. The cube dimensions were 0.2m x 0.2m x 0.2m , and the computational domain was the sphere of radius 1.0m. The time step of the simulation was 0.005s, 5 time steps per one outer iteration were executed, Euler implicit scheme for time integration was used. Few tests with Three-time-levels implicit scheme revealed instability of this scheme in body motion simulations, and therefore it was not used furthermore.

Fig.1 presents the mesh on the cube surface and one section of the mesh (o-grid type). Fig.2 presents the free surface shape and the cube location in two chosen instants of time.

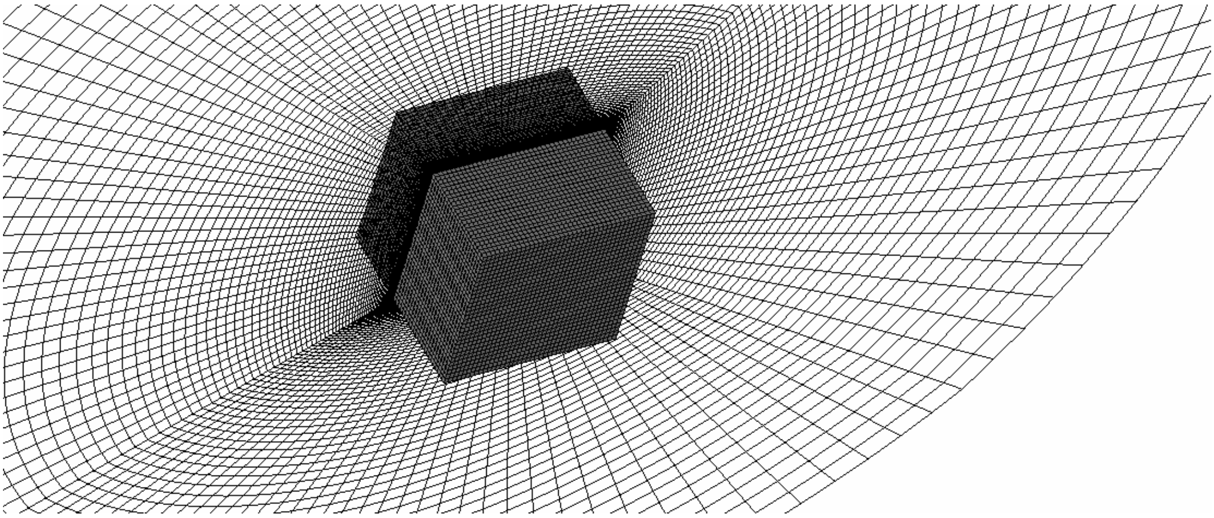

Fig. 1Computational mesh for the cube.

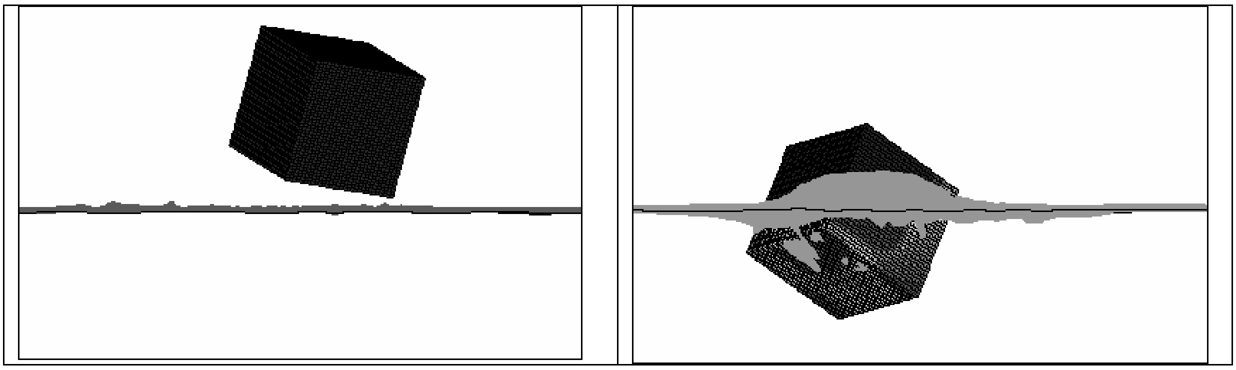

Fig. 2 Results of the free drop simulation.

No validation of the test case was done; the validity of the rigid body motion module was assessed basing on the motion animation only. No unphysical behaviour was observed, however, the accuracy of the method must be further validated basing e.g. on the high speed video recording of the experiment.

As mentioned above, the 6-DOF module is not prepared yet for ship seakeeping simulation, because the motion constraints are not implemented yet. However, simulation of the ship motion in 2D (pitch and heave) in heading and following seas is already possible, just by neglecting the motion in all other degrees of freedom. The results for two cases (Wigley hull and the megayacht) are presented here.

The boundary conditions for the simulation of ship behaviour in waves were defined as follows (*Wöckner et al., 2007*):

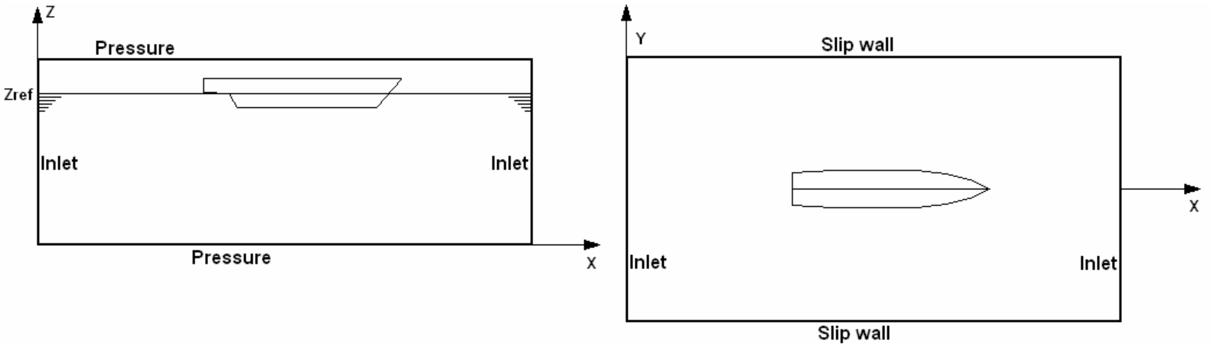

Fig. 3 Boundary conditions for the simulation of waves.

The formulae defining the velocity distribution at the inlets are:

$$V_X = e_X \cdot \left(V_0 + \omega_e \cdot \zeta \cdot \exp\left(k \cdot \left(z - z_{ref}\right)\right) \cdot \cos\left(k \cdot S - \omega_e \cdot t\right)\right)$$

$$V_Y = e_Y \cdot \left(V_0 + \omega_e \cdot \zeta \cdot \exp\left(k \cdot \left(z - z_{ref}\right)\right) \cdot \cos\left(k \cdot S - \omega_e \cdot t\right)\right)$$

$$V_Z = \left(\omega_e \cdot \zeta \cdot \exp\left(k \cdot \left(z - z_{ref}\right)\right) \cdot \sin\left(k \cdot S - \omega_e \cdot t\right)\right)$$

where:

V_0 – ship speed, k – wave number: $k = \frac{2\pi}{\lambda}$,

ω_e – encounter frequency: $\omega_e = \sqrt{g \cdot k} + V_0 \cdot k$

z_{ref} – average water level, ζ – wave amplitude, t - current time

$e = \left[e_X, e_Y\right]$ – unit vector defining the wave direction. In the coordinate system presented in Fig.3, $e = [-1{,}0]$ for heading seas and $e = [1{,}0]$ for following seas

S – coordinate measured along the wave direction: $S = e_X \cdot x + e_Y \cdot y$

The inlet boundary conditions defined as above are appropriate for the waves of arbitrary direction, which can be defined just by modifying the components of vector e. At the pressure boundary conditions, the pressure resulting from the wave motion was neglected, assuming the deep water conditions – only the hydrostatic pressure was taken into account.

The simulation for the first case (Wigley hull) was carried out for the following conditions:

- Hull length: 5m
- Hull speed: 0
- Wave length: $\lambda = 5m$
- Wave amplitude: $\zeta = 0.1m$

The mesh density for 3D case (Wigley hull) is presented in Fig.4 (deformed x-scale).

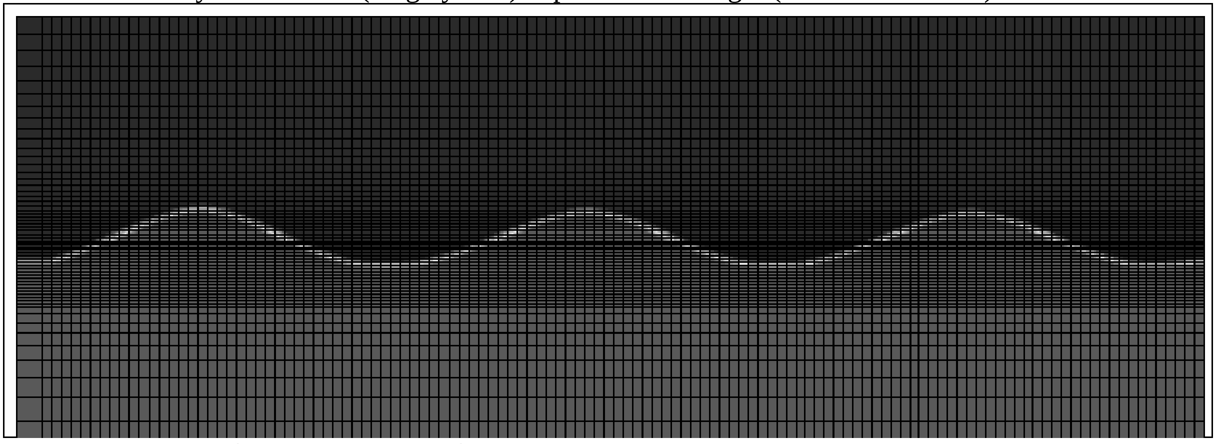

Fig. 4 Mesh density for the simulation of waves.

The parameters of unsteady simulation were similar to that used in the free drop simulation – time step 0.005 s, 5 outer iterations per time step. At the beginning of the simulation, the hull was kept fixed to let the flow stabilize, then after app. 3.5 seconds of simulation, the hull motion was released. The time history of pitch angle is presented in Fig.5.

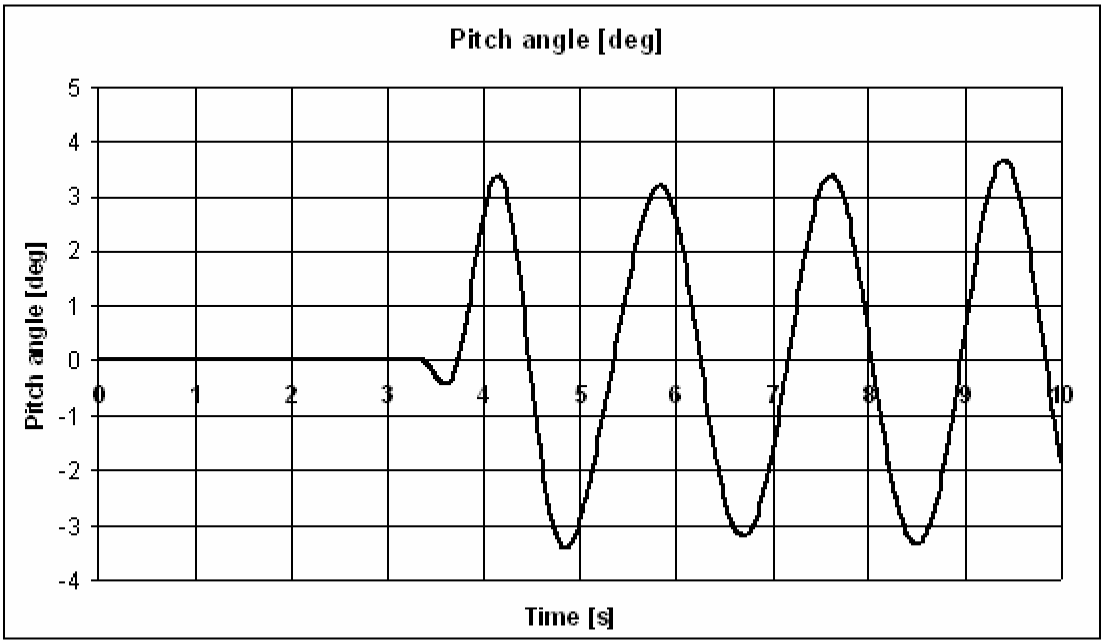

Fig. 5 Time history of pitch angle.

As can be seen in the sketch above, the computed hull motion is not perfectly periodic, however, the periodicity can be considered sufficient, moreover, the curve is very smooth, which proves high robustness of the method. It should be noted that, in the presented simulation, entire mesh is moving together with the hull. The location of the free surface in the domain in its initial position (0 pitch angle) and at the pitch angle close to maximum is presented in Fig.6

Fig. 6 Wave simulation in moving domain

The fact that the domain is pitching must be taken into account in the process of mesh generation – the mesh density should be kept high in the entire region where the free surface is expected to appear, so as to avoid smearing the wave. There should be also some space left between the free surface and the upper wall of the domain – if the free surface "touches" it, the solution diverges immediately.

Another attempt on the simulation of ship in waves was carried out for an existing ship hull in model scale – the 60m megayacht. Visualization of the solution for two chosen time instants is presented in fig.7.

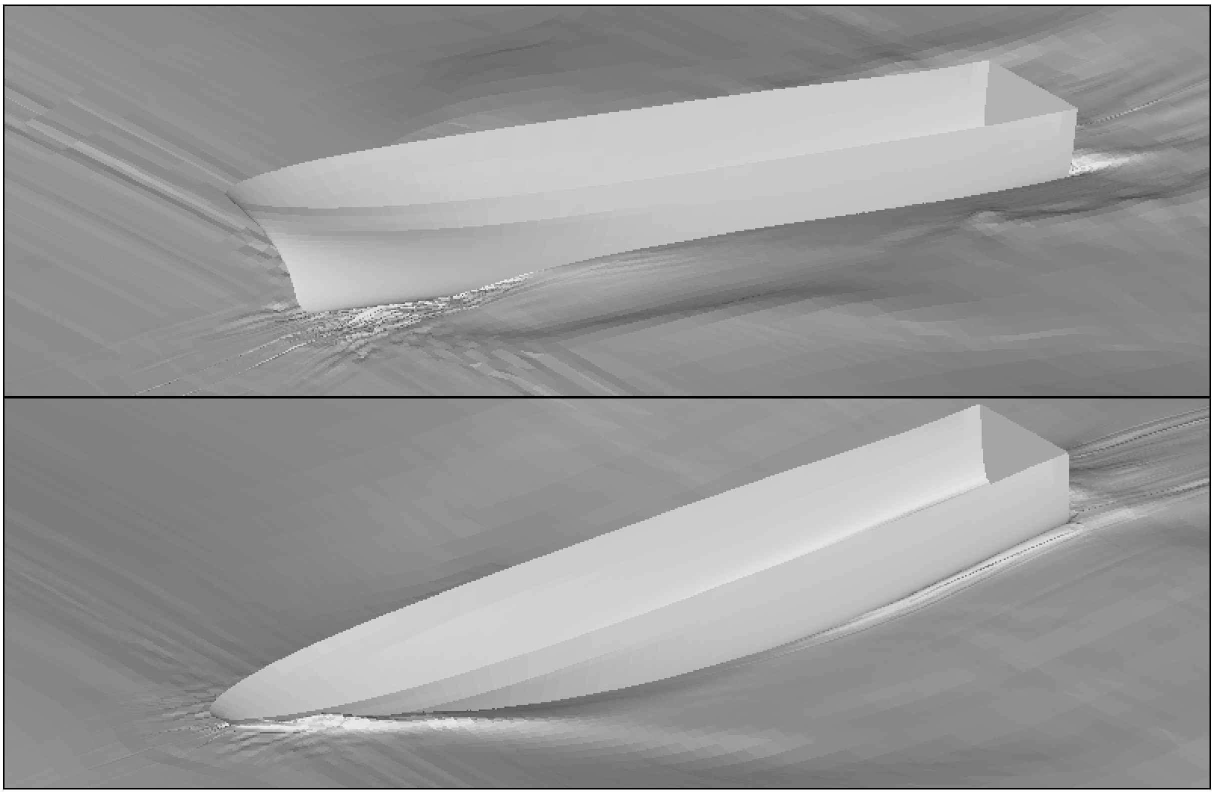

Fig. 7 Simulation of the megayacht in waves

Although in the beginning of the simulation the hull motion was looking correct, the solution diverged after first period of pitching, which indicates the need for further work on the stability of the method. The tasks for the nearest future can be then defined as follows:

- Analyze the phenomena based on model experiment.
- Solve the problem with the solution stability for the real hull shape (or, maybe, find the limitations of the method).
- Validate the results basing on the experiment.

The presented method will be used in the European project "CREATE3S" to check the possibilities of CFD in computing the added resistance in waves. The resistance will be compared for two container vessels, one with standard bow type and one with X-Bow. The results of the comparison will be especially interesting due to the fact that strip theory is not capable of producing reliable comparative results for this case.

References:
[1] Wöckner K., Soukup P., Rung T., 2007,*"Boundary conditions for free surface flow"*, NuTTS'07
[2] Azcueta R., 2001, *"Computation of Turbulent Free-Surface Flows Around Ships and Floating Bodies"*, PhD thesis

Numerical Analysis of the Three-Dimensional Viscous Flow around a Propelled Ship

Ana-Maria Tocu,* *Adrian Lungu*
Department of Ship Hydrodynamics, “Dunarea de Jos” University of Galati, Romania
Email: ana.tocu@ugal.ro

The design of the ship affects directly the quality, performance, safety and environmental elements. It has a significant impact on production, operation, and maintenance costs. The initial design stage is important for a successful design. It is essential to start with as optimal parameters as possible. By using information from a hull database it is possible to perform parametric hull optimization at a very early stage of the design process. For hydrodynamic assessment of ship hulls in the optimization process, CFD codes play an important role. Their use in the optimization chain requires that they are accurate, fast, reliable, and that they communicate with the other components in the chain. The paper focuses on numerical simulations of viscous flow around a blunt ship hull with and without an acting propeller. Both viscous and wave effects are numerically calculated directly using the complete Reynolds-averaged Navier-Stokes equations (RANS hereafter) for the entire flow field with a set of appropriate boundary conditions. The aim of application of the viscous flow calculation method is to quantify the available options for improving the hydrodynamic characteristics of the hull form. One of the most important application fields of viscous flow methods is the prediction of the wake distribution of full-scale ships. The flow around the stern of a ship hull is very complex: high Reynolds numbers, three-dimensionally curved surfaces and often a pair of longitudinal vortices. These are created where the flow passes over the region of high curvature between the bottom and the bilge. The bilge vortices hit the propeller disk and cause distortion of the flow into the propeller disk. Such distortions affect the efficiency of the propeller and can cause vibration, noise and cavitation. Lifting surfaces such as propeller blades have strong tip vortices that may induce cavitation and therefore noise. For the design of the propeller and hull is therefore important to be able to predict these vortices. The prediction of wake distribution, pressures on the hull and limiting streamlines are proved to provide reliable and valuable information of complicate phenomena, such as free-surface flow and hull-propeller interaction, still demand more detailed investigation and further validation. The flow field around a blunt hull form is numerically studied by solving the flow problem with and without free surface. Closure to the turbulence is attained through a modified k-ω SST based model. The paper focuses on numerical simulations of viscous flow around a ship hull with and without an acting propeller. Comprehensive analysis of the propeller behavior behind the ship is carried out to emphasize the predicted wake field as well as to grasp a global understanding on how the turbulence modeling works on such a strong vortical flow. The resistance coefficients computed by solving numerically the RANS equations are validated against model tests results.

Hull forms and grid generation

The aim of any numerical simulation of the flow around a ship is that of quantifying the hydrodynamic performances of the hull in order to optimize the lines plan for reducing the water resistance. The ability of carrying out effective numerical processes for the approximation of CFD problems depends on the geometric modelling and grid generation phases which often require up to 80% of the total labour cost. The hull chosen for the present study is a 7500 TDW chemical tanker having the main particulars summarized in Table 1. An offset file based entirely on the lines plan depicted in Figure 1 defines the geometry of the ship. The offset file has been carefully prepared to discretize the hull for the numerical investigation. Numerical grid generation is also a crucial initial step of any computational simulation problem. A high quality grid generation can avoid difficulties arising in the computational phase.

Table 1. Main particulars at full loading condition

LOA	115.4	[m]
LBP	112.6	[m]
Breadth moulded	18.2	[m]
Draught	6.4	[m]
Ship speed	15	[knots]

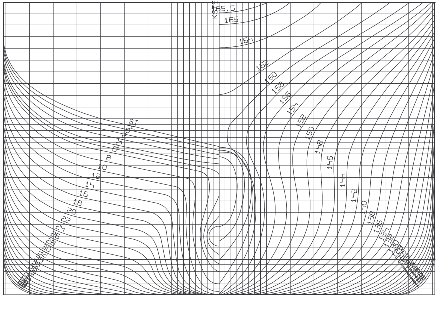

Figure 1. Lines plan

A mono-block 3D structured grid was generated at first, clustered created near the bow and stern regions in the longitudinal direction, as well as in the proximity of the hull surface in the normal direction. By using suitable parameters for viscous computations, the 3D overlapping grid generator provided a grid having 260x60x60 nodes in the longitudinal, transverse and normal direction, respectively, and the inner surface fitted to the hull, see Figure 2, which shows the grid around the ship extremities. Taking into account that the solver does not use wall laws, another clustering of cells was needed closest to the hull surface where the height of the cells should be very thin. For generating this single block grid, the program computes the outer boundaries, controlling permanently the orthogonality functions. Interpolation weighting factors are computed and saved for all interpolation points at the edge of each grid. To avoid mismatching, special techniques are used to handle the interpolation between the extremely thin cells close to boundaries where the no-slip condition is to be applied. After the viscous calculations of the flow around the ship without propeller, an additional cylindrical component grid (having 12x16x16 grid nodes) was added to simulate the operating propeller.

Figure 2 shows the circular grid fitted behind the ship to create both symmetric and three-dimensional effect of the propeller in order to compute the trust and torque. The actuator disk may simulate the propeller and the body forces can be computed by a lifting line propeller analysis method that runs interactively with the RANS solver. Using the velocity computed in each numerical cell within the propeller disk, the circulation is computed and therefore the axial and tangential body forces are computed. These forces are returned to the flow solver in an iterative process. No-slip faces resolved directly in the RANS approach represent the propeller and hull geometries and they become parts of the viscous flow solution. The method can provide a rather detailed information about the stern and propeller flows.

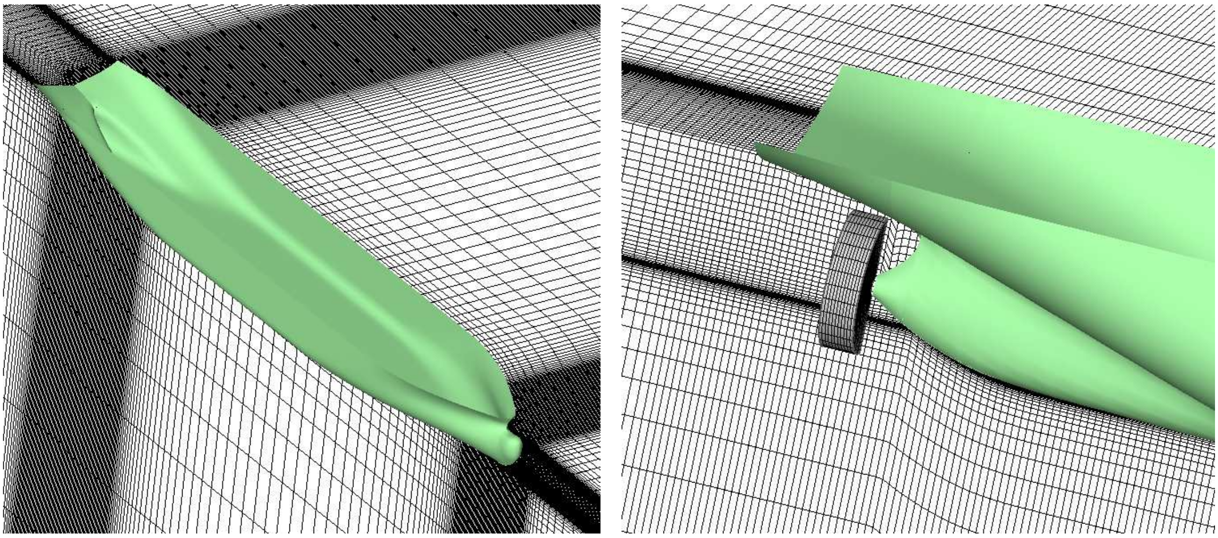

Figure 2. Computational grid

Numerical method

The reported research is based on the use of the Shipflow commercial code, in which the governing equations for turbulent flow are the RANS equations for momentum transport and the continuity equation for mass conservation. For turbulence closure, the k-ω SST model is employed. In a Cartesian tensor notation form, by making use of the Reynolds decomposition, the unsteady incompressible RANS and continuity equation may be written as follows:

$$\frac{\partial u_i}{\partial t}+\frac{\left(u_j u_i+\overline{u_j^{'} u_i^{'}}\right)}{\partial x_j}=\overline{R_i}-\frac{1}{\rho}\frac{\partial p}{\partial x_i}+\frac{\partial}{\partial x_j}\left(\nu\left(\frac{\partial u_i}{\partial x_j}+\frac{\partial u_j}{\partial x_i}\right)\right)$$

$$\frac{\partial u_i}{\partial x_i}=0 \qquad (1)$$

where x_i represents the Cartesian coordinates, $x_i=(x,y,z)$, u_i are the time averaged velocity components in Cartesian directions, R_i is the volume force, p is the time averaged pressure, $p^{'}$ is the fluctuating pressure, ρ is the density, υ is the kinematic viscosity, $\nu=\mu/\rho$, and μ is the dynamic viscosity. Using the Boussinesq approximation, the Reynolds stress tensor $\rho\overline{u_i^{'}u_j^{'}}$ can be written as:

$$\rho\overline{u_i' u_j'} = -\mu_T\left(\frac{\partial u_i}{\partial x_j}+\frac{\partial u_j}{\partial x_i}\right)+\frac{2}{3}\rho k\delta_{ij}$$

where δ_{ij} is Kronecker delta and k is the turbulent kinetic energy. The new averaged equations result in:

$$\frac{\partial u_i}{\partial t}+\frac{\partial\left(u_j u_i\right)}{\partial x_j}=\overline{R_i}-\frac{1}{\rho}\frac{\partial p}{\partial x_i}-\frac{2}{3}\frac{\partial k}{\partial x_i}+\frac{\partial}{\partial x_j}\left(\nu_E\left(\frac{\partial u_i}{\partial x_j}+\frac{\partial u_j}{\partial x_i}\right)\right) \tag{2}$$

where ν_E is the effective kinematic viscosity. The Reynolds stresses are related to the mean rate of strain through an isotropic eddy viscosity, ν_T calculated using Menters combination of k-ω and k-ε turbulence models:

$$\frac{\partial k}{\partial t}+\frac{\partial\left(u_j k\right)}{\partial x_j}=-\overline{u_i' u_j'}\frac{\partial u_i}{\partial x_j}-\beta^* k\omega+\frac{\partial}{\partial x_j}\left(\left(\nu+\sigma_k\nu_T\right)\frac{\partial k}{\partial x_j}\right) \tag{3}$$

$$\frac{\partial \omega}{\partial t}+\frac{\partial\left(u_j \omega\right)}{\partial x_j}=-\frac{\gamma}{\nu_T}\overline{u_i' u_j'}\frac{\partial u_i}{\partial x_j}-\beta^*\omega^2+\frac{\partial}{\partial x_j}\left(\left(\nu+\sigma_\omega\nu_T\right)\frac{\partial \omega}{\partial x_j}\right)+2\sigma_{\omega_2}\frac{1-F_1}{\omega}\frac{\partial k}{\partial x_j}\frac{\partial \omega}{\partial x_j} \tag{4}$$

Here $\beta^*, \gamma, \sigma_k, \sigma_{\omega_2}$ are the modeling coefficients for k-ω equations and F_1 is the switching function for handling the change between the ω and ε equations. Since the standard k-ε model often does not produce satisfactory results, the k-ω model may be chosen, because in some ways can perform better then the k-ε model. Menter [1] proposed a new shear stress transport k-ω model, with remarkable advantages when compared with k-ε and previous k-ω models. The model is based on the assumption that the principal shear stress is proportional to the turbulent kinetic energy, which is introduced into the definition of the eddy-viscosity. In the k-ω SST model the k-ω model is used near the wall and the k-ε model, transformed to resemble the k-ω model, is used outside of this region. With these approaches, it is possible to solve all equations without the use of wall functions, and this is itself a significant improvement. It is well known that the k-ω model performs very well close to walls in boundary layer flows, particularly under strong adverse pressure gradients [2]. However it is very sensitive to the free stream value of ω and unless great care is taken in setting this value, unrealistic results are obtained. The k-ε model is less sensitive to free stream values but generally inadequate in adverse pressure gradients and so Menter proposed this model that retains the properties of k-ω close to the wall and gradually blends into the k-ε model away from the wall. The model has been shown to eliminate the free stream sensitivity problem without sacrificing the k-ω near wall performance [3].

Boundary conditions

The boundary conditions for the flow inside the computational domain shown in Figure 3 are requiring the no-slip conditions on the hull surface for the velocity, an exact formulation of the Neumann-type condition for the pressure whereas the Dirichlet conditions are imposed for k and ω. Zero-gradient conditions are imposed for all the variables in the symmetry plane of the domain. At the upstream, k, ω and the velocity are supposed to be constant, whereas the pressure is extrapolated from inside with zero-gradient. At the downstream, the velocity, k and ω are extrapolated with zero-gradient, while the dynamic pressure is set to zero and kept unchanged during the computation. The bottom of the domain is placed far enough from the free surface such that zero-gradient extrapolation is used for all variables there.

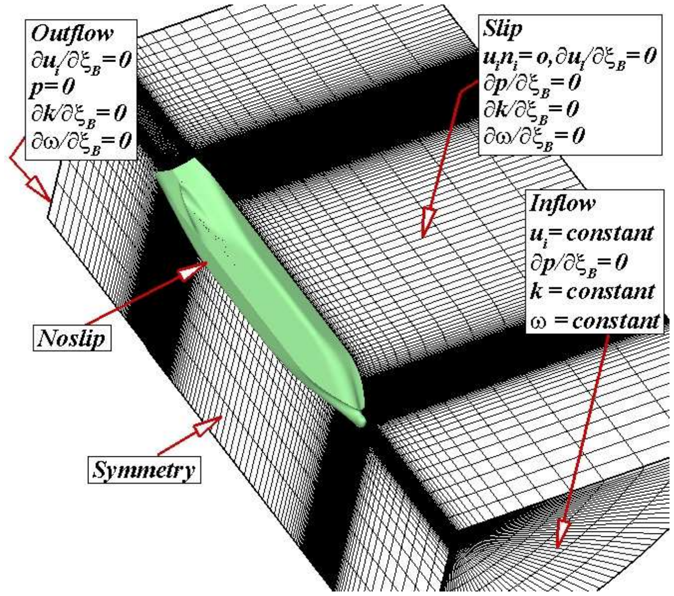

Figure 3. Boundary conditions

The free-surface has its geometry imported from the non-linear potential solution and is thought as a slippery wall during the viscous computation.

Results and discussions

One of the most important issues of each numerical simulation output is the detailed analysis of the physical parameters that describe the flow [4], [5]. A set of simulations was performed for a speed range between 14 and 16 knots for a better understanding on how the velocity affects the wave patterns on the hull. As expected, the more the speed increases, the higher the stern wave crest becomes. One of the key parameters in such a numerical simulation concerns not only the shape and the free-surface in the immediate proximity of the hull, but also the wave crests and troughs magnitudes since the ship resistance is the pressure integral over the wetted area of the hull. Figures 4 and 5 show comparatively the free-surface profile computed and measured for a speed of 15 knots. It is worth mentioning the good resemblance between the two topologies. Figure 6 depicts the wave profile non-linearly computed for the service speed. As it may be seen in the figure, the free-surface displays a rather large wave crest in the bow region that measures about 1.6 meters, a fact that proves a fairy poor geometry of the bulb. Things look better at the aft, where the crest magnitude is around 1.2 meters.

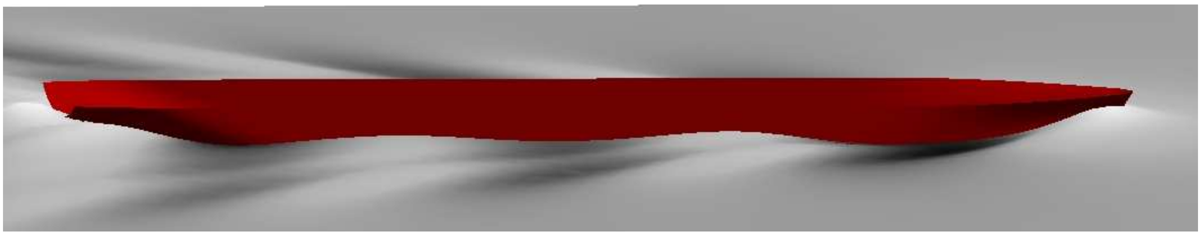

Figure 4. Computed free-surface profile for v= 15 knots

Figure 5. Measured free-surface profile for v= 15 knots

For validation purposes, a comparison between the computed total resistance and the measured one in the towing tank is further brought into focus in Figure 7. A rather large departure of the computed total resistance is seen for lower values of the Froude number, a fact that may suggest the insufficient resolution of the discretization grid for the low speed computations. That is, for an accurate representation of the wave profile, a minimum number of 50 nodes should be distributed over a wave-length, as proven previously in [8]. This condition is hard to fulfill for lower Froude numbers unless the available computer resources are powerful enough to host such computations.

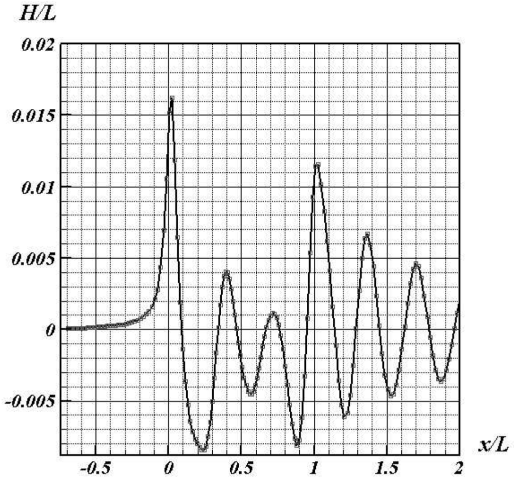

Figure 6. Wave profile non-linearly computed for a speed of 15 knots

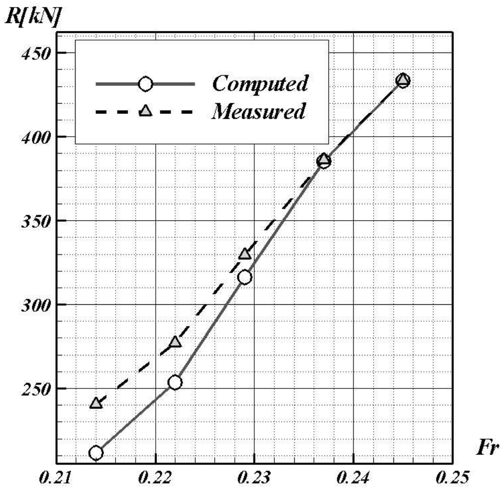

Figure 7. Comparison between the computed and measured total resistances

The viscous flow around the bare hull is computed at first and then, the acting propeller is taken into account. The propeller model calculates the body-forces based on the effective wake field, which means that the propeller solver, which is implemented in the CFD code, is running interactively with the RANS solver. The viscous module specifies the body forces in the cells of an additional cylindrical grid that covers the location of the propeller. The body forces are distributed between the hub and the maximum propeller diameter and also in the axial direction to avoid abrupt changes and concentration of introduced forces. Usually, the pattern of the iso-lines of the mean longitudinal velocity in the nominal wake reflects the frame shape of the aft body, but it is also clearly correlated with the structure of the transverse flow field: often the longitudinal velocity component exhibits a local minimum near the core of a longitudinal vortex.

The smallest axial velocity is usually found in the symmetry plane of the wake near the free surface, with some exceptions. When strong side vortices are produced, the minima occur near their cores, or directly below the free surface. For the present case, the iso-lines of the axial velocity component for some arbitrary slices are depicted in Figure 8. The wake of a ship with a running propeller is rather different from that of the corresponding towed hull (nominal wake). The differences are not only related to the diminished momentum deficit but also to the interaction between the propeller-induced flow and the bare hull wake. A propeller in a uniform onset flow tends to accelerate the flow ahead as well as in the jet behind, and to weakly decelerate the flow outside these regions. Obviously, in front of the propeller and just outside of the jet there is no propeller-induced rotation.

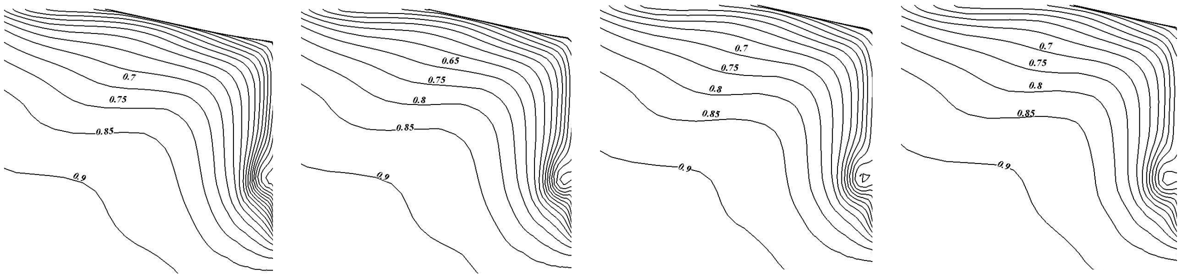

Figure 8. Nominal wake contours at x/L=0.99, x/L=0.995, x/L=0.997 and x/L=1, respectively

For a qualitative analysis of the interaction between the propeller and the nominal wake, one must recall that vorticity, once generated, is carried with the flow and is spread by diffusion, on the understanding that at a high Reynolds number the convection dominates the diffusion. Apparently the viscous diffusion effects are so strong as to more than neutralize the acceleration effect. The enhancement of the vortex strength by stretching effects is also responsible for the acceleration of the flow in the central region near the free surface. As bilge vortices in a nominal wake are effective in reducing the wake peak in the top sector of the propeller disk, the stronger vortices in the propelled-hull wake have a proportional effect on the flow in the central region near the free surface. The presence of a propulsion unit has a strong influence on the axial velocity distribution also. Of course the propeller jet appears as a dominant feature, but there are strong additional effects caused by the interaction between the propeller-induced flow and the longitudinal hull-vortices.

Usually the bilge vortex and the propeller jet are nearly coaxial. If, in addition, they are co-rotating an accumulation effect will occur. Such a completely three-dimensional viscous flow often leads to a non-uniform pressure field in the propeller, a fact that should be avoided for vibration reasons. The longitudinal velocity contours should indicate the characteristic “hook” shape in the central part of the wake correlated with the core of the longitudinal vortex. This small region is characterized by a nearly uniform streamwise velocity component, a linear variation of the vertical component preceding a maximum and again a hook shape of the pressure contours. These features confirm the existence of an intense longitudinal bilge vortex emerging from the hull. Figure 9 depicts the effective wake contours computed for the present study.

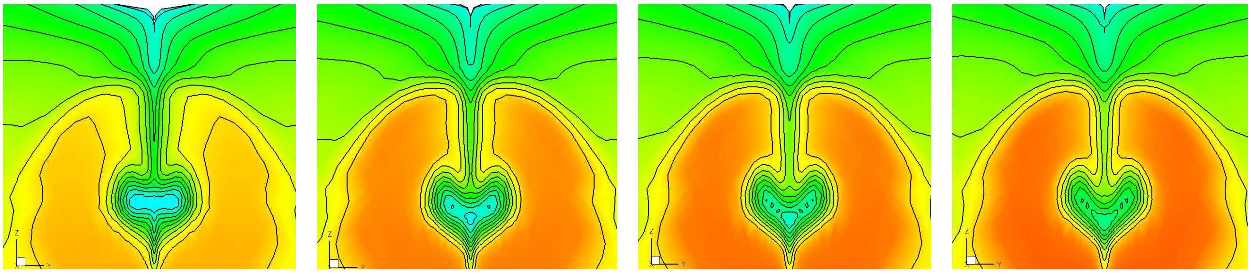

Figure 9. Wake contours at x/L=0.99, x/L=0.995 x/L=0.997 and x/L=1, respectively

The contours of the computed turbulent kinetic energy (TKE) and pressure distribution in the propeller plane are shown in Figure 10. The calculations proved that the TKE is higher in the boundary layer near the water-plane and in the neighborhood of the free vortex-sheet where either the TKE is more vigorously generated due to the large velocity gradient, or high TKE is determined from the upstream boundary layer, or both.

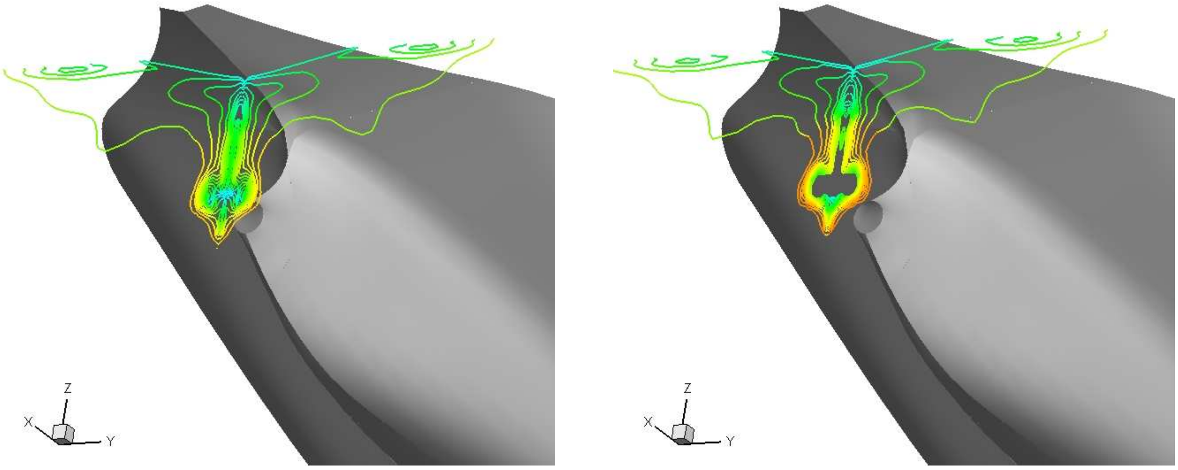

Figure 10. Turbulent kinetic energy distribution computed at x=0.99 station (left) and at x=0.995 station (right)

Concluding remarks

Summarizing the results, viscous flow around a chemical tanker hull was successfully computed and the flow features were determined through the numerical simulations. Based on the RANSE integration various simulations were carried out to compute the flow around the ship hull with and without an operating propeller (applying the body force method). The method appears to be useful in connection with studies of propeller-hull related flow problems. In general, rather accurate propeller characteristics were obtained. In the prediction of the wake details, turbulence modeling was the key issue. The results show that the $k-\omega$ SST model, due to its improved capacity of predicting the separation, is able to provide a realistic wake distribution with reasonable accuracy, therefore the propeller design may be done without any problem. It this respect, it is worth mentioning that the viscous flow calculation can be a very useful tool in initial design process of hull forms.

Acknowledgments

The reported research could not be possible without the generosity of the Romanian National Higher Education Research Council (CNCSIS) which is greatly acknowledged for the financial support provided through the Grants 180/2007, and 679/2007. All the numerical computations have been performed at the Department of Hydrodynamics of the "Dunarea de Jos" University of Galati, whereas the towing tank measurements were done at the Icepronav SA.

References

1. Menter, F.R., (1993), *Zonal Two Equation* $k-\omega$ *Turbulence Models for Aerodynamic Flows*, In 24th Fluid Dynamics Conference, Orlando, AIAA paper-93-2906.
2. Hellsten, A., (1998), *Some Improvements in Menter's* $k-\omega$ *SST Turbulence Model*, In 29th Fluid Dynamics Conference, Albuquerque, NM, AIAA paper-98-2554.
3. Merci, B., Vierendeels, J., Reimslaugh, K., Dick, E., (1985), *Computational Treatment of Source Terms in Two-Equation Turbulence models*, AIAA Journal, Vol.38, No.11, 2085-2093.
4. Xing, T., Kandasamy, M., Wilson, R. and Stern, F., (2004), *DES and RANS of Unsteady Free-surface Flows*, 42nd AIAA Aerospace Sciences Meeting, Reno, Nevada, Division for Fluid Dynamics.
5. Larsson, L., Stern, F., Bertram, V., (2003), *Benchmarking of Computational Fluid Dynamics for Ship Flows: The Gothenburg 2000 Workshop*, Journal Ship Research, Vol. 47, No. 1, pp. 63-81.
6. Zhang, D.H., Broberg, L., Larsson, L., Dyne, G., (1992), *A Method for Computing Stern Flows with an Operating Propeller*, Transactions, Royal Institution of Naval Architects, Vol. 134.
7. Larsson, L., Regnström, B., Broberg, L., Li, D., Janson, C.E., (1999), *Failures, Fantasies, and Feats in the Theoretical/Numerical Prediction of Ship Performance*, Twenty-Second Symposium on Naval Hydrodynamics, pp.11-30.
8. Lungu, A., (2007), *Free-surface turbulent flow around an LPG ship hull*, Proceedings of the 3rd Workshop on Vortex Dominated Flows Achievements and Open Problems, Timisoara, Romania, pp.61-68.

Wave Resistance Minimization for Ships Running under the Restricted Water Condition

Adrian Lungu, Florin Pacuraru*
Department of Ship Hydrodynamics, “Dunarea de Jos” University of Galati, Romania
Email: adrian.lungu@ugal.ro

Introduction

Shallow water flows feature often stronger non-linearities than deep-water flows making them in turn more difficult to solve numerically. Nevertheless, the CFD may be used since it helps in capturing more of the actual physics and thus reducing some of the inherent uncertainties introduced by assuming, e.g. that the form factor is not affected by the water depth. Basically, we are witnessing a "Bernoulli" effect, where the water velocity around the hull must be accelerated due to the restriction of shallow water. This increase in velocity results in a higher drag. In addition to this, the accelerating water can pull the vessel down (known as sinkage), causing the ship the act as if it had a larger displacement. It will therefore important to find out when the shallow water causes a measurable loss of speed. Shallow water increases friction resistance and also wave resistance. Near the unity depth Froude number the resistance is significantly increased. According to the Schlichting hypothesis, the wave resistance is the same if the wave lengths of the transversal waves are the same. For strong shallow water influence however, a simple correction is impossible as wave breaking, squat and deformation of the free-surface introduce complex physical interactions. In this case, only model tests or CFD may help. In the numerical simulation, the inclusion of shallow water is relatively simple. Boundary element methods based on Rankine elements use mirror images of the elements with respect to the water bottom. The image elements have the same strength as the original elements. This automatically yields zero normal velocity on the water bottom due to symmetry.

The relationship between speed and water depth is therefore encapsulated in the Froude depth number. In deep water, or at low speeds, the value of the Froude depth number is small or negligible and vessels behave benignly. However, when speed increases so that *FnH* approaches unity (the so-called critical speed) resistance increases markedly and wave wash can reach significant proportions. At speeds yielding *FnH* values in excess of unity (super-critical speeds) the wave pattern will have lost its transverse wave system and consist simply of diverging waves. Because modern powered commercial and leisure vessels are now able to reach high speeds, they will be able to enter, and pass, the critical regime for waters whose depths were once considered to be “deep”. Such waters, for such ships, are now, in effect, shallow. As a result of this, the so-called wash nuisance has become a feature on the coastlines, beaches and river banks where ships operate. Such a feature is not a consequence just of commercial ship operation; it can, to a greater or lesser degree, produce excessive wash, aggravated by limited water depth. Moreover, the critical speed regime may bring with it difficulties in passing through the resistance “hump” in this region. It is not unknown for some vessels to show no apparent change in speed with increasing propeller, only to accelerate rapidly up to speed, with no apparent warning, after a final engine movement. All these topics have been the subject of some active research programs in recent years. Much of the early work has been aimed at increasing our understanding, by measurement and theory; more recently, the intriguing possibility of reducing the problems by suitable hull design has been investigated. Although scarce, the literature reports measured residuary resistance coefficients for a model in two water depths (the water was quite shallow, with depth/length (*H/L*) ratios of 0.047 and 0.125, whereas the speed range was large, starting just below the critical regime and ending well above it) have proven the following:

- around the critical speed ($FnH=1.0$) a marked increase in residuary resistance coefficient occurs. This has a higher peak value in the shallower of the two water depths;
- in the supercritical speed range, the residuary resistance coefficient is constant, implying that it varies simply as the speed square.

The overall ship resistance is an important parameter that has been thoroughly studied by naval architects since this determines the power required to propel a ship. A ship-like body moving through a fluid is a fundamental concept in understanding resistance. Ideal potential flow fluid theory shows that positive pressure is produced on each end of the body with negative pressures along the ship middle body. Because of viscous effects from real fluids on the body surface, a boundary layer is generated along the body causing body frictional resistance. Flow separation will occur at the ship stern, causing increased resistance from eddy drag. The sum total viscous and eddy resistance of the ship is called the wetted surface drag and can be readily calculated or obtained from tabulated towing tank data. The ideal pressure distribution on the moving ship in deep water causes a system of waves on the free surface moving with the ship. The fact that a ship sailing in deep water at constant speed generates a wave system is well known by any sailor or casual observer. These waves are composed of both divergent and transverse waves and are generated at the bow and the stern of the ship as well as at various positions along the ship length. The waves at the free surface waterline are generated by the pressure distribution around the ship and cause significant resistance to the ship. More important to the navigation planner and designer is that the ship also sinks and trims with respect to the static ship. Thus, the ship will sink in the water and trim because of the wave train caused by the ship. While this occurs in deep water, the waves and ship sinkage become much more prominent in shallow water. The wave making by the ship, therefore, has an important impact on the design of the channel.

At very low speeds, most of the ship's resistance is the result of wetted surface drag; as the speed is increased, wave-making drag grows higher. The ship length Froude number (*Fn*) has been an important parameter in determining wave effects. This may be given as the ratio of ship's speed to the square root of the acceleration because of gravity and the ship's length. The normal value of this dimensionless parameter is usually very small for commercial ships — perhaps varying from near 0.04 for tankers at slow ship speeds near 5 knots to near 0.40 for fine-line containerships at 25 knots. Wave drag becomes increasingly important at Froude numbers of about 0.2 or higher and can become two or three times the ship's surface resistance at Froude numbers of 0.4. The total drag on a ship determines the selection of the ship thrust and power required to operate the ship at the design speed. On the other hand, the engine power is crucially important in the maneuverability of the ship, especially at the typical moderate harbor speeds, when engine acceleration effects are used to provide kick turns. The ratio of installed engine shaft horsepower to the ship deadweight tonnage may be called specific power and used to relate the relative ship powered maneuverability. A hull form design procedure accompanied by flow computations around a self propelled inland tanker have been employed not only to define the hull forms, but also to estimate the wave and total resistance. The main particulars of the ship are tabulated in Table 1. Because of the limitations imposed by the customer (given main dimensions, prescribed range for the speed, twin-tunnel aft, etc.) the initial forms led to a large block coefficient and significant geometric gradients of the waterlines at extremities. This was a consequence of the fact that the brief technical specification was only based on a scarce basic design estimation of the ship performances. Obviously, although a large block coefficient means a sufficient cargo space, it always leads to a high ship resistance. Consequently, an improved form had to be obtained from a successive adjustment process. A view of the hull forms is shown in Fig.1, which depicts the transversal projection of the lines plan drawn for the initial hull.

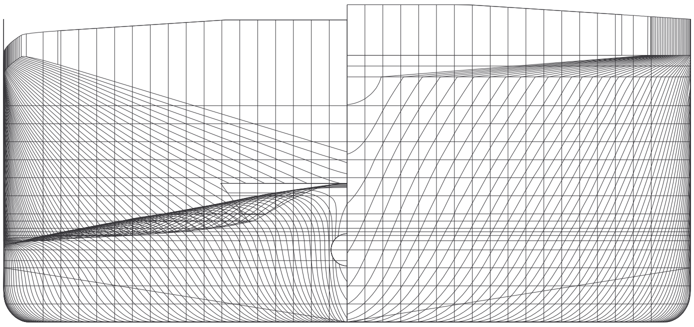

Fig.1 Hull forms

Table 1. Main particulars of the ship

LOA	Approx. 96.00 mtr.
Breadth	Approx. 9.60 mtr.
Depth	Approx. 4.40 mtr.
Draught	Approx. 2.80 mm
Speed	14-15 Km/h
Total Volume	2257.8267 m^3
LCB from AP	51.42% of LBP
KMT	4.2830 m from the BL
VCB	1.4452 m from the BL
WSA	1322.2039 m^2
C_M	0.9977
C_B	0.8810
C_p	0.8800

Ship Resistance Computations

A full set of numerical simulations were performed for the free-surface flow around the inland tanker. The unrestricted water case, as well as the shallow water computation was carried out. CFD computations were carried out using the Shipflow software. Both trim and sinkage were taken into account. Computational domain was extended a ship length in front of bow and away from ship side, and one and a half length and behind stern. The grid for the viscous computation consisted of 1.5 million nodes, and was generated to capture the flow features close to hull surface. In order to account for the effect of free water surface around the ship, both potential and the viscous volume of fluid models were used in computations. Two different draughts were considered: 2.0 and 2.8m respectively. The non-linear solutions were computed by employing a potential-based method. Computations were performed for the unrestricted water case as well as for two different limited draughts at 3.5 and 4.5 meters. All the numerical data were validated through comparisons with the experimental data obtained in the towing tank.

In the following, the output data of the numerical simulations will be given. Although the Shipflow code may compute the total resistance based on the friction component determined either by using the ITTC78 method, or by integrating the boundary layer equations, we have chosen the first method since it was the one employed at the towing tank measurements. The ship resistance was computed for speeds ranging from 10 to 20

Km/h. However, only the solutions computed for 15 Km/h will be discussed in the following. The choice is motivated by the foreseen operational speed for the ship. Several hull forms were successively considered in an attempt of reducing the overall ship resistance. Figures 2…5 show the free-surface profiles computed for the initial and final hull forms computed for the unrestricted, 4.5m and 3.5m water depth cases, draughts of 2.8 and 2.0m, respectively. Figures 2 and 3 show comparisons between the free-surface profiles computed for the initial hull forms and for the improved ones, in both navigation conditions, i.e., unrestricted water and 4.5m depth, respectively. The numerical simulations were performed for a draught of 2.8m. The shallow water solutions reveal a significant increase of the wave heights as well as a decrease of the wave length, as expected. Those modifications obviously lead to a ship resistance augmentation, as it will be discussed later.

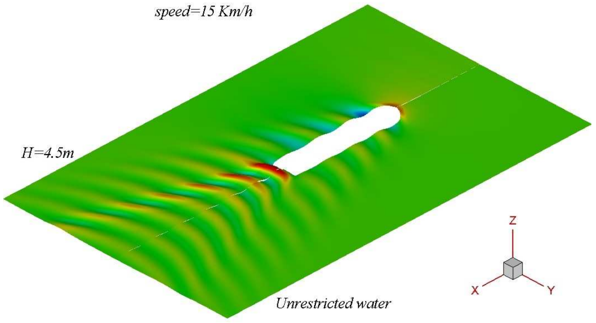

Fig.2 Comparison between the free-surface profiles on the initial hull forms computed for the unrestricted and 4.5m water depth cases. Draught of 2.8m.

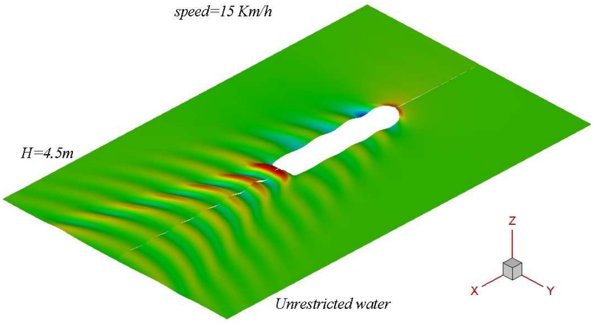

Fig.3 Comparison between the free-surface profiles on the final hull forms computed for the unrestricted and 4.5m water depth cases. Draught of 2.8m.

Same conclusions may be withdrawn from Figures 4 and 5, which show comparisons between the free-surface profiles computed for the initial hull forms and for the improved ones, in both navigation conditions, i.e., unrestricted water and 3.5m depth, respectively. The numerical simulations were performed for a draught of 2.8m.

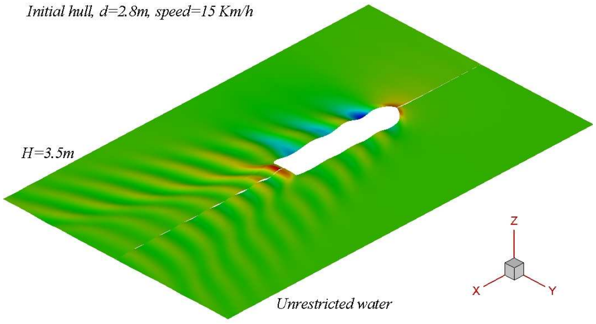

Fig.4 Comparison between the free-surface profiles on the initial hull forms computed for the unrestricted and 3.5m water depth cases. Draught of 2m.

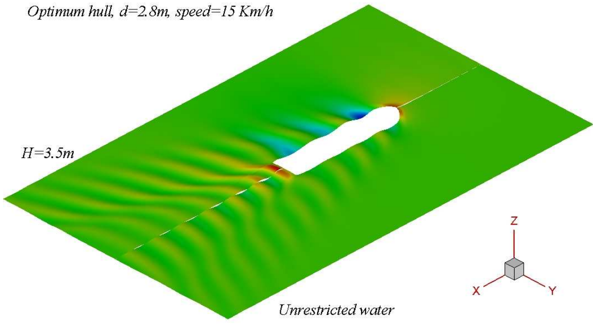

Fig.5 Comparison between the free-surface profiles on the final hull forms computed for the unrestricted and 3.5m water depth cases. Draught of 2m.

The increased frictional resistance and wave patterns in shallow water both modify the sinkage and running trim of the ship and required under keel clearance. For most merchant ships, which travel at moderate and low speeds, this effect becomes important when water depth-to-ship draft ratios (H/d) are less than 4.0. Since most ship navigation channels operate at very small depth to draft ratios (typically H/d less than 1.5), shallow-water effects have major impacts on ship navigation. The key parameter that governs ship waves in shallow water is the depth Froude number. As the ship speed increases, the shallow-water effects will increase up to the value of depth Froude number equal to unity, where critical open channel flow would occur. In practice, wave effects and ship resistance become very high at FnH values well below $FnH = 1.0$, so that normally a self-propelled merchant ship would not exceed FnH of about 0.6. This indicates that at "displacement" speeds, the vessel will slow down as water depth gets shallower.

Table 2. Speed loss with the Froude depth number

FnH	0.0-0.4	0.6	0.8	1.0
Speed loss	No loss	1%	4%	14%

Table 3. Speed loss with the minimum water depth

Speed [Kts]	Minimum depth for			
	No loss	1% loss	4% loss	14% loss
5	14+ ft	6 ft	-	-
10	55+ ft	24 ft	14 ft	9 ft
15	124+ ft	55 ft	31 ft	20 ft
20	220+ ft	98 ft	55 ft	35 ft

These are typical values only and each ship is somewhat different. One widely-used analysis of speed loss in shallow water is the Schlichting method. It can give us a general sense of the potential speed loss. He found that there is typically no measurable speed loss as long as *FnH* is less than about 0.4. As *FnH* increases, however, the speed loss begins to take effect. As a correlation line, the ITTC 1957 line already contains some allowance for three-dimensional effects, and two recent ITTC Committees have recommended that additional corrections not be made in routine resistance predictions of high speed craft. However, including a form factor specific to the hull form under consideration can often give better estimates of the viscous drag. This factor is difficult to estimate and may vary with speed because of (among other things) changes in trim and sinkage.

Table 4 gives the total resistance computed for a set of 16 velocities between 5 and 20 Km/h, not only for the unrestricted water case, but also for the two depths of the shallow water case. The solutions computed in Table 4 for the 2.0 draught are plotted in Fig. 6. The resistance augmentation produced by the finite depth varies from 4.95% that corresponds to the H=4.5m depth case and a speed of 5Km/h, to 95.89% which corresponds to the H=3.5m depth and a speed of 20 Km/h. The variation of the average percentage of the resistance augmentation with the water depth decrease for the hull at a draught of 2.0m is presented in Fig.7.

Table 4. Total resistances computed and measured for d=2.0m

Speed	Computed			Measured	Rt increase [%]	
[Km/h]	Unrestricted	H=4.5m	H=3.5m	H=3.5m	H=4.5m	H=3.5m
10	14257	16198	19084	29000	13.61	33.85
11	17280	19903	23429	35575	15.18	35.58
12	19236	22130	26165	41275	15.04	36.02
13	24121	27925	33308	49350	15.77	38.09
14	29070	33899	41716	59700	16.61	43.50
15	34128	40356	50175	69000	18.25	47.02
16	39387	46908	61318	85000	19.10	55.68
17	44200	52799	73648	118000	19.46	66.63
18	50745	61191	89533	145000	20.58	76.44
19	63389	77963	116393	192000	22.99	83.62
20	77900	97003	152597	241150	24.52	95.89

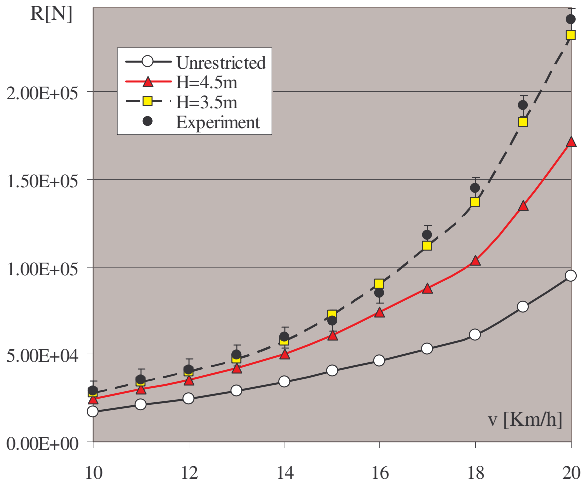

Fig.6 Ship resistance dependency on the water depth, computed and measured for a draught of 2.0m

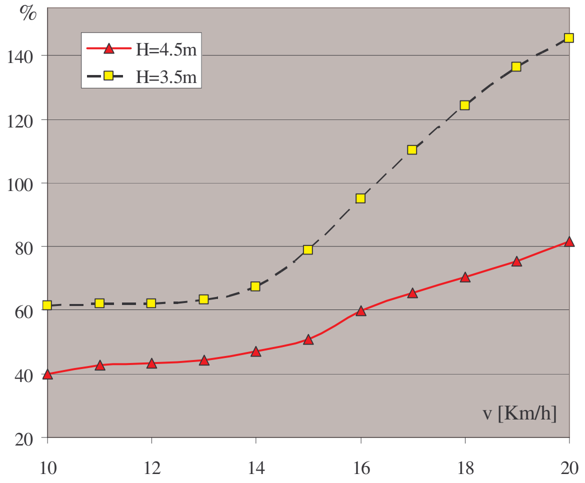

Fig.7 Variation of the average percentage of the computed resistance increase with the water depth, d=2.0m

On the other hand, Table 5 gives the total resistance computed for the same set of 16 velocities, only for the unrestricted water case, but also for the two depths of the shallow water computed at a draught of 2.8m. The solutions computed in Table 5 are plotted in Fig. 7. As it may be seen, the resistance augmentation produced by the finite depth varies from 8.41% that corresponds to the H=4.5m depth case, to 17.25% which corresponds to the H=3.5m depth computational case.

Table 5. Total resistances computed and measured for d=2.8m

Speed [Km/h]	Rt				Measured	Rt increase [%]	
	Unrestricted		H=3.5m	H=3.5m	H=3.5m	H=4.5m	H=3.5m
10	17310	48087	24241	27907	18000	40.04	61.22
11	21125	64554	30147	34216	21200	42.71	61.97
12	24497	81662	35106	39684	27475	43.31	62.00
13	29078	105013	41904	47433	34975	44.11	63.12
14	34313	133451	50429	57409	43800	46.97	67.31
15	40526	168873	61113	72471	48000	50.80	78.83
16	46342	205980	74077	90319	64375	59.85	94.90
17	53227	251371	88054	111822	77325	65.43	110.08
18	61033	305191	103995	136816	94000	70.39	124.17
19	77159	407262	135339	182365	124200	75.40	136.35
20	94522	525162	171556	231881	159975	81.50	145.32

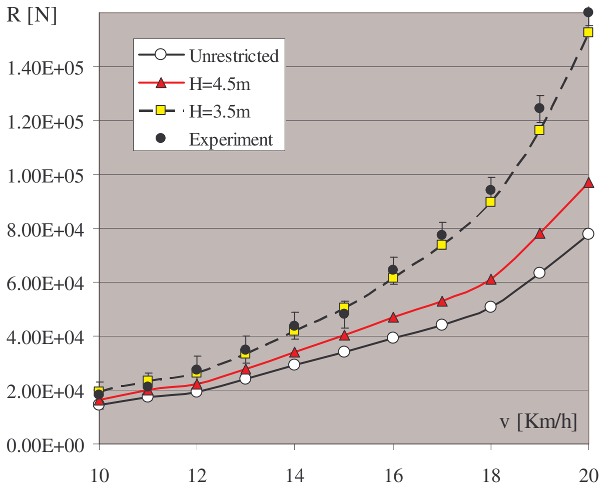

Fig.8 Ship resistance dependency on the water depth, computed and measured for a draught of 2.8m

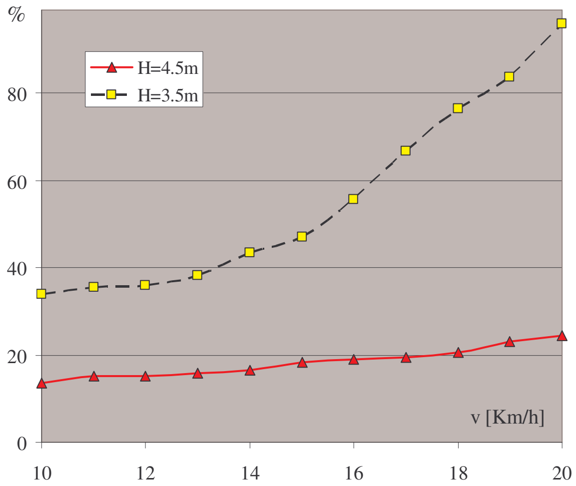

Fig.9 Variation of the average percentage of the computed resistance increase with the water depth, d=2.8m

The variation of the average percentage of the resistance augmentation with the water depth decrease for the improved hull with a draught of 2.8m is presented in Fig.8. The results given above are in good agreement with the literature in the field which is recommending for the shallow water case either percentages of resistance increase as a function of the *FnH*, or critical values of the water depths at which the velocity loss produced by the shallow water takes place. These recommendations are tabulated in Table 6 and Table 7, respectively.

Table 6 Depth Froude number

V [m/s]	*FnH*	
	H=4.5m	H=3.5m
1	2	3
2.50	🟨 0.376	🟩 0.427
2.78	🟩 0.418	🟩 0.474
3.06	🟩 0.461	🟩 0.522
3.33	🟩 0.501	🟩 0.568
3.61	🟩 0.543	🟦 0.616
3.89	🟩 0.585	🟦 0.664
4.17	🟦 0.628	🟦 0.712
4.44	🟦 0.668	🟦 0.758
4.72	🟦 0.710	🟧 0.806
5.00	🟦 0.753	🟧 0.853
5.28	🟦 0.795	🟧 0.901

Legend

🟨	No loss
🟩	1% loss
🟦	4% loss
🟧	14% loss

Table 7. Critical water depth for loss of velocity appearance

v [m/s]	Minimum depth for:			
	No loss	1% loss	4% loss	14% loss
1	2	3	4	5
2.50	🟨 4.3 m	🟩 1.8 m	🟦 -	🟧 -
2.78	🟨 16.8 m	🟩 7.3 m	🟦 4.3 m	🟧 2.7 m
3.06				
3.33				
3.61				
3.89				
4.17				
4.44				
4.72				
5.00				
5.28	🟨 38.1 m	🟩 16.8 m	🟦 9.5 m	🟧 6.1 m

Figures 10 and 11 show comparisons between the wave profiles drawn on the hull computed and measured at a draught of 2.8m in the first figure and 0f 2.0m in the second one. As shown in the two plots, the agreement between the theoretical and experimental data is fairly good, excepting the area around the firs wave crest and trough, where the computed solution seems to be underestimated, a fact that explains the smaller ship resistance computed numerically and tabulated in Tables 4 and 5.

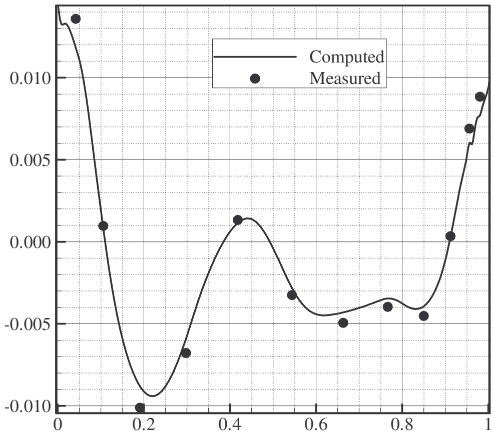

Fig.10 Comparison between the wave profile on the hull computed and measured at a draught of 2.8m

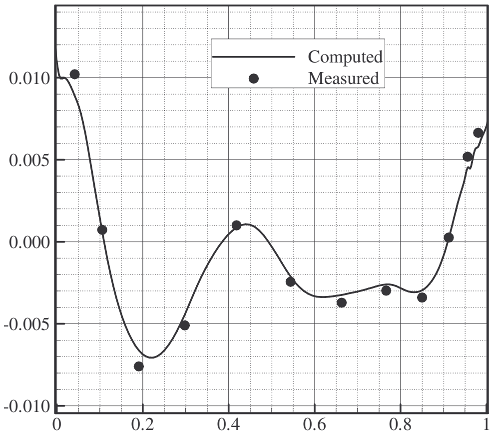

Fig.11 Comparison between the wave profile on the hull computed and measured at a draught of 2.0m

Concluding Remarks

1. Free-surface flow around the hull form was successfully computed. Ship resistance was determined through the numerical simulation. Both linear and non-linear approaches were used to solve the flow problem at different ship speeds, ranging from 10 to 20 km/h.
2. Computations proved that a decrease of the water depth may lead to an averaged increase of the total resistance of the ship by 51.80% and 84.80%, corresponding to a draught of 2.8m and water depths of 4.5 and 3.5m, respectively for the ship speed of 15 Km/h.
3. In the 2.0m draught case, an averaged increase of the total resistance of the ship by17.16%, and 51.09%, corresponding to water depths of 4.5, and 3.5, respectively was found for the ship speed of 15 Km/h.

Acknowledgments

The reported research could not be possible without the generosity of the Romanian National Higher Education Research Council (CNCSIS) which is greatly acknowledged for the financial support provided through the Grant 679/2007. All the numerical computations have been performed at the Department of Hydrodynamics of the “Dunarea de Jos” University of Galati, whereas the towing tank measurements were done at the Icepronav SA.

References

[1] Janson, C-E. ***Potential Flow Panel Methods for the Calculation of Free Surface Flows with Lift***, Ph.D. Thesis, Chalmers University of Technology, 1997.
[2] Dawson, C., ***A Practical Computer Method for Solving Ship Wave Problems***, 2nd International Conference on Numerical Hydrodynamics, Berkley, 1977.
[3] Raven, H.C., ***A Solution Method for the Non-linear Ship Wave Resistance Problem***, MARIN, Holland, Ph.D. thesis, Technical University of Delft, 1996.
[4] Jensen, P.S., ***On the Numerical Radiation Condition in the Steady State Ship Wave Problem***, Journal of Ship Research, vol. 31, nr.1, 1987.
[5] Millward, A., ***The Effect of Water Depth on Hull Form Factor***, International Shipbuilding Progress, Vol. 36, No. 407, 1989.
[6] Tabaczek, T., ***Computation of Flow around Inland Waterway Vessel in Shallow Water,*** ACME, Vol.VIII, No.1, 2008

VALIDATION AND VERIFICATION OF HULL RESISTANCE COMPONENTS USING A COMMERCIAL CFD CODE

C.A. Perez G, University of Southampton, UK. Universidad Pontificia Bolivariana, Colombia,
M. Tan and **P.A. Wilson** University of Southampton, UK.

SUMMARY

A mathematically defined Wigley hull form is used to investigate the application of a commercial CFD code in prediction of the total resistance and its components from tangential and normal forces on the hull wetted surface. The computed resistance and wave profiles alongside the hull were compared with experimental observations for six different Froude numbers to validate the simulations. The effects of grids, domain size and turbulence models were studied. A statistical hypothesis test was carried on these resistance data in order to determine the most suitable turbulence model for the lowest and highest Froude numbers.

1. INTRODUCTION

The resistance of a hull is a consequence of air and water forces acting against movement of the vessel. For this reason its determination is an important issue regarding the propulsion and ways to provide it. The water will have the major contribution to the resistance of a hull, unless there are strong winds. As a result, predictions on resistance are a good way to know how the energy is spent.

Traditional methods to predict resistance on real hulls are based on towing tank models running at corresponding Froude numbers and then scaling results taking into account a friction line for the respective Reynolds number. Advantages of these methods are the knowledge and experience acquired through the years that make results reasonably trustworthy. Disadvantages are the associated cost and the limitation on the availability of physical tanks and models for every single design. This has been one of the motivations of attempting to predict hull behaviours using computational tools, for this specific case, resistance. Although computations started in earlier 60's solving the simplified boundary layers equations[1], followed by methods based on potential flow theories and those to solve Reynolds Navier-Stoke Equations in the last two decades[2], experimental data are still required to validate computational results.

In order to obtain accurate results even in steady state simulations, the problem needs to be set-up carefully and this includes having sufficient nodes within the boundary layer, correct mesh for high gradient zones and suitable time step sizes. Comprehensive efforts have been made to the procedures to verify and validate computational data however there is still a lack of consensus of suitable techniques[3].

In the present study the commercial CFD code used is ANSYS-CFX 11.0 which adopts a false time step or pseudo-time step to solve equations as a means of under relaxation. The under relaxation is necessary to stabilize some iterative processes of obtaining steady state solutions[4]. It could be said that smaller physical time steps are more robust than larger ones[5]. Nonetheless, convergence will require more CPU time.

2. CFD SIMULATIONS

The Wigley hull was selected as a benchmark to gain understanding of free surface simulations using CFX. The hull was generated by a three variables parametric function in ANASYS ICEM and it is parabolic under the waterline and extends up vertically. Equation 1 describes the underwater hull shape and a sketch is given in the Figure 1.

$$y = \frac{B}{2}\left[1-\left(2x/L\right)^2\right]\left[1-\left(z/T\right)^2\right] \qquad (1)$$

In equation 1 x, y and z are the longitudinal, transverse and vertical ordinates of the hull surface and L,B and T are the length, the breadth and the draught of the hull, respectively. For this case L was chosen as 1m, B=0.10 m and T=0.0625m.

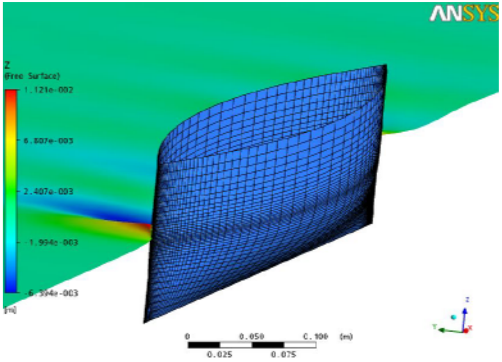

Figure 1. Wigley Hull.

A physical domain with water and air at standard conditions was specified and a homogeneous coupled Volume of Fluid model was selected as it is recommended for free surface flows where the free surface is well defined over the entire domain[5]. An homogeneous model allows two different phases when the interface is distinct and well defined everywhere, as it is the case of hulls riding on a free surface without breaking waves. For this initial simulation the k-ε turbulence model was used. The boundary conditions were imposed as follows, *Inflow*: normal free stream, *outflow*: hydrostatic pressure, *Top*: opening pressure, *Midplane*: symmetry, Side and *Bottom*: free slip. The Figure 2 shows the initial computational domain of 5m long 3m wide and 0.625m deep with 234,320 elements. Table 1 shows the results of the longitudinal components of the tangential and normal forces acting on the hull and experimental data from[6]. Also, figure 3 shows hull wave profiles in terms of non dimensional wave height compared with the data from same source[6].

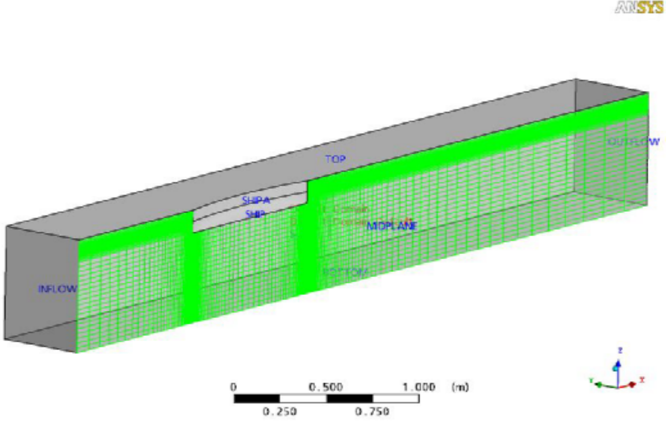

Figure 2. Initial Computational Domain.

Table 1. Computational and experimental resistance coefficients (×10^3)[6].

Froude Number	**0.250**	**0.267**	**0.289**	**0.316**	**0.354**	**0.408**
Ctang $_x$	4.77	4.72	4.65	4.58	4.47	4.34
Cnormal $_x$	1.03	1.12	1.47	1.75	1.72	2.69
Ctotal	5.80	5.84	6.12	6.33	6.19	7.03
Ctotal Exp	5.92	5.84	6.16	6.32	6.12	6.91
%Error	2.0%	0.1%	0.7%	0.2%	1.2%	1.7%

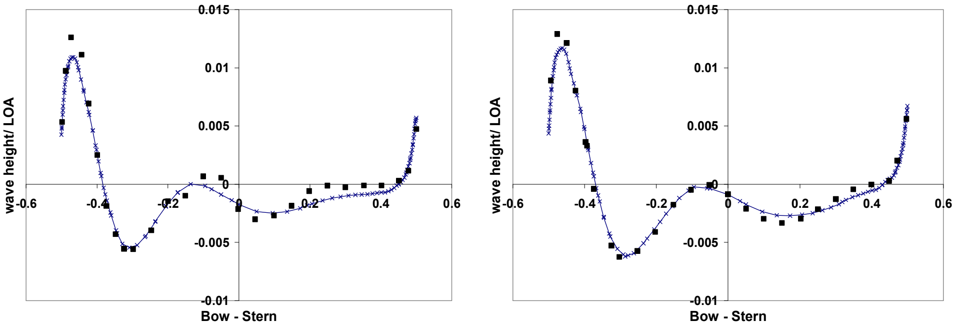

Fn=0.250

Fn=0.267

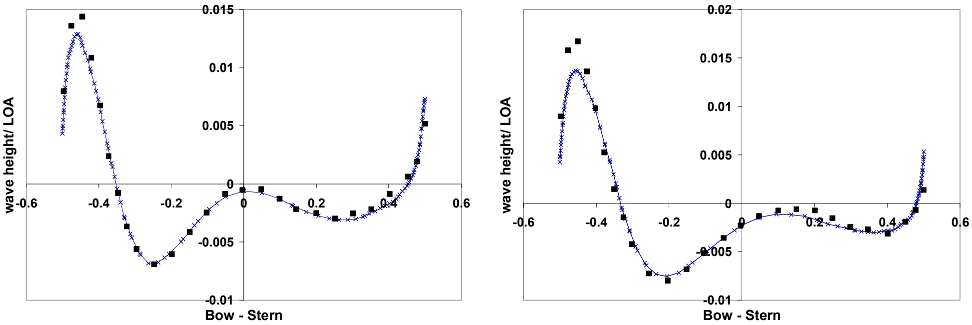

Fn=0.289

Fn=0.316

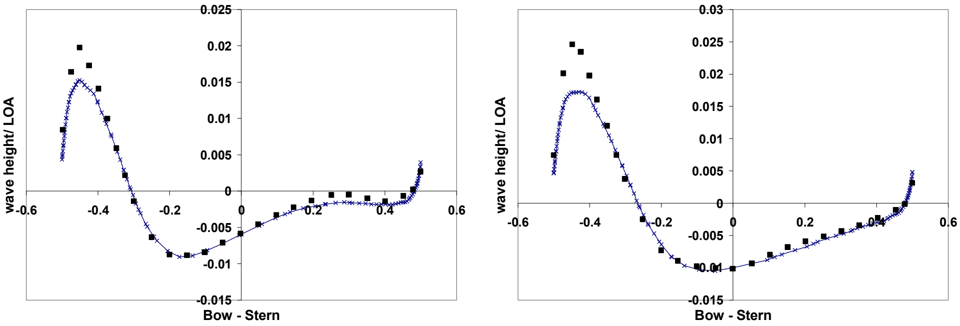

Fn=0.354

Fn=0.408

Figure 3. Computational (line) and experimental (dots) [6] wave profiles alongside the hull for six different Froude numbers.

3. MESH STUDIES

The grid quality is fundamental for the convergence and accuracy of CFD calculations. Gird qualities are discussed in detail by Thompson et al[7] however, for this study the criteria available in ANSYS ICEM such as, *3x3x3 Determinant*, *Aspect Ration* and *Skewness*, were used to determine the mesh quality. Although it is quite difficult to set up all those criteria with ideal values, a right balance on them gives a good mesh quality. Generally speaking, a value of *3x3x3 Determinant* over 0.4, an *Aspect Ratio* between 100 and 500 and, a *Mesh Expansion Factor* with a maximum 50 are good indicatives that a mesh could work properly.

Having tested the conditions on the CFX solver, with result presented on the previous section, a new reference domain was made. The mesh strategy was to keep the same number of nodes (306,240) reducing the domain in the three Cartesian directions in order to obtain different levels of refinement, mainly close to the hull, Figure 4 show a sketch of the domains. Table 2 shows the dimensions of the domains in term of length and draught of the hull. In the longitudinal direction the measures show the length ahead and behind the hull (L=1m).

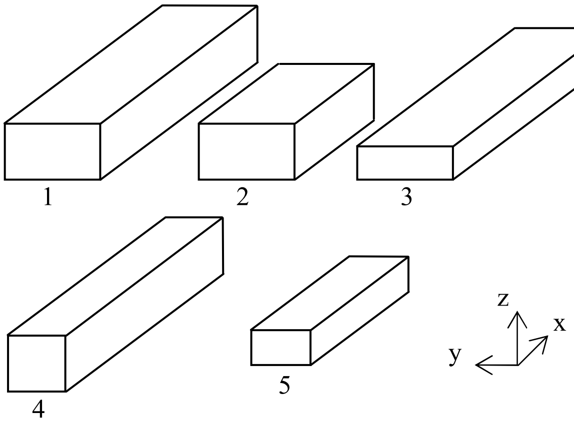

Figure 4. Domain sketches.

Table 2. Dimesion domains in terms of length and draught of the hull.

	Domain 1	Domain 2	Domain3	Domain 4	Domain 5
Length	L/2,L,1.2L	L/2,L,0.66L	L/2,L,1.2L	L/2,L,1.2L	L/2,L,0.66L
Width	L	L	L	L/2	L/2
Hight	L/2 + T	L/2 + T	L/3 + T	L/3 + T	L/3 + T

From the initial test, the highest percentage errors in total resistance coefficients were shown on the lowest and highest Froude numbers. Also, for those values, wave profiles along side the hull did not show good agreement with the experimental data, specially the height of the bow wave for the highest Froude number. Thus, Froude numbers of 0.250 and 0.408 were chosen to perform the mesh study for five domains and four different turbulence models. Figures 4 and 5 show the results, together with experimental data for those Froude numbers respectively.

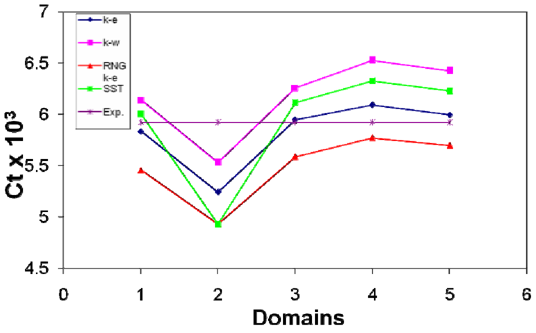

Figure 5. Total resistance coefficient for 5 domains and 4 turbulence models with 306,240 nodes each at Fn=0.250

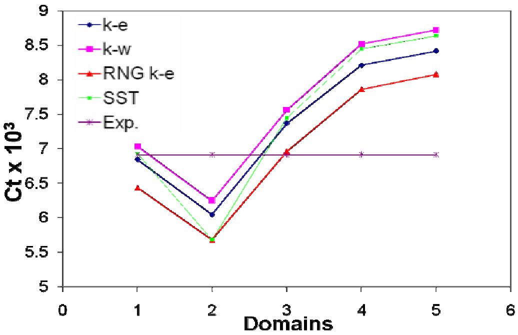

Figure 6. Total resistance coefficient for 5 domains and 4 turbulence models with 306,240 nodes each at Fn=0.40

4. VERIFICATION AND VALIDATION

As a preliminary step of verification, the longitudinal components of the normal and tangential forces alongside the hull can be used to give confidence on the value of the total drag, determined as the total force on the hull in the flow direction, see Table 1. However for specific Froude numbers the computational model could give misleading results. As a result it was decided to carry out mesh studies over different domains and different turbulence models at the lowest and highest Froude number, for this case 0.250 and 0.408 respectively.

From Figures 5 and 6, it could be said that domains 1 and 3 provide accurate results for resistance coefficients in both Froude numbers studied; this was also proved with percentage errors. The idea now is to determine which turbulence model fits better, taking the experimental data as an accurate resistance coefficient value. As it can be seen from those figures, the experimental data is a horizontal line with slope equals to zero and the intercept is the total resistance coefficient. In order to determine statistically the confidence of the conclusions for turbulence models, linear regressions were applied on the data for resistance coefficients and the following hypothesis tests were carried out. The domain 2 was discarded for the purpose of this analysis, as it was considered unusual since it produced a strange wave profile thus, just the other domains were taking into account for this analysis.

The hypothesis test[8] was applied regarding to the slope β_1 and to numerical data on linear regressions $y = \beta_1 x + \beta_0$, in this case experimental data is taken as a measure of validation pattern, hence

Ho: $\beta_1 = 0$ if $|t_o| < t_{\alpha/2, n-2}$ Numerical data slope is zero

Ha: $\beta_1 \neq 0$ if $|t_o| > t_{\alpha/2, n-2}$ Numerical data slope is not zero

Where:

Ho: Null Hypothesis

Ha: Alternative Hypothesis.

$t_{\alpha/2, n-2}$ The value of the t-distribution for $\alpha/2$ with n-2 degree of freedom

α : Significance level.

t_o : The test statistic value calculated as shown:

$$t_o = \beta_1 \Big/ \sqrt{M_{SE} / S_{xx}}$$

Where:

M_{SE} : The mean square error

S_{xx} : The sum of squares of the value minus the mean.

Ho: $\beta_o = C_t$ if $|t_o| < t_{\alpha/2, n-2}$ the numerical estimation is C_t

Ha: $\beta_o \neq C_t$ if $|t_o| > t_{\alpha/2, n-2}$ the numerical estimation is not C_t

t_o: The test statistic value calculated as shown

$$t_o = (\beta_o - C_t) \Big/ \sqrt{M_{SE}(1/n + (\bar{x})^2 / S_{xx})}$$

As a result of these tests, it could be said that turbulence models with less value of t_o produce closer values to the experimental results than those with high t_o values. Hence, for a Froude number of 0.250 the numerical total resistance coefficient is in accordance with the experimental data for the k-e model for the range of domains tested. Similarly, for the Froude number 0.408 the k-w model followed by SST predict betters the total drag.

5. CONCLUSIONS

The main aim of this study was to verify and validate the calculated hull resistance in terms of mesh and domain size, and to generate data to understand how many hull lengths are required ahead and behind the hull to obtain convergence and accurate data, which is not well defined by other authors. At least, for this case of a fixed Wigley hull, it has shown that even with short lengths between the stern and the outflow, accurate data can be obtained.

For the same number of elements, domains 1 and 3 showed better agreement with experimental data for total resistance coefficients. For the lowest Froude number, 0.250, the k-e turbulence model gave better agreement while for the highest Froude number, 0.408, the k-w model followed by SST predicted better the total resistance for those domains tested. However, the agreement for wave profiles at those Froude numbers tested did not improve.

FURTHER WORK

Simulations for more realistic hull forms under free to heave and pitch condition will be carried out based on the experience from the current work. Resistance data for verification and validation will be obtained from experimental work which will also measure the longitudinal wave cuts of the wave pattern instead of measuring the wave profile alongside the hull.

6. REFERENCES

---

[1] Zhang Z, Liu H, Zhu S, Zhao F. (2006) Application of CFD in ship engineering design practice and ship hydrodynamics. Conference of Global Chinese Scholars on Hydrodynamics.

[2] Gotman, A. (2007) Navigating the wake of past efforts. The Journal of Ocean Technology. Volume 2. Number 1. pp 74-96.

[3] The Resistance Committee (2005). Proceedings of the 24th IIT. Volume I. ITTC, 2005 U.K.

[4] Versteeg H.K, Malalasekera W. (1995). An introduction to Computational Fluid Dynamics. The finite Volume Method. Essex: Longman Scientific & Technical.

[5] CFX. CFX Manual V11. Ansys 2007.

[6] Kajitani, H et al (1983). The Summary of the Cooperative Experiments on Wigley Parabolic Model in Japan. Tokyo University. Japan

[7] Thompson J.F., Soni B.K., Weatherill N.P. (1999). Handbook of Grid Generation. CRC Press.

[8] Montgomery, D.(2005) Design and Analysis of Experiments. John Wiley & Sons, Inc.

Numerical analysis of ship-ship interaction by a high-order potential flow code with ship motions

Keun Woo Shin (kws@mek.dtu.dk), Harry B. Bingham, Poul Andersen

Dept. of Mechanical Engineering, Technical University of Denmark

1 Introduction

This work is motivated by the desire to include a rational prediction of the interaction effects between a maneuvering tug-boat and a steadily moving ship within a training simulator facility for tug-boat helmsmen. To this end, we investigate the performance of the high-order boundary element code AEGIR with respect to robustness and efficiency by comparing numerical calculations with experimental measurements.

The test case considered here involves a tug-boat and a tanker, both sailing at the same constant speed, but with different relative positions of the tug-boat. A range of speeds and lateral and longitudinal distances between the mid-points of the two ships is considered. Based on the comparison, we conclude that it is possible to capture the correct trends in the interaction forces to an acceptable accuracy in real time using this method.

2 Description of AEGIR

2.1 High-order boundary element method

For numerical stability, the perturbation velocity potential is decomposed into two components ϕ and ψ corresponding respectively to the impulsive and the memory effects of the ship's motion. The impulsive contributions are wave-less and are computed during the initial set-up, while the memory effects are held in the free-surface wave motion history.

The Neumann-Kelvin linearization is used for free-surface ship flows. The transient free-surface Green function is applied to the boundary integral equation and a free stream is considered as the basis flow.

The kinematic and dynamic free-surface conditions are linearized about the calm-water plane $z = 0$

$$\frac{\partial \zeta}{\partial t} - \vec{V} \cdot \nabla \zeta = \frac{\partial \phi}{\partial z} + \frac{\partial \psi}{\partial z} \quad , \quad \left(\frac{\partial}{\partial t} - \vec{V} \cdot \nabla \right) \psi = -g\zeta \quad , \quad \phi = 0 \quad \text{on} \quad z = 0 \tag{1}$$

where ζ is the free-surface elevation, $\vec{V}$ is the ship velocity.

The body boundary condition is linearized about the mean wetted-body surface $S_{\bar{B}}$

$$\frac{\partial \psi}{\partial n} = \vec{V} \cdot \vec{n} \quad , \quad \frac{\partial \phi}{\partial n} = \sum_{j=1}^{6} \left(\frac{\partial \xi_j}{\partial t} n_j + \xi_j m_j \right) \quad \text{on} \quad S_{\bar{B}} \tag{2}$$

where $\vec{\xi}_T = (\xi_1, \xi_2, \xi_3), \vec{\xi}_R = (\xi_4, \xi_5, \xi_6)$ are the translations and rotations expressing the ship motion $\vec{\delta} = \vec{\xi}_T + \vec{\xi}_R \cdot \vec{x}$ and $(n_1, n_2, n_3) = \vec{n}, (n_4, n_5, n_6) = \vec{x} \times \vec{n}$, $(m_1, m_2, m_3) = (\vec{n} \cdot \nabla)\vec{V}, (m_4, m_5, m_6) = (\vec{n} \cdot \nabla)(\vec{x} \times \vec{V})$.

The boundary integral equation for $\Phi = (\phi, \psi)$ is formulated by using the Rankine source potential $G(\vec{x}; \vec{x}') = 1/|\vec{x} - \vec{x}'|$

$$2\pi\Phi(\vec{x}) - \int\int_{S_F} \frac{\partial \Phi(\vec{x}')}{\partial z'} G(\vec{x}; \vec{x}') d\vec{x}' - \int\int_{S_{\bar{B}}} \frac{\partial \Phi(\vec{x}')}{\partial n'} G(\vec{x}; \vec{x}') d\vec{x}' + \int\int_{S_F \cup S_{\bar{B}}} \Phi(\vec{x}') \frac{\partial G(\vec{x}; \vec{x}')}{\partial n'} d\vec{x}' = 0. \tag{3}$$

The variable is approximated by a linear superposition of bi-quadratic spline basis function

$$\Phi(\vec{x}, t) = \sum_j \Phi_j(t)\, b(x)\, b(y) \tag{4}$$

where

$$b(x) = \begin{cases} \frac{1}{2h_x^2}(x + \frac{3h_x}{2})^2 & \text{for} \quad -\frac{3h_x}{2} < x < -\frac{h_x}{2} \\ \frac{1}{h_x^2}(-x^2 + \frac{3h_x^2}{4}) & \text{for} \quad -\frac{h_x}{2} < x < \frac{h_x}{2} \\ \frac{1}{2h_x^2}(-x + \frac{3h_x}{2})^2 & \text{for} \quad \frac{h_x}{2} < x < \frac{3h_x}{2} \end{cases} \tag{5}$$

and where h_x is the panel width.

2.2 Ship motions

The equations of motion for the ship can be written

$$([M]+[a_0])\ddot{\vec{\xi}}(t)+[b_0]\dot{\vec{\xi}}(t)+([C]+[c_0])\vec{\xi}(t)=\vec{F}_m(\dot{\vec{\xi}},\vec{\xi},t) \tag{6}$$

where $[M],[C]$ are the inertia and restoring force coefficient matrices, $[a_0],[b_0],[c_0]$ are the impulsive added mass, damping and restoring coefficients matrices, and $\vec{F}_m$ is the memory force computed through the solution of the wave pattern (see [2] for the details).

2.3 Wave radiation boundaries

To avoid the wave reflection at the outer boundary, the wave radiation condition is imposed by introducing a Newtonian cooling term ν in the kinematic free-surface condition

$$\frac{d\zeta}{dt}=\frac{\partial\psi}{\partial z}-2\nu\zeta+\frac{\nu^2}{g}\psi \tag{7}$$

where

$$\nu(r)=\frac{3C_s}{C_w^3}(r-r_0)^2 \qquad \text{for} \qquad 0\le r-r_0\le C_w \tag{8}$$

and where r is the radial distance from the wave-making source with the numerical beach starting at $r=r_0$ and extending over a width C_w, and C_s is the parameter dictating the overall cooling strength.

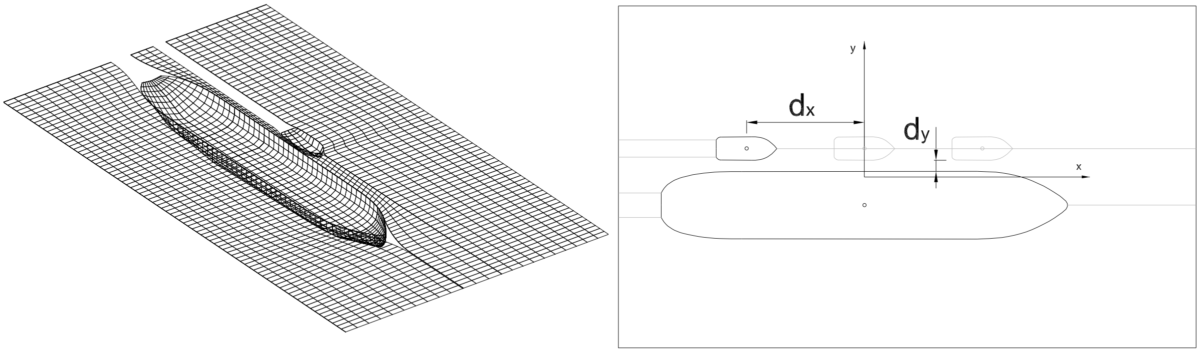

Figure 1: The meshed free surface and wetted hull surface (left) and the schematic presentation of ship-ship interaction case (right)

3 Numerical solution

3.1 Numerical model

The hull surfaces, consisting of third-order splines, are made by using the CAD software Rhinoceros, of which the 3D geometry file is supported by AEGIR. The numerical hull models are established for the tanker ($L_{pp}=186.2m, B=31.6, T=10.3$) and the tug-boat ($L_{pp}=25.6, B=11.0, T=3.9$) at full scale. The propeller boss on the tanker and the skeg keel on the tug-boat are neglected for computational efficiency.

The free-surface domain size, grid size on free surface and wetted hull surface and time-step are determined to achieve a robust and stable solution based on a series of numerical tests. The free-surface domain length $L_{fs}=280m$ and width $B_{fs}=160m$, grid size $\Delta x\simeq 3m$ and time-step $\Delta t=0.01\sim 0.02s$ are applied to the following numerical analysis. The meshed free surface and wetted hull surface are shown in Figure 1(left). The free-surface domain consists of two outer parts and an inner part between two ships. Both ships have a transom stern under the waterline. The free surface behind the transom stern is ignored. Due to the forward speed, the upstream free-surface length is $40m$ larger than the downstream one.

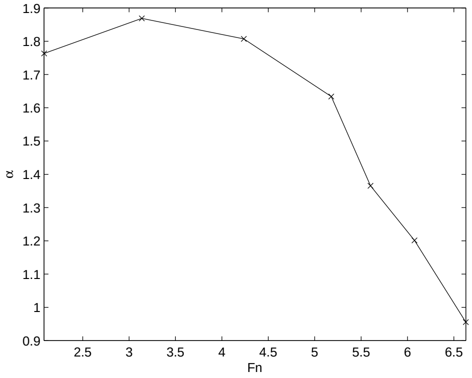

Figure 2: α as a function of Fn

3.2 Numerical result

Ship-ship interaction case with varying d_y

Both ships move with an identical forward speed of $Fn \simeq 0.2$. Varying the lateral distance d_y at three longitudinal distances d_x (See Figure 1(right)), the resistance and sway force on the tug-boat are computed. Positive d_x corresponds to placing the tug-boat towards the fore part of tanker. The force is nondimensionalized by dividing it by $0.5\rho U^2 L_{pp} T$. The resistance coefficient C_x and the sway force coefficient C_y are defined to be positive for resistance and for a repulsive force away from the tanker, respectively. Experiments were carried out at FORCE Technology, Denmark, in their small model tank with models at scale $1:25$. The computational results are compared with results of those experiments, as shown in Figure 3. The model was free to pitch and heave in the experiment, and the computations are conducted both with and without heave and pitch motions.

To avoid unwanted starting transients in the calculations, the forward speed is increased gradually to the specified one over $10s$. The simulation is conducted for $60s$. The average value of maximum and minimum in the last $10s$ is taken for the resistance F_x and sway force F_y.

A quantitative comparison between the computed and measured resistance forces requires an accurate assessment of the viscous forces, as well as a very accurate representation of the hull geometry, including appendages. As the goal here is to capture the interaction effects efficiently, we simply define a factor $\alpha = F_{x,comp}/F_{x,exp}$, based on the open water resistance of the tug-boat without the tanker. $F_{x,comp}$ is computed without ship motions and $F_{x,exp}$ is the total resistance including both viscous and residual resistances. α as a function of Fn is shown in Figure 2. In the following ship-ship interaction results, $C_{x,comp}$ is compared to $\alpha C_{x,exp}$ to highlight the interaction effects. The horizontal forces are however not modified.

While C_x, C_y show a relative error of $\epsilon = \sum((C_{comp} - C_{exp})/C_{exp})/n = 0.1 \sim 0.3, 0.1 \sim 0.4$, respectively, the comparison shows a good qualitative agreement except at a small lateral distance of $d_y \simeq 1m$. In all the cases, C_y from experiment is larger than that from numerical solution.

The converged solution is not achieved for $d_y < 0.7m$. The numerical result does not show a high peak in C_x and a sudden drop in C_y for $d_y \simeq 1m$. It is probably due to a high aspect ratio of the elements in a narrow free-surface area between two ships, and due to the conflict between the linearized free-surface condition and high wave elevation in a narrow area between two ships.

The inclusion of heave and pitch brings a damping in the longitudinal motion, hence C_x with heave and pitch is smaller in all the cases. The uncertainty in viscosity makes it difficult to say whether the inclusion of ship motions results in higher accuracy.

Ship-ship interaction case with varying Fn

Varying Fn for the case with $d_x = -54.475m$ and $d_y = 2.45m$, C_x and C_y are computed. In Figure 4, the numerical result is given with the experimental one. α is found at each different value of Fn. C_x from the experiment is multiplied by α at the corresponding Fn.

While C_x, C_y have $\epsilon \simeq 0.3, 0.1$, respectively, they have a qualitative agreement except for $Fn \simeq 0.42$.

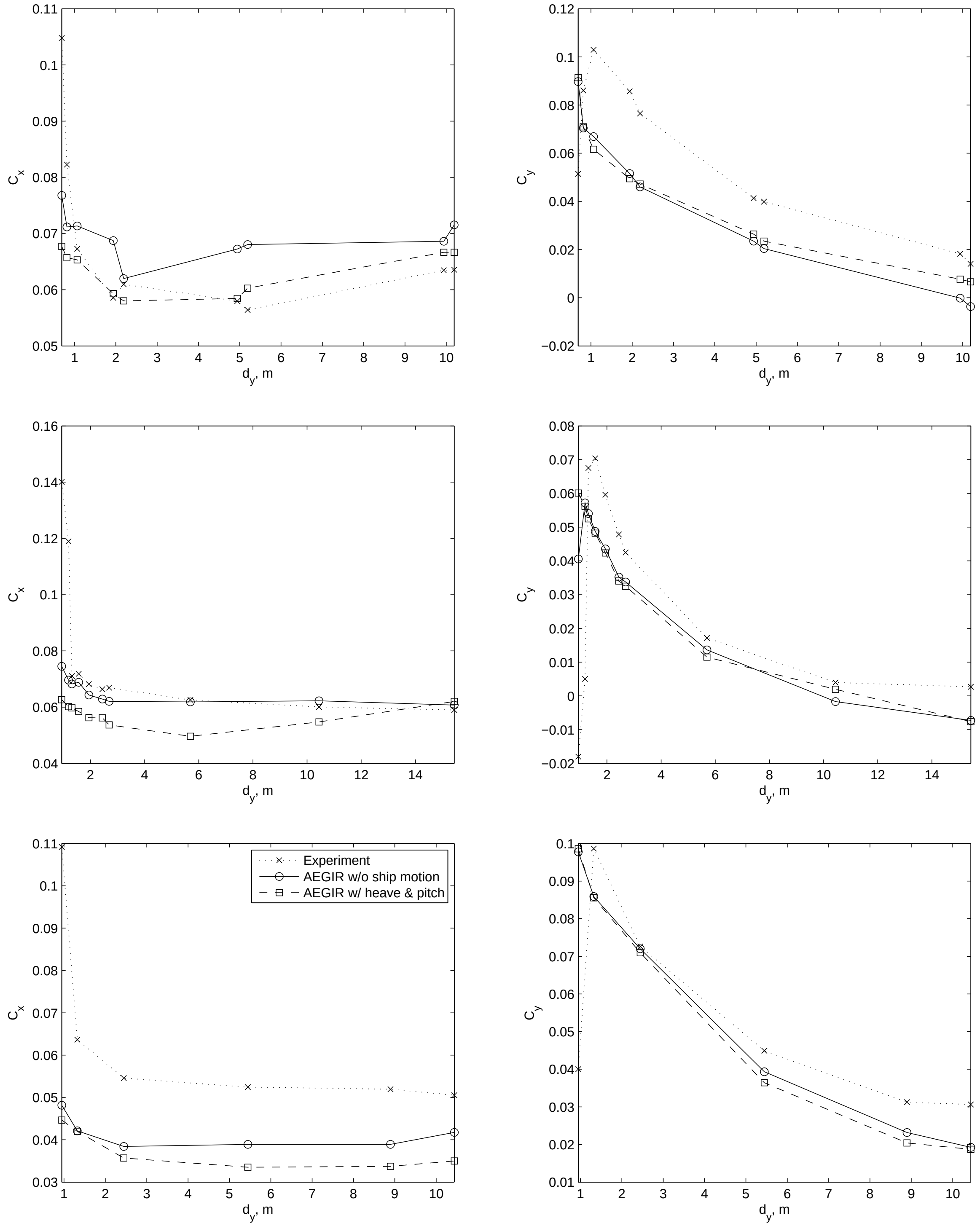

Figure 3: The resistance coefficient C_x (left) and sway force coefficient C_y (right) as a function of d_y for $d_x = 54.625m$ (top), $d_x = -0.675m$ (middle), $d_x = -54.475m$ (bottom) and $Fn \simeq 0.2$

3.3 Computational efficiency

The numerical model applied above has 2506 elements. For a $1min$ simulation with $\Delta t = 0.02s$, the CPU time is about $18min$ without ship motions and about $86min$ with ship motions on a $32 - bit$ $3.2Ghz$ Pentium-4, single-processor machine.

To improve the computational efficiency, we decrease the free-surface domain size and increase the grid size and time-step while checking the accuracy by comparing the result to the previous one. By varying the

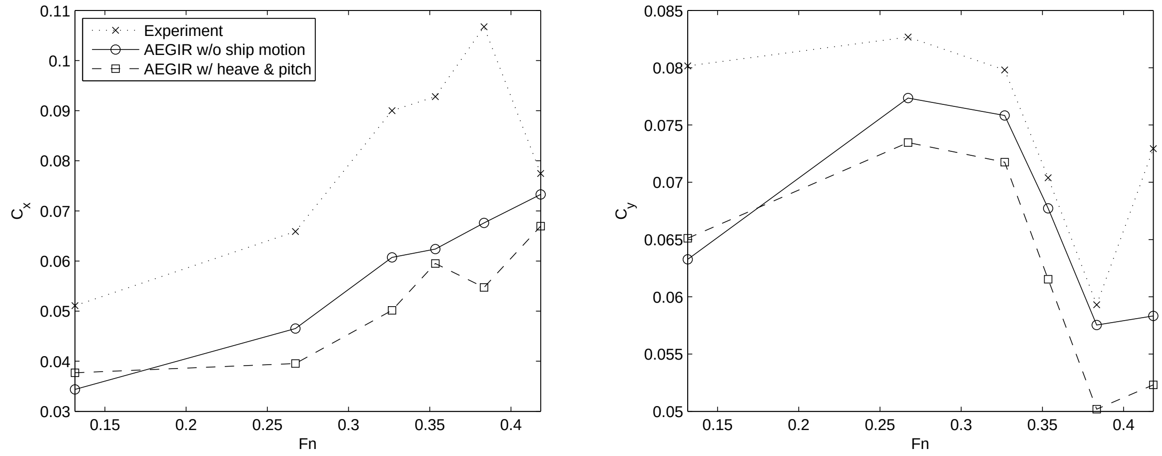

Figure 4: The resistance coefficient C_x (left) and sway force coefficient C_y (right) as a function of Fn for $d_x = -54.475$ and $d_y = 2.45m$

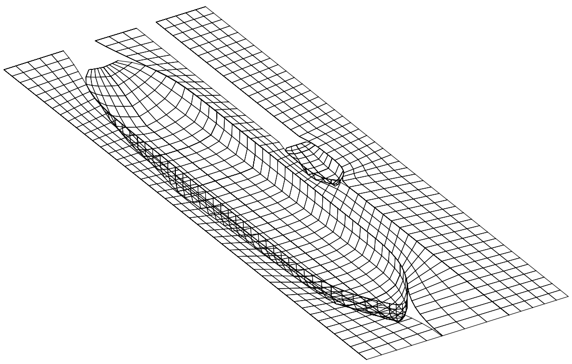

Figure 5: The optimized numerical model

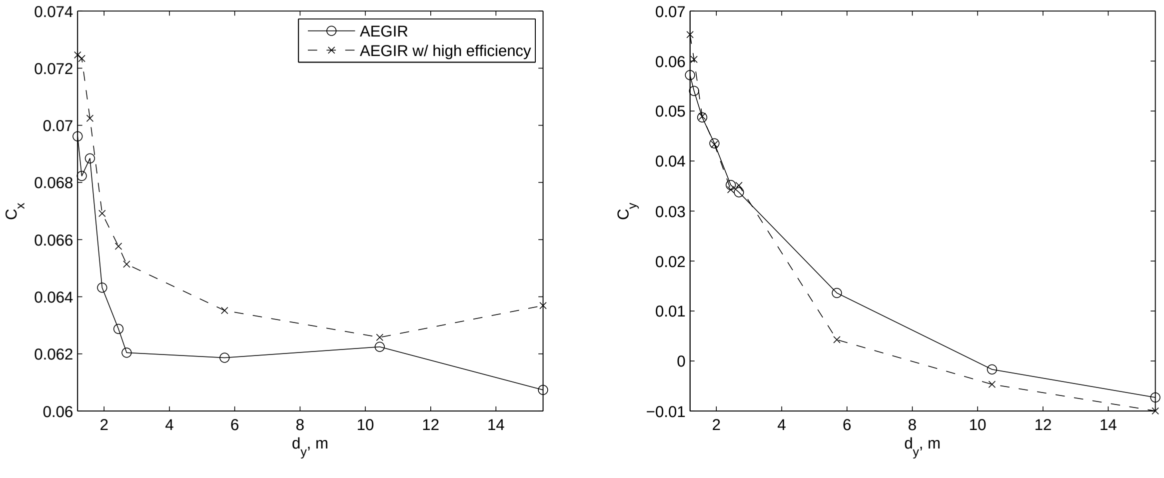

Figure 6: The resistance coefficient C_x (left) and sway force coefficient C_y (right) as a function of d_y for $d_x = -0.675$ and $Fn \simeq 0.2$ from the numerical model with a high efficiency

numerical properties, we find the optimum with a high efficiency and insignificant discrepancy from the above result. As shown in Figure 5, the optimized numerical model with $L_{fs} = 320m, B_{fs} = 80m, \Delta x \simeq 6m, \Delta t = 0.05s$ has 1045 elements. The CPU time for $1min$ simulation is $2.5min$ without ship motions.

The high-efficiency model is validated by a case with varying d_y for $d_x = -0.675m$ and $Fn \simeq 0.2$. As shown in Figure 6, the result is compared to the previous one. While the converged solution is not achieved for $d_y \leq 0.95m$, it shows an accuracy as high as in the previous model with $\epsilon \leq 0.1$.

4 Conclusion

A high-order boundary-element model has been used to consider the interaction effects between a sailing tanker and a nearby tug-boat for a range of speeds and relative positions. Although the absolute magnitude of the tug-boat resistance predicted by the numerical model is often quite different form the experimental measurements, the change in resistance with relative position as well as the transverse repulsive force are both reasonably well captured with typical discrepancies of around 10%. A similar correspondence is obtained even using a very coarse discretization which leads to calculation times which are only about 2.5 times larger than the real-time simulation at full-scale. This shows that with some further optimization of the numerical solution (and/or somewhat faster computers), the model can be used for real-time inclusion in a training simulator.

Future work with this model includes allowing for a variable speed of the tug-boat in three degrees of freedom (surge, sway and yaw) to consider more general ship-ship interaction cases in a variety of ship maneuvering situations.

References

[1] Kring, D.C., *Time domain ship motions by a three dimensional Rankine panel method*, PhD Thesis, MIT, Cambridge, MA, 1994

[2] Kring, D.C., Sclavounos, P.D., "Numerical stability analysis for time-domain ship motion simulations",*Journal of Ship Research*, 39, 1995

[3] Kring, D.C., Milewski, W.M., Fine, N.E., "Validation of a NURBS-based BEM for multihull ship seakeeping", *25th Symposium on Naval Hydrodynamics*, 2004

[4] Kring, D.C., Milewski, W.M., Connell, B., *Aegir, time-domain seakeeping program: main executable and I/O user notes v0.80*, 2007

[5] Nakos, D.E., Sclavounos, P.D., "Ship motions by a three-dimensional Rankine panel method", *18th Symposium on Naval Hydrodynamics*, 1990

RANS Simulation of the flow around a ship appended with rudder, ice fins and rotating propeller

Claus D. Simonsen[1], Rasmus Carstens[2]
[1]FORCE Technology, cds@force.dk, [2]MAN Diesel, Rasmus.Carstens@man.eu

Introduction

FORCE Technology and MAN Diesel A/S in Denmark are currently collaborating in a project under DCMT [Danish Centre for Maritime Technology]. The goal of the project is to test and demonstrate the capabilities of RANS in connection with complex ship flows. Focus is on a complete CFD model for hull, propeller and appendages, which can account for the mutual interaction between the components when the flow field is calculated. In RANS, propellers can be modeled by body-forces as in [1], but in the present work the real propeller geometry is modeled. More details can be found in [2]. A stepwise approach is followed, where the appended hull and the open-water propeller are first modeled individually. This is done by simulating the propeller and the appended hull in an open-water and a resistance test setup, respectively. After this the two models are combined by means of sliding interfaces in order to simulate the combined flow problem. This is done by simulating a cavitation tunnel setup at atmospheric pressure. In order to check the performance of the CFD model, the calculated results are compared with experimental data. All meshing and flow simulation are conducted with StarCCM+ from CD-adapco.

Numerical method

The computations are performed with the Reynolds Averaged Navier-Stokes (RANS) solver StarCCM+ from CD-adapco. The code solves the RANS and continuity equations on integral form on a polyhedral mesh by means of the finite volume technique. Both steady state and transient calculations are considered. For the steady state calculations the temporal discretization is based on a first order Euler difference, while a second order difference is used for transient calculations. Spatial discretization is performed with second order schemes for both convective and viscous terms. The pressure and the velocities are coupled by means of the SIMPLE method. Closure of the Reynolds stress problem is achieved by means of the isotropic blended k-ε/k-ω SST turbulence model with an all Y^+ wall treatment. The rotating propeller is treated in different ways. For open-water calculations the propeller inflow is uniform, so the moving reference approach is applied, i.e. the blade velocity is set on the propeller blades and centripetal effects are included in additional source terms in the momentum equations. For the propeller rotating behind ship, a rigid body approach is applied. The free surface is modeled with the two phase volume of fluid technique (VOF). Further details about the code can be found in [3].

Ship condition and computational grids

The study is carried out for a model of a 70m inspection vessel with appendages and propeller, Figure (1) and Figure (2). The model is in scale 1:14.15. The main particulars and propeller data are shown in Table 1. Speeds and propeller RPM are given below in the sections describing the results.

Model data	
L_{pp} [m]	4.3107
B [m]	1.0325
T [m]	0.3495
S [m^2]	5.4895
C_b [-]	0.44
D_p [m]	0.2332
N [blades]	4
P_{07}	1.2018

Table (1). *Hull and propeller data.*

Figure (1). *70m inspection vessel.*

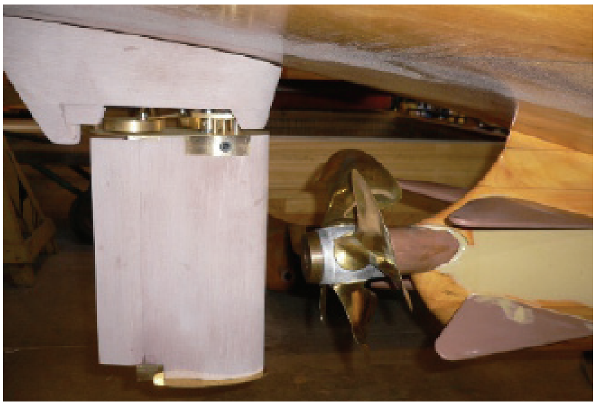

Figure (2). *Model rudder-propeller arrangement.*

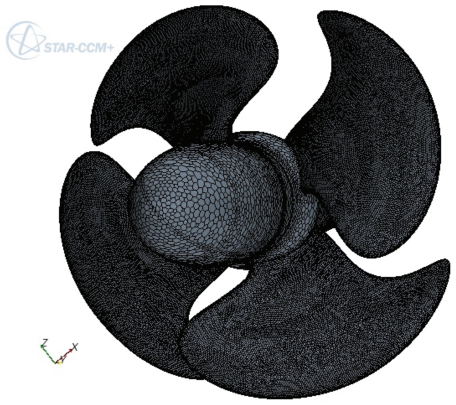

Figure (3). *Computational grid on propeller.*

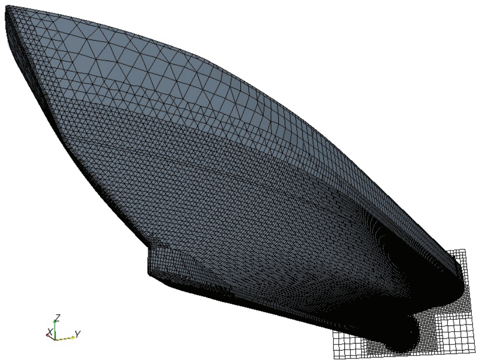

Figure (4). *Computational grid on hull.*

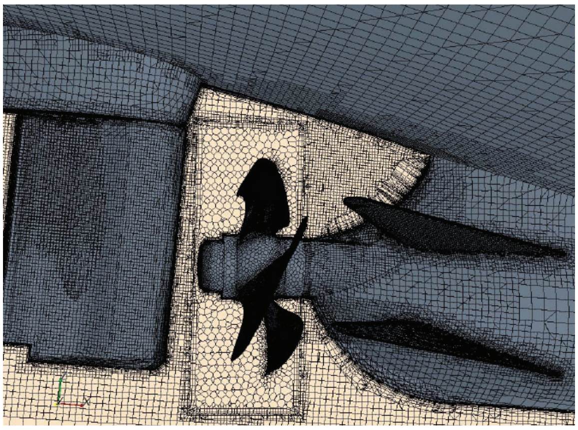

Figure (5). *Computational grid on hull and propeller.*

Concerning the grid, the computations are performed with unstructured grids generated in Star-CCM+. The propeller is modeled with a polyhedral mesh. The open-water mesh consists of approximately 2 million cells. The ship is modeled with a trimmed mesh, which is a hexa-dominant polyhedral mesh. The mesh for the ship alone contains approximately 3.4 million cells. Since the propeller is running behind the ship, both sides are considered instead of exploiting the centre plane symmetry. The grids are shown in Figure (3) to Figure (5). The near wall spacing of the grids on no-slip surfaces are in the range from $y^+ \approx 1$ to $y^+ \approx 30$. Concerning verification, a grid refinement study was made for the hull alone and the propeller alone. Error estimates with unstructured grids are not possible but the systematic refinement has been used to check the trend of the solution changes with the fineness of the mesh.

Results for open water propeller calculation

The open water test was carried out at the same running conditions as used in the experimental set up at FORCE Technology. The solution domain was chosen to extend 10 propeller diameters in front of the propeller, 18 diameters in the radial direction and 30 diameters behind the propeller. The flow solver was run in steady mode and the rotation of the propeller was accounted for by using the moving reference frame approach. This approach works fine in open water, where the propeller sees a completely uniform inflow field. The calculation was carried out for advance coefficients in the range from J=0.0 to J=1.1.

Like in the experiment the computed thrust and torque on the propeller were converted into the dimensionless thrust coefficient K_T, torque coefficient K_Q and the open water coefficient η_0 was calculated. The advance ratio J and the three coefficients are defined as

$$J = \frac{U_a}{n\,D}$$

where U_a is the speed of advance, n is the propeller revolution rate and D is the propeller diameter.

$$K_T = \frac{T}{\rho n^2 D^4}$$

where T is the measured thrust and ρ is the water density.

$$K_Q = \frac{Q}{\rho n^2 D^5}$$

where Q is the measured torque.

$$\eta_0 = \frac{J}{2\pi}\frac{K_T}{K_Q}$$

With respect to the grid study, it showed that the calculated K_T changed with 2.7% when going from coarse to medium grid, while the change was reduced 1.3% when going from medium to fine grid. For K_Q the changes were 3.2% and 1.6% from coarse to medium and medium to fine, respectively. The number of cells in the fine mesh, which was used for the final open water calculation, was 1,963,001.

For the results of the open water calculation, a study of the flow field shows that the propeller, as expected, accelerate the flow over the blades and introduces swirl in the flow downstream of the propeller. On the blades themselves the pressure field shows low pressure on the suction side and high pressure on the pressure side. Figure (6) illustrates the pressure distribution on the suction side.

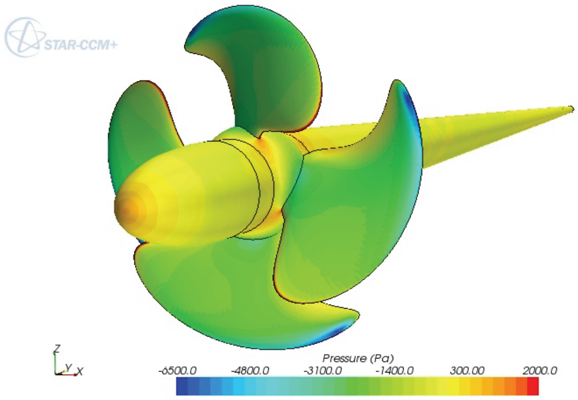

Figure (6). *Pressure distribution on suction side of propeller.*

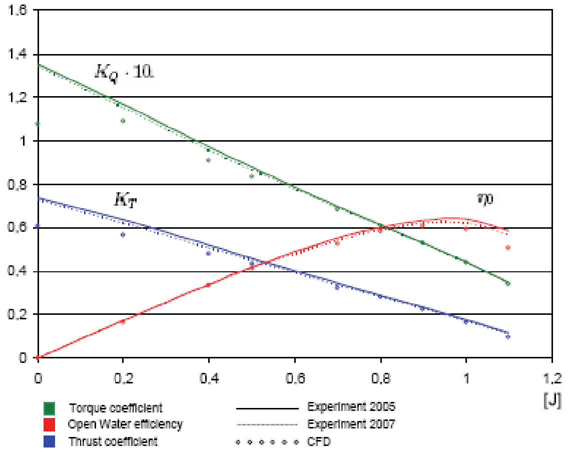

Figure (7). *Computed and measured open-water curves.*

Figure (7) shows the calculated open water curves together with the measured curves [4]. Two sets of measured data are shown. The first set was measured in 2005, but the test was repeated in connection with the present project to check the repeatability of the measurement and as seen the two data sets are in fairly good agreement. When it comes to a comparison between the calculated and measured data, it is seen that fairly good agreement is achieved. Particularly in the region around J=0.8, which is the point where the ship usually operates. Table 2 summarizes deviations between the two data sets. It is seen that the deviations increase as J is reduced. Smaller J values means conditions closer to the bollard pull condition, which again means that the propeller loading is increasing. Higher loading means that larger gradient have to be resolved, which again requires more of the numerical method. The results for small J could probably have been improved by refining the mesh.

	Deviation in percent	
J	K_T	$K_Q \cdot 10$
0.0	17.853	20.484
0.2	10.935	6.538
0.4	7.479	6.607
0.5	6.066	4.716
0.7	6.531	2.267
0.8	3.412	0.516
0.9	4.568	-0.208
1.0	7.898	0.896
1.1	15.439	1.987

Table (2). *Difference between CFD and measurement.*

Resistance calculation for hull with appendages

The numerical appended hull model without propeller was tested in a resistance test setup, where the model was positioned according to the dynamic sinkage and trim position and locked. The model speed was 1.915 m/s, which corresponds to a Froude number equal to 0.289 and a model Reynolds number equal to *Re*=7.24 million.

As mentioned above a grid stud was made for the hull model. Grid refinement between grids was obtained by applying a refinement factor of $\sqrt{2}$ to the mesh reference length when generating the three grids. The grid study showed that the calculated resistance changed 11.4% when going from coarse to medium grid, while the change was reduced 0.6% when going from medium to fine grid. A comparison between the computed fine-grid resistance and experimental data from the towing tank [4] showed that the calculated resistance was under predicted with 2.4%.

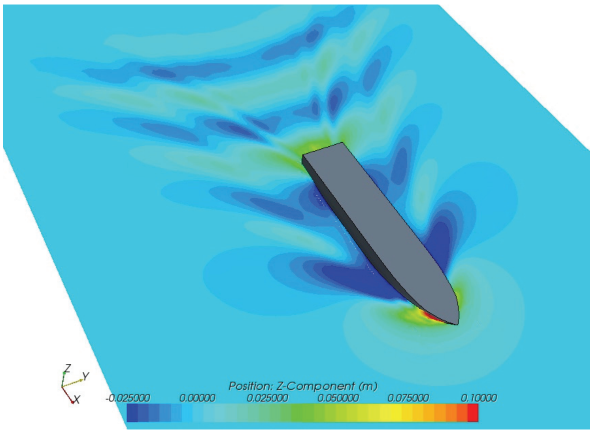

Figure (8). *Calculated free surface elevation.*

With respect to the field quantities the results are briefly summarized as follows: 1) High pressure occurs in the bow region where the flow is slowed down and the bow wave is formed due to stagnation. 2) The pressure decreases around the shoulders, where the flow is accelerated to get around and below the hull. 3) Further downstream the pressure recovers and basically constant flow properties along the prismatic section of the hull are seen. 4) At the aft shoulders, i.e. the region where the hull form start to narrow in towards the stern and the water starts to flow into the wake region, the pressure decreases again. 5) The pressure increases again in the stern region and formation of the wake field with lower velocities is seen. The pressure field is not shown here. Figure (8) shows the calculated wave elevations around the ship and reveals a typical Kelvin wave pattern. Finally, Figure (9) shows the calculated nominal wake field behind the ship at a cross section located at the propeller plane. Due to the relatively slender shape of the ship, the bilge vortices, which normally are observed in the centre plane wake, are relatively weak. Consequently the contours appear smoother, and the traditional hook shape is not observed.

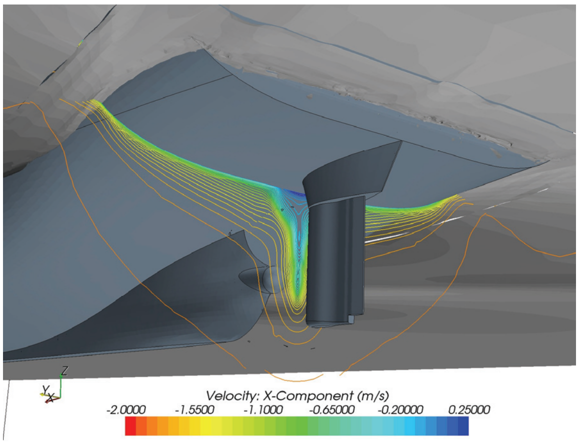

Figure (9). *Calculated wake field.*

Simulation of appended hull with rotating propeller

The goal of the present project is to simulate the complete ship with hull, rudder and propeller including the free surface around the ship. However, for the initial with-propeller calculations the problem was simplified by neglecting the free surface and using a setup similar to what is used in a cavitation tunnel. This means that only the underwater part of the ship was considered and a symmetry condition was applied on the still water surface. The model speed was 4.53 m/s, which corresponds to a model Reynolds number equal to *Re*=17.1 million. Atmospheric pressure was used in the simulation in order not to introduce cavitation on the propeller.

Compared to the open-water calculation, which could be run in steady state mode, the simulation with the propeller behind the ship must to be run in transient mode, i.e. time accurate. However, the different time scales of the propeller and the hull flow then become an issue in startup phase of the computation. The problem is that the time step is closely related to the rate of rotation of the propeller. In the present simulations the time step is chosen so the propeller rotates approximately three degrees per time step. This corresponds to time steps in the order of 3 to 5 10^{-4} sec. If the ship has to travel a couple of ships lengths in order for the boundary to build up on the hull this would take maybe 10 sec, so with the small time step this would take a very long time to calculate. In order to speed the calculation the model was first run in steady mode with moving reference frame for the propeller. After the hull boundary layer then had developed, the transient solution was initiated and the propeller was rotated by means of a rigid body motion and sliding interfaces.

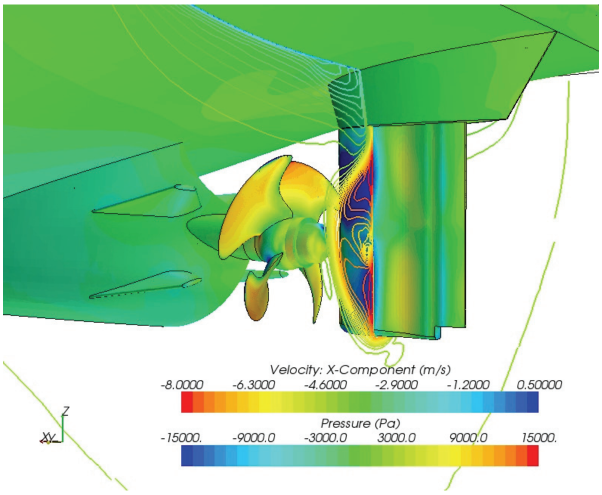

Figure (10). *Calculated pressure and wake fields. Line contours represent the axial wake velocity.*

A study of the field quantities, i.e. velocities and pressure in the stern region shows a time varying, but periodic flow field, which to a high degree is related to the blade frequency of the rotating propeller. Figure (10) and Figure (11) give an example of the pressure field in the stern region and the axial velocity contours in a cross section at the rudder position. With respect to the velocity field, it shows that the propeller accelerates the flow and introduces swirl in the flow downstream of the propeller. Consequently, the rudder sees an accelerated rotating flow field, which results in varying angles of attack along the span of the rudder. The pressure field on the propeller blades themselves varies with the blade position due to the non-uniform inflow field in the wake field. When the blade passes the centre plane wake around the twelve or six o'clock positions the low axial inflow velocity to the blade in these regions results in higher loading on the blade compared to when the blade is in the three o'clock position for instance. Also the loading depends on whether the blades move upwards in the wake (starboard side) or downward (port side). The reason is that the cross flow, which has an upwards direction on both sides results in different angles of attack for the blades which consequently experience different loadings. The highest loading occurs on port side where the cross flow and propeller motion have opposite directions.

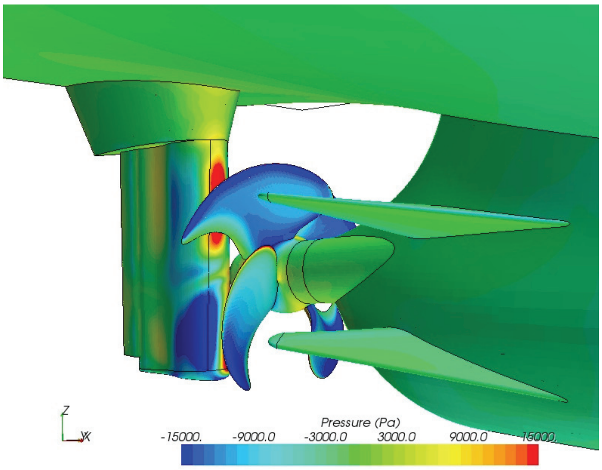

Figure (11). *Calculated pressure on the suction side of the propeller.*

As seen the wake deficit of the hull strongly influences the propeller, but the propeller also influences the hull flow. The influence is most clearly seen in the pressure field. Upstream of the propeller the hull experiences suction, which reduces the pressure and increases the resistance. The effect is usually expressed as the thrust deduction. Another region of the hull that feels the presence of the propeller is the region above the propeller. In this region the passing blades will introduce pressure pulses on the hull, which in critical cases can lead to noise or vibration problems in the structure.

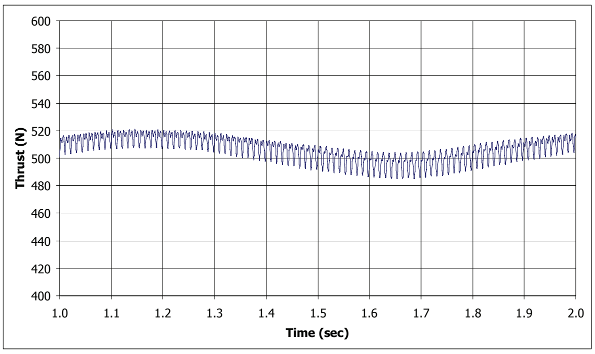

Figure (12). *Time series for the calculated thrust.*

Concerning the integral quantities for the present hull-propeller configuration, focus was placed on the propeller thrust and torque, since measured data for comparison was available from a previous cavitation test [5]. Four different propeller loading conditions were calculated, but detailed results will only be discussed for one condition here. In this condition, the propeller was rotating with 22.57 rps. The time history of the calculated thrust and torque are shown in Figure (12) and Figure (13), respectively.

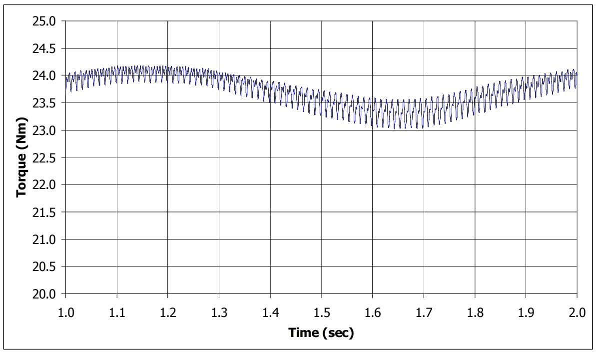

Figure (13). *Time series for the calculated torque.*

From the two figures it is seen that the time series consist of a slowly varying signal overlaid with high frequency oscillations. In order to determine the dominant frequencies in the signals FFT analysis was used. Figure (14) shows the frequency spectrum for the thrust. Having a blade frequency of 90.3Hz it is seen that the dominant frequencies are multiples of the blade frequency. However, in addition to these frequencies there is also a peak at a very low frequency around 1Hz, but this should also be the case since Figure (12) and Figure (13) showed a slowly global variation in the signals. It is difficult to say exactly what causes this low frequency behavior, but it is believed to come from the hull wake, which easily can be a little unsteady behind the ship.

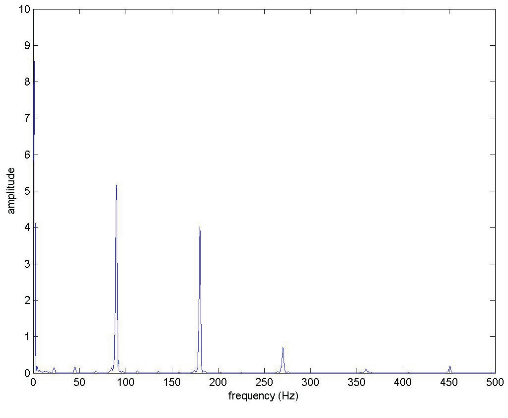

Figure (14). *Frequency spectrum from FFT analysis of thrust signal.*

After studying the detailed behavior of the time series for the propeller quantities the mean values from the four calculations were compared with measured data from the cavitation tunnel. Figure (15) shows the calculated propeller thrust, torque and efficiency together with the measured values. Figure (16) shows the deviations in %. It is seen that CFD slightly under predicts the quantities, but also the fairly good agreement is achieved. For the considered J values, the deviations seem to be slightly smaller compared to the open water calculation. It is difficult to say why this is the case, because the inflow field is somewhat more complicated than the uniform open-water inflow. One reason could be that the propeller mesh used behind the ship is slightly finer than the open-water mesh and another could be that the computed wake field is a little different from the real inflow field which may cancel out some of the propeller errors. However, without measured velocity date for comparison this is not possible to say for sure.

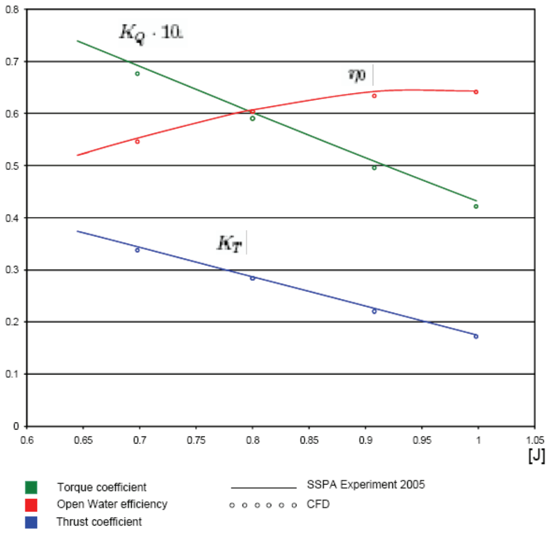

Figure (15). *Comparison of measured and calculated propeller quantities.*

Run No.	K_T	$K_Q \cdot 10$	ETA
	Deviation in percent		
1	1.24	2.231	0.24
2	2.37	2.35	1.18
3	1.08	1.88	0.5
4	2.29	2.40	1.18

Figure (16). *Deviations between calculation and measurement for propeller behind ship condition.*

Concluding remarks

In the present work RANS simulations have been conducted for: a propeller in open water, an appended ship in a resistance test setup and a combined ship-propeller configuration in a cavitation tunnel setup at atmospheric pressure. The open water and resistance calculations were steady state computations, while the combined case was run time accurate.

Grid studies were made for the open water propeller and the appended hull calculation. A formal verification was not conducted, so the grid uncertainty was not estimated. Only changes in solutions between grids were considered. For the medium and fine grid solutions the two studies showed changes in integral quantities between grids of 1.6% and 0.6%, respectively.

Concerning the results of the calculation all the three considered configurations showed promising results. The open-water calculation showed that thrust and torque could be predicted within 3.5% and 0.5% of measured data, respectively, at the point where the propeller works when behind the ship. At higher propeller loadings, i.e. lower *J*, larger deviations were observed. However, it is believed that the grid was not fine enough to resolve this condition. For the resistance test setup, the simulation showed a typical ship flow field and the resistance was predicted within 2.4% of measured data. Finally, the simulation of the cavitation tunnel setup at atmospheric pressure, showed a complex time varying flow field and mutual interaction between hull, rudder and propeller. When compared to measured data it was found that CFD predicted both thrust and torque within 2.4% of the measured data.

Future activities

Within the present project two more tasks will be covered. One is to run the model in the cavitation tunnel setup used above, but at low pressure with inclusion of a cavitation model in order to study the propeller cavitation. The second is to run a ship-propeller simulation which includes the free surface at the self-propulsion point and compare the results with towing tank test data.

Acknowledgements

This research is sponsored in parts by The Danish Maritime Foundation through DCMT and MAN Diesel A/S.

References

[1] Simonsen, C.D. and Stern, F., “RANS maneuvering simulation of Esso Osaka with rudder and a body-force propeller,” J. of Ship Research, Vol 49, No. 2, June 2005.
[2] Carstens, R., Numerical investigation of flow around a ship’s hull and cavitation prediction using RANS CFD, Master thesis, Aaborg University, Denmark, 2008.
[3] StarCCM+ Users manual
[4] FORCE Technology report no. 2005072-4B (Confidential)
[5] SSPA Report no. 20053790-1 rev A. (Confidential)

Adaptive grid refinement for ISIS-CFD

Jeroen Wackers and Michel Visonneau
Laboratoire de Mecanique des Fluides, Ecole Centrale de Nantes
CNRS-UMR 6598, 44321 Nantes Cedex 3, France
Jeroen.Wackers@ec-nantes.fr

1 Introduction

Adaptive grid refinement is a technique to increase the accuracy and efficiency of numerical simulations for flows with localised flow phenomena. To obtain acceptable numerical errors near these structures, fine grids are needed there; for efficiency, coarse grids are desired in the rest of the domain. Adaptive grid refinement creates these grids by locally dividing the cells of an initial coarse grid into smaller cells.

The water flow around a ship contains many local features. For a Volume-of-Fluid (VoF) discretisation, the water surface appears as a numerically smeared discontinuity in the volume fraction; to capture the surface sharply, very fine cells are needed around this discontinuity. Also the orbital velocity field of the ship's waves is local. It appears below the weater surface, in the wave train. And lastly, the bilge vortices, that play an essential role in the velocity field encountered by the propeller, consist of local very strong gradients.

Thus, to efficiently obtain highly accurate simulations of ship flow, adaptive grid refinement is an excellent choice. This is even more evident for unsteady ship flow, where the position of the local features changes in time. To be successful for ship flow, the adaptive refinement technique must work for different types of flow features.

An adaptive grid technique has recently been developed for the ISIS-CFD flow solver developed by EMN (Equipe Modélisation Numérique, i.e. CFD Department of the Fluid Mechanics Laboratory). The technique is inspired partially by the earlier Ph.D. work of A. Hay in this group [2, 3]. In order to work together smoothly with ISIS-CFD and to efficiently handle different flow conditions, the method is based on the following principles:

1. *Flexibility* of the refinement criterion (which defines where to refine the grid). It is easy to choose between different refinement criteria for different problems and to develop and include new criteria.

2. *Generality* in the types of grid and refinement. Directional refinement (refining cells in one direction only) has been included from the beginning. And while the present method only refines unstructured hexahedral meshes, it is constructed such that other cell types can be easily included.

3. *Parallel* implementation. To function together with the parallelised code ISIS-CFD, the grid refinement must be performed in parallel, on distributed grids. Any work on a single processor would slow the refinement down unacceptably.

To be effective for unsteady flow, the method features derefinement: it can undo the refinements made in earlier steps, to arrive at the original coarse mesh again. Thus, flow features can be followed without leaving behind unnecessarily refined cells.

In this paper, after a short description of the ISIS-CFD solver in section 2, an overview of the refinement procedure is given in section 3. Then section 4 presents a first refinement criterion: refinement around the water surface. With this criterion, the method is tested in section 5 on the calculation of steady wave patterns for two ships, the Series 60 and the VIRTUE Container Ship. Section 6 concludes the paper and outlines further developments that are planned for the method.

2 The ISIS-CFD flow solver

ISIS-CFD, available as a part of the FINE$^{\text{TM}}$/Marine computing suite, is an incompressible unsteady Reynolds-averaged Navier-Stokes (RANSE) method [1, 6]. The solver is based on the finite volume method to build the spatial discretisation of the transport equations. The unstructured discretisation is face-based, which means that cells with an arbitrary number of arbitrarily shaped faces are accepted.

The velocity field is obtained from the momentum conservation equations and the pressure field is extracted from the mass conservation constraint, or continuity equation, transformed into a pressure equation. In the case of turbulent flows, transport equations for the variables in the turbulence model are added to the discretisation. Free-surface flow is simulated with a multi-phase flow (VoF) approach: the water surface is captured with a conservation equation for the volume fraction of water, discretised with specific compressive discretisation schemes [6].

The method features sophisticated turbulence models, 6 DOF motion for simulated ships [4], and the possibility of modelling more than two phases. For brevity, these options are not further described here.

3 Refinement method

This section describes the technical basis of the refinement method: the grids that are created and the procedure that is followed.

Globally, the method works as follows: the flow solver is run on the initial grid for a limited number of time steps. Then the refinement procedure is called. If the refinement criterion, based on the current flow solution, decides that parts of the grid are not fine enough, the cells there are refined and the solution is copied to the refined grid. On this new grid, the flow solver is started again. Then the refinement procedure is called again, to further refine or to derefine the mesh. This cycle is repeated several times. For steady flow, the procedure eventually converges: when the refinement procedure is called, it no longer changes the grids.

3.1 Grids and data structure

Our refined meshes consist of simple geometrical cell types (currently only hexahedra, but prisms, pyramids, and tetrahedra can be added without problems). But we allow the faces of these cells to be divided into smaller faces. Thus, cells can be refined into smaller cells, while their neighbour cells remain the same (see figure 1 for a hexahedron divided in four and the resulting divided face of its neighbour cell). Even the original grid may have these divided faces: the HEXPRESS$^{\text{TM}}$ grid generator of FINE$^{\text{TM}}$/Marine generates such meshes. ISIS-CFD does not care, as its face-based discretisation can handle any type of cell.

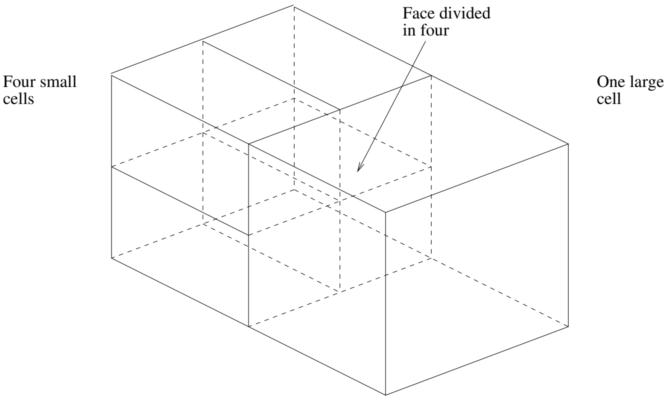

Figure 1: Two hexahedra, one of which is refined in four cells. The other has a divided face.

To store the refined grids, the normal ISIS-CFD data structure is used. This data structure contains the locations of the nodes and connectivity pointers between cells, faces, and nodes. For refinement, only a few extra pointers are added. These include an indicator of the basic type of each cell (hexahedron etc.) and pointers to indicate those faces that form one divided face.

The most important addition are the cell family ties. These store the history of the refinement, so refined cells can be derefined again to recover the original grid. When a cell is refined, all the new small cells get a ‘mother’ pointer to the old big cell and ‘sister’ pointers to each other. Thus, the group can be found again later and changed back into the single large cell. The large cell is saved as a ‘dead’ cell, that has no faces nor a state vector, only family ties. Thus, it remembers its own sisters and mother (probably ‘dead’ as well), in case it has to be derefined itself, after being restored.

3.2 Refinement procedure

Each time the grid is to be adapted, the refinement procedure is called. To ensure maximum flexibility, the procedure is divided into three distinct parts that exchange only minimal information. These parts are:

Refinement criterion. The criterion determines which cells will be refined or derefined. It could be based on anything: gradients of the solution, distance to the water surface (see section 4 for an example), or sophisticated error estimators. In our implementation, the refinement criterion is a scalar or vector field, like the state variables. Cells are refined where the criterion is high and derefined where it is low. The important thing is, that the criterion in a cell may *not* depend on the cell type, nor on its orientation (or at least not more than, for example, the pressure). This makes it easy to change criteria, as it is never necessary to write a separate criterion for each cell type. For different refinement criteria, this part is the only one that changes.

Refinement decision. In the second part, the refinement criterion is transformed into the refinement decision: a list of flags indicating which cells will be refined and in which direction. This decision depends on the cell type, but not on the way the refinement criterion was computed. It is simply an evaluation of the criterion field.

Step one of the decision is the evaluation of the refinement criterion in each cell. A cell will be refined if the criterion in that cell exceeds a certain threshold and derefined if it is below another, lower threshold. Vector criteria are used for directional refinement. A hexahedron can be refined in three different directions; in each, it is refined if the criterion component in that direction is high enough (see figure 3).

Step two is the adaptation of the decision in each cell to its neighbour cells. To produce good solutions, the adapted grid must satisfy certain quality criteria. The most important are given in figure 2. A face of a cell may not be divided two times, which would cause too great differences in the sizes of its neighbour cells. And the angle between face normals an lines cell centre - face centre may not be too great: this reduces the quality of the state reconstruction at the faces [6].

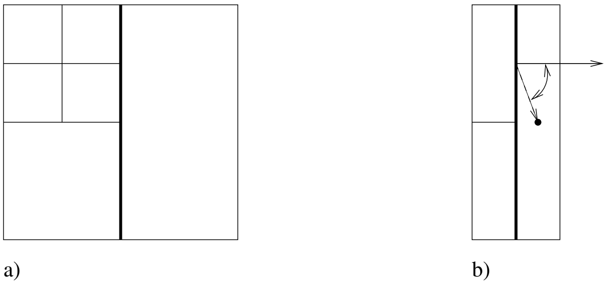

Figure 2: Grid quality criteria. Forbidden are: (a) twice divided faces, (b) too large angles between face normals and lines cell centre - face centre. 2D examples.

Thus, refining a cell may require the refinement of its neighbour cells or may prevent them from being derefined. So in an iterative process, refinement decisions are added and derefinement decisions are removed. The decision process for the whole grid is completed before a single cell is refined, which gives great advantages. For example, it is much easier to remove a decision to derefine a cell than to undo an already completed derefinement.

Refinement. The last step is the actual refinement of the grid. First, all cells selected for derefinement are derefined, then all cells to be refined are refined. During refinement, new small cells are created, faces and nodes are added between them, and the cell family ties are adjusted; for derefinement, small cells are merged into their original large cells, unnecessary faces are removed, and the original family ties are restored. In parallel, once the refinement decisions are taken, the grid in each block can be refined without any communication with the other blocks.

Both refinement and derefinement are done cell by cell, to ensure maximum generality and robustness of the code. After the treatment of each single cell, a correct grid with all its pointers is left, even if some pointers have to be changed again later when a neighbour cell is refined. This way, a cell to be refined can treat all its faces and neighbours the same, no distinction is needed between cells that are already refined, cells that still have to be refined, and cells that are not refined at all.

To further increase the generality of the code, the parts that refine cells and faces are completely decoupled. Thus, for example, all directional refinements of hexahedral cells can be performed with only the capacity to split a quadrilateral face in two or in four.

4 Water surface refinement criterion

A logical refinement criterion for two-phase flow is refinement around the free surface. For the tests in the following section, the refinement criterion gets a nonzero value in those cells where the volume fraction is between 0.1 and 0.9. To be safe, a few layers of refined cells are added around these cells.

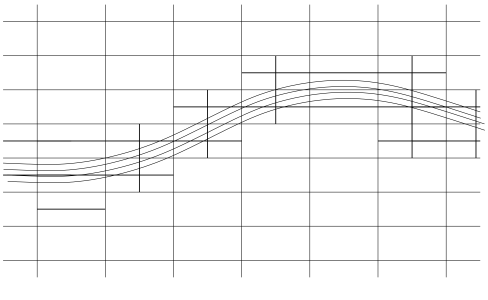

Figure 3: Directional refinement at the free surface. The curves represent volume fraction isolines.

A vector criterion is used to get directional refinement: the criterion vectors are placed normal to the water surface. Thus, isotropic refinement is used where the surface is diagonal to the grid and directional refinement where it is parallel to a grid direction (figure 3). Compared with isotropic refinement everywhere, the directional refinement greatly reduces the number of refined cells.

5 Test cases

Our grid refinement method with the criterion from section 4 is tested on two cases of steady ship flow, the Series 60 and the VIRTUE Container Ship. Both are at model scale with fixed trim and sinkage.

5.1 Series 60

The first test case is the Series 60 ($C_b = 0.6$) ship at $Fr = 0.316$ and $Re = 5.3 \cdot 10^6$. Measurements for this case have been performed at IIHR [5].

The grids for this test case are based on a grid that is rather coarse (550k cells), but still has the $\Delta z = 0.001L$ grid spacing round the free surface that is advised for ISIS-CFD. From this grid, another grid is derived that is identical, except it has $\Delta z = 0.002L$ at the surface. This (330k cells) grid is used as the initial grid for the refinement. The first grid, unrefined, is used as a reference. All flows are calculated on four processors.

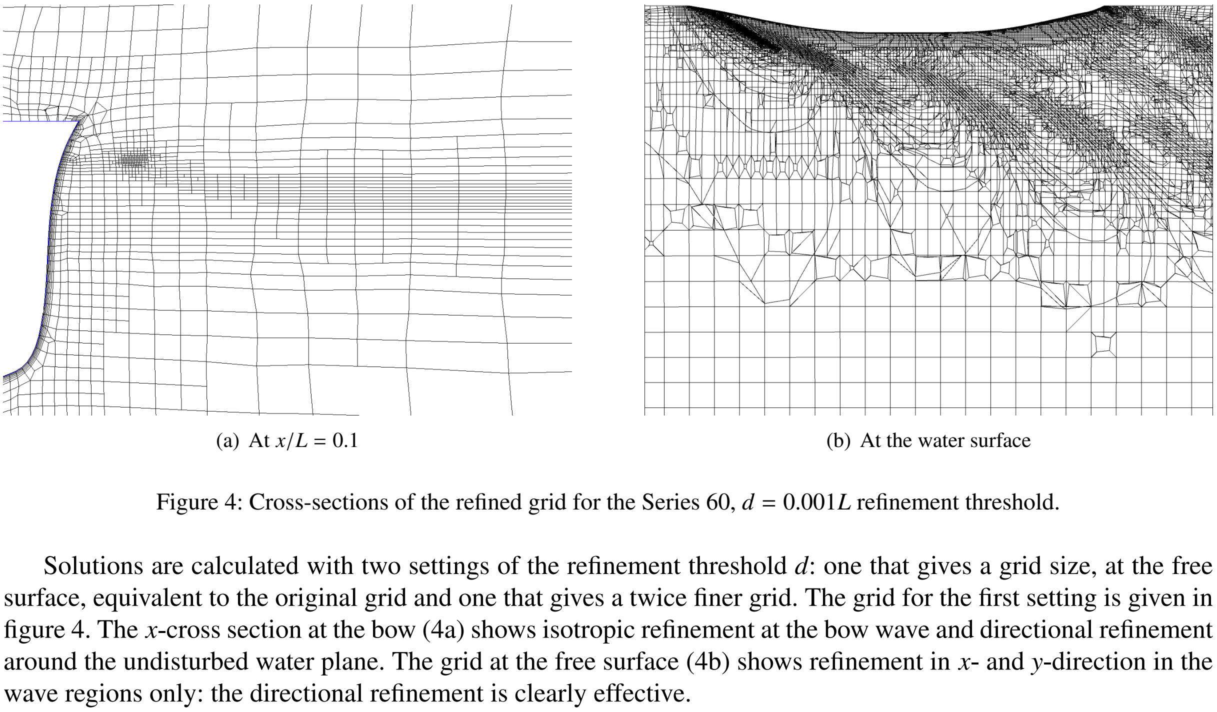

(a) At $x/L = 0.1$

(b) At the water surface

Figure 4: Cross-sections of the refined grid for the Series 60, $d = 0.001L$ refinement threshold.

Solutions are calculated with two settings of the refinement threshold d: one that gives a grid size, at the free surface, equivalent to the original grid and one that gives a twice finer grid. The grid for the first setting is given in figure 4. The x-cross section at the bow (4a) shows isotropic refinement at the bow wave and directional refinement around the undisturbed water plane. The grid at the free surface (4b) shows refinement in x- and y-direction in the wave regions only: the directional refinement is clearly effective.

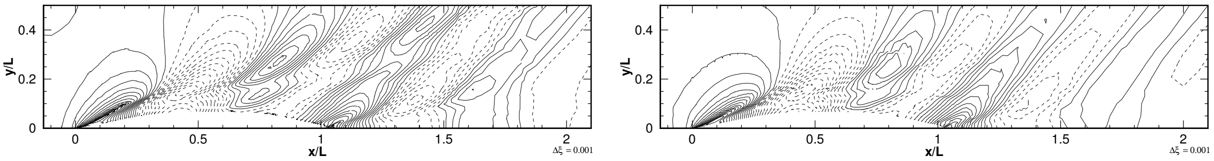

(a) BRICS, $d = 0.001L$

(b) BRICS, original grid

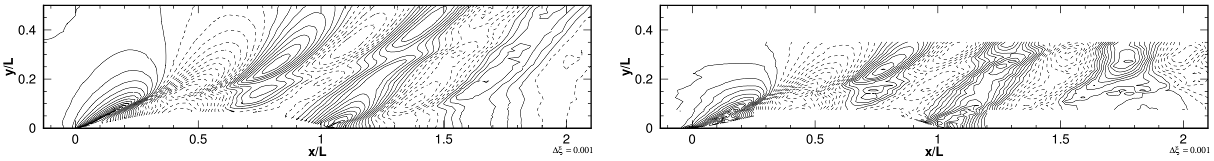

(c) BRICS, $d = 0.0005L$

(d) Experiment

Figure 5: Series 60, wave profiles.

Compared with the original grid, both refined grids give better wave patterns (figures 5 and 6a). This is due to the refinement in x- and y-direction in steep waves. Especially the coarsest refined grid (figure 5a) is spectacular, as it has fewer cells (506k) than the original grid in figure 5b, so the solution is computed faster. The finer refined

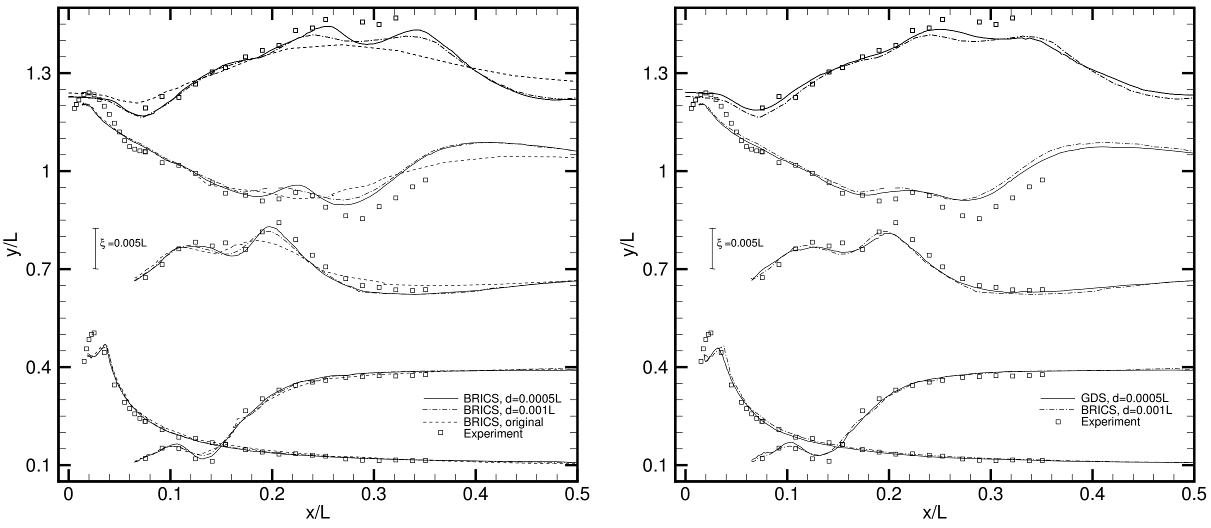

(a) (b)

Figure 6: Series 60, x = const. wave cuts for two refinement thresholds (a) and for non-compressive (GDS) versus compressive (BRICS) volume fraction discretisations (b).

grid offers only a small extra improvement, despite its 1.30M cells.

As a final experiment, the compressive BRICS discretisation used so far for the volume fraction, is replaced by the non-compressive GDS scheme. This scheme is less accurate than BRICS, but it allows much larger time steps, so it gives faster computation times. And accuracy can be provided with local refinement; GDS with the fine threshold (1.15M cells) produces about the same result as BRICS with the large threshold (see figure 6b), yet the solution was about four times faster.

5.2 VIRTUE Container Ship

The second test is the VIRTUE Container Ship at $Fr = 0.272$, $Re = 1.84 \cdot 10^7$, and draft 0.388m (full-scale 11.3m). This ship is a test case for the European project VIRTUE, in which EMN participates. Measurements have been performed by HSVA in Hamburg. The flow is more challenging than the Series 60, as the ship has a bulb, a breaking bow wave, and a (dry) transom.

A fine grid (3.07M cells) is used as the basis for refinement. By setting $d = 0.0005L$, about one level of refinement is added. The original grid is already quite fine in x- and y-direction, so most cells are refined in z-direction only. Thus, the refined grid is not much larger (3.68M cells) than the original grid. The compressive BRICS scheme is used. The flow is solved on 18 processors; as it was started from the converged original grid solution, the refined grid computation takes only about 40% extra computation time.

The improvement in the solution is spectacular. Waves are steeper and the wave pattern has more detail (figure 7). Agreement with the experiments is much better than for the original grid: figure 8a shows that the waves are diffused less and that even the small wave details are resolved well. Also near the stern (figure 8b) the general shape of the waves has greatly improved and the breaking part of the rooster tail is captured well.

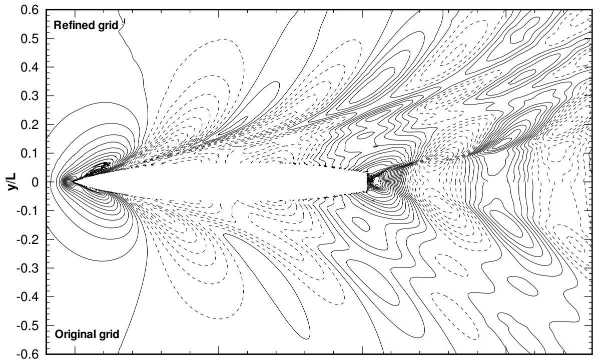

Figure 7: VIRTUE Container Ship, wave profiles on refined and original grid.

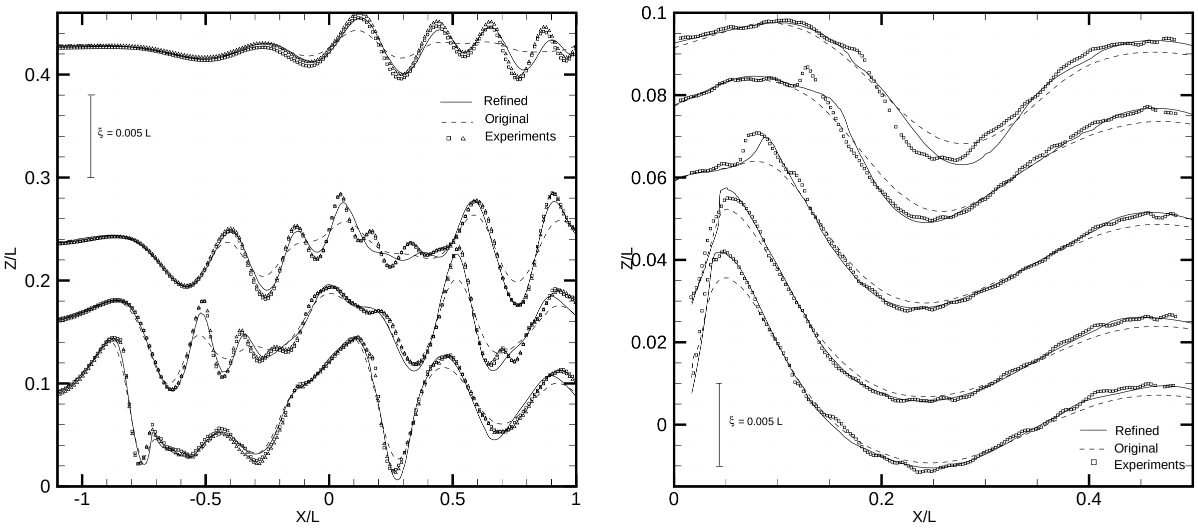

(a) (b)

Figure 8: VIRTUE Container Ship, y = const. wave cuts at the side of the ship (a) and behind the stern (b). The ship is located between $x/L = -1$ and $x/L = 0$, the stern is at $x/L = 0$.

6 Conclusions and perspectives

We presented an adaptive grid refinement method for a parallelised unstructured finite-volume code. The method currently provides directional refinement for unstructured hexahedral meshes. To get a flexible and general method, the refinement criterion, the decision whether or not to refine each cell, and the actual refinement are strictly separated. Also, the refinement of cells and faces is decoupled. Results for a free-surface refinement criterion on two steady ship test cases show significant increases in accuracy and efficiency, compared to non-refined grids.

Work in progress includes dynamic load balancing (the redistribution of the cells over the processors after each refinement) and unsteady problems; due to its derefinement capability, the method is suitable for those. The main long-term goal is the development of more sophisticated refinement criteria. These can go from combinations of the present criterion with a gradient-based criterion refining in the zones below the waves, to error estimators and adjoint-based methods. Finally, the current method is three-dimensional, but extension to two dimensions is straightforward.

Acknowledgement

Part of the work described in this article was performed in work package WP1 of the VIRTUE Project, an Integrated Project in the 6th Framework Programme "Sustainable development, global change and ecosystems" under grant 516201 from the European Commission. This support is gratefully acknowledged.

References

[1] R. Duvigneau, M. Visonneau, and G.B. Deng. On the role played by turbulence closures in hull shape optimization at model and full scale. *J. Marine Science and Technology*, **8**(1), 1–25, (2003).

[2] A. Hay, P. Queutey, and M. Visonneau. Computation of three-dimensional free-surface flows with an automatic adaptive mesh refinement and coarsening strategy. In *Proceedings of the 25th Symposium on Naval Hydrodynamics*, St John's, Newfoundland and Labrador, (2004).

[3] A. Hay and M. Visonneau. Error estimation using the error transport equation for finite-volume methods and arbitrary meshes. *Int. J. Computational Fluid Dynamics*, **20**(7), 463–479, (2006).

[4] A. Leroyer and M. Visonneau. Numerical methods for RANSE simulations of a self-propelled fish-like body. *J. Fluid & Structures*, **20**(3), 975–991, (2005).

[5] J. Longo and F. Stern. Effects of drift angle on model ship flow. *Experiments in Fluids*, **32**, 558–569, (2002).

[6] P. Queutey and M. Visonneau. An interface capturing method for free-surface hydrodynamic flows. *Computers & Fluids*, **36**(9), 1481–1510, (2007).

Preliminary LBM study of hydrodynamic problems

G. Colicchio, C. Lugni
INSEAN, Rome/Italy, c.lugni@insean.it

1 Introduction

The Lattice Boltzmann methods (LBM) were developed for the lattice gas automata (LGA) (see [1], [2]), more recently they have been used to study a variety of fluid dynamic problems. Differently from the classical CFD methods that solve the macroscopic variables $\boldsymbol{u}$ and ρ in the Navier Stokes equations, the LBE approaches solves the kinetic equation for the particle velocity distribution function $f(\boldsymbol{x}, \xi, t)$ in which ξ is the particle velocity vector, $\boldsymbol{x}$ is the spatial position vector and t is the time. The macroscopic function ρ and $\rho\boldsymbol{u}$ are obtained from the evaluation of the hydrodynamic moments of the distribution function. This approach was first proposed by Qian et al. [3], Chen et al. [4], and dHumieres [5] and it is becoming more common because of the flexibility of the method to deal with compressible and incompressible flows and because it does not need any iterative solver for the pressure equations. More recently it has also been adapted to problems with a free surface, even though these applications are still limited. This work aims to study to application of this method to naval problems, through the analysis of classical test cases in 2D.

2 General LBM algorithm D2Q9 BGK model

A popularly adopted kinetic model for the solution of the Lattice Boltzmann equation is the single-relaxation-time (SRT) approximation, the so called Bhatnagar-Gross-Krook (BGK) model [6]:

$$\frac{\partial f}{\partial t} + \boldsymbol{\xi}\nabla f = -\frac{1}{\lambda}(f - f^{eq}) \tag{1}$$

where λ is the relaxation time and f^{eq} is the equilibrium distribution function (the Maxwell-Boltzmann distribution function).

In the discrete form of the LBM method, the distribution function is represented on a lattice unit, that is a cell with a number of nodes on which f is distributed. The number of nodes can vary according to used representation. The most classical one for the 2D problems is the D2Q9 lattice cell shown in figure 1, with nine nodes, one in the centre, four in the centre of the each side and four on each corner.

The macroscopic variables are then linked to the distribution function through the equations:

$$\sum_{i=0,8} f_i(x,t) = \rho(x,t) \tag{2}$$

$$\sum_{i=0,8} \boldsymbol{e}_i f_i(x,t) = \rho(x,t)\boldsymbol{u}(x,t) \tag{3}$$

where $\boldsymbol{e}_i$ are the velocity vectors in the lattice unit (see figure 1). In the discrete form the BGK equations become:

$$f_i(\boldsymbol{x} + \boldsymbol{e}_i\delta t, t + \delta t) - f_i(\boldsymbol{x},) = -\frac{1}{\tau}(f_i(\boldsymbol{x},t) - f_i^{eq}(\boldsymbol{x},t)) \tag{4}$$

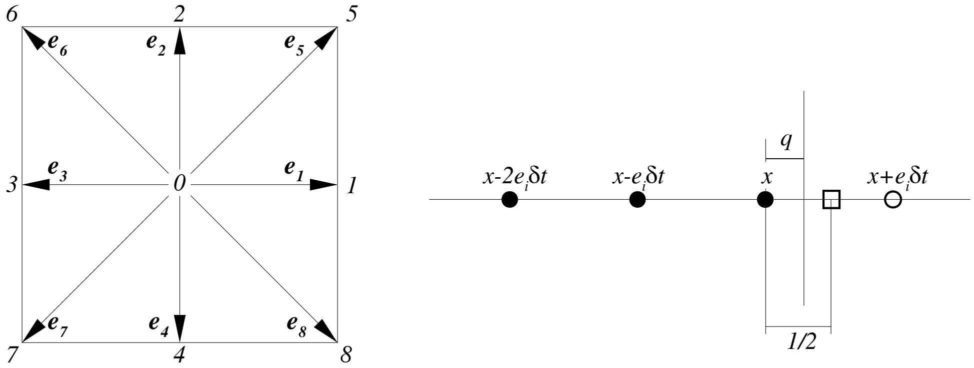

Figure 1: Left: Definition of the lattice cell and of its velocities. Right: Details of the collision process for velocities close to the boundaries.

with $\tau = \lambda/\delta t$, they are solved using the two steps:

$$\begin{array}{ll} \text{collision} & \hat{f}_i(\boldsymbol{x}, t+\delta t) = f_i(\boldsymbol{x},) - \frac{1}{\tau}(f_i(\boldsymbol{x}, t) - f_i^{eq}(\boldsymbol{x}, t)) \\ \text{streaming} & f_i(\boldsymbol{x} + \boldsymbol{e}_i \delta t, t+\delta t) = \hat{f}_i(\boldsymbol{x}, t+\delta t) \end{array} \tag{5}$$

where the equilibrium distribution is of the form

$$f_i^{eq} = \rho w_i \left[1 + \frac{3}{c^2} \boldsymbol{e}_i \cdot \boldsymbol{u} + \frac{9}{2c^4} (\boldsymbol{e}_i \cdot \boldsymbol{u})^2 - \frac{3}{2c^2} \boldsymbol{u} \cdot \boldsymbol{u} \right] \tag{6}$$

and w_i are the weighting factors given by

$$w_i = \begin{cases} 4/9, & i = 0, \\ 1/9, & i = 1, 2, 3, 4 \\ 1/36, & i = 5, 6, 7, 8 \end{cases} \tag{7}$$

The Navier-Stokes equations are obtained through a multi-scale expansion, the Chapman-Enskog expansion, with time and space rescaled as

$$\begin{array}{l} t_1 = \epsilon t, \qquad t_2 = \epsilon^2 t, \qquad x_1 = \epsilon x, \\ \\ \dfrac{\partial}{\partial t} = \epsilon \dfrac{\partial}{\partial t_1} + \epsilon^2 \dfrac{\partial}{\partial t_2}, \qquad \dfrac{\partial}{\partial x} = \epsilon \dfrac{\partial}{\partial x_1} \\ \\ f_i = f_i^0 + \epsilon f_i^1 + \epsilon^2 f_i^2 + O(\epsilon^3) \end{array} \tag{8}$$

In the incompressible limit of $|\boldsymbol{u}|/c_s << 1$, where the speed of sound $c_s = 1/\sqrt{3}$, the mass and momentum conservation equation are recovered from equation (4) when $\nu = (\tau - 1/2) c_s^2 \delta t$.

3 Boundary conditions

Solid boundaries To deal with solid boundaries, several schemes have been proposed. The earliest one is the bounce-back condition [7] that reflects the outgoing weights inside the field. This model is easily applied to boundaries parallel to one of the directions of the lattice cell but

q	BB 1/2	ULI [0,1/2]	DLI [1/2,+∞[
χ_1	1	2q	1/2q
χ_0	0	1-2q	0
$\hat{\chi}_{-1}$	0	0	(2q-1)/2q
w_q	2	2	1/q

Table 1: Coefficient of different boundary conditions and their range of validity: bounce back (BB), upwind and downwind linear interpolation (ULI ad DLI).

it fails to describe properly curved boundaries. So Bouzidi et al. [8] proposed a description of the boundary according to its distance from the wall q. Altering the post collision distortions (see right side of figure 1), the new distribution function in the boundary cells are written as:

$$f_{i'}(\boldsymbol{x}, t+\delta t) = \chi_1 \hat{f}_q(\boldsymbol{x}, t) + \chi_0 \hat{f}_i(\boldsymbol{x} - \boldsymbol{e}_i \delta t, t) + \hat{\chi}_{-1} \hat{f}_{i'}(\boldsymbol{x}, t) - c_s^2 w_q w_i j_i \tag{9}$$

where $\boldsymbol{e}_{i'} = -\boldsymbol{e}_i$ and j_i is the the $i-th$ component of the momentum. The coefficients χ are given in table 1. In the following, the linear upwind and downwind interpolation will be used for all the cases that have been tested.

Free surface When a free surface delimits the fluid domain, the cell are subdivided into three categories: 1) fluid cells (completely filled with liquid), 2) gaseous cells (empty) and 3) interface cells (partially filled with liquid). The solution is calculated only in the cells of types 1 and 3, while the dynamic of the gas is neglected and its density is assumed uniform and equal to $\rho_A = 1$ so that the air pressure (or reference pressure) is equal to $p_0 = c_s^2$. The free surface is tracked through a volume fraction $m(\boldsymbol{x}, t)$ as in the fashion of the VOF (Volume of fluid) methods and it is advected with the fluid velocity:

$$\frac{\partial m(\boldsymbol{x}, t)}{\partial t} = -\boldsymbol{u} \cdot \nabla m(\boldsymbol{x}, t) \tag{10}$$

During the flow evolution, cells can change their state from 1 to 2 and to 3. When a cell initially empty (type 2) is partially filled (type 3), the distribution function has to be initialized in it. Some node i are initialized by the *propagation* step, in their complements this is done trough the following algorithm [9]:

$$f_{i'}(\boldsymbol{x}, t+\delta t) = f_i^{eq}(\rho_A, \boldsymbol{u}) + f_{i'}^{eq}(\rho_A, \boldsymbol{u}) - f_i(\boldsymbol{x}, t) \tag{11}$$

where $\boldsymbol{u}$ is the velocity at the cell position $\boldsymbol{x}$ at the time t.

4 Test cases

Couette flow The classical Couette flow has been used to test the boundary conditions and their convergence. A constant body force is applied to an otherwise still channel flow. When the flow has reached steady state conditions, the horizontal velocity has a parabolic profile in the y direction and its maximum is equal to $a_x/(8\nu)$ where a_x is the acceleration associated to the body force. The boundary conditions along the x direction are assumed periodic, i.e. the flow outgoing the section $x = L$ is the incoming flow in the section $x = 0$ and *viceversa*. Figure 2 shows the horizontal velocity profiles for different discretizations. Comparing the numerical results to the analytical solution, it is possible to obtain an order of convergence of 1.58 for $q = 1/2$. If the distance is either increased or diminished, the order of accuracy reaches 2.

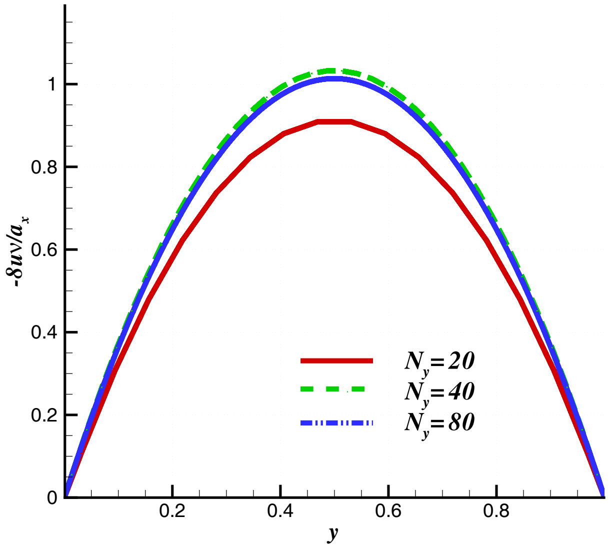

Figure 2: Horizontal velocity profiles along the y direction for different discretizetions.

Re	10	20	40
θ	142	134	127
L/D	0.4	1.05	2.25

Table 2: Angle of separation, and length of the wake for low Reynolds number flows behind a circular cylinder ($D/\delta x = 20$).

Flow behind a circular cylinder The second test case deals with a curved boundary, i.e. a cylinder immersed in a uniform flow. Velocity boundary conditions are given at the boundaries of the domain. They are assumed far away enough from the cylinder to avoid any blockage effect on it. These conditions are enforced as if the boundaries of the domain where solid boundaries with given velocities. Figure 3 shows the flow around the cylinder for three different Reynolds numbers respectively Re=10,20,40. For each of these numbers, the flow is in the stationary regime. In it, it is possible to measure the following quantities: the angle of separation and the length of the wake, reported in table 2. Numerical data agree quite well with the experimental data by Wu et al. [10] and Taneda [11] for all the values even though the mesh is coarse ($D/\delta x = 20$).

For Reynolds numbers higher then 45, the flow becomes non-stationary and it is possible to calculate a Strouhal number $St = D/TU$, where T is the period of vorticity released behind the cylinder (see figure 4). Its value as a function of the Re is reported in table 3. The results are again in good agreement with the numerical and experimental results presented in table I by He and Doolen [12].

Re	50	100	150	200
St	0.13	0.16	0.18	0.186

Table 3: Srouhal number for high Reynolds number flows behind a circular cylinder ($D/\delta x = 20$).

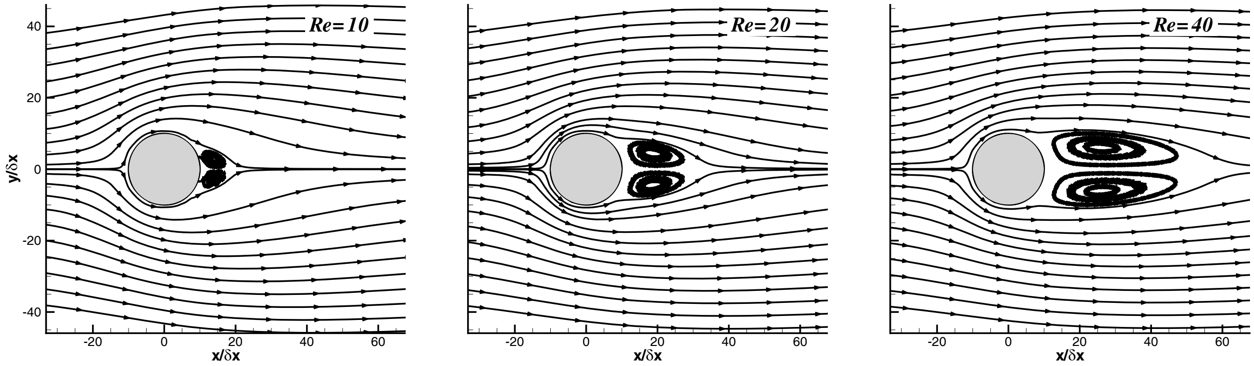

Figure 3: Flow around a circular cylinder at low Reynolds numbers ($D/\delta x = 20$).

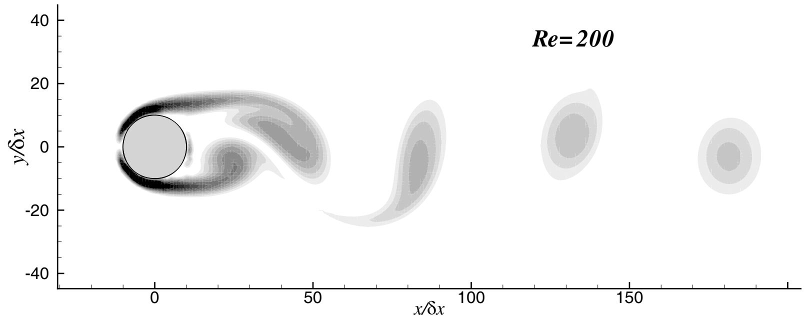

Figure 4: Vorticity released behind a cylinder at Re=200 ($D/\delta x = 20$).

Dam break problem The last test case deals with the violent deformation of the free surface. One of the vertical wall delimiting a rectangular reservoir ($100\delta x$ x $80\delta x$) of water is suddenly released. The water flows on the open side along the bottom. If a wall is positioned downstream, the water impacts on it and rises upward. Figure 5 shows the flow evolution form the release of the dam to the impact on the downstream wall. The solver is able to handle the evolution of the free surface, but the coarse mesh used enlarges the boundary layer creating a sub-layer with almost zero velocity that influences the evolution of the free surface. A further study is necessary to introduce an adaptable mesh whose size fits the details of the locally described flow. Moreover an algorithm for the wetting and drying of the solid walls is necessary to describe the local features that have not been completely captured with the described algorithm. In fact, a thin layer of water is left attached on the left wall, while the bottom, along which, the water flows is never completely wetted. This I due to the no slip condition described above, a zero velocity on the solid boundaries prevents the water either to detach or to be attached to the walls.

5 Conclusions

Even though the LBM method has been implemented in a simple way, it has shown its ability to describe complex flow conditions with solid and free surface boundaries of curved shapes. The lack of an adaptive mesh and of a proper wetting and drying algorithm has made the

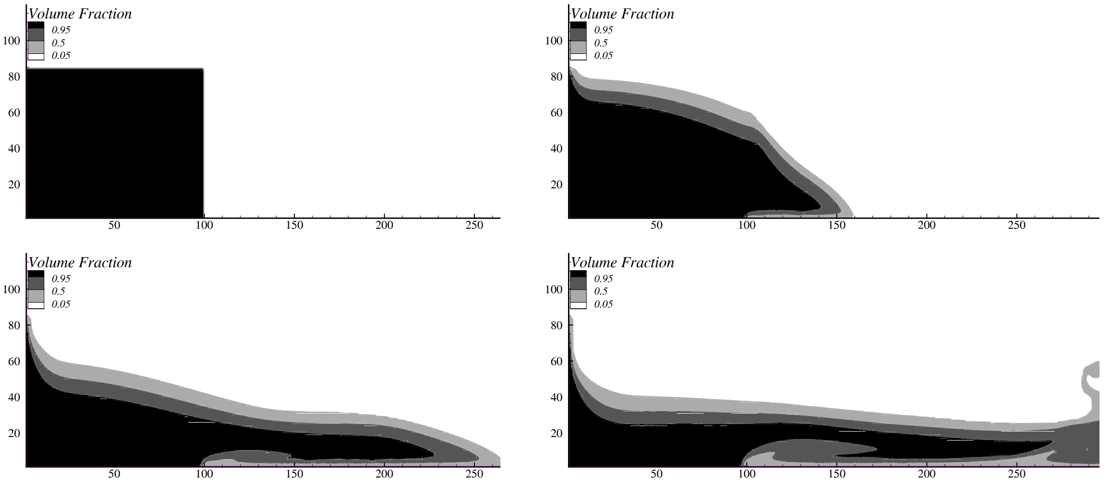

Figure 5: Evolution of the flow field in the dam break case.

description of the free surface pour, nonetheless it has shown its potentialities as a quick and easily parallelizable solver.

The present research activity is supported by the within the framework of the 'Programma di Ricerca di Idrodinamica Navale 2007-2009' and of the 'Programma Sicurezza 2006-2008' funded by *Ministero Infrastrutture e Trasporti*.

References

[1] Hardy J, de Pazzis O, Pomeau Y. Molecular dynamics of a classical lattice gas: transport properties and time correlation functions. Phys Rev A 1976;13:1949-61.

[2] Rivet J-P, Boon JP. Lattice Gas Hydrodynamics. Cambridge, UK: Cambridge University Press, 2001.

[3] Qian YH, dHumi"eres D, Lallemand P. Lattice BGK models for Navier Stokes equation. Europhys Lett 1992;17:479-84.

[4] Chen H, Chen S, Matthaeus WH. Recovery of the NavierStokes equations using a lattice-gas Boltzmann method. Phys Rev A 1992;45:R5339-42.

[5] dHumieres D. Generalized lattice Boltzmann equations. In: ShizgalD, Weaver DP, editors. Rarefied Gas Dynamics: theory and simulations. Prog Astronaut Aeronaut 1992;159:450-8.

[6] Bhatnagar PL, Gross EP, Krook M. A modelfor collision processes in gases, I. small amplitude processes in charged and neutralone-com ponent system. Phys Rev 1954;94:511-25.

[7] Frisch U. , dHumieres D., Hasslacher B., Lallemand P., Pomeau Y., Rivet J.-P., Lattice gas hydrodynamics in two and three dimensions, Complex Syst. 1987; 1, 649.

[8] Bouzidi M, Fridaouss M, Lallemand P. Momentum transfer of a Boltzmann-lattice fluid with boundaries, Phys of Fluids 2001;13:3452-59.

[9] Xing X.Q., Butler C.L., Yang C. Lattice Boltzmann-based single-phase method for free surface tracking of droplet motions, Int. J. Numer. Meth. Fluids 2007; 53:333-351.

[10] Wu M.H., Wen C.Y, Yen R.H., Weng M.C., Wang A.B. Experimental and numerical study of the separation angle for flow around a circular cylinder at low Reybolds number, J. Fluid Mech. 2004; 515: 233–260.

[11] TANEDA S, J Physic Soc Japan, 1972, V33.

[12] He X., Doolen G.D. Lattice Boltzmann method on a curvilinear coordinate system: Vortex shedding behind a circular cylinder, Phys. Rev. E, 1997, vol. 56, no 1, pp. 434-440

A Comparative Study of DDES and URANS by an Unstructured Grid based NS Solver

Kunihide Ohashi, Takanori Hino
National Maritime Research Institute, Japan
e-mail: k-ohashi@nmri.go.jp, hino@nmri.go.jp

1.Introduction

Recently, computational fluid dynamics are employed in various engineering problems. While the Reynolds averaged Navier-Stokes(RANS) simulation results show useful accuracy in mild flow separations, unsteady RANS(URANS) predictions of highly separated flows have been unreliable. The relatively poor performance of URANS has motivated the increased applications of large eddy simulation(LES). The cost arises when applied LES to complex configurations at high Reynolds numbers because of the resolution required in the boundary layers and wakes. Detached eddy simulation(DES) is a hybrid method which has RANS behavior near the wall and becomes a large eddy simulation in the regions away from solid boundary. DES is considered to require much less computational resources than LES and easy to implement to a RANS solver through the modification of the turbulence models.

DES has the problem which is known as modeled stress depletion(MSD) when applied to the ambiguous grid. DES uses a limiter which is based on the grid spacing like sub-grid-scale model of LES. It usually works well, however the limiter reduces the eddy viscosity and modeled Reynolds stress, without any sizeable resolved stress to restore the balance in 'ambiguous grid'. A new version of DES which is named Delayed DES(DDES) is proposed. DDES keeps the RANS behavior in boundary layer to prevent MSD.

Numerical study of DES, DDES and URANS for a simple geometry are carried out in this paper. Flows around a circular cylinder of DES, DDES and URANS are shown, and the pressure distributions on the cylinder are compared with measurement result. Capability of DES and DDES is examined in the present study.

2.Numerical Method

2.1 Navier Stokes Solver ***SURF***

The flow solver used in this study is called SURF ("Solution algorithm for Unstructured RaNS with FVM") which is under development at National Maritime Research Institute[1][2]. The governing equations are the unsteady 3D Reynolds averaged Navier-Stokes equations for incompressible flows. Coupling between pressure and a velocity field is made by artificial compressibility approach. Dual time integration method is used for a unsteady simulation.

The final form can be written as follows:

$$\frac{\partial \mathbf{q}^*}{\partial t} + \frac{\partial \mathbf{q}}{\partial \tau} + \frac{\partial (\mathbf{e} - \mathbf{e^v})}{\partial x} + \frac{\partial (\mathbf{f} - \mathbf{f^v})}{\partial y} + \frac{\partial (\mathbf{g} - \mathbf{g^v})}{\partial z} = 0$$

and

$$\mathbf{q} = [\ p \quad u \quad v \quad w\ ]^{\mathbf{T}}, \quad \mathbf{q}* = [\ 0 \quad u \quad v \quad w\ ]^{\mathbf{T}}$$

In the above, all variables are nondimensionalized using the reference density ρ_0, velocity U_0 and length L_0. The velocity components in the (x, y, z) direction is expressed as (u, v, w). Physical time (t) and pseudo-time (τ) derivative terms are required for a unsteady simulation.

The inviscid fluxes $\mathbf{e}$, $\mathbf{f}$ and $\mathbf{g}$ and the viscous fluxes $\mathbf{e^v}$, $\mathbf{f^v}$ and $\mathbf{g^v}$ are defined as:

$$\mathbf{e} = \begin{bmatrix} \beta u \\ u^2 + p \\ uv \\ uw \end{bmatrix}, \ \mathbf{f} = \begin{bmatrix} \beta v \\ vu \\ v^2 + p \\ vw \end{bmatrix}, \ \mathbf{g} = \begin{bmatrix} \beta w \\ wu \\ wv \\ w^2 + p \end{bmatrix},$$

$$\mathbf{e^v} = \begin{bmatrix} 0 \\ \tau_{xx} \\ \tau_{xy} \\ \tau_{zx} \end{bmatrix}, \ \mathbf{f^v} = \begin{bmatrix} 0 \\ \tau_{xy} \\ \tau_{yy} \\ \tau_{yz} \end{bmatrix}, \ \mathbf{g^v} = \begin{bmatrix} 0 \\ \tau_{zx} \\ \tau_{yz} \\ \tau_{zz} \end{bmatrix}$$

where β is a parameter for artificial compressibility and $\tau_{ij} = \left(\frac{1}{R} + \nu_t\right)\left(\frac{\partial u_i}{\partial x_j} + \frac{\partial u_j}{\partial x_i}\right)$. R is the Reynolds number defined as $U_0 L_0/\nu$ where ν is the kinematic viscosity. ν_t is the non-dimensional kinematic eddy viscosity.

Since a basic numerical procedure for the Navier-Stokes equations are described in references[1][2], only the brief outline is given here.

Spatial discretization is based on a cell-centered finite-volume method. A computational domain is divided into unstructured polyhedral cells and flow variables (pressure, velocity and eddy viscosity) are stored in the center of each cell. Cells whose shape are hexahedra, tetrahedra, prisms or pyramids can be used and the combinations of these cells give greater flexibility for handling complex geometry.

For the inviscid fluxes (convection terms and pressure gradient terms), the second order upwind scheme based on the flux-differencing splitting of Roe with the MUSCL approach is employed. The viscous fluxes are evaluated by the second order central scheme. Thus, the overall accuracy in space is the second order.

The backward Euler scheme is used for the pseudo-time integration. The physical time derivative term is evaluated in second order scheme.

Local time stepping method is used in pseudo-time, in which time increment is determined for each cell in such a way that the CFL number is globally constant. The linear equations derived from the pseudo-time linearization of the fluxes are solved by the Gauss-Seidel iteration. The pseudo-time iteration continues until the averaged residual is less than a threshold value or the iteration number reaches its pre-set value. As a threshold value and maximum number of iteration, the values of 1.0×10^{-3} and 60 are given in present study.

2.2 Turbulence Model

DES and DDES are based on the Spalart-Allmaras[3] one equation turbulence model. In the S-A model, the working variable $\tilde{\nu}$ is used to form the eddy viscosity and its transport equation takes the form[4],

$$\begin{aligned} \frac{\partial \tilde{\nu}}{\partial t} + u\frac{\partial \tilde{\nu}}{\partial x} + v\frac{\partial \tilde{\nu}}{\partial y} + w\frac{\partial \tilde{\nu}}{\partial z} &= c_{b1}[1 - f_{t2}]\tilde{S}\tilde{\nu} + \frac{1}{\sigma}\left[\nabla \cdot \left\{\left(\frac{1}{R} + \tilde{\nu}\right)\nabla\tilde{\nu}\right\} + c_{b2}(\nabla\tilde{\nu})^2\right] \\ &- \left[c_{w1} f_w - \frac{c_{b1}}{\kappa^2} f_{t2}\right]\left(\frac{\tilde{\nu}}{d}\right) + f_{t1}\Delta U^2 \end{aligned}$$

The eddy viscosity ν_t is obtained from

$$\nu_t = \tilde{\nu} f_{v1}, f_{v1} = \frac{\chi^3}{\chi^3 + c_{v1}^3}, \chi = \tilde{\nu} R$$

The production term is expressed as as

$$\tilde{S} = |\omega| + \frac{\tilde{\nu}}{\kappa^2 d^2} f_{v2}, f_{v2} = (1 + \frac{\chi}{c_{v2}})^{-3}$$

where $|\omega|$ is the vorticity magnitude. The function f_w is defined as

$$f_w = g \left[\frac{1 + c_{w3}^6}{g^6 + c_{w3}^6} \right]^{1/6}, g = r + c_{w2}(r^6 - r), r = \frac{\tilde{\nu}}{\tilde{S}\kappa^2 d^2}$$

where d is the distance from the closest wall.

The function f_t2 is defined as

$$f_{t2} = c_{t3} exp(-c_{t4}\chi^2)$$

The trip function f_{t1} is specified in terms of the distance d_t form filed point to the trip, the wall vorticity ω at the trip, and ΔU, which is the difference between the velocity at the field point and that at the trip

$$f_{t1} = c_{t1} g_t exp\left(-c_{t2} \frac{\omega_t^2}{\Delta U} [d^2 + g_t^2 d_t^2] \right)$$

where g_t =min$(0.1, \Delta U/\omega_t \Delta x)$, where Δx is the grid spacing along the wall at the trip. The model parameters are given the same values as reference[3].

2.3 Detached-Eddy Simulation(DES) formulation[4]

The DES formulation is obtained by replacing the distance to the nearest wall in all terms, d, by $\tilde{d}$, where $\tilde{d}$ is defined as

$$\tilde{d} = min(d, C_{DES}\Delta)$$

Δ is the largest grid spacing among all directions. The model constant $C_{DES} = 0.65$ was set for a homogeneous turbulence flow and is used in the present work.

In addition, the trip term $f_{t1}\Delta U^2$ is neglected in DES and DDES in view of the numerical results with an unrealistic phenomenon that ν_t is observed in front of the cylinder.

2.4 Delayed DES(DDES)[5]

'Ambiguous grid' is used in DES, the DES limiter reduces the eddy viscosity and modeled Reynolds stress. This is referred as modeled stress depletion(MSD). The remedy is proposed as Delayed DES(DDES). In DDES the length of scale $\tilde{d}$ is redefined as,

$$\tilde{d} = d - f_d max(0, d - C_{DES}\Delta), f_d = 1 - tanh([8r_d]^3), r_d = \frac{\nu_t + 1/R}{\sqrt{U_{i,j}U_{i,j}}\kappa^2 d^2}$$

where $U_{i,j}$ is velocity gradients. The new version of the model keeps the RANS mode in boundary layer.

3. Simulation Model

A circular cylinder is used for present study. The length scale is non-dimensionalized by the diameter of cylinder. The computational grids are shown Figures 1 and 2. All grids consist from hexahedra cells. Spanwise extent is 2.0 which means twice of a diameter and the distance from cylinder to outer boundary is set as 15.0 in all other directions.

Three grids are generated in the manner of circumferential direction(N_c) and spanwise direction division number(N_s). Table 1 shows the detail of computational grids. Coarse grid is consisted from 1.23 million cells, spanwise refinement grid is consisted form 2.02 million cells and 1.62 million cells for fine grids. Computational grids are concentrated in the field behind the cylinder to capture the separated flow structure.

Table 1 Detail of Computational Grid

	N_c	N_s	Cells
Coarse Grid(CS)	129	37	1.23 million
CS+Spanwaise Refinement(CS+SF)	129	73	2.02 million
Fine(F)	257	37	1.62 million

As the boundary conditions, the side boundary is set as symmetric condition and the outer boundary is set as outflow that pressure is zero and Neuman condition for velocities.

Reynolds number is set as 5.0×10^6. The nondimensional physical time step size is $\Delta t = 0.033$.

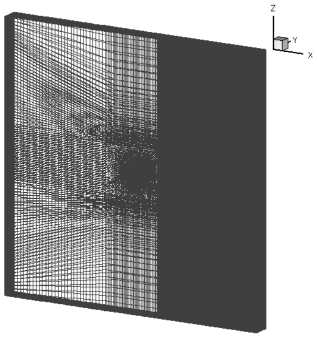

Figure 1: Computational Grid(Total View)

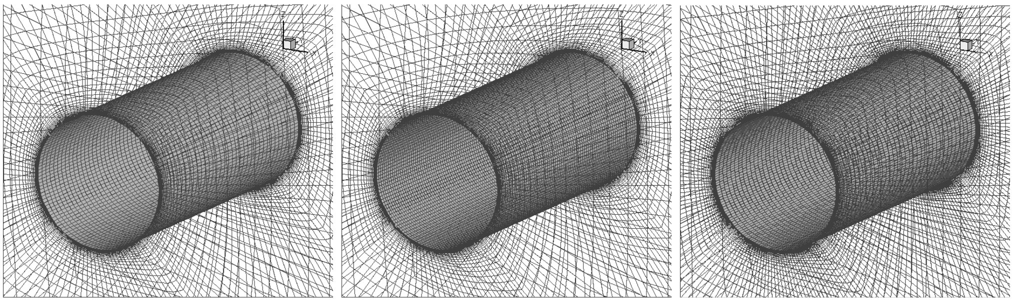

Coarse Grid(CS)　CS+Spanwise Refinement　Fine Grid

Figure 2: Computational Grid(Near Cylinder)

3.Results and Discussions

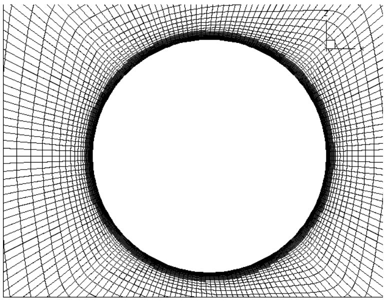

Figure 3: RANS and LES Regions for DES

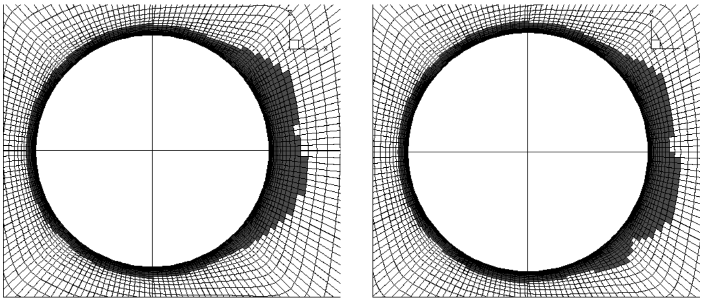

Figure 4: RANS and LES Regions for DDES in two snapshots

Figures 3 and 4 show the RANS and LES regions of DES and DDES. It is obviously shown in DES formulation, the RANS regions of DES is unchanged to physical time. On the other hand, RANS regions of DDES is varied with time due to the velocity gradient and ν_t. From Figure 4, the RANS regions especially just behind the cylinder are changed in two snap shots. This “gray area” has a possibility of accelerating growth of natural instabilities in regions where modeled Reynolds stress should dominate the total stress[5]. However, these instabilities can not be observed in the present study.

Figure 5 shows the iso-surfaces flow structure of $\nu_t = 7.5 \times 10^{-4}$ in snapshot. URANS shows two-dimensional structure of ν_t. Both DES and DDES results show three dimensional flow structure. DES and DDES results are considered as the realistic phenomenon in highly separated flow.

Table 2 shows the comparisons of time averaged drag coefficient C_D and Strouhal number St. Strouhal number is computed by a frequency analysis of lift coefficient.

DES and DDES results show the drastic improvement of prediction. C_D and St of DDES shows little grid dependence in the present study, although the study for other simple and complex geometry should be carried out. Also C_D of DES and DDES results still show a slightly higher than measured results. The reason for the difference is considered as below.

Table 2 Comparisons of C_D and Str

	C_D	St
Meas.$^{ref.7}$	0.68-0.74	0.27
URANS(F)	0.34	0.12
DES(F)	0.83	0.30
DDES(CS)	0.83	0.30
DDES(CS+SF)	0.83	0.30
DDES(F)	0.85	0.30

Figure 6 shows the time averaged pressure distributions on the half cylinder surface. θ is the angle measured from the stagnation point.

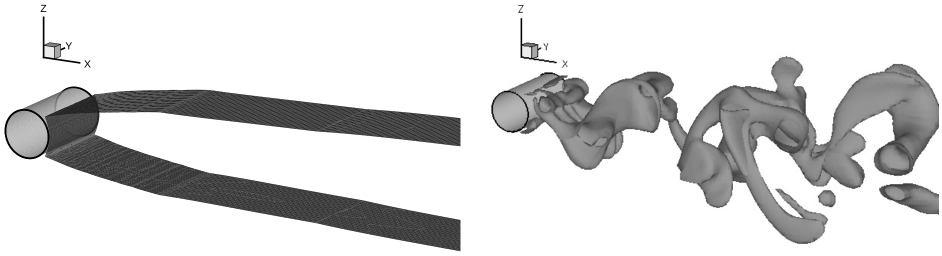

URANS DES

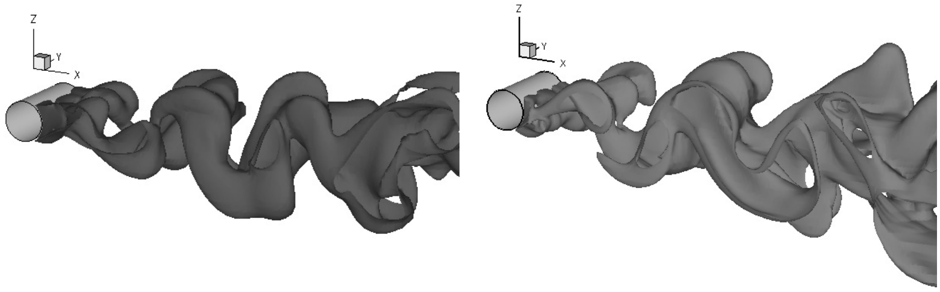

DDES(Coarse Grid) DDES(CS+Spanwise Refinement)

DDES(Fine Grid)

Figure 5: Instantaneous $\nu_t = 7.5 \times 10^{-4}$ iso-surfaces

URANS result deviates from the measured result from the point of $\theta = 100$ deg. DES and DDES show the improvement of accuracy in separated flow region but still have the difference in the region where θ is greater than 150 deg. The reversed flows are observed in these regions(Figure 7). The pressure distributions of cylinder surface becomes lower due to these reversed flows and C_D becomes higher than measured results. The reversed flows may be resulted in the narrow spanwise extension although the verification is not yet made.

4. Conclusion and Acknowledgment

Numerical study of DES and DDES for the simple geometry, a circular cylinder, is carried out. Both of DES and DDES results show the improvement of prediction of drag coefficient and Strouhal

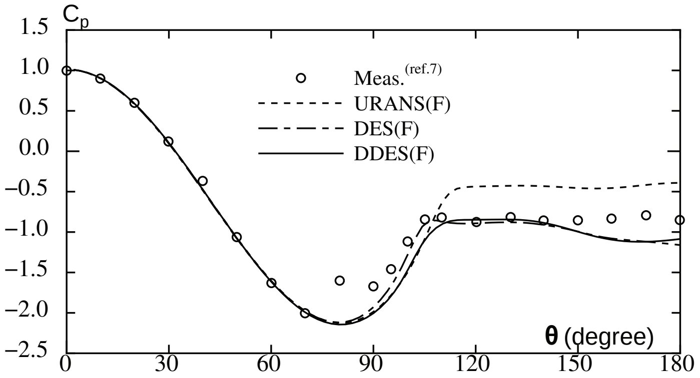

Figure 6: Comparisons of Pressure Distributions

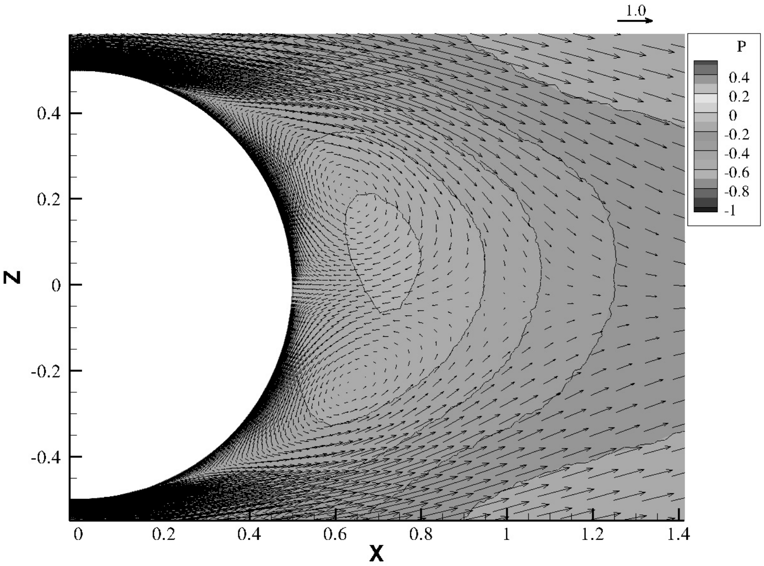

Figure 7: Reversed Flows behind Cylinder(DDES)

number. Also DES and DDES results show the complex flow structure behind the cylinder. Thus, present results demonstrate the effectiveness of DES and DDES in highly separated flow.

Finally, the authors acknowledge the valuable discussions with the members of Center for CFD Research of NMRI regarding numerics of DES and DDES.

References

[1]Hino, T. : Navier-Stokes Computations of Ship Flows on Unstructured Grids, Proc. of the 22nd Symp. on Naval Hydro., (1998)

[2]Hino, T. : An Inteface Capturing Method for Free Surface Flow Computations on Unstructured Grids, J. of the Soc. Naval Archit. Japan , Vol.186, pp.173-183, (1999)

[3]Spalart, P.R., Allmaras S.R. : A One-Equation Turbulence Model for Aerodynamics Flows, *La Rescherche Aerospatiale*, No.1, pp.5-21, (1994)

[4]Squires, K.D. et al.: Detached-Eddy Simulation of the Separated Flow Over a Rounded-Corner Square, Journal of Fluid Engineering, Vol.127, pp.959-966, (2005)

[5]Spalart, P.R. et al. : A new version of detached-eddy simulation, resistant to ambiguous grid densities, Theor. Comput. Fluid Dyn., 20, pp.181-195, (2006)
[6]Kuroda, M. et al. : Detached Eddy Simulation for Separated Flow around a Cylinder Using Unstructured Grids, Proceedings of 21st Computational Fluid Dynamics Symposium, (2004) [in Japanese]
[7]Roshko, A. : Experiments on the Flow past a Circular Cylinder at Very High Reynolds Number, Journal of Fluid Mechanics, Vol.10(3), pp.345-356, (1961)

NUMERICAL SIMULATIONS OF THE FLOW AROUND A 6:1 PROLATE SPHERIOD

A. Karlsson[‡], R. Bensow[‡] & C. Fureby[†,‡]
[‡]Dept. of Shipping and Marine Technology, Chalmers
University of Technology, SE-412 96, Göteborg, Sweden
[†]Defense Security Systems Technology, The Swedish Defense Research Agency – FOI,
SE 147 25 Tumba, Stockholm, Sweden

Introduction and Background

The hydrodynamics of ships, submarines, and other underwater vehicles are often rather complicated and fully three-dimensional (3D). The phenomena of 3D open flow separation, which is one of many features exhibited by the 6:1 prolate spheroid case, is of importance in many fluid dynamic applications, such as the flow over cars, high-speed trains, ships and submarines, and puts up a challenge for all Computational Fluid Dynamic (CFD) models. When it comes to engineering applications are Reynolds Average Navier-Stokes (RANS) models, [1], quickly becoming possible, considering both computational resources and solution accuracy. But it has been reported, [2], that RANS in some applications can be insufficient. For example where small-scale flow phenomena, physical processes beyond the incompressible Navier Stokes model and unsteadiness are of interest and when new designs are to be developed. These problems can be diminished using Detached Eddy Simulation (DES), [4], or Large Eddy Simulation (LES), [5-8] models, this approach however result in an increased computation time and a need for more detailed boundary condition and geometrical data, [3]. For internal flows and combustion applications are DES and LES already widely used. But for flows like those past a ship hull, an aircraft fuselage or past a high-speed train, all of which is external and comes with a high Re number, is the cost-effective use of LES as a design tool yet not clear. Consequently, more detailed studies concerning RANS, DES and LES are needed to outline the optimal combined use of these methods.

This paper aims at comparing RANS, DES and LES predictions of the flow about a prolate spheroid, with a 6:1 major–minor semi-axis ratio, at α=10 and 20 degrees angles of attack. There have previously been a variety of RANS, DES and LES simulations performed, [9-12], thus this case is fairly well known. However in this study the same code and grids will be used for all simulations, which results in a reduction of the model uncertainties. The simulations are compared with experimental data from previous experimental investigations made by Chesnakas & Simpson, [13], and Wetzel *et al.*, [14], and also with the experimentally-based visualization studies of Han & Patel, [15], and Goody *et al.*, [16], providing a detailed understanding of the surface flow pattern. The observed flow field is well-defined and relatively simple but exhibits all the fundamental transition and separation phenomena of a 3D flow. The flow separating from the lee-side rolls up into a strong vortex on each side of the body, figure 1. In the 20 degrees of attack case a second smaller vortex, associated with a separation and reattachment line, accompanies the primary vortex. The accuracy of the different RANS, DES and LES models is estimated through agreement with the experimental data available for the boundary layer profiles and vortex systems, [13-14, 16]. The boundary layer velocities, being strongly affected by the separation pattern, the vortex systems and highly sensitive to minute changes in the flow over the body, constitutes good quantities when it comes to validation.

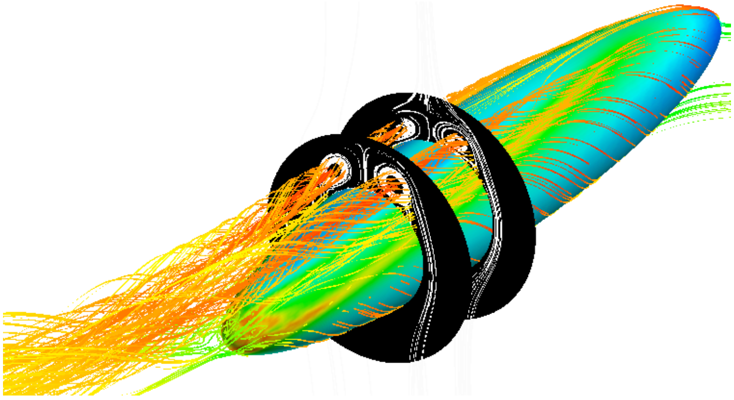

Figure 1. Perspective views of the flow in terms of streamlines, friction velocity on the hull and contours of vorticity at x/L=0.600 and 0.772, respectively, for the 20 degree angle of attack case.

Governing Equations

The governing equations of an incompressible flow consist of the equations relating mass and momentum for a linear viscous (or Newtonian) fluid, [25],

$$\begin{cases} \nabla \cdot v = 0, \\ \partial_t(v) + \nabla \cdot (v \otimes v) = -\nabla p + \nabla \cdot S + f, \end{cases} \tag{1}$$

where v is the velocity, p the pressure, $S = 2\nu D$ the viscous stress tensor with ν the kinematic viscosity and $D = 1/2(\nabla v + \nabla v^T)$ the rate-of-strain tensor and f the external forces. To close the equations initial and boundary conditions needs to be added.

Turbulence Modelling Approaches

A turbulent flow consists of a large span of turbulent scales, the largest ones being nearly as large as the characteristic width of the flow and the smallest ones in theory in size of the Kolmogorov length scale decreasing as $\mathrm{Re}^{-1/2}$, [26]. It's without turbulence modelling, due to time limitation and insufficient computational resources, in almost all hydrodynamic/aerodynamic applications not possible to numerically resolve this wide range of scales.

In this section is a short summary of Reynolds Averaged Navier Stokes (RANS), Detached Eddy Simulation (DES) and Large Eddy Simulation (LES) models presented.

Reynolds Averaged Navier Stokes (RANS) models

In RANS models the flow is assumed to fluctuate about a stationary solution which make it possible to decompose the velocity v into its mean $\langle v \rangle$ and fluctuation v', so that $v = \langle v \rangle + v'$,

[26]. Using this representation and the proper mathematical operations the Navier-Stokes equations (NSE, [Ekv.1]) can be transformed into the RANS equations [Ekv.2],

$$\begin{cases} \nabla \cdot \langle \mathbf{v} \rangle = 0 \\ \partial_t(\langle \mathbf{v} \rangle) + \nabla \cdot (\langle \mathbf{v} \rangle \otimes \langle \mathbf{v} \rangle) = -\nabla \langle p \rangle + \nabla \cdot (\langle \mathbf{S} \rangle - \mathbf{R}) + \langle \mathbf{f} \rangle \end{cases} \tag{2}$$

To solve these equations the Reynolds stress tensor $\mathbf{R} = \langle \mathbf{v}' \otimes \mathbf{v}' \rangle$ needs to be modeled using a turbulent closure model. In this study we have employ the Launder Sharma model, [17], capable of handling both separated flows and boundary layer flows.

Large Eddy Simulations (LES)

In LES, [5-8], as well as in DES, [4], all turbulent motions larger than the characteristic grid spacing, Δ, are resolved using a space and time accurate scheme and by modeling the influence of the unresolved subgrid scales. The flow and geometry dependency of the larger scales makes both LES and DES more reliable than RANS, [18], especially in cases where large-scale unsteadiness is significant. Far from walls, the details of the subgrid models are of less importance, as long as it provides sufficient dissipation to emulate the subgrid turbulence. Used in this study is the One Equation Eddy Viscosity (OEEVM) model, [19], the Mixed Model (MM), [20], and the Wall Adaptive Localized Eddy viscosity model (WALE), [21].

The LES equations are derived from (Ekv.1) by low pass filtering, using a kernel $G = G(\mathbf{x}, \Delta)$, such that,

$$\begin{cases} \nabla \cdot \overline{\mathbf{v}} = m^p, \\ \partial_t(\overline{\mathbf{v}}) + \nabla \cdot (\overline{\mathbf{v}} \otimes \overline{\mathbf{v}}) = -\nabla \overline{p} + \nabla \cdot (\overline{\mathbf{S}} - \mathbf{B}) + \overline{\mathbf{f}} + \mathbf{m}^v \end{cases} \tag{3}$$

Compared to the original NSE (Ekv.1) three new terms is introduced. The unresolved transport term $\nabla \cdot \mathbf{B}$, where $\mathbf{B} = (\overline{\mathbf{v} \otimes \mathbf{v}} - \overline{\mathbf{v}} \otimes \overline{\mathbf{v}})$ is the subgrid stress tensor, the commutation error terms $m^p = [G^*, \nabla]\mathbf{v}$ and $\mathbf{m}^v = [G^*, \nabla](v \otimes v + p\mathbf{I} - \mathbf{S})$ where $[G^*, \nabla]f = \overline{\nabla f} - \nabla \overline{f}$ is the commutation operator.

Detached Eddy Simulation (DES)

The primary practical difference between DES and LES is the treatment of walls; in DES the subgrid model is designed to switch to a RANS model (e.g. the Spalart-Almares model, [22], as will be employed here) close to the wall, whereas in LES either a sufficiently fine grid is required to resolve the near-wall structures (wall-resolved LES), or a separate wall model (wall-modeled LES) is required, [23]. There is insufficient understanding of how RANS, DES and LES behave when applied to complex wall-bounded flows and with the current work we hope to shed some new light on how different models behave and which features to be particularly concerned with. One such issue is the boundary layer tripping employed in the experiments at 20% of the hull length in order to increase the experimental repeatability. Due to the physical size of a typical trip device and the flow structures generated by it we believe that it either has to be a part of the geometrical model or the physical model. In the first case the grid needs to be fine enough to resolve the trip-induced structures and their evolution and in the latter, a separate trip model has to be developed and employed.

Numerical Approach

A finite volume method for arbitrary cell-shapes and a segregated approach described in [24] is used to discretize the flow equations. The space discretization uses linear reconstruction of the convective fluxes and central differencing of the viscous flux terms with compact 2^{nd} order stencils and time integration is performed by explicit 2^{nd} order backward differencing which thus guarantees overall 2^{nd} order accuracy and low numerical diffusion. The pressure-velocity coupling is handled with a PISO procedure based on a modified Rhie & Chow interpolation for the cell-centered data storage structure. The equations are solved sequentially, with iteration over the explicit source terms, with a Courant number limitation of about 0.3.

Results and Discussion

Presented in figure 2 are results from different LES, DES and RANS models. In figure 2a and 2b is the predicted and measured velocity components represented in the body surface coordinate system at the azimuthal angle of ψ=120° and at x/L=0.600 and 0.772. With U tangent to the hull surface in the body axial direction pointing toward the tail, V in the hull surface's outward normal direction and W tangent to the hull surface in completing a right-handed coordinate system. The angle, ψ=120°, was chosen to catch the complexity of the flow directly underneath the primary vortex. Both OEEVM+VM and the MM+WM, where +VM indicates the use of a wall model, [23], show reasonable agreement with experimental data. The WALE model predicts a too thin boundary layer, even though it theoretically has a better near wall scaling then the OEEVM. The RANS model simulation gives a result close to the experimental data, but doesn't capture its characteristic shape. The DES, in this case benefitting from the RANS wall model, gives surprisingly good result for x/L=0.772. Figure 2c show the secondary streamlines superimposed on the local mean velocity magnitude, $|U|/U_{tot}$, to the right and on the turbulent kinetic energy to the left, with the data taken in a plane perpendicular to the body axis at x/L=0.772. The lowest velocities are observed just beneath the separation lines. For both angles of attack a groove of low-velocity fluid is found between the two separation lines, corresponding to regions with large pressure and velocity fluctuations, since the primary vortices sweep up the low momentum fluid near the wall and that this fluid then accumulates between the primary vortex itself and the separation line. In figure 2d we compare the friction velocity, u_τ, between the different simulations and the experimental data. Surprisingly good agreement is found for the OEEVM+WM and MM+WM, whereas the WALE model under-predicts u_τ by a factor of about 2.

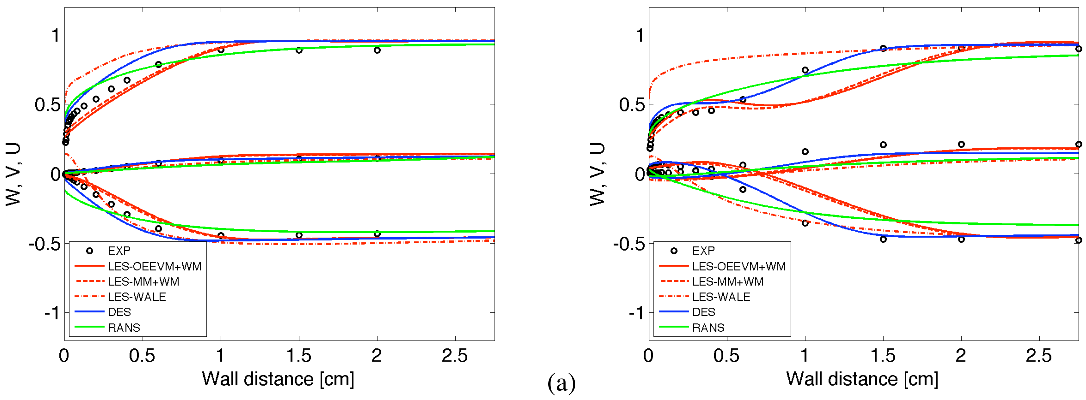

(a)

(b)

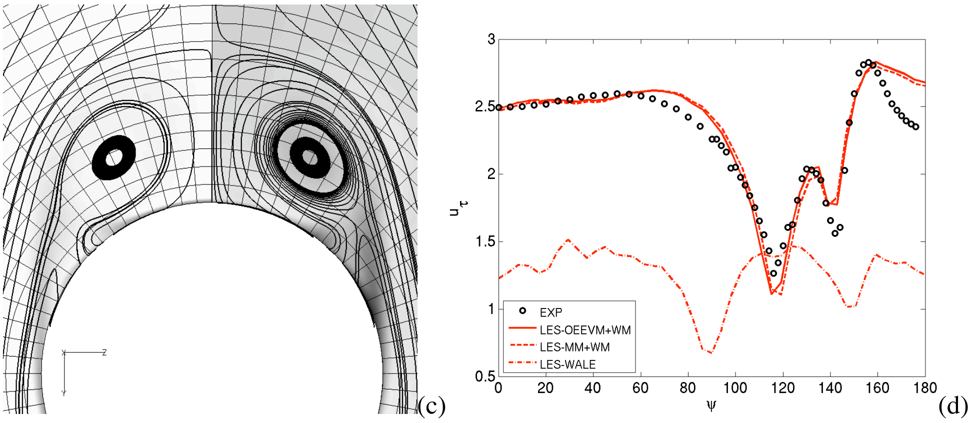

Figure 2. Comparison of selected statistical quantities between the simulations. (a) u/u_0, v/u_0 and w/u_0 at ψ=120° and x/L=0.600, (b) u/u_0, v/u_0 and w/u_0 at ψ=120° and x/L=0.772, (c) secondary streamlines superimposed on contours of the local mean velocity magnitude to the right and the turbulent kinetic energy to the left, and (d) friction velocity at x/L=0,729.

Concluding Remarks

In this study the flow about a 6:1 prolate spheroid is simulated using a set of RANS, DES and LES models. The results are to draw conclusions of the predictive capabilities compared to the experimental data of Simpson *et al*. [13-14, 16], in which a circumferential trip was placed at x/L=0.2 to improve the repeatability of the experiments. The employed RANS model is the Launder Sharma model, [17]. For LES three different models were used: the Wall Adaptive Localized Eddy viscosity model (WALE), [21] and together with a wall model (+VM), [23], the One Equation Eddy Viscosity Model (OEEVM), [19] and the Mixed Model (MM), [20]. The RANS model in the DES case was the Spalart-Almares model.

The OEEVM+VM, the MM and the DES models give reasonable agreement in a comparison with experimental data. When it comes to the RANS and the WALE model it's clear that they doesn't provide the correct flow field. For the latter model however we suspect, due to the thin boundary layer in the prediction, that a trip model might improve the result. In the future work the impact of the trip needs to be examined and simulations performed on a sequence of grids to further document the predictive capabilities.

References

[1] Wilcox, D.C.; 1993, "Turbulence Modeling for CFD", DCW Industries.

[2] Davidson L. 2005, "Test Case 11.2 – 3D Hill,,, Proceedings of the 11th Ercoftac/IAHR Workshop on Refined Turbulence Modeling.

[3] Grinstein F.F.; 2006, "On Integrating Numerical and laboratory Turbulent Flow Experiments", AIAA 06-3048.

[4] Nikitin N.V., Nicoud F. Wasistho B. Squires K.D. & Spalart P.R.; 2000, "An Approach to Wall Modelling in Large Eddy Simulation", Phys. Fluids, 12, p 1629.

[5] Ferziger J.H. & Leslie D.C.; 1979, "Large Eddy Simulation - A Predictive Approach to Turbulent Flow Computation", AIAA 79-1441.

[6] Sagaut P.; 2001, "Large Eddy Simulation for Incompressible Flows", Springer Verlag.

[7] Grinstein F. F., Margolin, L. G. & Rider W. J. (Eds); 2007, "Implicit Large Eddy Simulation Computing Turbulent Fluid Dynamics", Cambridge University Press.

[8] –

[9] Tsai C.-Y. & Whitney A.K.; 1999, "Numerical Study of Three-Dimensional Flow Separation from a 6:1 Ellipsoid", AIAA 99-0172.

[10] Rhee S.H. & Hino T.; 2000, “Computational Investigation of 3D Turbulent Flow Separation around a Spheroid using an Unstructured Grid Method”, J. Soc. Naval Architects of Japan, 188, p 1.

[11] Constantinescu G.S., Pasinato H., Wang Y.-Q., Forsythe J.R. & Squires K.D.; 2002, “Numerical Investigation of Flow past a Prolate Spheroid”, AIAA 02-0588.

[12] Wikström N., Svennberg U., Alin N. & Fureby C.; 2004, “LES of the Flow past an Inclined Prolate Spheroid”, J. Turbulence 5, p 29.

[13] Chesnakas C.J. & Simpson R.L.; 1996, “Measurements of Turbulence Structure in the Vicinity of a 3D Separation”, J. Fluids Eng., 118, p 268.

[14] Wetzel T.G., Simpson R.L. & Chesnakas C.J.; 1998, “Measurement of Three-Dimensional Crossflow Separation”, AIAA J. 36, p 557.

[15] Han T. & Patel V.C.; 1979, “Flow Separation on a Spheroid at Incidence”, J. Fluid Mech. 92, p 643.

[16] Goody M., Simpson R.L. & Engel M.; 1998, “Mean Velocity and Pressure and Velocity Spectral Measurements within a Separated Flow Around a Prolate Spheroid at Incidence”, AIAA Paper 98-0630.

[17] Launder B. E. & Sharma B. I.; 1974, “Application of the Energy-Dissipation Model of Turbulence to the Calculation of Flow Near a Spinning Disc”, Letters in Heat and Mass Transfer, 1, p. 131.

[18] Fureby C. & Bensow R. 2007, “LES at Work: Quality Management in Practical LES”, Invited Review paper at QLES 2007. To appear in the Proceedings of the Conference, Springer Verlag.

[19] Schumann U.; 1975, “Subgrid Scale Model for Finite Difference Simulation of Turbulent Flows in Plane Channels and Annuli, J. Comp. Phys., 18, p 376.

[20] Bensow R. & Fureby C., 2006, “On the Justification and Extension of Mixed Models in LES”, J Turbulence 8, p N54.

[21] Nicoud F. & Ducros F.; 1999, “Subgrid-Scale Stress Modeling Based on the Square of the Velocity Gradient Tensor”, Flow, Turb. & Comb. **62**, p 183.

[22] Spalart P.R. & Allmaras S.R.; 1992, “A One-Equation Turbulence Model for Aerodynamic Flows”, AIAA 92-0439.

[23] Fureby C.; 2007, “On LES and DES of Wall Bounded Flows”, Ercoftac Bulletin No 72, Marsh Issue.

[24] Weller H.G., Tabor G., Jasak H. & Fureby C.; 1997, “A Tensorial Approach to CFD using Object Oriented Techniques“, Comp. in Physics, 12, p 629.

[25] Panton, R.L., 1996, “Incompressible flow”, New York: John Wiley & Sons.

[26] Pope, S.B., 2000, “Turbulent Flows”, Cambridge University Press.

Trajectory prediction by coupling Euler-Newton equations and flow models

Floc'h F., Laurens J.M., Kerampran S. and Leroux J.B.
france.floch@ensieta.fr

1 Introduction

Nowadays, progress in mesh generation techniques and solver performance has been such that it is now possible to compute any trajectory of an object moving in free motion within a fluid. Nevertheless, a complete model of the maneuverability is necessary to predict submerged body trajectories. In classical models, hydrodynamics forces are globally introduced, by the mean of coefficient identified with experimental data, in the equations of motion. Unsteady forces are neglected for large object such as ship or submarine but must be taken into account for smaller object such as AUV, torpedos or countermeasure. The present study consists of coupling the equations of motion with a flow solver. To validate the model, the construction of a 2D hydrodynamic channel is in progress. To solve the equations of Euler-Newton of a solid in void, in air or in water is of increasing difficulty. In fact, the water is heavy compared to air and its density is, in most cases, close to the density of the solid body. Fluid inertia forces are represented by an added mass in phase with the acceleration. The corresponding term makes the explicit scheme unstable.

Söding [2001] first mentioned this problem for most naval applications. Since, Leroux et al. [2007] proposed to overcome this difficulty by using a Crank-Nicholson scheme. This scheme is presented in this study. First, a Navier-Stokes solver is used to solve the flow in order to simulate motion of an arbitrary submerged body. After verification, to validate the model, a cylinder and a parallelepiped lighter or heavier than water are released in a tank. Trajectories and velocities are compared to numerical data obtained thanks to the Navier-Stokes solver. Moreover, this Navier-Stokes solver has permitted to design a 2D hydrodynamic channel with a uniform horizontal flow. Conclusions about the design are presented in this article. The method is also coupled with a potential solver. The range of applications is much more restricted since the viscosity is ignored and only profiled bodies can be considered. Thus, it could permit to make advances in propulsion considering the bio-mimetism : fast fish propel themselves in water through rhythmic motion of their tail. Such motions are studied in Guglielmini et al. [2003], Guglielmini and Blondeaux [2003], Triantafyllou et al. [2000], Schouveiler et al. [2005], Barrett et al. [1999], Pedro et al. [2003]. These articles could be split in two types: half of them deals with the lift due to vortex generation and the others with the characteristics of the motion : tail form and the Strouhal number which ranges from 0.2 to 0.4 for fish and cetacean. Here, attention is payed to thrust produced by forcing the heave and the pitch.

2 Solving the Euler-Newton equations

2.1 Numerical scheme

Hydrodynamics forces are computed from a Navier-Stokes or a potential solver. Then, they are introduced in the numerical scheme. As explained in the introduction, forces contain a term depending on the acceleration. First, an explicit scheme is studied and its stability criterion determined. Next a Crank-Nicholson scheme is used to solve the stability problem.

The vector $F(v)$ represents the total forces and moments acting on the solid body and $-m_a\dot{v}$ the inertial forces depending on the acceleration. $f(v) = F(v) + m_a\dot{v}$ contains no term depending on the acceleration. The equation of motion is then written as :

$$m\dot{v} = F(v) = f(v) - m_a\dot{v} \tag{1}$$

The stability criterion of the numerical scheme depends on the added mass. Let us consider first a classic explicit Euler scheme :

$$m\frac{v^{n+1} - v^n}{\Delta t} = f(v^n) - m_a\frac{v^n - v^{n-1}}{\Delta t}$$

$$v^{n+1} = (1 - \frac{m_a}{m})v^n + \frac{f(v^n)\Delta t}{m} + \frac{m_a}{m}v^{n-1} \tag{2}$$

The error ε^n is introduced on v^n:

$$v^{n+1} + \varepsilon^{n+1} = (1 - \frac{m_a}{m})(v^n + \varepsilon^n)$$

$$+\frac{f(v^n + \varepsilon^n)\Delta t}{m} + \frac{m_a}{m}(v^{n-1} + \varepsilon^{n-1}) \tag{3}$$

But : $f(v^n + \varepsilon^n) = f(v^n) + \frac{\partial f}{\partial v}\varepsilon^n + O(\varepsilon^n)$. By considering only the first order in ε and by subtracting 2 to 3, the following expression is obtained :

$$\varepsilon^{n+1} = (1 - \frac{m_a}{m})\varepsilon^n + \frac{m_a}{m}\varepsilon^{n-1} + \frac{\partial f}{\partial v}\frac{\Delta t}{m}\varepsilon^n \tag{4}$$

If the added mass is zero, the scheme is stable only if $\frac{\partial f}{\partial v} \leq 0$. In the following, the precedent hypothesis is verified and the damping will be neglected. By solving equation (4), considering the error propagation constant, it appears that the error is composed by a constant part and by a part multiplying by $-\frac{m_a}{m}$. The stability criterion sums up to :

$$\left|\frac{m_a}{m}\right| < 1 \tag{5}$$

This condition is generally not respected in naval hydrodynamics. To overcome the stability problem, a Crank-Nicholson scheme is used. This scheme corresponds to the sum of an implicit Euler scheme and an explicit Euler scheme. The following scheme is then obtained :

$$m\frac{v^{n+1} - v^n}{\Delta t} = F(v^n) + A\frac{v^n - v^{n-1}}{\Delta t} - \frac{A}{2}\frac{v^{n+1} - v^{n-1}}{\Delta t} \tag{6}$$

In this equation, the term f has been replaced by the expression depending on F, the total forces acting on the solid body. The solver provides the total forces that contain a term depending on the real added mass m_a of the object. To calculate the criterion stability, this term must appear. By making the same hypothesis than before, we obtain:

$$(m + \frac{A}{2})\varepsilon^{n+1} + (m_a - A - m)\varepsilon^n + (\frac{A}{2} - m_a)\varepsilon^{n-1} = 0 \tag{7}$$

The stability criterion deduced from equation (7) is composed of a constant part and a part multiplied by $-\frac{A-2m_a}{2m+A}$. The stability criterion is then: $\left|\frac{A-2m_a}{2m+A}\right| < 1$

Let us consider the function $f(x) = \frac{x-2m_a}{2m+x}$ defined on $[-\infty; +\infty]$ for $x \in [0; +\infty]$. The function study shows that $f(x)$ is once equal to -1. This value is obtained for $A = m_a - m$. The only limit of the stability criterion resulting in a divergent scheme is finally $A < m_a - m$ that means for the stability criterion :

$$\frac{m_a - A}{m} < 1 \tag{8}$$

It appears that the scheme is always stable when A is over-estimated. A cube, for instance, has an added mass superior to its displacement. We first chose to test the scheme on the case of an submerged cube falling in a straight course. In this case, the analytical solution is well-known. The numerical solutions obtained with a Euler or Crank-Nicholson scheme are compared with the analytical solution on figure 1. As expected, the simple explicit scheme (equation(2)) diverges. Here, the forces were included directly in the stand-alone routine.

2.2 Implementation

The scheme has been embedded in a routine written in C. It is able to work independently

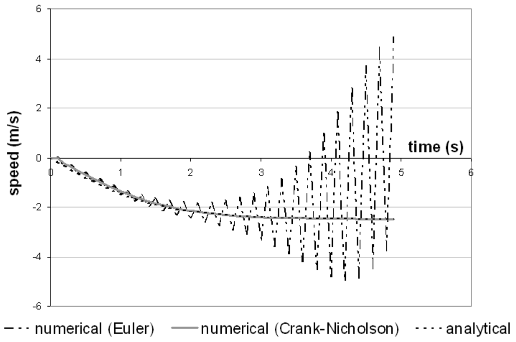

Figure 1: Comparison between Euler and Crank-Nicholson scheme and analytical solution for $\frac{m_a}{m} = 2$

or coupled with a solver. 2D or 3D is possible. The program just needs the forces acting at the body center of gravity to calculate its trajectory. When it works in a stand-alone mode, unless the solid is moving in void, the hydrodynamics forces must be known. For simple cases, the code can be used in a stand-alone mode at least for verification.

This program has two input files: one contains the characteristics of the solid body (mass, volume, density, inertial matrix, initial speed) and the other, the external forces. In brief, the routine performs the following stages:

1. It reads the input files. Since the file is read at the beginning of each time step, it is possible for instance, to simulate ballasting and/or propulsion.
2. Then it reads the file containing the saved velocities of the two previous time steps and Euler angles.
3. It gets hydrodynamics forces, moments as computed by the flow solver.
4. These data are converted into the local system of coordinates.
5. Total forces are computed.
6. Accelerations are computed in the local system of coordinates.
7. The new velocities are computed using the Crank-Nicholson scheme described in equation (6.)
8. Velocities are written as such for the next time step and converted to the global system of coordinates before they are passed to the flow solver which performs the hydrodynamic simulation for the current time step.

The total forces of stage 5 contain of course the weight and inertia forces and moments but also any other non-hydrodynamic forces to be considered such as ballast or propulsion.

3 Coupling with a RANSE solver

The scheme is embedded in the commercial Navier-Stokes solver Fluent. This solver admits user defined functions (UDF) which must be written in C.

3.1 Simulation results

In Koutsavdis [2002], results of a user defined functions called Six Degrees Of Freedom (6DOF) were presented for a bomb leaving a bomber. Although this presentation was a major stage, for the reasons discussed in the introduction, it could not be applied for underwater vehicles. Inspired by the work of Koutsavdis [2002], the user defined function has been rewritten to include the Crank-Nicholson scheme written in equation (6).

The simple case considered afterwards is the falling cylinder with a mass of 1.3 kg. The cylinder is represented with a large mesh. This representation enables, thanks to an in-house code, to calculate the added mass matrix and the inertia matrix of the solid body. We find an added mass equal to 1.26 kg and a dimensionless inertial matrix:
$I =$

$$\begin{bmatrix} 6.73\times10^{-1} & -6.45\times10^{-3} & -1.62\times10^{-1} \\ -6.45\times10^{-3} & 6.73\times10^{-1} & -1.62\times10^{-1} \\ -1.62\times10^{-1} & -1.62\times10^{-1} & 1.51\times10^{-3} \end{bmatrix}$$

It appears that a 2D simulation is a good approximation of the motion.

Concerning the Navier-Stokes solver, a representation of the 2D problem is necessary. A particular attention is brought to the mesh. In fact, because of the motion of the body, the remeshing of the domain is important during the simulation. That test shows that the numerical scheme is stable and that the Navier-Stokes solver coupled with the routine presents some realistic results (see figure 2). Then, series of simulation were performed with a parallelepiped lighter and heavier than water with an initial pitch angle non equal to zero. As expected, in a static fluid and for a Archimedes number

$$A = \frac{\Delta\rho g r_{eq}^3}{\rho_f \nu^2}$$

big enough , the motion of the submerged body not showing a preferential direction is chaotic, Jenny et al. [2003]. Here, r_{eq} stems from $\frac{4}{3}\pi r_{eq}^3 = V$ with V the volume of the submerged body, Fernandes et al. [2005]. Hence, a parameters study should be performed to identify the limit of such behavior. To validate our model, the trajectory should not be chaotic. A zero flow velocity stabilizes the trajectory and thus could permit to validate the model. Moreover, because the three-dimensional simulations require too much computing time, it has been decided to examine the feasibility of an experimental device to validate the model in 2D.

3.2 Experimental validation

First of all, a bidimensional tank was built in order to check the bidimensionality of the motion : cylinders with different thicknesses, chosen to allow for a minimal looseness between the body and the inner wall without disturbing its motion, were released and their trajectories and velocities recorded (see figure 2). The inner tank is 0.8 m height, 0.4 m wide and 0.02 m thick. The cylinder which reached the analytical limit speed has a looseness of 0.2 mm. However, since the motion is chaotic in a static fluid, an hydrodynamic channel is necessary to validate the model. The design is in progress. The aim is a velocity range [20 cm/s : 40 cm/s], test section dimension 0.8 × 0.8 × 0.02 and a system to release object from the top or the bottom. These parameters contribute to the uniformity of the flow.

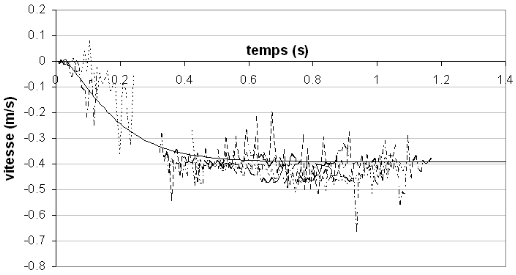

Figure 2: Comparison between experimental (dashed lines), numerical and analytical (straight line) velocity of a falling cylinder in a two-dimensional hydrodynamic channel

4 Coupling with a potential flow solver

The routine was also coupled to a potential solver. It is a Boundary Element Method (BEM) code. This belongs to what Hoeijmakers [1992] refers to as "second generation" panel methods involving the Dirichlet condition. Body surfaces are discretised into first order panels carrying constant source and doublet distributions. The wake developing behind the wing is formed with a sheet of first order panels carrying constant doublet distributions and it is generated with time in a Lagrangian manner. To verify our method, a NACA 23012 with an angle of attack of 6° and an initial speed of 4 m/s is placed in an invert flow of 2 m/s. From there, we simulate natural decreasing speed due to drag. The theoretical speed is calculated by solving the fundamental principle of dynamics:

$$(m + m_a)\frac{\partial v}{\partial t} = \frac{1}{2}\rho C_D S(v(t) - U_\infty)^2 \qquad (9)$$

with m, the mass of the profile in kg; m_a, its added mass in kg; S its lift area; C_D, its drag coefficient and ρ, the fluid density in kg/m^3.

$$v(t) = \frac{1}{-\beta t + \frac{1}{v0-U_\infty}} + U_\infty \qquad (10)$$

with $\beta = \frac{\rho C_D S}{2(m+m_a)}$, $v0$ the initial speed — taken equal to -4 m/s — and U_∞ the flow velocity. The drag coefficient is in Abbott and von Doenhoff [1949] : for a NACA 23012 with an attack angle 6° and a Reynolds number close to one million, the coefficient C_l is 0.75. the profile aspect ratio is $\Lambda = \frac{length^2}{S} = 3$. According to the Hembold formula :

$$C_L = C_l * \frac{\Lambda}{\sqrt{\lambda^2+4}+2}$$

Considering a 3D problem : $C_D = C_L/(\pi\Lambda)$, thus C_D is 0.04. In order to obtain the added mass, simulations of a motion with a constant acceleration have been performed. Therefore, from the forces provided by the potential flow code, it is possible to calculate m_a depending on the flow.

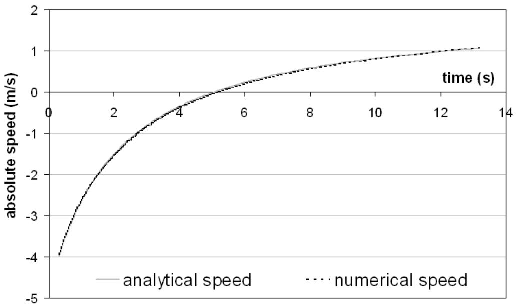

Figure 3: Comparison between theoretical and coupling codes results

On figure 3, it appears that numerical and theoretical results are similar.

As mentioned in the introduction, the coupling with a potential solver offers the opportunity to make progress in propulsion considering the bio-mimetism. By forcing pitch and heave as sinusoidal functions $\frac{\pi}{4}$-dephased (see figure 4), thrust is produced. A limit speed is reached. Its value depends on the characteristics of the motion like the amplitude of heave z_0, the amplitude of pitch α_0, the motion frequency f_0, the wing length L and chord c. Let us apply the buckingham theorem.

$$f(V_{lim}, z_0, \alpha_0, f_0, L, c) = 0$$

These variables are expressible in terms of two independent fundamental physical quantities : meter and second. Considering six variables, the $f-$expression is equivalent to an equation involving a set of four dimensionless variables.

$$F(\frac{V_{lim}}{cf_0}, \frac{z_0}{c}, \alpha_0, \frac{L}{c}) = 0$$

Two known dimensionless numbers appear : the Strouhal number $St = \frac{cf_0}{V_{lim}}$ and the wing aspect ratio $\Lambda = \frac{L}{c}$. Then :

$$F(St, \Lambda, \frac{z_0}{c}, \alpha_0) = 0 \qquad (11)$$

Then, a series of simulation has been launched. Strouhal number appears to be similar to those of cetacean i.e. about 0.2 which could be understood considering that cetacean have a rigid tail like in our simulations.The possibility opens a wide range of applications and further studies.

Furthermore, for additional verification, the added mass matrix computed from a potential solver is directly introduced in the stand-alone routine. The speed limit obtained this way is lower than our simulation by about 30%.

$$m_{a_{ji}} = \rho \iint_S \phi_i \frac{\partial \phi_j}{\partial n} dS \qquad (12)$$

The discrepancy is to be blamed on equation (12). This equation, although standard to compute the added masses, is only valid for non-lifting bodies.

5 Conclusion

A numerical method has been developed to simulate the free motion of a submerged body. The method involves a Navier-Stokes or a potential solver coupled with a routine solving the equations of motions. The model has been verified and the simulations performed so far indicate that the numerical scheme is stable and produces realistic results. The design of the experimental device to validate the Navier-Stokes

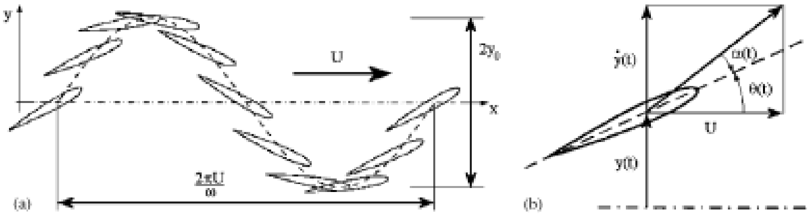

Figure 4: (a) Kinematical parameters of the foil motion and (b) efinition of the angle of attack $\alpha(t)$, from Guglielmini et al. [2003]

model is in progress. The coupling with the potential flow solver provides a motion with a Strouhal number similar to those of cetacean.

References

I. Abbott and A. von Doenhoff. *theory of wing sections*. Dover publications, 1949.

D. Barrett, M. Triantafyllou, D. Yue, M. Grosenbaugh, and M. Wolfgang. Drag reduction in fish-like locomotion. *JFM*, 392: 183–212, 1999.

P. Fernandes, P. Ern, F. Risso, and J. Magnaudet. Mouvements oscillatoires de corps en ascension dans un fluide peu visqueux : l'effet du rapport de forme. *Mécanique & Industries*, 6:279–283, 2005.

L. Guglielmini and P. Blondeaux. Propulsive efficiency of oscillating foils. *European Journal of Mechanics B/Fluids*, 23:255–278, october 2003.

L. Guglielmini, P. Blondeaux, and G. Vittori. A simple model of propulsive oscillating foils. *Ocean Engineering*, 31:883–899, march 2003.

H. Hoeijmakers. Panel method for aerodynamics analysis and design. *AGARD report*, 783: 5.1–5.47, 1992.

M. Jenny, G. Bouchet, and J. Dusek. Non vertical ascension or fall of a free sphere in a newtonian fluid. *Phys. Fluids*, 15:L9–L12, 2003.

E. Koutsavdis. Store separation analysis. *Fluent News fall*, IX:8–10, 2002.

J.-B. Leroux, J.-M. Laurens, and S. Kerampran. Simulation and validation of the free motion of a submerged body. *CFD in Ship Design*, september 2007.

G. Pedro, A. Suleman, and N. Djilali. A numerical study of the propulsive efficiency of a flapping hydrofoil. *IJNMF*, 42:493–526, 2003.

L. Schouveiler, F. Hover, and M. Triantafyllou. Performance of flapping foil propulsion. *JFS*, 20:949–959, 2005.

H. Söding. How to integrate free motions of solids in fluids. *4^{th} Numerical Towing Tank Symposium*, pages 23–25, september 2001.

M. Triantafyllou, G. Triantafyllou, and D. Yue. Hydrodynamics of fishlike swimming. *ARFM*, 32:33–53, 2000.

Numerical predictions and experimental verifications for the hydrodynamic performance of horizontal axis marine current turbine

Ruijun Fan [a], Zhou Zhou [a]

[a] Northwestern Polytechnical University (NPU), P.R.China r.j.fan@soton.ac.uk

Abstract

This paper presents the numerical predictions of 3D CFD rotor computations of an 800mm diameter model of marine current turbine (MCT). In the paper CFD is applied to a rotor at stationary hydrodynamic conditions, using the commercial multi-purpose CFD solvers ICEMCFD 11.0 and ANSYS CFX 11.0. Consequently, numerical predictions need to be verified. Simulations from the numerical prediction are compared with experimental measurements of the model of MCT which is experimented on in a cavitation tunnel and a towing tank. The experimental data includes measurements of power and thrust generated by the turbine, in both a cavitation tunnel and a towing tank, for a series of blade pitch settings and speeds. The numerical predictions show similar results and provide a satisfactory representation of the experimental turbine performance. Such results provide confidence in using the CFD computation tools to develop the forthcoming design of marine current turbines.

Keywords: CFD, marine current turbine (MCT), ANSYS CFX, cavitation tunnel

1 Introduction

Marine currents are increasingly being recognized as a resource to be exploited for sustainable generation of electrical power. Many devices are being studied for marine current energy conversion although most are designed around horizontal axis turbines, known as a marine current turbine (MCT). The success of using MCT to tap the ocean currents is partly dependent on predicting their hydrodynamic performance.

It is therefore important to be able to predict energy yields for this technology which will allow appropriate designs to be qualified and validated. To this end, Methodologies need to be established which will describe the physical and operational performance of the turbines in this paper.

The rotor hydrodynamics of a MCT is influenced by rotational wake effects downstream of the turbine and effects of wind blockage upstream of the turbine. Closer to the turbine, three-dimensional effects originating from a combination of radial flow and coriolis forces play an important role on the inboard part of the blades. In general the three-dimensional effects on this part of the turbine have a positive effect on the lifting performance of the inboard blade sections as compared to 2D airfoils characteristics. This phenomenon is often referred to as stall-delay.

Additionally, highly three-dimensional flow is occurring at the blade tips due to the formation of tip vortices. Several variable external factors such as blade surface roughness and turbulence generated from nearby and located on the turbine complicate the hydrodynamics of MCT even further. Finally, a MCT is a dynamic structure that constantly undergoes structural deformations which in turn influence the hydrodynamics.

The experimental results from cavitation tunnel tests and towing tank tests, discussed and used for the verification of the numerical methods used within this paper are taken from a large set of tests. This included cavitation inception observations, the effect of yaw, the effect of tip emersion and dual rotor interactions. The corrected results from these experiments are used to verify and compare with the simulation result of CFX based upon the Reynolds Averaged Navier-Stokes (RANS) equations.

2 Methodology for CFD

First study in this paper is computation of the 3D MCT model in laboratory scale using ANSYS CFX.

All the computations are performed by the commercial CFD software package (ANSYS CFX™ 11.0) which utilizes a finite-volume method based structured multigrid. The structured grids were generated by ICEM CFD 11.0 around a digital turbine model of the experiment (Figure 1). The computations have been performed with the incompressible version of the Reynolds Averaged Navier-Stokes (RANS) equations and the SST turbulence models.

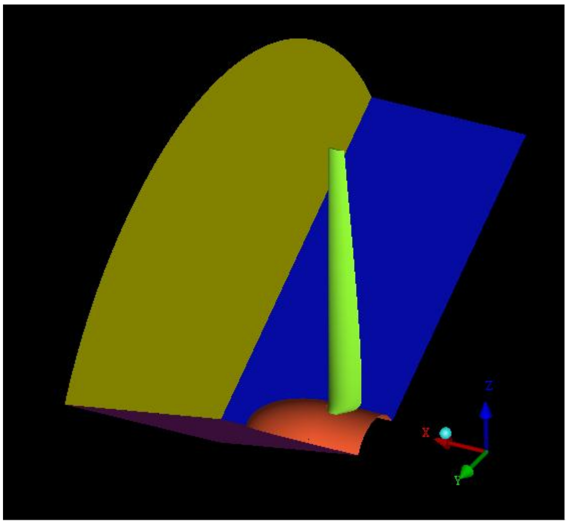

Figure 1. Rotation domain of digital turbine model.

Due to the long computational times and hardware restrictions simulation has selected one blade of MCT to be applied the periodic boundaries on in the circumferential direction. The whole flow area is divided to two parts: one is rotational domain and one is far field domain. GGI (General Grid Interface) connections are applied to connect between these two domains. (Figure 2~4)

The simulation is used to determine the lift and drag forces on the blade. The integration of these values across the blade allows the derivation of thrust and power coefficients for a range of rpm and flow speed on the turbine.

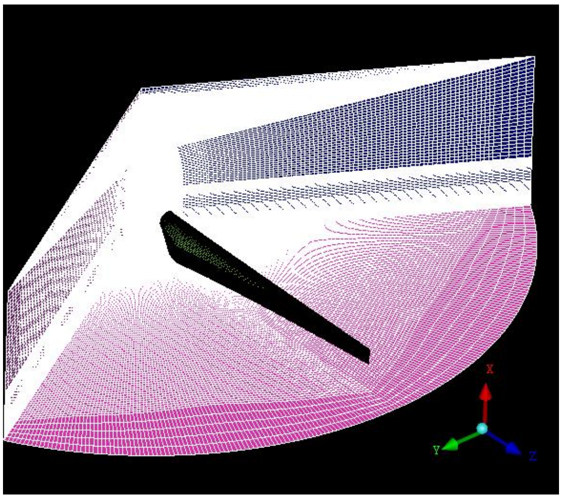

Figure 2. Computational mesh: rotation domain.

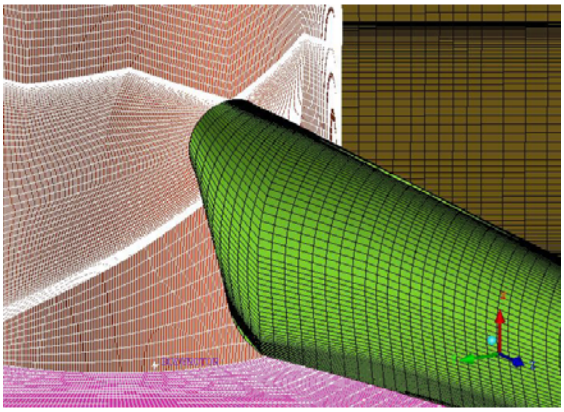

Figure 3. *Computational mesh: zoom in on blade and hub.*

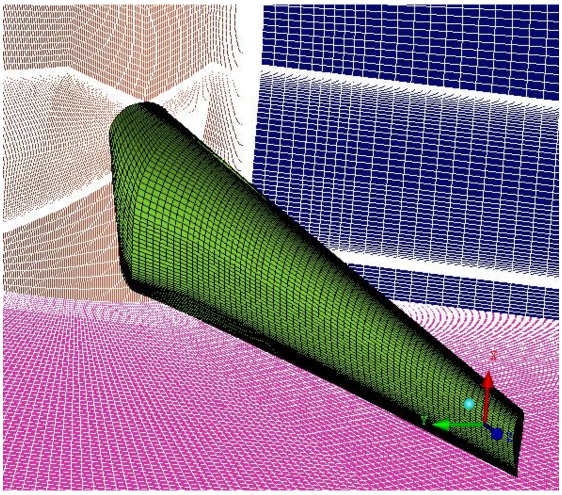

Figure 4. *Computational mesh: blade.*

3 Experiment verification

3.1 Models

A rotor diameter of 800mm was chosen as a compromise between maximizing Reynolds number and not incurring excessive tunnel blockage correction. The boss diameter to suit the test rig was 100mm. The blades were developed from the profile shape of a NACA 63-8xx and appropriate chord, thickness and pitch distribution.

The model blades were manufactured from 3D model drawings derived from 2D section coordinates interpolated from coordinate-based data for NACA 63-812, 63-815, 63-818, 63-821 and 638-24 for 17 stations along the blade. The blades were machined from T6082-T6 aluminum alloy on a 5-axis computer numerical control (CNC) machine at the University of Southampton to an order of accuracy of ± 0.05mm. They are then brought to a smooth hydrodynamic finish and anodized for protection. (Figure 5~6)

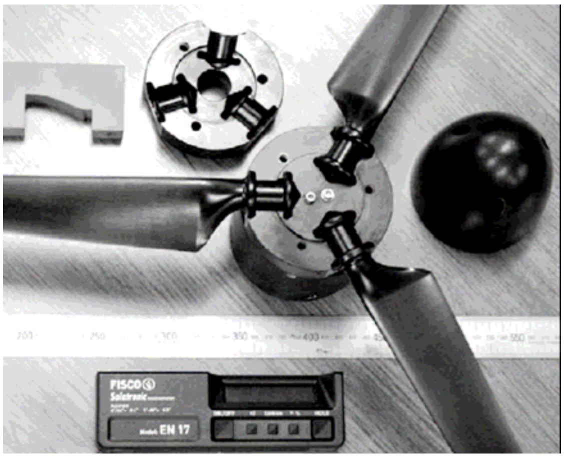

Figure 5. *Photograph of the blade and the hub test components.*

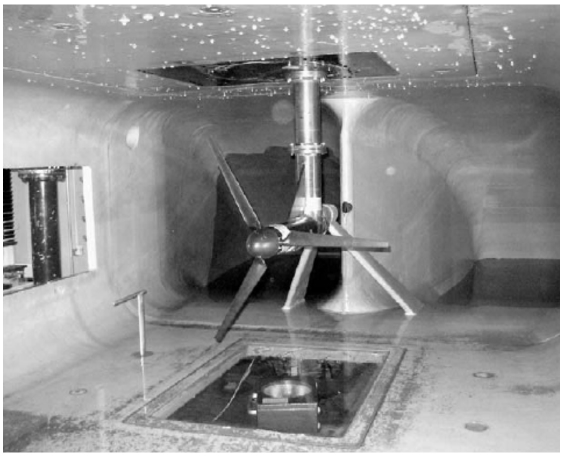

Figure 6. *Photograph of the assembled test rig in the cavitation tunnel.*

3.2 Cavitation Tunnel and Towing Tank

Measurements of the torque and thrust characteristics of the 800mm marine current turbine are carried out in a cavitation tunnel at Qinetiq, Haslar and a towing tank at Southampton Solent University. The tunnel has working section of 2.4m × 1.2m and a maximum flow speed of 8m/s. The rotor was centered in the tunnel. This provides a controlled environment for the principal measurements. The towing tank has a length of 60m, breadth of 3.7m and depth of 1.8m. The rotor was close to being centered at 0.84m below the free surface of water.

We can get the reliable set of MCT performance characteristics under controlled conditions in the mentioned experiment. This would entail the measurement of power and thrust performance characteristics over a range of flow speed, rotor revolutions and rotor blade pitch settings.

3.3 Date reduction and presentation

For a given tunnel flow speed and rotational speed, the torque and the thrust were acquired from the dynamometer. The averaged excitation voltages from the torque and thrust bridge circuits were corrected for zero offset and then multiplied by the calibration factor to resolve the torque (Q) and thrust (T). The TSR, power (CP) and thrust (CT) coefficients were non-dimensionalised in the following:

Tip Speed Ratio: $TSR = \frac{\Omega R}{U_0}$

Power coefficient: $C_P = \frac{Q\Omega R}{(1/2)\rho U_0^3 A}$

Thrust coefficient: $C_T = \frac{T}{(1/2)\rho U_0^2 A}$

Where Ω is rotation speed, U_0 is speed, R is the rotor radius and $A = \pi R^2$.

4 Results and Analysis

The results of the CFD simulation are compared with a set of experimental tests and the computation of SERG-Tidal(a tidal turbine prediction program developed at the University of Southampton is based on a BEM program) for MCT at set angles from 0° to 13° as shown in Figure 7 to 10. A comparison with the towing tank experiments at set angles of 5° and 10° is presented in Figure 8 and 9 as well. The results show good agreement, which gives confidence in both the results corrections and the appropriateness of using the towing tank. The towing tank data has a larger scatter in results, mainly due to the brief time window to take measurements caused by the short tank length.

The predictions from ANSYS CFX and SERG-Tidal CFD program demonstrate general agreement for TSR = 4-7 for all cases. The closest agreement was found for the design case with a set angle of 5° and TSR = 6. For TSR > 7 both CFD simulations tend to over predict the power coefficients for set angles 5°-13°. For these cases the thrust coefficients of the experiment are higher. At 0° set angle in Figure 7 both CFD programs fail to predict the sharp drop in power and thrust coefficients with TSR > 7.

There is a general trend when comparing the results of CFX simulation at TSR higher than the design case. CFX has a general tendency to slightly overestimate the power whilst it to some extent underestimates the thrust. This is evident for set angles of 5°–13° in Figure 8 to 10. Either reason may be, due to errors in the large blockage corrections applied to the experimental data or possible different turbulent model used in CFX computations. As at high TSR the turbulent wake correction becomes more important in CFX model. Consequently, this correction may need some adaptation.

The relevance of the results is examined for full scale deployment of marine current turbine. The accuracy of the predictions will be analyzed to determine the satisfactory for using the CFD numerical tools for parametric studies. The limitations of the CFD modeling will also be examined, and opportunities for refinement will be noted.

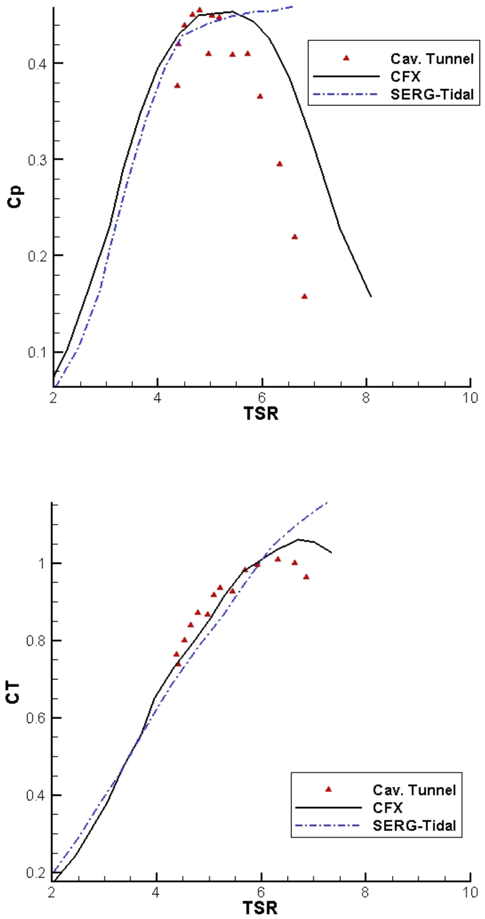

Figure 7. *Comparisons between experiments and numerical simulations at 0^o set angle.*

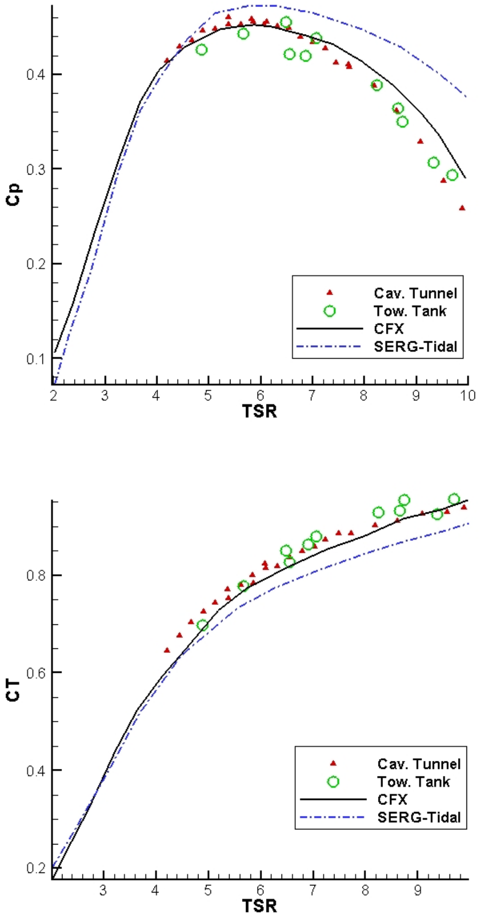

Figure 8. *Comparisons between experiments and numerical simulations at 5^o set angle.*

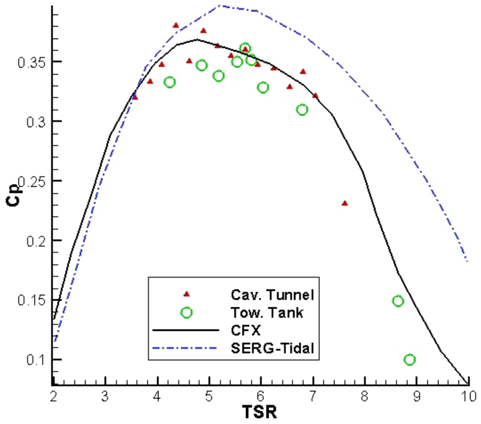

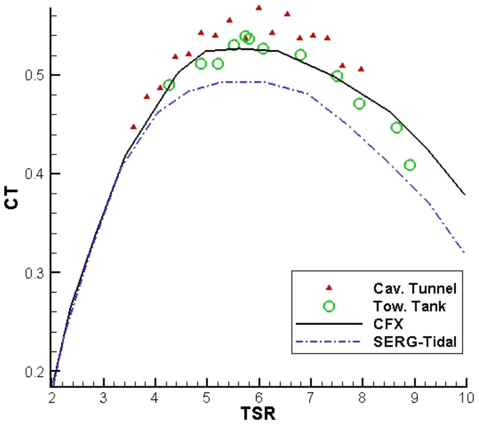

Figure 9. *Comparisons between experiments and numerical simulations at 10^o set angle.*

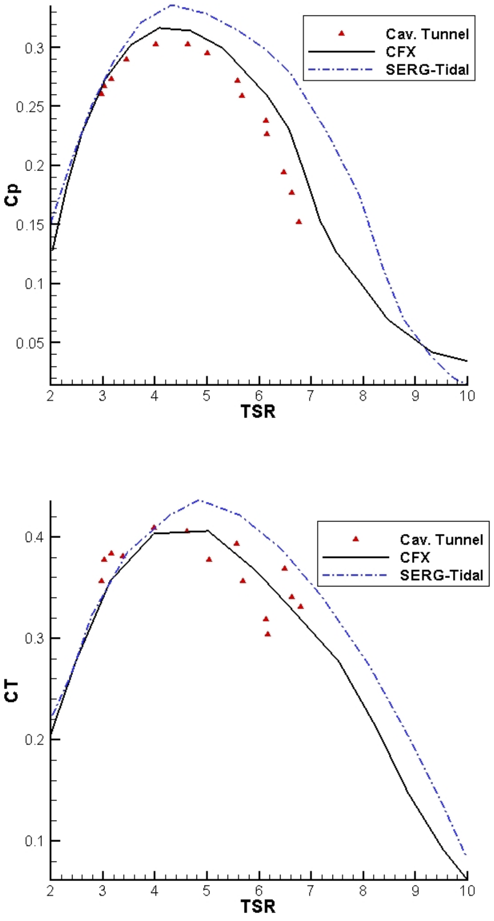

Figure 10. *Comparisons between experiments and numerical simulations at 13^o set angle.*

5 Conclusions

This paper studies the hydrodynamic performance of horizontal axis marine current turbine using CFD techniques. Methods are validated by comparison with results of the experiments in cavitation tunnel and a towing tank.

A comparison of the experimental results shows the applicability of using CFD as the tools to predict the characters of MCT. The accuracy of the predictions is satisfactory for using the developed theoretical tools for design exercises and parametric studies. The closest agreement between all experiments and predictions was for the design case. In general, for off-design cases, ANSYS CFX tends to slightly overestimate the power and underestimate the thrust.

Reference

[1] Power and thrust measurements of marine current turbine under various hydrodynamic flow conditions in a cavitation tunnel and a towing tank. A.S. Bahaj, A.F. Molland, J.R. Chaplin. Renewable energy 2007; 32:407–426.

[2] Fraenkel PL. Power from marine turbines. Proc Inst Mech Eng A: J Power Energy 2002;216(A1):1–14.

[3] European Commission. The exploitation of tidal marine currents. Report EUR16683EN, 1996.

[4] Experimental investigation into the hydrodynamic performance of marine current turbines. Bahaj AS, Batten WMJ, Molland AF, Chaplin JR. Sustainable energy series, Report 3, University of Southampton, March 2005.

[5] Measurements and predictions of forces, pressures and cavitation on 2-D sections suitable for marine current turbines. Molland AF, Bahaj AS, Chaplin JR, Batten WMJ. Proc Inst Mech Engrs M: J Eng Maritime Environ 2004;218(2):127–38.

[6] Viscous-Inviscid Analysis of Transonic and Low Reynolds Number Airfoils. Drela M and Giles MB, 1987. AIAA Journal, 25(10): 1347-1355.

[7] Development of a design tool for tidal current turbines. McCann G and Rawlinson-Smith R. Proceedings of 6th European wave and tidal energy conference, Glasgow, 289-294.

[8] Experimental verifications of numerical predictions for the hydrodynamic performance of horizontal axis marine

current turbine. A.S. Bahaj, W.M.J Batten, G McCann. Sustainable Energy Series, Report No. 3, Southampton University.
[9] Simulated electrical power potential harnessed by marine current turbine arrays in the Alderney Race. Myers LE and Bahaj AS, 2005. Renewable Energy, 30(11): 1713-1731.
[10] Langtry RB, Menter FR. Overview of Industrial Transition Modeling in CFX. Technical Report, ANSYS 2006.
[11] Profile investigations on a rotating airscrew. Himmelskamp H. MAP Volkenrode. Reports and Translation 1947; No. 832.
[12] A study on stall-delay for horizontal axis wind turbine. Hu D, Hua O, Du Z. Renewable Energy 2006; 31:821-836.
[13] Fluid mechanics fifth edition. John F. Douglas, Janusz M. Gasiorek. 2005.
[14] Aerodynamics of Wind Turbines. Martin O. L. Hansen. 2000.

Prognosis of Rudder Cavitation Risk in Ship Operation

Lars Greitsch, TUHH, Hamburg/Germany, lars.greitsch@tu-harburg.de

1 Introduction

In the course of increase of the requirements, the necessity of more precise rudder cavitation forecasts becomes obvious. Especially for vessels with alternating operation conditions (e.g. short sea shipping) the design conditions are not easy to define. The practice of performing model tests is not able to cover the influence of the occurring operation conditions. Therefore the following approach gives an opportunity to benchmark different rudder designs regarding cavitation in the expected operation conditions. The rudder design itself can be improved by optimising the shape of the rudder sections. Therefore a method of determining similar flow conditions for the different rudder sections is presented. The following work identifies with three different design stages the opportunities of modern rudder design.

2 Rudder in Ship's Operation

For determining the occurring conditions for the rudder the measurements of six months of ship's operation have been analysed. This led to about 12.000 data points, each of them representing the average value of 30 minutes of measurement. For estimating the operation conditions of the rudder the measured rudder angles and ship speeds have been transferred to frequency distributions and cumulative density distributions as seen in figure 1 and figure 2.

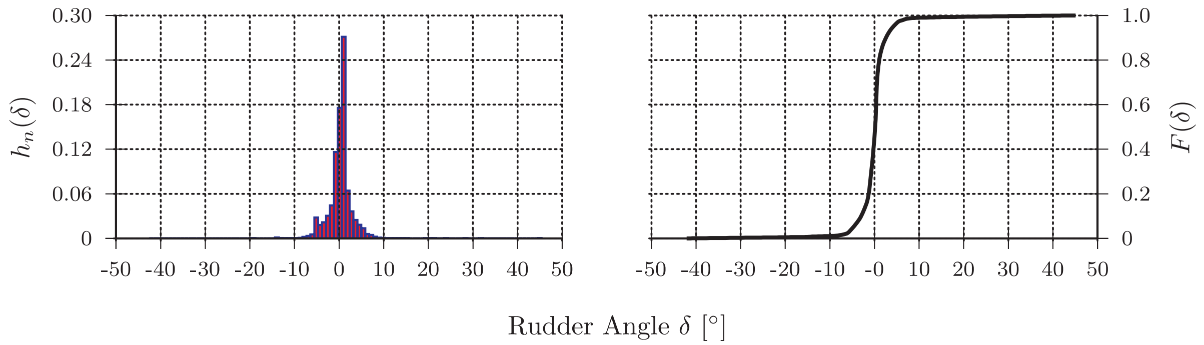

Fig.1: Frequency Distribution and Cumulative Density of Rudder Angles

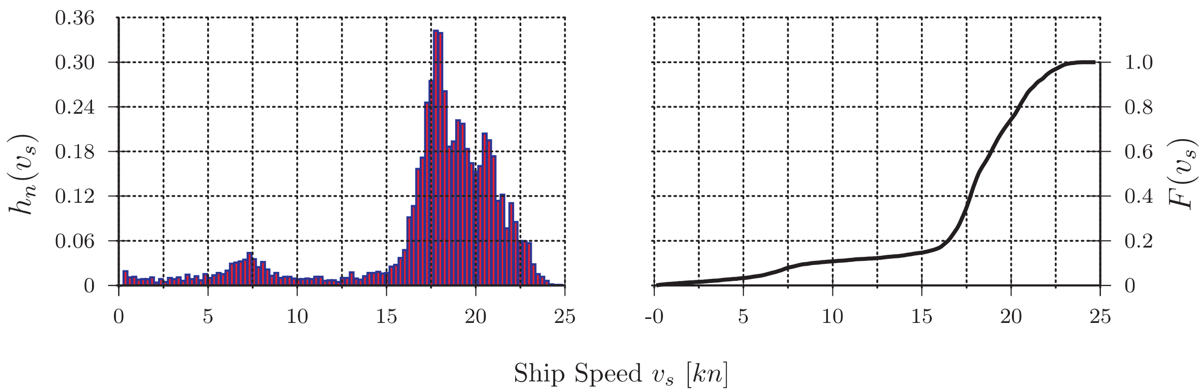

Fig.2: Frequency Distribution and Cumulative Density of Ship Speeds

Considering the frequency distributions of rudder angles and vessel speeds it is noticable that the rudder angles are Gaussian distributed as expected. On the other hand the vessel sails most of the time with average speed values about 5 knots below design speed. In addition there is a small cumulation of occurred vessel speeds in the range of 7,5 knots, which indicates slow speed manoeuvring.

In this first development status of this rudder design procedure the frequency distribution and cumulative density function of rudder angles or vessel speeds result from the measurements. In our further work the values of rudder angles and ship speeds indicating the operation conditions will result from course keeping calculations based on the cumulative density function for specific parameters regarding shipping routes and vessel types (e.g. sea state, wind, draft, etc.). The relation between frequency and cumulative density distribution is given in equation (1).

$$F(\delta) = \sum_{\delta_i \leq \delta} h_n(\delta) \tag{1}$$

In the following work the focus is put on a new rudder design procedure and the calculation of the cavitation risk for different rudder versions based on the described measurements.

3 Hydrodynamic Calculations

The cavitation prognosis is carried out with a panel code based on the potential flow theory. This allows very fast calculations and therefore the analysis of the large number of observed operation cases in a finite time period. The used CFD code takes in account the wake field of the observed vessel and the propeller slipstream calculated with the lifting line method. An example of a calculated pressure distribution on the rudder geometry is given in figure 3. The cavitation is calculated by comparing the local pressure with the vapour pressure of the passing water at the observed location. There is no difference made between higher and lower pressure gradients. The interpretation of the results is carried out by a cavitation coefficient c_{cav} as a saltus function which has the value 0 for non-cavitating situations of this panel and the value 1 in case of cavitation on the observed panel.

In order to benchmark the cavitation risk for different regions on the rudder the cavitation occurrence on each panel is weighted by the frequency of the operation situation. This leads to a safety against cavitation S_{cav} for each panel:

$$S_{cav} = 1 - \sum_{i=1}^{n} (c_{cav,i} \cdot h_n(\delta_i) \cdot h_n(v_{s,i})) \tag{2}$$

A value of $S_{cav} = 1$ specifies a 100 percent safety against cavitation for the observed panel in the range of operation situations. Resulting from the saltus function there can be be no safety greater than 1. In the same manner a value of $S_{cav} = 0$ indicates, that the observed panel would cavitate in all operation situations.

4 Rudder Shape Optimisation

The technical description of rudder geometries is carried out by defining constructional sections for certain rudder heights. The conventional rudder design is characterised by constant symmetric profile shapes for all rudder sections. Regarding the inhomogeneous propeller wake more modern rudder designs use asymmetric profiles for avoiding high flow velocities at the leading edge. This can be achieved by an alignment of the profiles along the streamlines to obtain an almost shock free flow around the leading edge of the profile. The inclination toward the streamlines is fulfilled either by using profiles with cambered mean lines or by inclining only the leading edge of the profile up to a certain ratio of the chord length. In the case of the twisted rudder design versions presented in 5 the inclination is optimised by diversifying the twist angle and the length of cambered mean line. The pressure distribution of the optimised profile should lead to a smaller value of the pressure minimum c_{min} according to the amount.

The optimising of the profiles for the different constructional sections is based on pressure distributions calculated by the airfoil theory. The section-wise analysis of flow conditions and design of new profile shapes is valid by reason that the flow around the rudder even in the propeller slipstream has only insignificant velocity components in direction of the span as seen in figure 3.

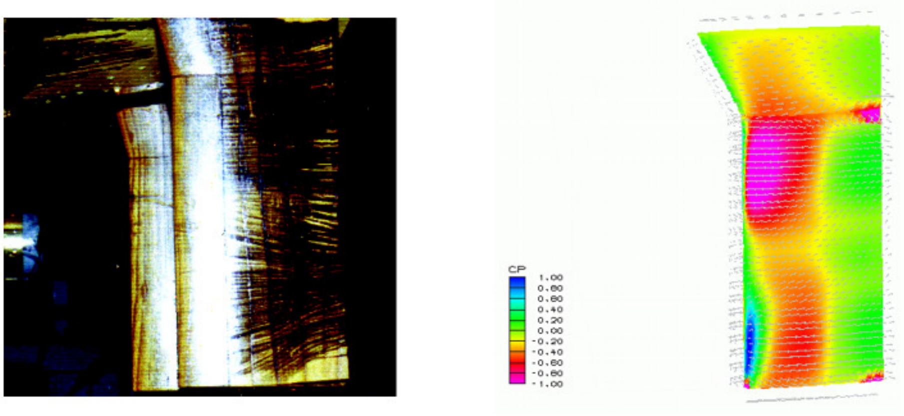

Fig.3: Paint flow test and calculated pressure distribution

In case of optimising the shape of foils with the aid of the profile theory, there is to keep in mind that the flow around the two-dimensional profile differs from the flow around a section of the three-dimensional rudder geometry. In contrast to the 3D-calculations, the calculation in terms of the profile theory does not cover either the finite span or the influence of hull, wake field and propeller slipstream. So there is to define an equivalent flow. Our approach defines the equivalent flow on base of equivalent pressure distributions.

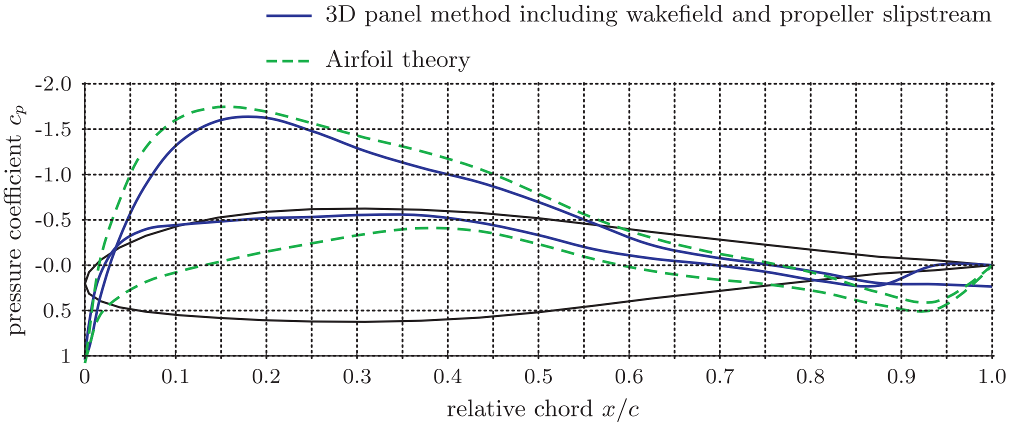

Fig.4: Equivalent Flow

The task is to find a combination of reference speed and angle of attack where the two-dimensional calculation leads to equivalent pressure coefficients as the three-dimensional calculation at the considered rudder section. The criterion for equivalent flow conditions is found by the method of least squares. An example for the comparison of the pressure coefficients of two-dimensional and three-dimensional case is shown in figure 4.

With the identified pairs of angle of attacks and inflow speeds for the equivalent flow the inflow conditions for the profiles of each constructional section now consider even three-dimensional effects like span and hull influence. A comparison of the angle of attack α along the rudder height is given in figure 5. The difference between the distributions of α affect the inclination of the rudder design.

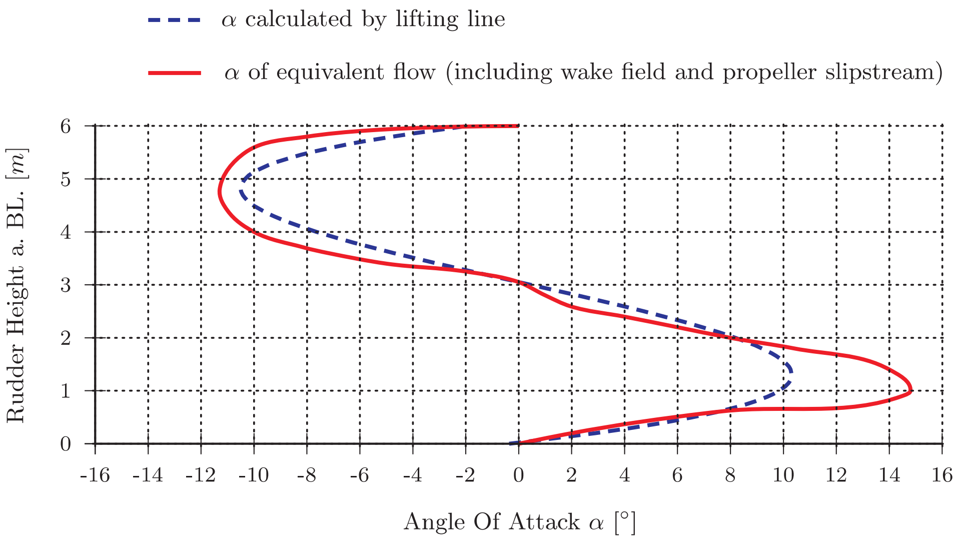

Fig.5: Inflow Conditions

5 Results

According to the rudder shape optimisation procedure three different rudder designs have been investigated (figure 6). The first design is a non-twisted rudder with Costa propulsion bulb in agreement with the classification rules. The second design step is a twisted rudder where the inclination of the profile sections is optimised for inflow conditions calculated by the lifting line method. The third and final rudder design is a twisted rudder as well, but the optimisation of the inclination of the leading edge is based on the inflow conditions gained by the method of equivalent flow.

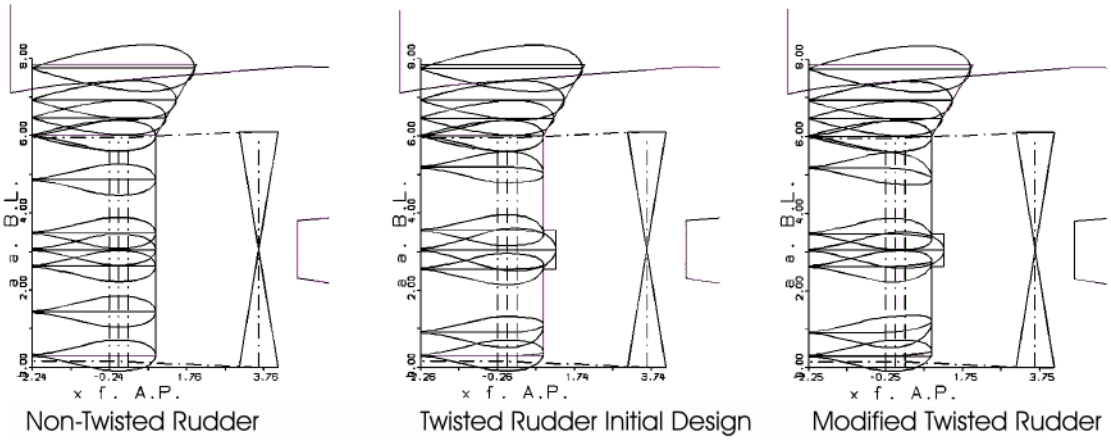

Non-Twisted Rudder

Twisted Rudder Initial Design

Modified Twisted Rudder

Fig.6: Observed Rudder Designs

The profiles for the design sections of all rudder versions are derived from the profile type HSVA MP-73 of the Hamburg Ship Model Basin. The profile type and the maximum relative thickness $t_{max}/c = 25\%$ for the different sections is the same for all design versions. Only the inclination angle and the length of the uncambered meanline differ.

The calculation of the cavitation risk for the different rudder versions was carried out by determining the cavitating panels for 625 different combinations of rudder angles and ship speeds. The results shown in figures 7 to 9 are based on the definition of the cavitation risk described above (see:3).

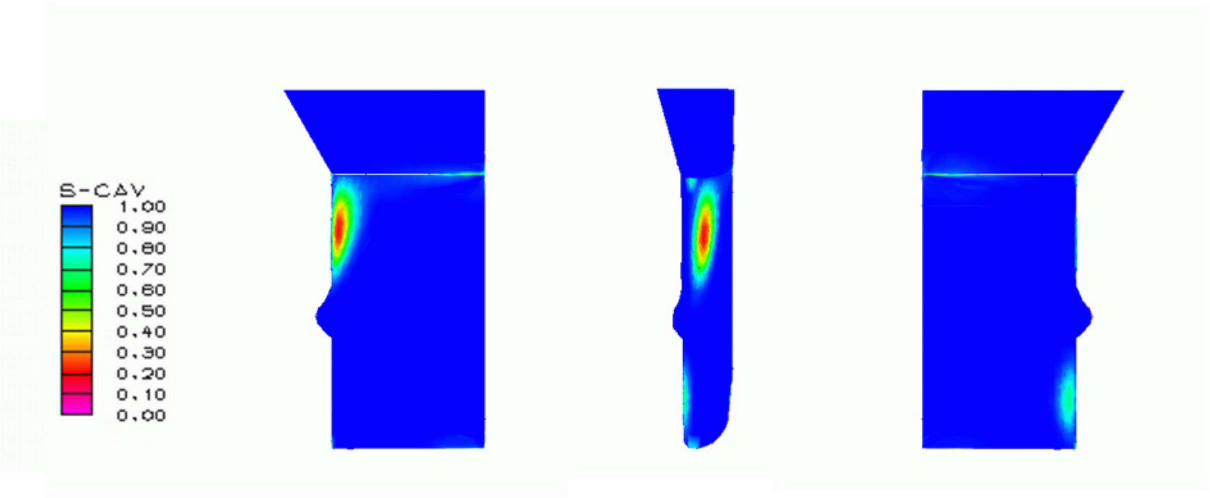

Fig.7: Cavitation risk for non-twisted rudder

In the case of the non-twisted rudder, the influence of the rotation of the propeller slipstream on the pressure distribution is obvious. At the leading edge both below and above the Costa bulb there are regions with a high cavitation risk. Because of the lower static pressure the risk of cavitation at the head is increased. This critical rudder zone cavitates in 80 percent of the operation situations.

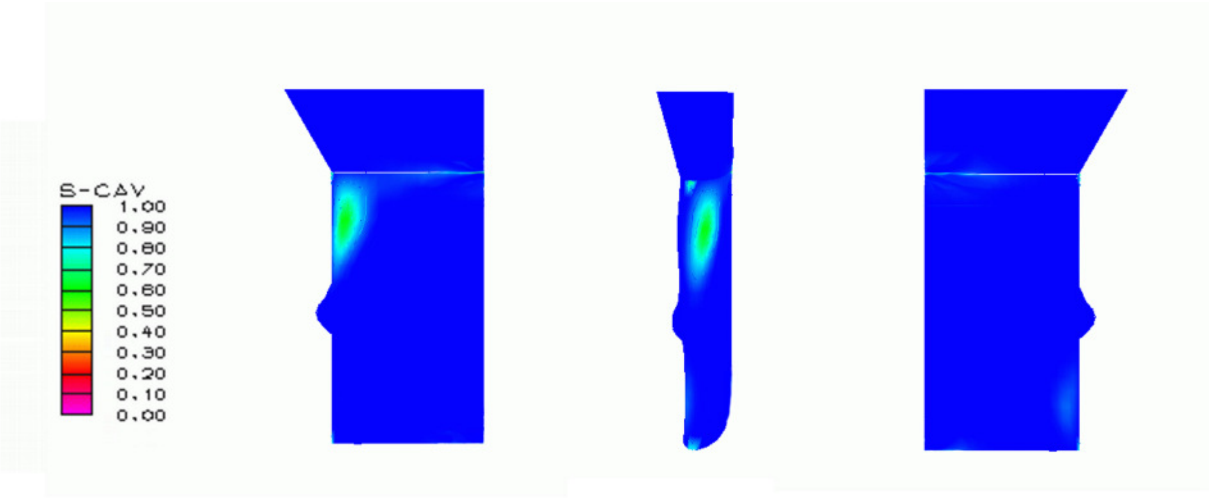

Fig.8: Cavitation risk for twisted rudder - initial design

The second design version with the twisted sections shows a lower cavitation risk at the critical zone, but even in this case the region cavitates in about 40 percent of the calculated situations.

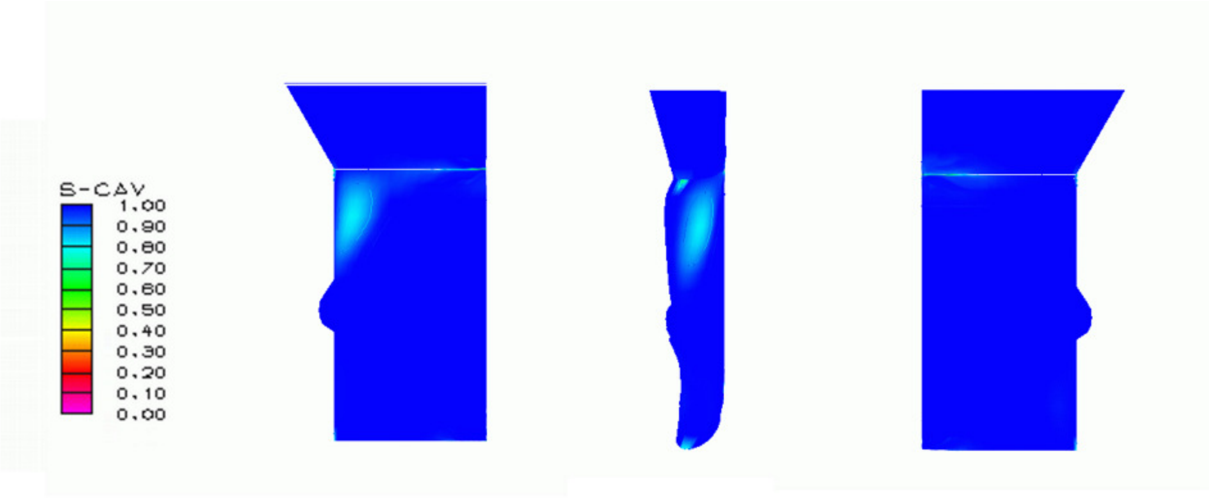

Fig.9: Cavitation risk for the modified twisted rudder

After optimising the profiles corresponding to the inflow conditions of the equivalent flow, the risk of cavitation is reduced to 20 percent of the operation cases. This is quite acceptable, in particular due to the conservative cavitation criterion based on the comparison with the vapour pressure.

6 Conclusion

A route based rudder design procedure has been developed. Therefore a criterion for benchmarking different rudders for a set of operation conditions has been introduced. Based on measured data three different rudder designs have been compared.

For optimising the profiles a new method allows the determining of the occurring inflow conditions based on equivalent pressure distributions. This leads to changed inflow conditions compared with the conventional procedure with the lifting line method. The optimisation based on these new inflow conditions leads to a rudder shape with much more safety against cavitation.

References

KRÜGER, S. (2002), *Kavitation an Halbschweberudern schneller Fähren*, TU Hamburg Harburg, Technical Report

SÖDING, H. (1998), *Limits of Potential Theory in Rudder Flow Predictions*, Ship Technology Research, Vol. 45.3, TU Hamburg Harburg

KRÜGER, S. (1998), *A Panel Method for Predicting Ship-Propeller Interaction in Potential Flow*, Ship Technology Research, Vol. 45.3, TU Hamburg Harburg

SCHLICHTING, H.; TRUCKENBRODT, E. (1959), *Aerodynamik des Flugzeuges*, Springer-Verlag, Berlin

Numerical Simulations of Cavitating Flow Around a 2D Hydrofoil Using OpenFOAM and FLUENT

N-X Lu, N Berchiche, R E Bensow

Department of Shipping and Marine Technology,
Chalmers University of Technology,
SE 412 96 Gothenburg, Sweden

Email: naixian.lu@chalmers.se

1. Introduction

Cavitation is defined as the phenomenon of formation of vapour bubbles of a flowing liquid in a region where the pressure of the liquid falls below its vapour pressure. It often has negative effects such as performance degradation in turbomachinery, hydroturbines and propulsion systems, noise and vibration, and cavitation erosion. Therefore, research on cavitation is of particular interest in marine and hydropower industries. Although cavitation tunnel experiments can offer straight-forward visualizations of the occurring phenomena, measurable quantities are quite limited. Benefited from the development of powerful computers, more physics can be incorporated into the models, making it possible to model cavitation behavior in a physically more realistic manner. Comparing with non-cavitating flow, extra consideration should be given to two main problems when computing the cavitating flow, the phase interface and the mass transfer from one phase to the other.

Available computational tools at hand are open source solver OpenFOAM and commercial codes FLUENT. Hence, a verification exercise with respect to the examination of cavitation modeling rises up by itself. In the work presented hereafter, both non-cavitating and cavitating flow conditions are compared between the two codes. In FLUENT, Reynolds Averaged Navier Stokes approach was carried out for modeling the flow where a RNG k-ε model with standard wall function was applied, cavitating flow modeling was taken care by Singhal model. Results from OpenFOAM are obtained by implementing Large Eddy Simulation (LES) methodology and cavitation was modeled by Kunz' mass transfer model.

The test case performed is the flow around a two dimensional (2D) NACA0015 hydrofoil at 6° angle of attack. Reynolds number is 1.2×10^6 and cavitation number is 1. It is a simple geometry and simple flow thereby limiting effects of complex flow phenomena etc. Although experiments using this foil is planned, validation against experimental data is out of the working scope since comparison between different solvers is more of interest at this stage and 2D LES is on the other hand quite questionable. However, since 2D computations are very fast and the parameters of the models can be varied for better understanding of their effects, compromise is made.

2. Flow Modelling

The governing equations of an incompressible flow consist of the balance equations of mass and momentum for a linear viscous (or Newtonian) fluid,

$$\partial_t(v) + \nabla\cdot(v\otimes v) = -\frac{\nabla p}{\rho} + \nabla\cdot S,\ \nabla\cdot v = 0 \qquad (1)$$

where v is the velocity, p the pressure, $S = 2\nu D$ the viscous stress tensor, $D = \frac{1}{2}\left(\nabla v + \nabla v^T\right)$ the rate-of strain tensor and ν the kinematic viscosity.

2.1 Reynolds Averaged Navier Stokes

The most commonly used turbulence modeling approach in industry today is based on Reynolds-Averaged Navier Stokes (RANS) equtions, which sorts out the fluctuations of the instantaneous flow by introducing a statistically modeled Reynolds stress into the time-averaged equations.

$$\begin{cases} \nabla\cdot\langle v\rangle = 0 \\ \partial_t\langle v\rangle + \nabla\cdot\left(\langle v\rangle\otimes\langle v\rangle\right) = -\dfrac{\nabla\langle p\rangle}{\rho} + \nabla\cdot\left(\langle S\rangle + R\right) \end{cases} \qquad (2)$$

where $\langle\bullet\rangle$ denotes the time-average and $R = -\langle v\otimes v\rangle$ is the Reynolds stress tensor giving the effect of the fluctuations on the mean flow. To close the RANS equations (2) and to describe the Reynolds stresses, a statistical turbulence model is used. This model is often a combination of algebraic and transport equations relating the turbulence parameters to the flow variables. To this end, R is often modeled using the Boussinesq hypothesis $R = 2\nu_t\langle D\rangle_D$, where $\nu_t = \nu_t(k,\varepsilon)$ is the turbulent eddy-viscosity and $\langle D\rangle$ the mean rate-of-strain tensor, k is the turbulent kinetic energy and ε is its dissipation rate. From dimensional analysis, $\nu_t = c_\mu k^2/\varepsilon$, with c_μ as a model coefficient that may be a function of the flow. There are also a number of models based on other quantities, such as k and the specific dissipation rate ω. In this work, a RNG k-ε model with standard wall function is used.

2.2 Large Eddy Simulation

Although RANS correctly predicts the mean flow in many cases, it is less precise when facing more complex flows, or when applied to flows dominated by unsteady effects. Large Eddy Simulation (LES) is an alternative approach to RANS under the demand of more accurate and detailed flow information. The basic idea of LES is to filter the Navier Stokes equations (NSE) using an anisotropic kernel, G, which is usually based on the grid size. This kernel splits the flow into two regimes, resolved large grid scales and modeled small subgrid-scales. Large energy containing eddies are computed directly since they are flow and geometry dependent, therefore it gives LES more generality than RANS although at the expense of higher computational resources. Subgrid-scale details, on the other hand, are of less importance as long as sufficient dissipation is produced to emulate the subgrid turbulence and to stabilize the simulation.

By applying low-pass filtering to NSE, using a pre-defined filter kernel function $G = G(x,\Delta)$, the LES equations are derived as:

$$\begin{cases} \nabla \cdot \bar{v} = m_1 \\ \partial_t(\bar{v}) + \nabla \cdot \overline{(v \otimes v)} = -\nabla \bar{p} + \nabla \cdot (\bar{S} - B) + m_2 \end{cases} \quad (3)$$

where the over-bar denotes the low-pass filtered dependent variables. $B = (\overline{v \otimes v} - \bar{v} \otimes \bar{v})$ is the subgrid stress tensor, representing the influence of the small, unresolved eddy scales on the larger, resolved flow scales. The commutation error terms, $m_1 = \nabla \cdot \bar{v} - \overline{\nabla \cdot v}$ and $m_2 = \nabla \cdot (\overline{v \otimes v}) - \overline{\nabla \cdot (v \otimes v)} + \nabla \bar{p} - \overline{\nabla p} - \nabla \cdot \bar{S} + \overline{\nabla \cdot S}$ are expected to be significantly smaller than the subgrid terms therefore these terms will be set to zero.

Present approaches to model the unclosed subgrid stress tensor B can broadly be classified as functional or structural models. Functional models try to reproduce the effects of the small, unresolved scales on the resolved ones. Structual models, on the other hand, aim at predicting the subgrid flow (or the subgrid stress tensor) directly and mimic the kinetic energy cascade from large to small scales, rather than only recovering their effects on the resolved scales. Another way of dealing with the energy cascade from large scales is to use implicit diffusion where it is considered that the action of the subgrid scale is equivalent to a strictly dissipative action. This is achieved by letting the leading order truncation error in the discretization of the fluxes emulate the energy dissipation. [2] In this work the One Equation Eddy Viscosity Model (OEEVM) [1] is implemented.

3. Modelling of Cavitating Flow

3.1 Singhal Model in FLUENT

The cavitation model of FLUENT is based on the so-called “full cavitation model” developed by Singhal et al but unlike the original approach assuming single-phase, the cavitation model in FLUENT involves two phases (liquid and vapour) and a certain fraction of separately modeled non-condensable gases, whose mass fraction is known in advance. Both bubble formation (evaporation) and collapse (condensation) are taken into account in the model.

The continuity equation and momentum equation for the mixture of the three are

$$\partial_t(\rho_m) + \nabla \cdot (\rho_m \vec{v}_m) = 0 \quad (4)$$

$$\partial_t(\rho_m \vec{v}_m) + \nabla \cdot (\rho_m \vec{v}_m \vec{v}_m) = -\nabla p + \nabla \cdot \left[\mu_m \left(\nabla \vec{v}_m + \nabla \vec{v}_m^T\right)\right]$$
$$+\rho_m \vec{g} + \vec{F} + \nabla \cdot \left(\sum_{k=1}^{n} \alpha_k \rho_k \vec{v}_{dr,k} \vec{v}_{dr,k}\right) \quad (5)$$

where $\vec{v}_m$ is the mass-averaged velocity $\vec{v}_m = \frac{\sum_{k=1}^{n} \alpha_k \rho_k \vec{v}_k}{\rho_m}$ and ρ_m is the mixture density $\rho_m = \sum_{k=1}^{n} \alpha_k \rho_k$, α_k is the volume fraction of phase k, n is the number of phases, and μ_m is the viscosity of the mixture $\mu_m = \sum_{k=1}^{n} \alpha_k \mu_k$. $\vec{v}_{dr,k}$ is the drift velocity for secondary phase k: $\vec{v}_{dr,k} = \vec{v}_k - \vec{v}_m$.

A vapour transport equation governs the vapor mass fraction f, given by

$$\partial_t(\rho f) + \nabla(\rho \vec{v}_v f) = \nabla(\gamma \nabla f) + R_e - R_c \quad (6)$$

$\rho = \alpha_v \rho_v + \alpha_g \rho_g + (1 - \alpha_v - \alpha_g)\rho_l$ is the mixture density where ρ_l ρ_v and ρ_g are the densities of the liquid , the vapor and the non-condensable gases. $\vec{v}_v$ is the velocity vector of the vapor phase, γ is the effective exchange coefficient, and R_e and R_c are the vapor generation and condensation rate terms (or phase change rates). The rates are functions of the instantaneous, local static pressure. [3]

3.2 Kunz’ Mass Transfer Model in OpenFOAM

In OpenFOAM, the phase interface is taken care of using a Volume of Fluid (VOF) approach, where the interface is tracked using a volume fraction equation. The mass transfer process is modeled by some mass transfer model which is incorporated in the Navier-Stokes equations (NSE) as a source terms in the continuity equation and the volume fraction equation since the mass transfer occurs at length scales that are not supported by the continuum assumption.

By incorporating the transport equation for the volume fraction into the filtered equations of continuity and momentum,

$$\begin{cases} \nabla \cdot \bar{v} = 0 \\ \partial_t\left(\rho \bar{v}\right) + \nabla \cdot \left(\rho \bar{v} \otimes \bar{v}\right) = -\nabla \bar{p} + \nabla \cdot \rho\left(\bar{S} - B\right) \\ \partial_t \gamma + \nabla \cdot \bar{v}\gamma = 0 \end{cases} \tag{7}$$

where *γ=volume liquid/total volume* is the liquid volume equation fraction, with γ=1 corresponding to pure water. It is defined as

$$\gamma = \lim_{\delta \to 0} \frac{\delta V_l}{\delta V_l + \delta V_v} \tag{8}$$

and is used to scale the physical properties of vapour and liquid as

$$\begin{cases} \rho = \gamma \rho_l + (1-\gamma)\rho_v \\ \mu = \gamma \mu_l + (1-\gamma)\mu_v \end{cases} \tag{9}$$

Alternatively, the vapour volume fraction *α=volume vapour/total volume*, defined as

$$\alpha = \lim_{\delta \to 0} \frac{\delta V_v}{\delta V_v + \delta V_l} \tag{10}$$

can be used, where now α=1 corresponds to pure vapour, and solved with an identical transport equation $\partial_t \alpha + \nabla \cdot \bar{v}\alpha = 0$,yielding

$$\begin{cases} \rho = \alpha \rho_v + (1-\alpha)\rho_l \\ \mu = \alpha \mu_v + (1-\alpha)\mu_l \end{cases} \tag{11}$$

When the flow starts to cavitate a source term is needed in equation (7) to account for production and destruction of vapour. Moreover, the flow will no longer be divergence free, and consequently a source term, S_p, is needed also in the continuity equation. To find an expression for this source term, the transport equation for the volume fraction can be used. The source term in the volume fraction equation will be equal to the phase transfer rate

$$\begin{cases} \partial_t \alpha + \nabla \cdot \bar{v}\alpha = -\dfrac{\dot{m}}{\rho_v} \\ \partial_t \gamma + \nabla \cdot \bar{v}\gamma = \dfrac{\dot{m}}{\rho_l} \end{cases} \tag{12}$$

where $\dot{m}$ is the specific mass transfer rate. Using that γ+α=1, we can sum equation (12_1) and (12_2) which gives the source term

$$S_p = \left(\rho_l^{-1} - \rho_v^{-1}\right)\dot{m} \tag{13}$$

The bulk density for liquid and vapour, ρ_l and ρ_v, are kept constant throughout the computation. Now all that is needed to finalize the mass transfer modeling is to find an expression for the mass transfer rate $\dot{m}$. The mass transfer model used in the present work is primarily inspired by the work of Kunz (Kunz, 2000).

Kunz' mass transfer model for cavitating liquid

The mass transfer in this model is based on two different strategies, as compared to most similar models which only rely on a single strategy for both creation and destruction of vapour. The destruction of liquid, or creation of vapour, $\dot{m}^+$, is modeled to be proportional to the amount by which the pressure is below the vapour pressure and the destruction of vapour $\dot{m}^-$ is based on a third order polynomial function of the volume fraction *γ=volume liquid/total volume*

$$\begin{cases} \dot{m}^+ = \left(C_{prod} / U_\infty^2 t_\infty\right)\rho_v / \rho_l \cdot \gamma \min\left[0, \bar{p} - p_v\right] \\ \dot{m}^- = \left(C_{dest} / t_\infty\right)\rho_v \cdot \gamma^2\left[1-\gamma\right] \end{cases} \tag{14}$$

where the specific mass transfer rate is computed as $\dot{m} = \dot{m}^+ + \dot{m}^-$, $\bar{p}$ is the filtered pressure, p_v is the vaporization pressure and C_{prod}, C_{dest}, U_∞ and t_∞ are empirical constants based on the mean flow. As all properties within the parenthesis in equation (11) are constants and combining them into a single constant gives the mass transfer terms as

$$\begin{cases} \dot{m}^+ = A^+ \rho_v / \rho_l \cdot \gamma \min\left[0, \bar{p} - p_v\right] \\ \dot{m}^- = A^- \rho_v \cdot \gamma^2\left[1-\gamma\right] \end{cases} \tag{15}$$

Now A^+ and $A^-$are the only two constants of the model. This shows that vaporization occurs when the pressure is below the vapour pressure and there exist some liquid to vaporize, while condensation is restricted to the surface of the cavity with a maximum at γ=2/3. [2]

4. Computational Configuration

4.1 Geometry and numerical grid

With the chord length c=200mm. the NACA0015 profile is rotated 6° around the center of gravity and set in the domain of 1400 x 570 mm, extending 2 chord lengths ahead of the leading edge, ending 4 chord lengths behind the trailing edge (in relation to 0° angle of attack) and with a vertical extent reflecting the size of the cavitation tunnel where the foil will be tested. The grid is a C-grid type consisting in 41923 cells. *Figure 1* shows a close-up view of the grid around the foil.

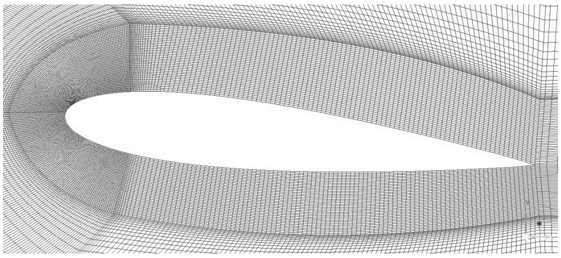

Figure 1 Grid around the wing

The boundary conditions were set as follow: a fixed value velocity, 6m/s was implemented at the inlet, a pressure outlet at the downstream boundary, and symmetry conditions for the upper and lower boundaries of the domain.

5. Computational Results

In this section, results of the wetted flow and cavitating flow calculations with a cavitation number $\sigma=1$ are presented. The aim of these computations is to compare the computed cavitation patterns (cavity size, shedding frequency) and the general behavior of re-entrant jet. Cavitating flow simulations were started from fully wetted flow.

In OpenFOAM, One Equation Eddy Viscosity Model (OEEVM) is employed for the LES subgrid model. Values of all the nodes are resolved to the wall. Time step was set to be 1e-05s. The outlet pressure was 0 Pa and vaporization pressure was -18000 Pa. In Kunz' cavitation model, the vaporization constant A^+ was set to be 1e+07, and the condensation constant A^- to be 1e+02. The cavitation source was implied on the NSE in 100 time steps.

In FLUENT, a RNG k-ε model with standard wall function was applied. Unsteady RANS computations were carried out and time step was set to be 1e-04s. The RNG k-ε model with standard wall functions is used. The amount of non-condensable gas (NCG) mass fraction was set to 2e-06. [4] The outlet pressure was 20335.4Pa and vaporization pressure to be 2367.8Pa.

5.1 Non-cavitating flow

Figure 2 presents the pressure coefficient distributions obtained by OpenFOAM and FLUENT along the wing before the flow starts to cavitate. The two curves show consistency with each other.

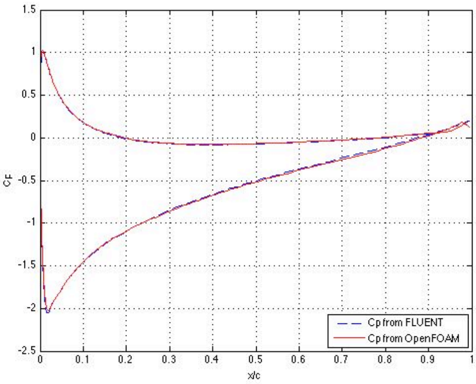

Figure 2 Pressure coefficient distribution for wetted flow

5.2 Cavitating flow

5.2.1 General behavior

Many interesting features of cavitating flow are captured by the computations, such as re-entrant jets and periodic shedding. A sequence of instantaneous vapour volume fraction illustrating the periodic shedding of cavitation is presented in *Figure 3* and *Figure 4*. The minimum threshold of the vapour volume fraction is set to 0.1.

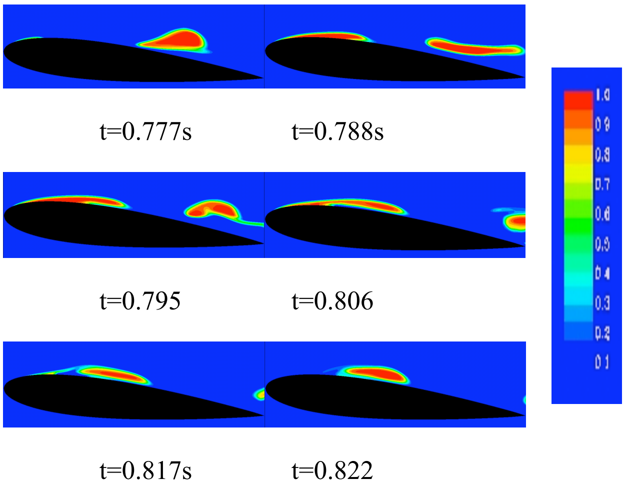

t=0.777s t=0.788s

t=0.795 t=0.806

t=0.817s t=0.822

Figure 3: Development of cavities simulated by OpenFOAM

A sheet cavity starts at the leading edge, whereby the cavity is transported along the surface of the foil and when it exceeds a certain size, it becomes unstable and sheds periodically. This process is controlled by a re-entrant jet which is forming downstream of the cavity and travels in the opposite direction to the outer flow towards the leading edge. The re-entrant jet cuts the cavity resulting in a shedding of cloud cavitation which is transported with the free stream towards the trailing edge.

Results from OpenFOAM show that for some cycles, the re-entrant jet seems to appear before the cavity has reached its maximum length, an example illustrating this behavior is shown in *Figure 3*: at t=0.788s, a sheet cavity has already developed at the leading edge. In the next time frame t=0.795s, the cavity has grown and the re-entrant jet is already visible at the rear end of the cavity. The cavity continues to extend in the following time frame while the re-entrant jet keeps its motion in the opposite direction until it finally cuts the cavity at t=0.817s. It is noticeable that the shape and development of the sheet cavity from OpenFOAM is quite different from one cycle to another.

The early development of the re-entrant jet before the cavity reaches its maximum length has not been observed in FLUENT simulation as it is the case in OpenFOAM. Another observation is that the cavities are bigger in shape generally for all cycles than OpenFOAM predicted result. *Figure 4* illustrates the development of the cavity in one cycle.

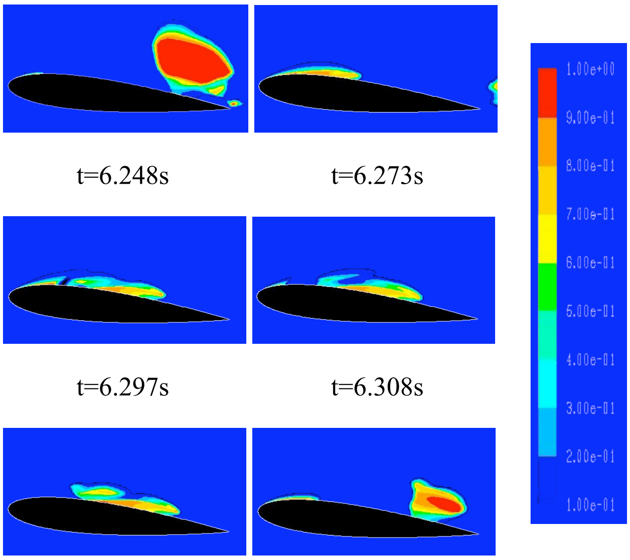

t=6.248s t=6.273s

t=6.297s t=6.308s

t=6.317s t=6.348s

Figure 4: Development of cavities simulated by FLUENT

5.2.2 Cavitating flow patterns

The values of cavity length L_{cav}, and shedding frequency f_{cav} presented in the below table are the averaged values of 10 cycles.

Cavity Patterns	OpenFOAM	FLUENT
L_{cav}/C	0.436	0.515
f_{cav} (Hz)	21.73	16.75

Table 1 Cavity Patterns computed by OpenFOAM and FLUENT

The model constants are crucial in terms of the shape and development of cavities. Although comparisons between cavity patterns obtained by different model constants were not shown in this report, visual comparison shows that the cavity shape is quite sensible to the constant values.

6. Conclusions and Discussions

In non-cavitating conditions, the calculated flow fields are in good consistency between the two codes which is expected since LES and RANS should have less difference when dealing with stable flows. For cavitating flow, the cavities obtained by OpenFOAM are rather sharply defined compared to those predicted in FLUENT. Re-entrant jet has a tendency of earlier development in OpenFOAM before the cavity has reached its maximum length and that might be the reason why the shedding frequency is higher and cavity length is smaller in OpenFOAM.

However, since the cavitating flow field is largely dominated by the model constants, production and destruction terms of vapour in OpenFOAM, and the non-condensable gas mass fraction in FLUENT. The comparison between the two codes needs to be further investigated by implementing different combinations of the constants.

Reference:

[1] Schumann U., 1975, Subgrid scale model for finite difference simulation of turbulent flows in plane channels and annuli, *J.Comp. Phys.*, 18, p376

[2] T. Huuva, 2008, Large eddy simulation of cavitating and non-cavitating flow, Thesis for the degree of Doctor of Philosophy

[3] Fluent 6.3 User's Guide

[4] N. Berchiche and G. Bark, 2006, Numerical studies of cavitating flows around 2D foils, VIRTUE EU-Project Report

Influence of the near wall treatment on the flow features around a two-dimensional hydrofoil close to the free surface

Andrea Califano (`califano@ntnu.no`)
Rolls-Royce University Technology Center 'Performance in a Seaway'
Norwegian University of Science and Technology - Trondheim, Norway

1 Introduction

This work was performed in the framework of a numerical study aiming at modeling the ventilation phenomenon, which has been recognized to be important for marine screws, rudders and submerged hydrofoils (see experiments by Nishiyama, 1961; Shiba, 1953; Koushan, 2006). The present analysis focuses on the validation and verification of the solver adopted in the case of a two-dimensional hydrofoil close to the free surface.
This problem has caught much attention after the experiments carried out by Duncan (1983), who observed breaking and non-breaking waves over a hydrofoil model and measured the free-surface profile. Several authors have attempted to reproduce Duncan's experiments using different numerical approaches. Among them, the inviscid BEMs by Landrini et al. (1999) and Faltinsen and Semenov (2008) have reproduced accurately the experimental results until breaking occurs. The following flow evolution can not be handled by potential flow solvers. RANS simulations capture the correct form of the wave and are intrinsically able to handle breaking waves, but tend to under-predict the wave amplitude. Some authors have better captured spilling breakers (Rhee and Stern, 2002; Muscari and Di Mascio, 2003) implementing a breaking-wave model based on empirical data (Cointe and Tulin, 1994).

Two cases are studied here, chosen among those tested by Duncan (1983), corresponding to a breaking and a non-breaking wave condition. As depicted in Figure 1, a NACA0012 foil at incidence of 5 deg with a chord length $c = 0.203$ m is fixed in water at a submergence $h = 0.261$ m and 0.185 m, subject to an incident current $U = 0.8$ m/s. The bottom of the tank is located 0.175 m below the foil, as in the experiments.

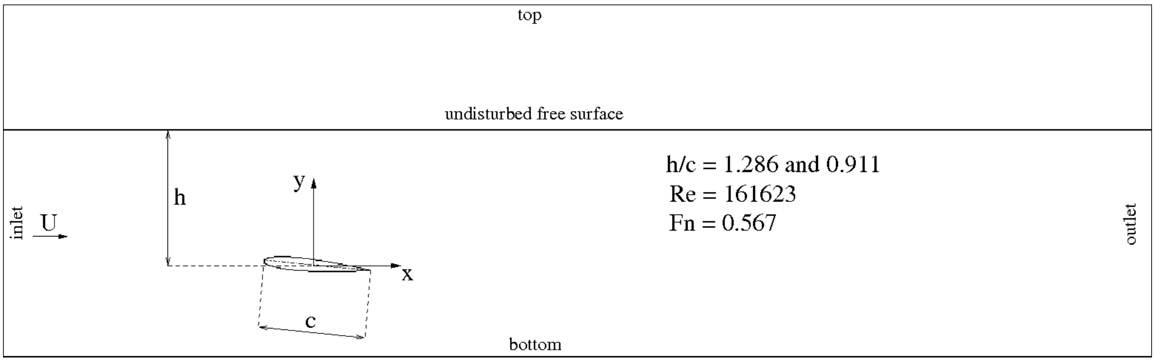

Figure 1: Numerical domain and definition of main parameters

2 Numerical method

The described problem is solved assuming a viscous, incompressible, two-phase (air and water) flow. The commercial RANS code Fluent (2006) has been used for the computations.
The momentum equation and those for the turbulence closure are solved with a second order upwind scheme. The Body Force Weighted discretization algorithm is used to interpolate the node values of the pressure from the cell values, as required by the solver. The pressure-velocity coupling is achieved using a SIMPLE algorithm. In order to capture possible unsteadiness of the flow, a time-dependent approach is chosen using a first order implicit scheme. The free surface evolution is handled using an implicit formulation of the Volume Of Fluid method with a modified High Resolution Interface Capturing scheme.

Further details about the solver can be found in the Fluent manual (Fluent, 2006).

Boundary conditions The undisturbed free surface elevation is assigned both at the inlet and outlet boundaries. At the inlet the free stream velocity is also specified. A zero flux of all quantities is enforced across the top and bottom boundaries. Unless otherwise specified, a no-slip condition on the hydrofoil is set.

Grid The domain is divided in blocks allowing refinements in the near wall region, around the wake and across the free surface, as depicted in Figure 2a. A close up of the near wall mesh region is shown in Figure 2b.

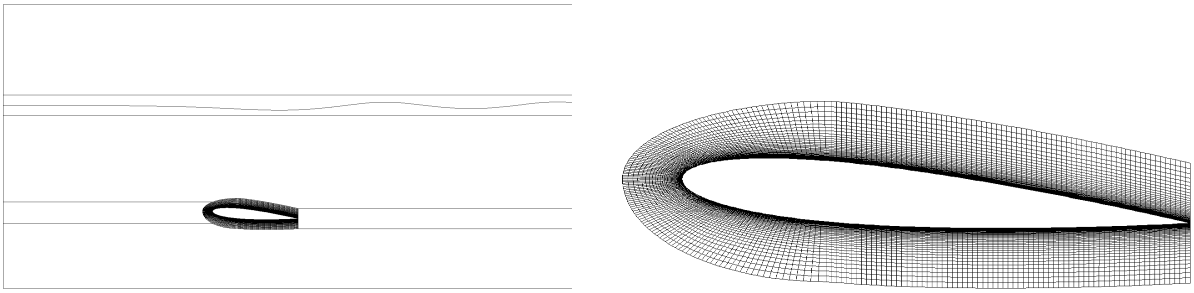

(a) Multiblock domain

(b) Near wall mesh

Figure 2: Multiblock domain and near wall mesh

A convergence analysis has been carried out in three manners, refining the grid (i) in the whole domain but in the near wall region, (ii) locally near the free surface and (iii) in the near wall region of the hydrofoil shown in Figure 2b. The results from (i) and (ii) did not show any significant change in the amplitude of the free surface waves, whereas the results from (iii) highlighted an effect on the solution, as discussed in Section 3. For this last case (iii) four levels of grid refinement were used, as given in Table 1. The first wall cell of the coarse grid lies within the log layer of the boundary layer, whereas all the three fine meshes are within the sub-viscous layer.

grid	**y/c ($\cdot$1E-04)**	**y$^+$**
coarse	141.4	50
fine	5.8	4
2fine	2.7	0.75
3fine	1.4	0.35

Table 1: Near wall region grid refinement

Turbulence model The near-wall region is modelled with Standard Wall Function for the coarse grid, whereas for the three fine grids the viscosity-affected region is resolved with a mesh all the way to the wall, including the viscous sub-layer.

Two models have been employed for the turbulence closure, the realizable k-ϵ (Shih et al., 1995) and the SST k-ω (Menter, 1994) model. The k-ϵ model is robust and widely used in different kinds of fluid flows. The SST k-ω model is a variation of the standard k-ω model (Wilcox, 2004) incorporating modifications for low-Reynolds-number effects, compressibility, and shear flow spreading. It is widely used in lifting surfaces such as foils and propellers.

In order to assess the numerical damping in the field solver an inviscid simulation was attempted. A stable solution for the very fine wall refinement could not be achieved so, as an approximation of inviscid conditions, the flow was assumed laminar with a fictitious molecular viscosity in water μ_{fict} small relative to the physical one μ (μ_{fict}/μ = 7E-04). This was combined with a free-slip condition at the foil, in order to approach the inviscid behavior. In the following this solution will be recalled as 'inviscid'.

In order to check the influence of the wall boundary condition on the turbulence model, two simulations were performed using free-slip condition on the wall, (a) with the SST k-ω model and (b) with laminar flow.

3 Results

The results obtained for the submergence ratios *h/c* = 1.286 and *h/c* = 0.911 are discussed in the following section.

h/c = 1.286 Figure 3a shows the free-surface deformation along the free-stream direction, as predicted by the present solver with a SST k-ω turbulence model. The wave behavior is captured already by the *coarse* mesh, but the wave amplitude is underestimated. The under-predicted wave amplitude was widely found in other RANS simulations (Mori and Shin, 1988; Hino, 1997; Rhee and Stern, 2002; Muscari and Di Mascio, 2003) and could be attributed to the under-prediction of the suction side pressure. Using a finer near wall mesh improves the accuracy up to the *2fine* mesh, for which a mesh independent solution is achieved. Figure 4b shows the comparison between the converged results and the experiments by Duncan (1983). The solutions of the BEM by Landrini et al. (1999) and the RANS solver by Rhee and Stern (2002) are also reported, the latter being performed using a SST k-ω turbulence model. The improvement of the present solution in terms of wave-height with respect to the RANS simulation by Rhee and Stern (2002) could be ascribed to a greater refinement in the near wall region, but no sufficient details are given in Rhee and Stern to assess it. Among the three numerical solvers, the BEM by Landrini et al. (1999) gives the best results and reproduces correctly the experiments.

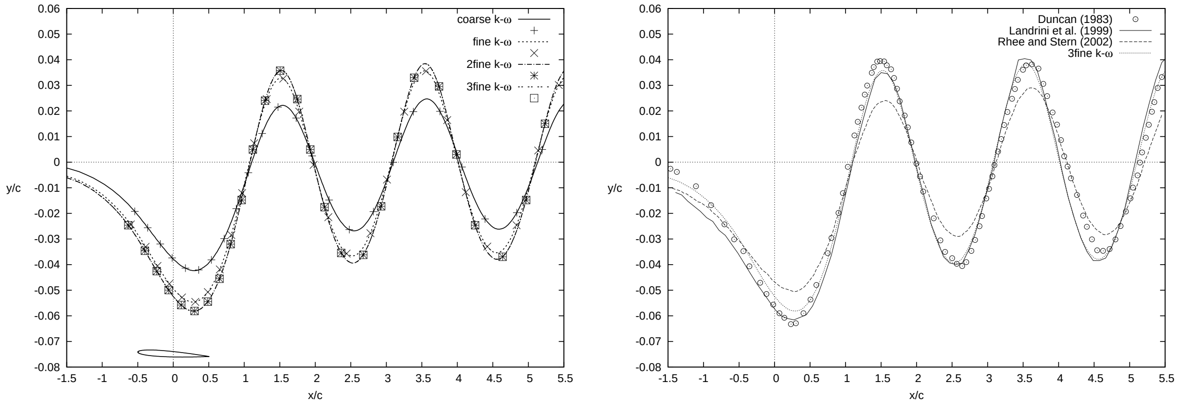

(a) Present results

(b) Comparison of *3fine* grid with available data

Figure 3: Free-surface deformation (h/c = 1.286, SST k-ω turbulence model)

Figure 4 gives the same variable, but present results have been obtained with the realizable k-ϵ turbulence model. Figure 4b shows a larger under-prediction of the wave amplitude, which suggests that the k-ϵ model is more diffusive than the k-ω model.

From Figure 4a, using a *fine* near wall mesh improves the accuracy, but further refinements confirm a mesh independent solution. Tzabiras (1997) has simulated an experiment by Duncan (1983) with submergence $h = 0.193$ m using a standard k-ϵ model with wall functions. The corresponding prediction of the free-surface characteristics are in satisfactory agreement with the measured data; the tested ranges of y^+, from 20 to 40, did not affect practically the results. Present analysis highlighted an effect of the near wall mesh size when resolving directly the boundary layer.

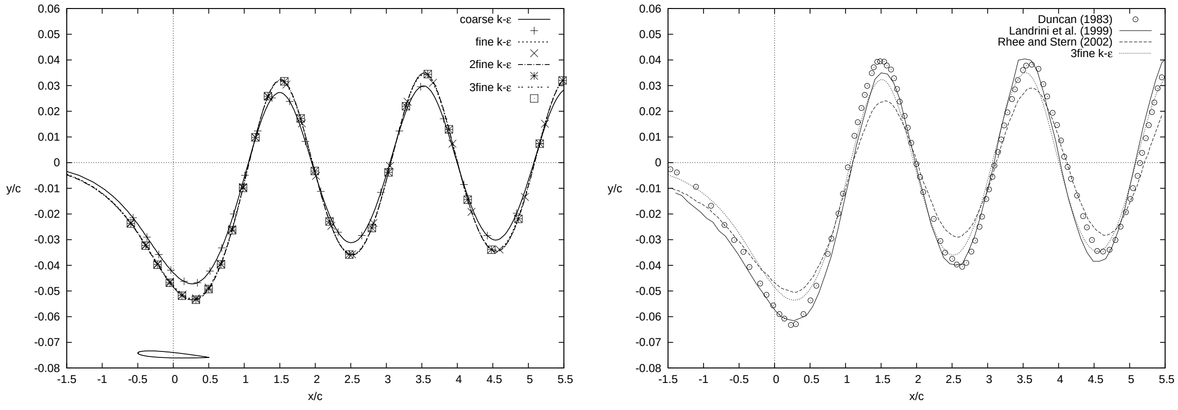

(a) Present results

(b) Comparison of *3fine* grid with available data

Figure 4: Free-surface deformation (h/c = 1.286, realizable k-ϵ turbulence model)

Figure 5 gives the results of the 'inviscid' solution and the SST k-ω simulation using a free-slip condition on the wall. Removing the no-slip condition from the turbulent flow improves the accuracy with respect to the

corresponding simulation with no-slip condition. The free-slip laminar solution coincides with the free-slip SST k-ω one, and thus has not be plotted. The 'inviscid' solution is the closest to the BEM results, which in turn match the corresponding experiments.
Adopting a turbulent formulation for the present problem, where the influence of the viscosity is negligible, affects significantly the accuracy of the results, by introducing diffusion terms.

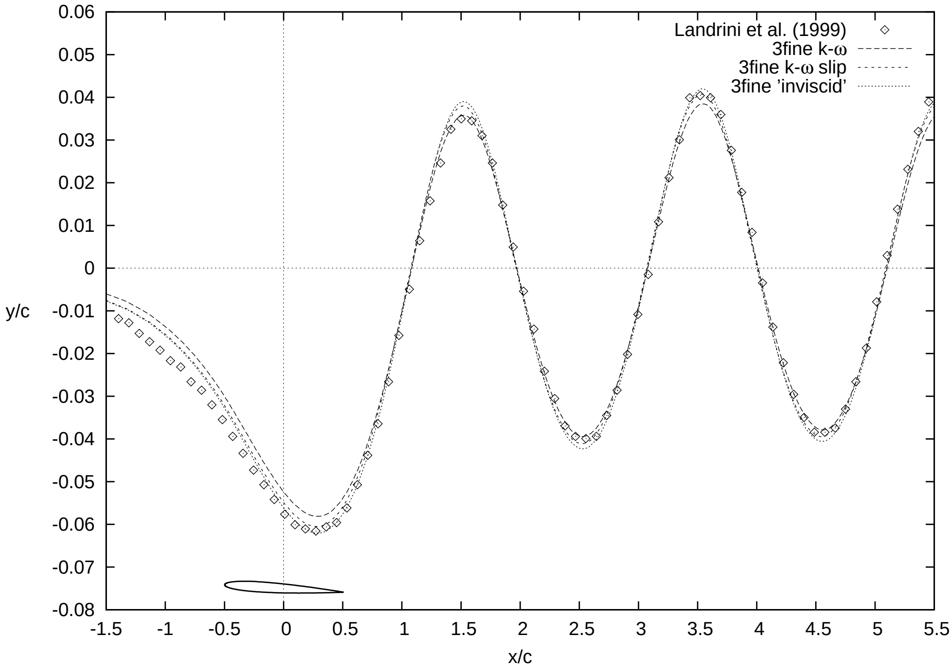

Figure 5: Free-surface deformation (h/c = 1.286, *3fine* mesh)

Table 2 summarizes the present results obtained for the first trough amplitude (Table 2a) and the lift coefficient (Table 2b), in terms of relative error with respect to the experiments and the BEM solution by Landrini et al. (1999), respectively. An increasing lift coefficient corresponds to a more accurate representation of the free surface. The advantages of using a SST k-ω turbulence model with a fine grid and the effect of different wall conditions are confirmed.

	k-ϵ	k-ω	k-ω **slip**	**'inviscid'**
coarse	-23.1%	-31.1%		
fine	-13.4%	-11.0%		
2fine	-13.4%	-5.4%		
3fine	-12.6%	-5.4%	-1.4%	1.0%

(a) First trough amplitude

	k-ϵ	k-ω	k-ω **slip**	**'inviscid'**
coarse	-25.7%	-38.1%		
fine	-12.7%	-11.4%		
2fine	-12.0%	-4.5%		
3fine	-11.7%	-2.3%	2.3%	5.6%

(b) Lift coefficient

Table 2: Relative error of the present solution with respect to the experiments (a) and the BEM solution (b)

h/c = 0.911 For this shallower submergence the experiments by Duncan (1983) show a clear spilling breaking-wave condition. Here it is not attempted to capture the fine details of spilling breakers described by Duncan (2001) and investigated by some authors (Muscari and Di Mascio, 2003; Rhee and Stern, 2002) also including an empirical breaking wave model. No breaking-wave model is adopted, while this more complex case is used to further test the adopted solver as it is.

The present converged unsteady simulation for the *2fine* mesh shows small oscillations of the forces on the hydrofoil and of the free surface, more pronounced around the breaking region, with a period 3.8*T*, where *T* is the period of a linear wave with the same phase speed as the breaker. A more accurate explicit simulation in time was performed obtaining the same oscillating behavior, whose maximum double amplitude could be quantified in 9% for the lift coefficient and 18% for the first trough amplitude, with respect to their corresponding mean values.

No oscillatory behavior is mentioned by Duncan (1983) in the case object of this study. However, Duncan (1981) observed small oscillation in the length of the breaking region while testing the same configuration, but

with a free-stream velocity slightly different, $U = 0.82$ m/s. The experiments showed an oscillation period of $3.9T$ and Duncan (1981) argued that the oscillations are due to wave components generated when the foil is started from rest. Qualitative observations showed that the amplitude of the oscillation decreased as the wave progressed.
The small amplitude of the oscillation recorded numerically in the present study is deemed as not affecting the speculation on the near wall treatment, but the performed analysis is not sufficient to state whether the oscillation detected by the code is physical or numerical, despite the consistency with observations by Duncan (1981).

Two extremes of these oscillations are shown in Figure 6, as representative of the minimum and maximum wave height detected. The present solution is compared with the experiments by Duncan (1983) and the RANS simulations by Muscari and Di Mascio (2003) and by Rhee and Stern (2002), the last two taken without the inclusion of a breaking wave modeling.

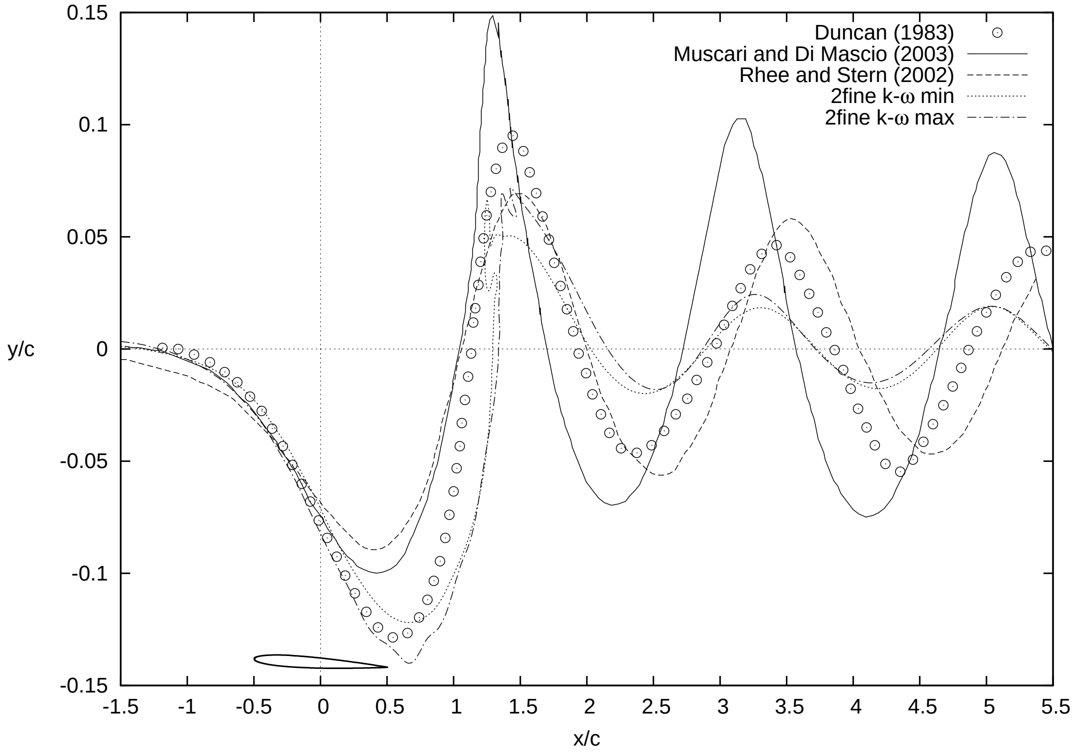

Figure 6: Free-surface deformation (h/c = 0.911, SST k-ω turbulence model)

All numerical results show a large deviation from the experimental data with respect to the non-breaking wave case, both in terms of wave amplitude and phase. The present study captures more accurately the first trough amplitude above the hydrofoil, embracing the corresponding experimental value between its two extremes. Despite this apparent improvement, the following wavetrain is under-predicted, and a thorough sensitivity analysis would be required to assess the influence of the main numerical parameters, as performed for the submergence ratio $h/c = 1.286$.

4 Concluding remarks

A two-dimensional hydrofoil close to the free surface has been simulated using the commercial RANS code Fluent (2006). Two submergences were considered, corresponding to a breaking and non-breaking condition of the wave behind the hydrofoil. The obtained results have been compared with experiments by Duncan (1983) and with three different numerical solvers.

The present converged viscous analysis of the non-breaking wave case shows a satisfactory agreement with the experimental results and the potential flow solution, both in terms of free surface deformation and lift coefficient. A sensitivity analysis has been performed in terms of (i) turbulence modeling, (ii) near wall grid size and (iii) boundary condition on the foil (free- and no-slip). This analysis shows that for such a problem, where viscosity is not dominant, the diffusion introduced by the solver affects significantly the accuracy of the results and care must be taken in treating the near wall region for a correct solution. The forces exerted by the foil are the key mechanism driving the deformation of the free-surface. The best viscous solution was achieved using the SST k-ω turbulence model (Menter, 1994) with convergence for $y^+ \simeq 0.75$.

A more complex case corresponding to a breaking wave condition was used to further test the adopted solver, as it is, without implementing a breaking-wave model. While the first trough amplitude is well captured for this shallower submergence, the breaking wave and the following wavetrain are under-predicted. This study confirms the results obtained for the non-breaking case in terms of first trough amplitude, whereas a correct evaluation of the following waves would require an accurate modeling of the breaker.

Acknowledgment The author gratefully acknowledges the Rolls-Royce University Technology Center in Trondheim for supporting the present research.
The discussion with Prof. M. Greco has been vital to the present work and is thankfully acknowledged.
This project was partially supported by the Norwegian HPC project NOTUR that granted access to its computer facilities.

References

Cointe, R. and Tulin, M. P. (1994). A theory of steady breakers. *Journal of Fluid Mechanics Digital Archive*, 276(-1):1–20.

Duncan, J. H. (1981). Experimental investigation of breaking waves produced by a towed hydrofoil. *Proceedings of The Royal Society of London, Series A: Mathematical and Physical Sciences*, 377(1770):331 – 348.

Duncan, J. H. (1983). Breaking and non-breaking wave resistance of a two-dimensional hydrofoil. *Journal of Fluid Mechanics*, 126:507 – 520.

Duncan, J. H. (2001). Spilling breakers. *Annual Review of Fluid Mechanics*, 33:519 – 547.

Faltinsen, O. M. and Semenov, Y. A. (2008). The effect of gravity and cavitation on a hydrofoil near the free surface. *Journal of Fluid Mechanics*, 597(-1):371–394.

Fluent (2006). *Fluent 6.3 User's Guide*. Fluent Inc.

Hino, T. (1997). An unstructured grid method for incompressible viscous flows with a free surface. In *35th Aerospace Sciences Meeting & Exhibit.*, number AIAA-97-0862.

Koushan, K. (2006). Dynamics of ventilated propeller blade loading on thrusters. In *World Maritime Technology Conference - WMTC'06*.

Landrini, M., Lugni, C., and Bertram, V. (1999). Numerical simulation of the unsteady flow past a hydrofoil. *Ship Technology Research*, 46(1):14 – 30.

Menter, F. (1994). Two-equation eddy-viscosity turbulence models for engineering applications. *AIAA Journal*, 32(8):1598 – 1605.

Mori, K. H. and Shin, M. S. (1988). Sub-breaking wave: Its characteristics, appearing condition and numerical simulation. In *Proceedings 17th Symposium on Naval Hydrodynamics*, The Hague, The Netherlands.

Muscari, R. and Di Mascio, A. (2003). A model for the simulation of steady spilling breaking waves. *Journal of Ship Research*, 47(1):13–23.

Nishiyama, H. (1961). Air-drawing and ventilating flow characteristics of shallowly submerged hydrofoil sections. *American Society of Naval Engineers – Journal*, 73(3):593 – 602.

Rhee, S. H. and Stern, F. (2002). Rans model for spilling breaking waves. *Journal of Fluids Engineering, Transactions of the ASME*, 124(2):424 – 432.

Shiba, H. (1953). Air-drawing of marine propellers. In *Report of Transportation Technical Research Institute*, volume 9. Unyu Gijutsu Kenkyujo.

Shih, T.-H., Liou, W. W., Shabbir, A., Yang, Z., and Zhu, J. (1995). New k-ϵ eddy viscosity model for high reynolds number turbulent flows. *Computers and Fluids*, 24(3):227 – 238.

Tzabiras, G. (1997). Numerical investigations of 2d, steady free surface flows. *International Journal for Numerical Methods in Fluids*, 25(5):567 – 598.

Wilcox, D. C. (2004). *Turbulence Modeling for CFD*. DCW Industries, Inc., 2nd edition.

WALL PRESSURE FLUCTUATIONS ON LIFTING BODIES IN TRANSIENT REGIMES

Antoine Ducoin, Jacques André Astolfi, François Deniset
Institut de Recherche de l'Ecole Navale EA 3634
Ecole Navale
29240 Brest Armées
France
Email: antoine.ducoin@ecole-navale.fr

Jean-François Sigrist,
DCNS Propulsion
44620, La Montagne
France
Email: jean-francois.sigrist@dcnsgroup.com

INTRODUCTION

The load prediction of lifting bodies such as rudders, stabilizers or marine propellers in forced motion of large amplitude is fundamental in the context of marine design. It requires a good understanding of phenomena such as transition, turbulence and stall ([1]). The knowledge of the pressure field distribution on the body and its evolution in time can then bring new elements in the understanding of the phenomena of dynamic loading. It includes the boundary layer study in forced unsteady regime which has always been the object of many researches, including its prediction in RANSE based codes in the context of industrial applications. [2] has shown the accuracy of RANSE codes to predict hydrodynamic loading in cases of low angles of incidence, and highlighted the turbulence model dependency when separation becomes high. This has been studied by [3] on a NACA0015 and a NACA0012. The influence of pitching velocities can be also of primary importance on loading prediction. This has been studied numerically by [4] in the case of low Reynlods numbers. Inertia effects are increasing with pitching velocities and the authors include non-dimensionnalized parameters useful in transient regimes which are performed in the present paper. An experimental study is presented in [5] for an oscillating airfoil at various reduced frequency and at $Re = 1.35 \times 10^5$. For small values of reduced frequencies, boundary layer events produce variations in lift, drag and moment coefficient. As well, it has some influence on boundary layer transition caused by laminar separation which is delayed and promoted when reduced frequency increase. The lift coefficient and lift-curve slope has also slight improvement but it has been shown that the laminar bubble length is insensitive to reduced frequency. Recent works focus on the impact of transition modeling in RANSE based codes([6], [7], [8]). It appears to have impact on stall and loading prediction. [9] show that fully turbulent computations over predict lift and drag. [6] include transition model and show the impact on hydrodynamic coefficient.

The present paper focuses on the spatio-temporal evolution of the wall pressure field of an hydrofoil arising from transient pitching motion at $Re = 0.75 \times 10^6$. Both experimental and numerical approaches has been developed. The experiment is based on the wall pressure measured by transducers on several points at the suction side of an hydrofoil. Computations are led with the CFD RANSE based code CFX.
The first aim of this study is a better understanding of hydrodynamic loading responses on flow phenomena like transition and of laminar separation induced transition. Another challenging task is to verify the accuracy of the RANS simulation to predict them, and to evaluate their limitations.

The flow is first studied in the case of a slow rotation velocity based on wall pressure near the leading edge and the trailing edge and numerical separation and transition localization on the hydrofoil. Then the influence of the 4 rotation velocities on the boundary layer events is analyzed with CFD results. Then Local wall pressures are integrated in order to define a suction side loading which will allow to compare measurement and calculation on the basis of a reconstructed hydrodynamic loading. The global numerical coefficient can then be analyzed and dynamic contribution of the pitching velocity is highlighted.

EXPERIMENTAL SET UP

Measurements are carried out in the cavitation tunnel at IRENav. The test section is 1 m long and has a 0.192m square section. It allows to control the velocity range between 0 and 15m/s and pressure range from 30 mbar to 3 bars.The hydrofoil is mounted horizontally in the tunnel test section. The chord is c=0.150 m and the span is b=0.191 m. The camber is about 2% to 50% from the leading edge(

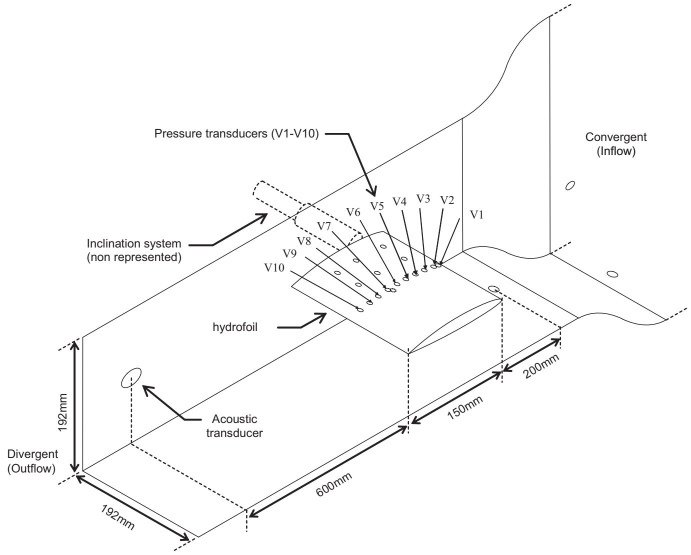

Figure 1. HYDROFOIL INSTRUMENTATION AND TUNNEL TEST SECTION

[10]).

Pressure measurements are carried out using seventeen piezo-resistive transducers (Keller AG 2 MI PAA100-075-010) of 10 bars maximum pressure. The pressure transducers are mounted into small cavities with a 0.5 mm diameter pinhole at the hydrofoil surface. The wall pressure spectrum measured by the transducer is attenuated from the theoretical cut off frequency $f_c = 9152 Hz$. Experiments are led with a sample frequency of f=20kHz.

The transducer locations are given in Figure 1. As shown, one set of ten transducers is aligned along the chord of length on the suction side, starting from the leading edge at reduced coordinate x/c=0.05 up to the trailing edge at coordinate x/c=0.90 with a step of 0.10 c from x/c=0.10.

Two sets of three transducers are arranged in parallel to this line in order to analyze three-dimensional effects. The transducers responses are found to be linear and the coefficients of the linear regression are used to convert Volts in Pascals. To control any deviation during the experiments, the calibration procedure is performed systematically before and after each series of measurements. Signals from the wall-pressure transducers are amplified and collected through a simultaneous sampling 16 channel, 16 bit A/D digitizer VXI HPE1432A, having maximum available sampling frequency of 51.2 kHz.

The nominal free stream velocity U_∞ was 5 m/s, corresponding to a Reynolds number based on the foil chord length of $Re = 0.75 \times 10^6$. The hydrofoil rotated about an axis located at 25% from the leading edge. The angle of incidence vary from $0°$ to $15°$ then come back to $0°$, with at least 2 periods of accelerations and 2 periods of deceleration.

As shown in figure **??**, four rotation velocities are defined, from a considered slow rotation velocity to a high rotation velocity.

The average rotation velocity is defined as:

$$\dot{\alpha} = 2\alpha_{max}/t_f \qquad (1)$$

with t_f the total time of transient motion. Let's introduce a similarity parameter based on the chord length c and the upstream velocity U_∞:

$$\dot{\alpha}^* = \frac{\dot{\alpha} \times c}{U_\infty} \qquad (2)$$

FLOW MODELING AND NUMERICAL RESOLUTION

The fluid problem is solved with the finite volume technique ([11]), using the CFD code CFX. Equations of mass and momentum are integrated over a control volume Ω_F of boundary $\partial\Omega_F$, using the Leibnitz rule and the Gauss theorem. It is then discretized using a finite volume method. The fluid domain is divided into elementary fluid cells, for which an integrated conservation equation is written. The time dependent terms are approximated by an Euler scheme, and convective and diffusive terms are calculated using finite difference approximations. Nodal values are computed with a high resolution upwind scheme.

Turbulence and transition modeling

The calculations are led with the CFD RANSE based code CFX. The $k-\omega SST$ model appears to be an accurate turbulence model for boundary layer detachment prediction ([12], [13], [14]).
The $k-\omega SST$ turbulence model is coupled with a transition model $\gamma - Re_\theta$ which uses experimental correlations based on local variables([15], [16], [17]). The model is based on two transport equations. The first one is for intermittency γ which triggers the transition process:

$$\frac{\partial(\varphi\gamma)}{\partial t} + \frac{\partial(\varphi v_j \gamma)}{\partial x_j} = P_\gamma + E_\gamma + \frac{\partial}{\partial x_j}\left[(\mu + \frac{\mu_t}{\sigma_f})\frac{\partial\gamma}{\partial x_j}\right] \qquad (3)$$

where P_γ and E_γ are the transition sources based on empirical correlations. μ_t is the friction velocity.

The transport equation for the transition momentum thickness Reynolds number $\overline{Re\theta_t}$ is given by:

$$\frac{\partial\left(\rho\overline{Re_{\theta t}}\right)}{\partial t} + \frac{\partial\left(\rho U_j \overline{Re_{\theta t}}\right)}{\partial x_j} = P_{\theta t} + \frac{\partial}{\partial x_j}\left[\sigma_{\theta t}\left(\mu + \mu_t\right)\frac{\partial\overline{Re_{\theta t}}}{\partial x_j}\right] \qquad (4)$$

with $P_{\theta t}$ a source term which force $\overline{Re_{\theta t}}$ to match the local value of $Re_{\theta t}$ based empirical correlation. $\sigma_{\theta t}$ is a source term diffusion control.
In this formulation, only local information is used to activate the production term in the intermittency equation. This

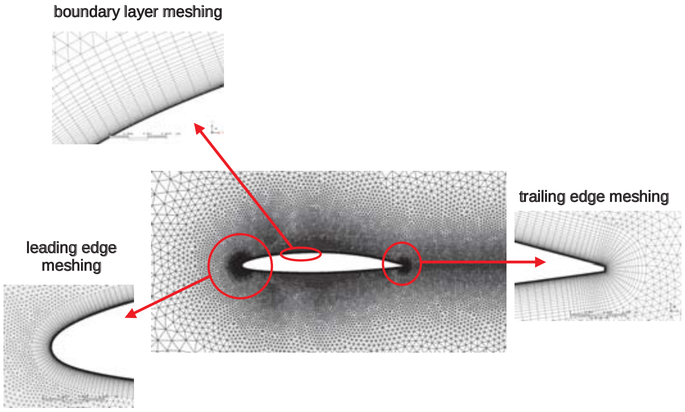

Figure 2. HYDROFOIL MESH

model allows to capture major transition effects and is accurate in the case of separation induced transition. The intermittency is modified to accept values larger that 1 at separation in order to have a correct transition length. Complete transition formulation is given in [17].

Boundary conditions and Discretization

The domain dimensions corresponds to the tunnel test section at IRENav. The ratio between the square section h and the chord length c is h/c=0.7. The inlet velocity is set to U=5m/s and the taken outlet reference pressure is set to 0. Symmetries conditions are set on horizontal wall and a no slip condition is imposed on the hydrofoil surface. Transients computations are initialized with a stationary converged computation. As shown in figure 2, the mesh is composed of 66,000 elements and 50 layers are used in the structured near wall zone. The other part of the domain is discretized with unstructured triangle elements. The boundary layer is discretized in order to satisfies $y^+ = \frac{yu_\tau}{\nu} = 1$. This ensure low Reynolds resolution. Mesh refinements is done at the leading edge, the trailing edge and in the wake. The hydrofoil motion is taken into account with boundary condition modification at wall. To do that, mesh coordinates are calculated at each time step and the whole domain is then meshed again. This technique used a diffusivity applied in the mesh displacement equation which induced a mesh stiffness([18], [19], [20]). This one is set to be inversely proportional to the wall distance in order to limit mesh distortion near the wall region. The Navier-Stokes equations are resolved in an arbitrary referential with the ALE formulation ([19]).

RESULTS AND DISCUSSION

Figure 3 shows a typically evolution of the measured pressure coefficient at x/c=0.3 during the transient motion from 0° to 15° compared to the computed one. As shown, there is a good agreement between the experimental and the numerical results except high frequency fluctuations which are not observed by the computation.

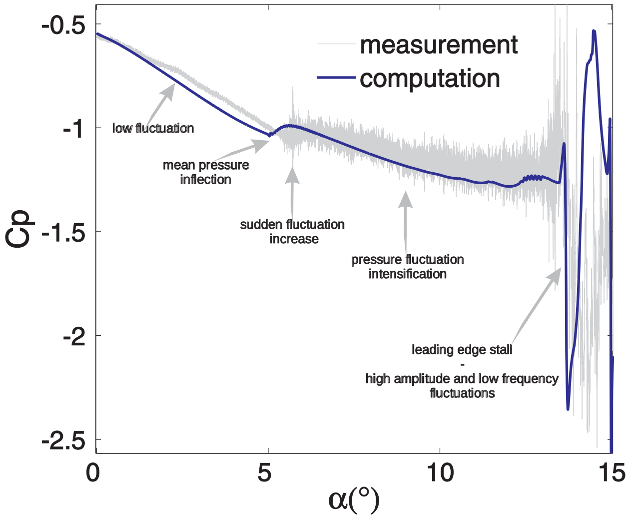

Figure 3. EXPERIMENTAL AND NUMERICAL PRESSURE COEFFICIENT AS FUNCTION OF THE ANGLE OF INCIDENCE AT x/c=0.3 DURING THE TRANSIENT MOTION

From 0° to 5°, the pressure decreases with low fluctuations. At 5°, the pressure stops to decrease and shows an inflection with a high level of fluctuations. Then the pressure continues to decrease with significant fluctuations, whose intensity increases from 6° to 13°. A more precise analysis has shown that these fluctuations are quasi-periodic and then can be related to vortex shedding downstream a laminar separation bubble as shown later. From 13° a strong pressure overshoot is observed, then low frequency fluctuations with large amplitude are observed resulting of stall. The relative complex characteristic of the wall pressure evolutions comes from the various features of the boundary layer flow during foil rotation.

Flow analysis

As an example, the flow is analyzed for the lowest pitching velocity $\dot{\alpha}^* = 0.18$. At 0°, a reversed flow is located at x/c=0.8 resulting from a Laminar Separation Bubble (LSB) inducing a transition to turbulent flow at reattachment. The displacement of LSB toward the leading edge zone is present up to 5°. At 5° the trailing edge LSB is replaced by a leading edge LSB. Then stall is observed at 13.3° with leading edge vortex shedding. A maximum under-pressure appears at $\alpha = 13.9°$. Then two contra-rotative vortices are shed from the trailing edge. This scenario is repeated periodically 3 times. A reverse scenario is observed during downward rotation of the hydrofoil.

Separation points and transition location have been located using wall shear stress equal 0. The transition point is defined as the reattachment turbulent point. Figure 4 summarizes the separations and transition location from α= 0° to 12° (before stall). The vertical axis is the x/c location on chord from leading edge (x/c=0) to trailing edge (x/c=1). The trailing edge separation point is located very close to the trailing edge for 0°, and moves slowly toward the leading edge when the angle of incidence increases. For $\alpha = 0°$ to $5°$ the two characteristics points (separation and reattachment) are between $(x/c)_{sep}$=0.85 to 0.69 and $(x/c)_{reattach}$=0.74 to 0.66. As a matter of fact, global length of LSB tends to decrease as α increases. At $\alpha = 5°$, the trailing edge LSB disappears and a shorter LSB induced by higher pressure gradient is formed at the leading edge which induces a sudden move of the transition location from x/c=0.65 to x/c=0.08. As well, the trailing edge separation suddenly moves from x/c=1 to x/c=0.9.

Figure 5 shows the experimental and computed wall pressure coefficient evolutions at x/c=0.8 **(a)** and x/c=0.3 **(b)**. First, wall pressure coefficient at x/c=0.8 shows a sudden increase at $\alpha = 2°$. According to figure 4, the LSB turbulent reattachment point is just passing up to this point at $\alpha = 2°$. Measurements show an increase of pressure fluctuations around this angle of incidence while a maximum is around $\alpha = 3°$. For both computation and measurement, there is a global pressure inflection at $\alpha = 5°$ as transition is passing near the leading edge. Figure 5 **(a)** and **(b)** show that the pressure fluctuations measured increase highly at this angle and continue to increase slowly up to $\alpha = 12°$.

At the same time, wall pressure on x/c=0.8 reaches a maximum value at $\alpha = 10°$ which corresponds to the trailing edge separation, see figure 4.

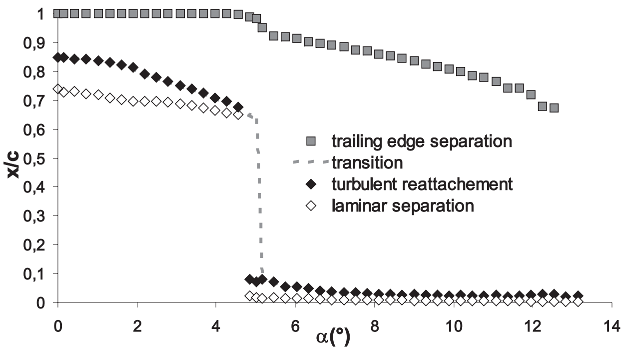

Figure 4. SEPARATION POINTS AND TRANSITION LOCATION AT SUCTION SIDE AS A FUNCTION OF THE ANGLE OF INCIDENCE

Dynamic effects of pitching velocity on boundary layer events

Figure 6(a) represents the transition and the trailing edge separation and Figure 6(b) the LSB length , for the considered pitching velocities. It is observed that transition is delayed when pitching velocity increases. Trailing edge separation point is delayed which induces a higher lift coefficient before stall. Pitching velocity does not have impact on the LSB size. Few variation appears when it formed (delayed with transition as shown on transition point location on chord) but from $\alpha = 7°$ to stall, bubble lengths are the same. This correlation agrees with the idea that high pitching velocities delayed the separation induced transition phenomenon whereas boundary layers thickness and separation length are conserved. All these points influences hydrodynamic loading of the foil.

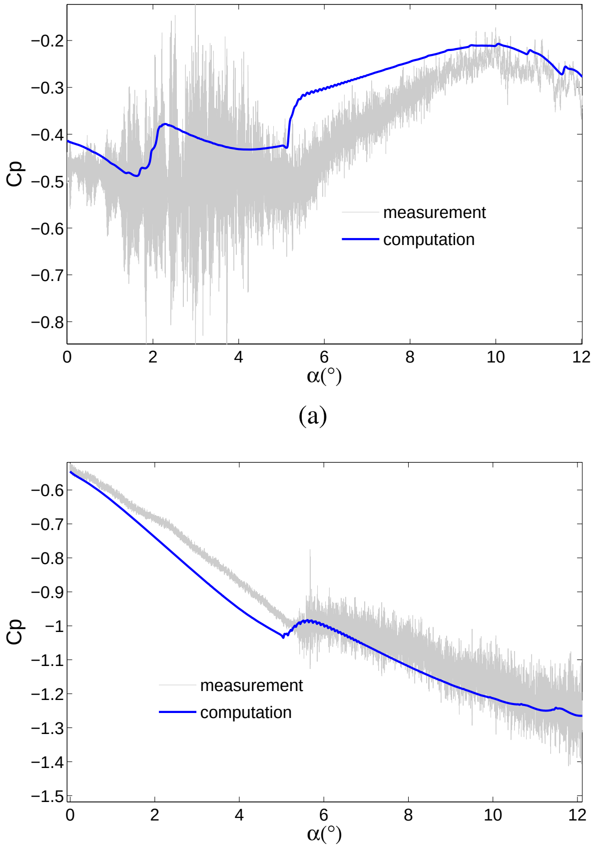

(a)

(b)

Figure 5. PRESSURE COEFFICIENT AT $\dot{\alpha}^* = 0.18$, α=0 to 12° BEFORE STALL: **(a)** x/c=0.8 AND **(b)** x/c=0.3 AS FUCTION OF THE ANGLE OF ATTACK

Suction side loading analysis

Based on available experimental data, an analysis of suction side loading can be done by summing pressure coefficient on the suction side. The approximation can be written as:

$$C_l^+(t) = \sum_{i=2}^{10} C_p(\frac{x_i}{c},t)\ \Delta(\frac{x_i}{c}) \tag{5}$$

where $C_p(\frac{x_i}{c},t)$ is the pressure coefficient at location $\frac{x_i}{c}$ and $\Delta(\frac{x_i}{c})$ is the non dimensional distance between two consecutive transducers. The procedure is applied to numerical data for comparison. Figure 7 shows the results obtained for the 4 rotation velocities. As shown, there is a good agreement between measurements and computations. The difference is very weak at the beginning of pitching and the inflection is accurately predicted by the transition model which appears at 5° for the lowest pitching velocity. It is delayed when pitching velocity increases and disappears even completely at the highest pitching motion for both approach. High amplitude fluctuations at low frequency induced by leading edge vortex shedding is over predicted by computation but starts at an angle of incidence very close to measurement.

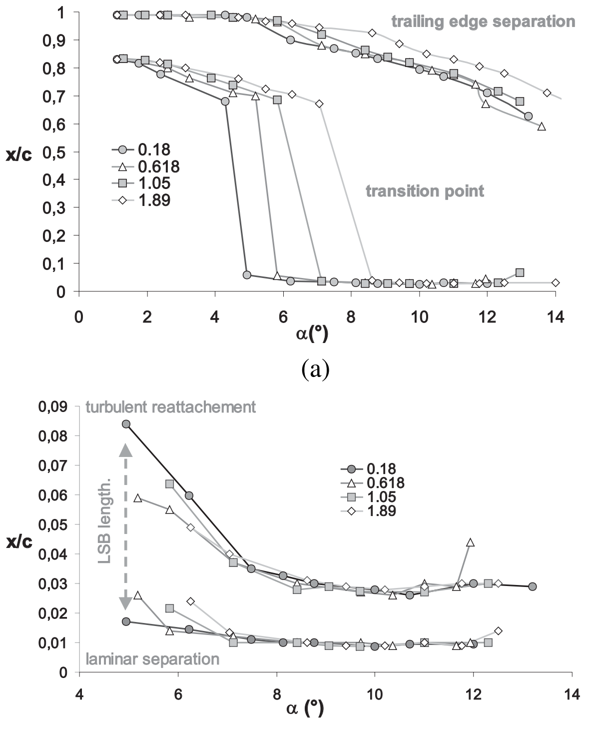

(a)

(b)

Figure 6. **(a)**: BOUNDARY LAYER SEPARATION AT LEADING EDGE AND TRANSITION LOCATION ON CHORD DURING PITCHING MOTION, **(b)**: LSB LENGTH AT LEADING EDGE FOR VARIOUS $\dot{\alpha}^*$

The return to 0° shows hysteresis induced by a delay in the reattachment. Again, computations agree well to measurements even if the model tends to over predict the loading when the pitching velocity increases.

Then it allows to analyze the influence of pitching velocity on global coefficients obtained by computations.

Dynamic effects: numerical lift coefficient

Figure 8 shows the numerical lift coefficient evolution as a function of the angle of incidence during pitching motions. Transition model appears to have a significant impact on lift when the rotation velocity is weak. An inflection is followed by a slope modification at 5° for $\dot{\alpha}^* = 0.18$ and 7° for $\dot{\alpha}^* = 1.05$ which tends to disappear for $\dot{\alpha}^* = 1.89$. Then lift amplitude before stall is higher at high velocities. Stall appear at 13.3° for the weakest velocity and is delayed at 14.4° for the highest velocity. It is shown that high lift fluctuations induced by leading edge vortex shedding appears at all pitching velocities, about three times for the weakest pitching velocity and one time for the other ones. The reattachment is also delayed with high velocities which induce hysteresis. As a consequence, lift evolution is symmetric for $\dot{\alpha}^* = 0.18$ where the reattachment is located for $C_L = 1.33$ whereas $C_L = 0.16$ for $\dot{\alpha}^* = 1.89$.

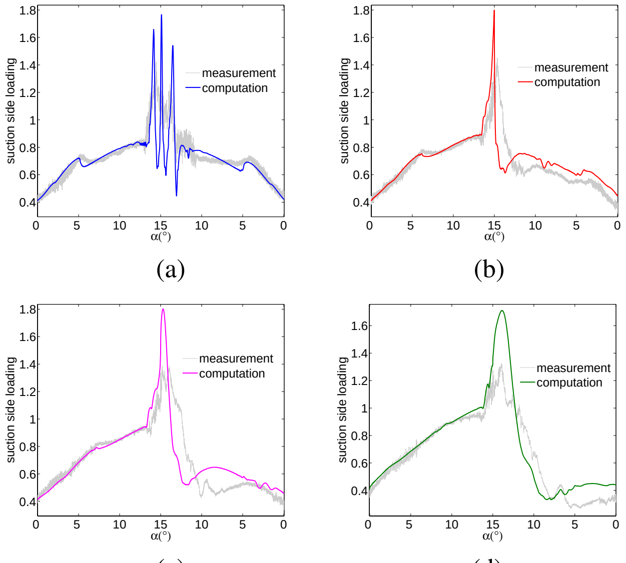

(a)

(b)

(c)

(d)

Figure 7. SUCTION SIDE LOADING DURING PITCHING MOTION: $\dot{\alpha}^* = 0.18$ **(a)**, $\dot{\alpha}^* = 0.618$ **(b)**, $\dot{\alpha}^* = 1.05$**(c)** AND $\dot{\alpha}^* = 1.89$ **(d)**

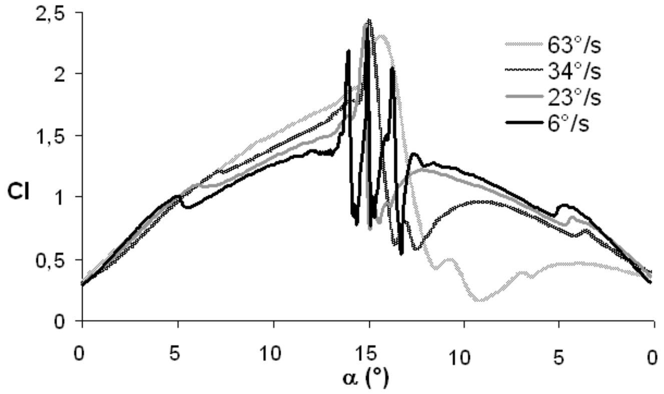

Figure 8. LIFT COEFFICIENT AS A FUNCTION OF THE ANGLE OF INCIDENCE, $0 - 15°$ AND RETURN TO $0°$, FOR 4 PITCHING VELOCITIES

CONCLUSION

The spatio-temporal evolution of the wall pressure field around an hydrofoil arising from a transient pitching motion at a $Re = 0.75 \times 10^6$ has been carried out for both experimental and numerical approaches. Four pitching velocities have been studied from a slow one $\dot{\alpha}^*$=0.18 to a high one $\dot{\alpha}^*$=1.89. The repartition of transducers location along the suction side of the hydrofoil at reduced coordinates from x/c=0.10 to x/c=0.90 with a step of 0.10 c has led to both global and local analysis.

Local wall pressure coefficients near the trailing edge at x/c=0.8 and near the leading edge at x/c=0.3 allow to know the transition behaviour. There is a good agreement between measurements and calculations. Trailing edge separation is accurately predicted in agreement with the lift inflection after that the boundary layer transition passes from the trailing edge toward the the leading edge. The author associates those fluctuations to vortex shedding of a laminar separation bubble. Based on the good agreements between experimental and numerical results, the influence of pitching velocity has been studied. Higher pitching velocities show a delay of transition and LSB length is constant. Suction side loading shows a good agreement between measurements and computations. Global effect of transition are accurately predicted by the RANSE code whereas wall pressure fluctuations are not captured. Numerical lift coefficients for the various pitching velocities highlight the impact of transition for slow motions which induces a significant lift coefficient slope modification at $\alpha = 5^\circ$. Higher pitching velocities has an impact on boundary layer transition effect on hydrofoil loading which induced a higher value before stall. During the the return step to $\alpha = 0^\circ$, an hysteresis effect induced by the massive stall is very marked for the highest velocity .

ACKNOWLEDGMENT

The authors gratefully acknowledge the technical staff of IRENav for its contribution to the experimental set up.

REFERENCES

[1] Triantafyllou, G., Triantafyllou, M., and Grosenbaugh, M., 1993. "Optimal thrust development in oscillating foils with application to fish propulsion.". *Journal of Fluids and Structures,* **7**(2), pp. 205–224.

[2] Srinivasan, G., Ekaterinaris, J., and McCroskey, W., 1995. *Evaluation of Turbulence Models for Unsteady Flows of an Oscillating Airfoil*. Pergamon; National Aeronautics and Space Administration; National Technical Information Service, distributor.

[3] Barakos, G., 2000. "Unsteady separated flows over manoeuvring lifting surfaces". *Philosophical Transactions: Mathematical, Physical and Engineering Sciences,* **358**(1777), pp. 3279–3291.

[4] Hamdani, H., and Sun, M., 2000. "Aerodynamic forces and flow structures of an airfoil in some unsteady motions at small Reynolds number". *Acta Mechanica,* **145**(1), pp. 173–187.

[5] Lee, T., and Gerontakos, P., 2004. "Investigation of flow over an oscillating airfoil". *Journal of Fluid Mechanics,* **512**, pp. 313–341.

[6] Shelton, A., Abras, J., Hathaway, B., Sanchez-Rocha, M., Smith, M., and Menon, S., 2005. "An Investigation of the Numerical Prediction of Static and Dynamic Stall". *Proceedings of the 61" American Helicopter Society Annual Forum, Grapevine,* **10**(10), p. 6.

[7] Studer, 2005. "Experimental and numerical study of laminar-turbulent transition in unsteady flow". PhD thesis, Ecole nationale supérieure de l'aéronautique et de l'espace.

[8] Richez, F., Mary, I., Gleize, V., and Basdevant, C., 2006. "Near stall simulation of the flow around an airfoil using zonal RANS/LES coupling method". *36 th AIAA Fluid Dynamics Conference and Exhibit*.

[9] Smith, M., Wong, T., Potsdam, M., Baeder, J., and Phanse, S., 2004. "Evaluation of CFD to Determine Two-Dimensional Airfoil Characteristics for Rotorcraft Applications". *American Helicopter Society 60 thAnnual Forum, Baltimore, MD, June*.

[10] Leroux, J., Coutier-Delgosha, O., and Astolfi, J., 2005. "A joint experimental and numerical study of mechanisms associated to instability of partial cavitation on two-dimensional hydrofoil". *Physics of Fluids,* **17**, p. 052101.

[11] Ferziger, J., and Peric, M., 2002. *Computational methods for fluid dynamics*. Springer New York.

[12] Menter, F., 1993. "Improved Two-Equation k-Turbulence Models for Aerodynamic Flows". *NASA Technical Memorandum,* **103975**, p. 34.

[13] Menter, F., Kuntz, M., and Langtry, R., 2003. "Ten Years of Industrial Experience with the SST Turbulence Model". *Turbulence, Heat and Mass Transfer,* **4**, pp. 625–632.

[14] Haase, W., Aupoix, B., Bunge, U., and Schwamborn, D., 2006. "FLOMANIA-A European Initiative on Flow Physics Modelling". *Berlin: Springer, 2006. ISBN 3-540-28786-8*.

[15] Abu-Ghannam, B., and Shaw, R., 1980. "Natural transition of boundary layers-The effects of turbulence, pressure gradient, and flow history". *Journal of Mechanical Engineering Science,* **22**, pp. 213–228.

[16] Steelant, J., and Dick, E., 1996. "Modelling of bypass transition with conditionned intermittency transport equation". *International journal for numerical methods in fluids,* **23**, pp. 193–220.

[17] Menter, F., Langtry, R., and Völker, S., 2006. "Transition Modelling for General Purpose CFD Codes". *Flow, Turbulence and Combustion,* **77**(1), pp. 277–303.

[18] Maman, N., and Farhat, C., 1995. "Matching fluid and structure meshes for aeroelastic computations: A parallel approach". *Computers and Structures,* **54**(4), pp. 779–785.

[19] Farhat, C., Lesoinne, M., and Le Tallec, P., 1998. "Load and motion transfer algorithms for fluid/structure interaction problems with non-matching discrete interfaces: Momentum and energy conservation, optimal discretization and application to aeroelasticity". *Computer Methods in Applied Mechanics and Engineering,* **157**(1-2), pp. 95–114.

[20] Tezduyar, T., Sathe, S., Keedy, R., and Stein, K., 2006. "Space–time finite element techniques for computation of fluid–structure interactions". *Computer Methods in Applied Mechanics and Engineering,* **195**(17-18), pp. 2002–2027.

Numerical Determination of the Propeller Design Velocity Field Including Scale Effect and Rudder Influence

Tadeusz Koronowicz (ttk@imp.gda.pl), Zbigniew Krzemianowski (krzemian@imp.gda.pl),
Institute of Fluid Flow Machinery, Polish Academy of Sciences, Gdansk, Poland
Jan A. Szantyr (jas@pg.gda.pl)
Gdansk University of Technology, Gdansk, Poland

Possibly accurate determination of the propeller design velocity field is one of the most important factors in the design of the ship propulsion systems. It is decisive in achieving high propulsive efficiency and in making accurate propulsive prediction for the ship. Moreover, it enables the detailed design analysis of the unsteady flow phenomena taking place on and around the propeller, resulting in unsteady cavitation, in generation of high pressure pulsation and acoustic emission and in generation of high amplitude unsteady bearing forces. This analysis leads to the development of the optimum propeller design, fulfilling different contradictory criteria in the best possible compromise way.

In the traditional approach the propeller design velocity field was determined during the hydrodynamic model experiments with the ship hull model without rudder and without operating propeller. This so called "nominal" velocity field was corrected for the scale effect and for the effect of propeller operation using simple semi-empirical procedures, leading to the rather approximate design velocity field. Recently it became apparent that also the influence of thick rudders on this velocity field can not be neglected.

In this paper a more rational and accurate method for determination of the propeller design velocity field is presented. This method is based on numerical prediction of flow around the ship hull including the effect of the operating propeller and (optionally) the rudder. The flow around the hull is calculated in two stages [1, 2, 3, 4]: at first the potential flow with free surface effect is computed using first order source panels distribution on the hull (cf. Fig. 1) and then the viscous flow in the hull boundary layer is computed by solving the integral boundary layer equation along respective streamlines determined in the potential flow calculation.

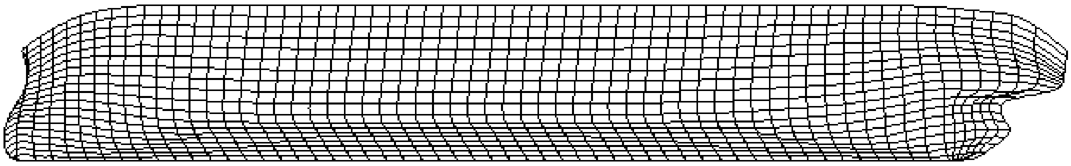

Fig. 1 Source panels distributed on the hull surface

The effect of propeller operation on the hull flow is computed using the unsteady lifting surface theory [4, 5], taking into account the exact propeller geometry. The propeller induced velocity is computed in the specially selected points C' on the hull plane of symmetry, corresponding to the points C located on the hull surface (cf. Fig. 2). This approach takes into account the fact that streamlines passing through the propeller disk have different form for the open water propeller and for the hull-propeller system.

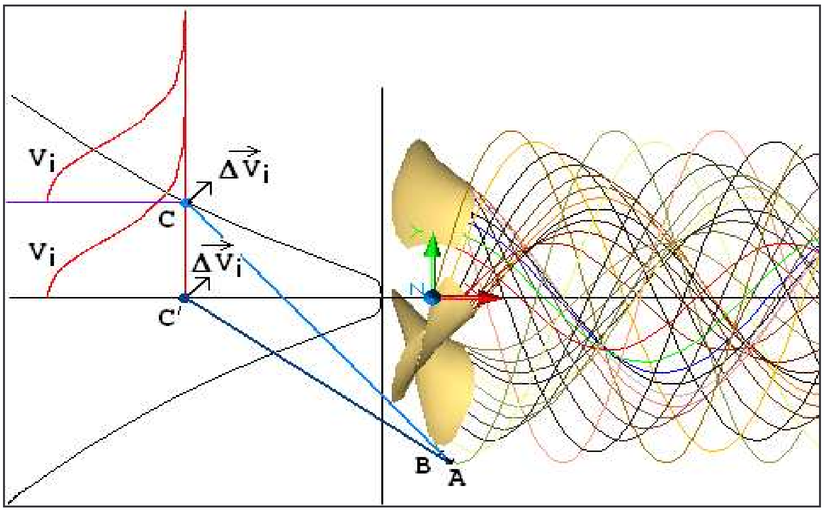

Fig. 2 Calculation of the propeller-induced velocity

The rudder is also represented by first order source panels distributed on its surface, similarly to the ship hull. The computational procedure works in the following sequence [3]:

- the flow around the ship hull in model scale without the propeller is calculated,
- the flow around the ship hull in full scale with the operating propeller is calculated (and optionally with the rudder),
- the differences between the results of both above calculations in the corresponding points of the flow field are determined,
- the above differences are added to the results of model scale measurements of the “nominal” velocity field (i.e. without propeller and rudder).

The accumulated experience with the above described computer program showed that direct calculation of the full scale design velocity field is not always sufficiently accurate for a high quality propeller design. Therefore it was decided to develop the above procedure as a sophisticated correction to the results of standard model experiments. This approach has proved to produce high accuracy results. The magnitude of the calculated corrections for the axial, tangential and radial component of the velocity is shown in Figs 3, 4 and 5.

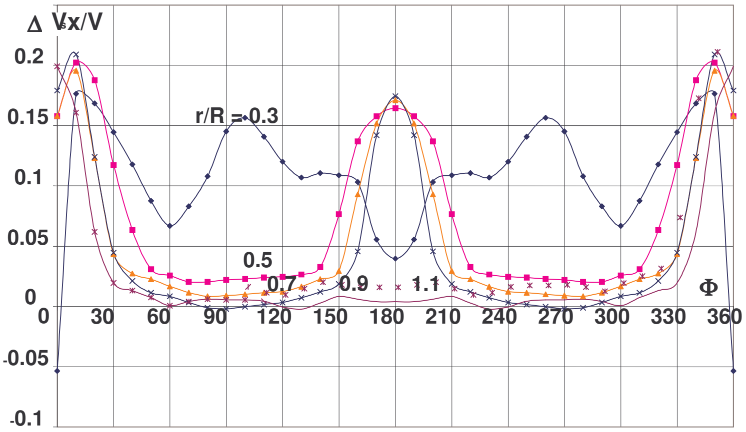

Fig. 3 Differences between axial component of the nominal velocity field for the 4 [m] model and the design velocity field for the corresponding 200 [m] Series 60 ship.

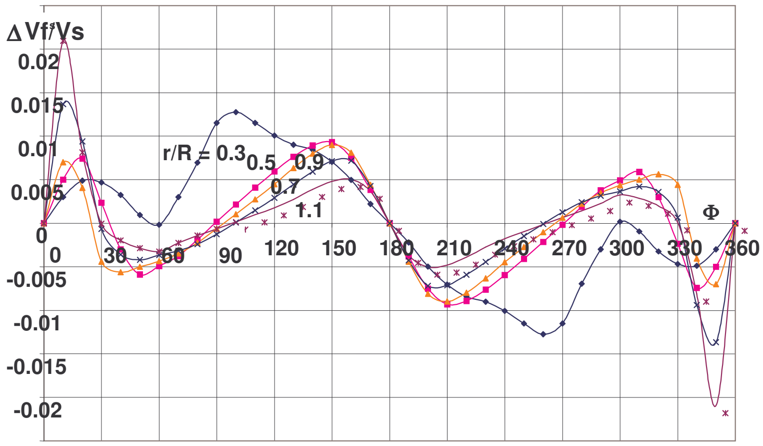

Fig. 4 Differences between tangential component of the nominal velocity field for the 4 [m] model and the design velocity field for the corresponding 200 [m] Series 60 ship

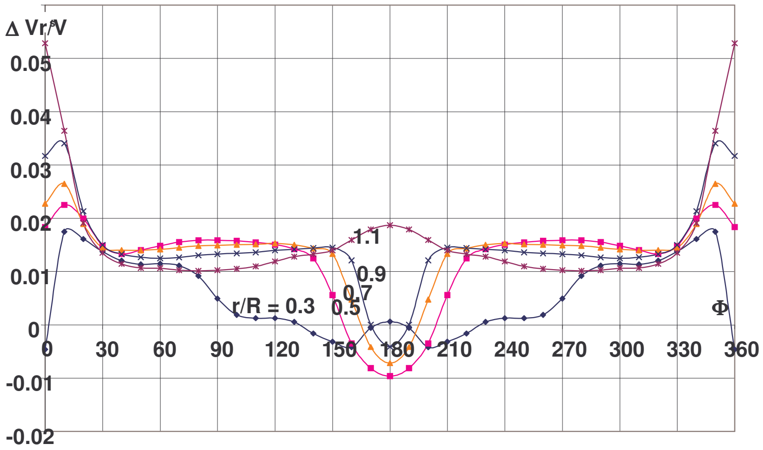

Fig. 5 Differences between radial component of the nominal velocity field for the 4 [m] model and the design velocity field for the corresponding 200 [m] Series 60 ship

The accuracy of this procedure was tested on the basis of model and full scale measurements of the propeller design velocity field of the well-known HSVA tanker [1, 2]. The following figures show the comparison of measured and calculated distributions of the axial velocity component on the radii r/R=1.0, r/R=0.7 and r/R=0.5.

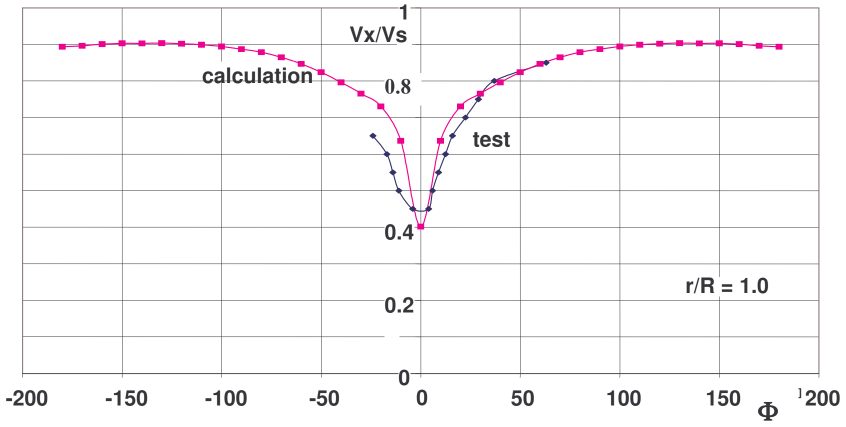

Fig. 6 Comparison of the measured and calculated axial component of the design velocity field at radius r/R=1.0 for the HSVA tanker case

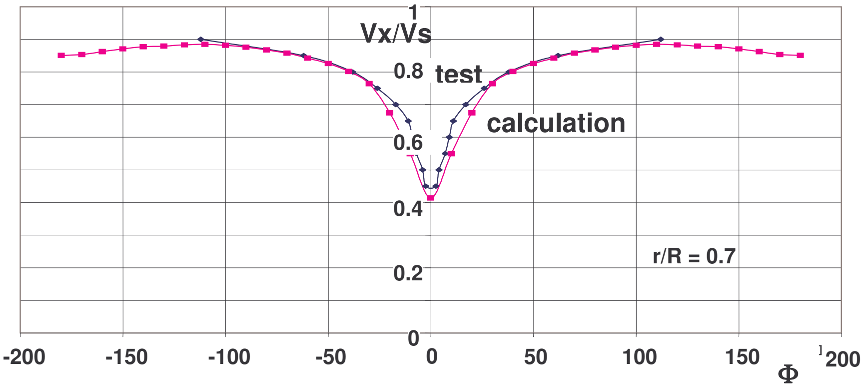

Fig. 7 Comparison of the measured and calculated axial component of the design velocity field at radius r/R=0.7 for the HSVA tanker case

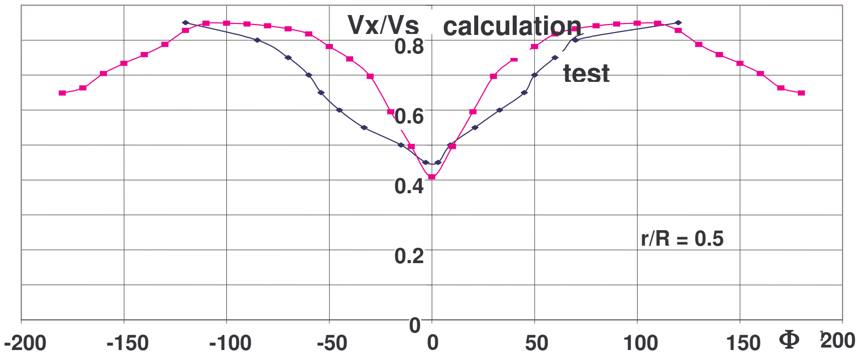

Fig. 8 Comparison of the measured and calculated axial component of the design velocity field at radius r/R=0.5 for the HSVA tanker case

The above figures show astonishingly high accuracy of computations for radii 1.0 and 0.7. The results for the radius 0.5 are slightly less accurate. It should be stressed that the scale effect and propeller influence are visible not only in the local but also in the circumferentially averaged values of velocity – see Fig. 9. This picture shows that inaccurate determination of the propeller design velocity field may lead to serious errors in propeller design, adversely affecting propeller performance.

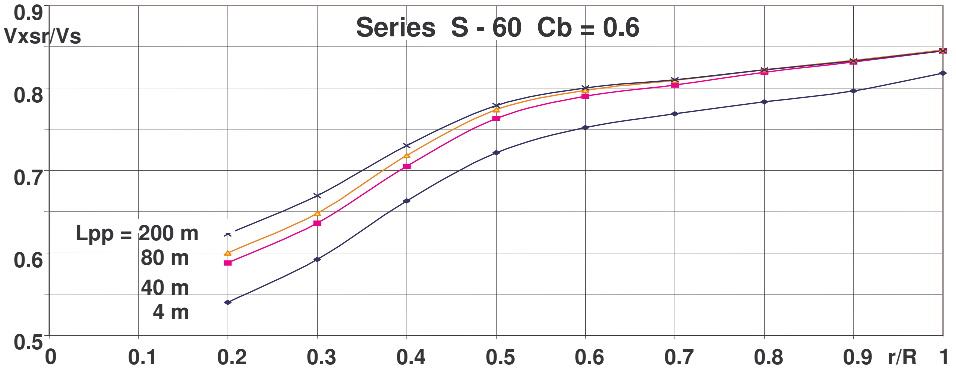

Fig. 9 The scale effect and propeller influence of the circumferentially averaged axial component of the propeller design velocity field.

The effect of ship rudder on the propeller design velocity field has been known for a long time. Its importance has increased recently with growing application of relatively thick rudders. The effect of the rudder was studied numerically in [1], using the above described computer system. One of the analyzed configurations is shown in Fig. 10. Rudders of different thickness, but based on the same outline and the same NACA profile 0018/0024, were studied. The results showed quite significant influence of the rudder on the local (cf. Figs 11, 12 and 13) and averaged (cf. Fig. 14) values of the propeller design velocity field. Neglecting of this effect may lead to designing of hydrodynamically "too heavy" propellers (i.e. with too high pitch).

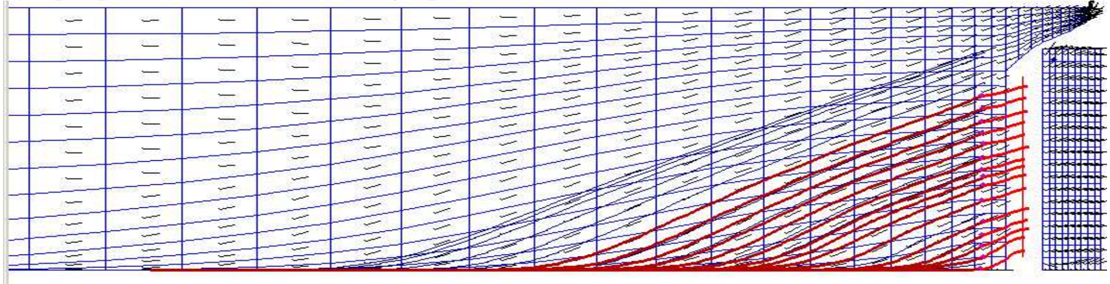

Fig. 10 Analyzed hull-rudder configuration

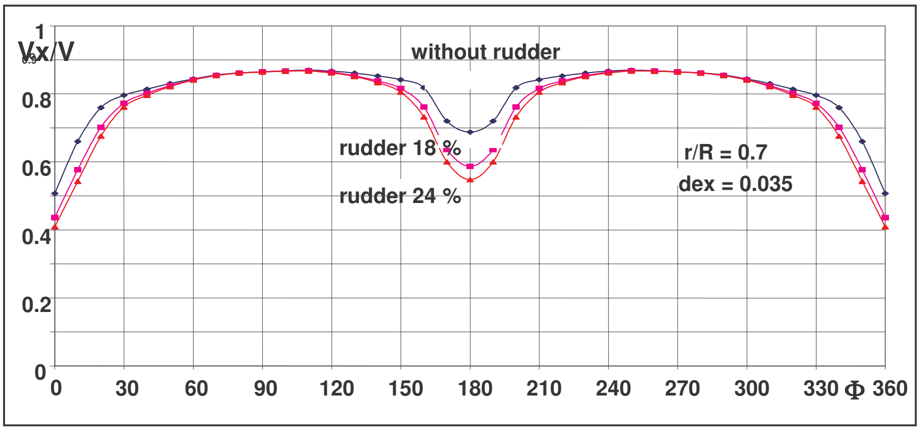

Fig. 11 Axial component of the velocity field with two rudders of different thickness and without rudder.

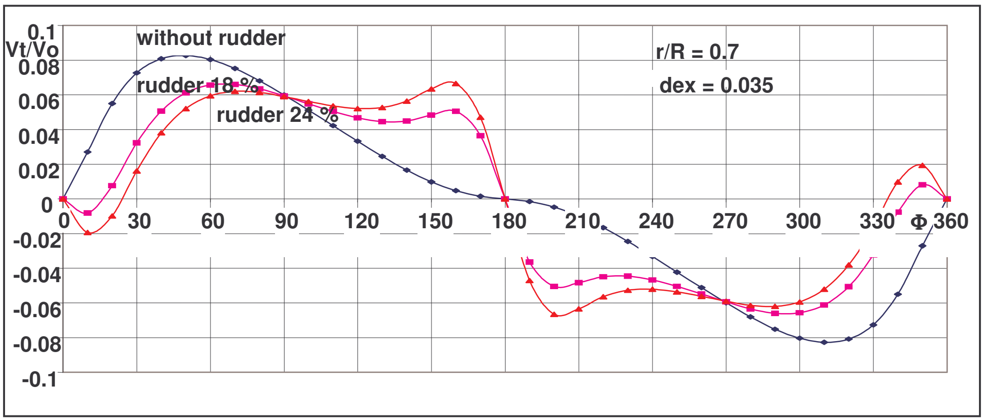

Fig. 12 Tangential component of the velocity field with two rudders of different thickness and without rudder

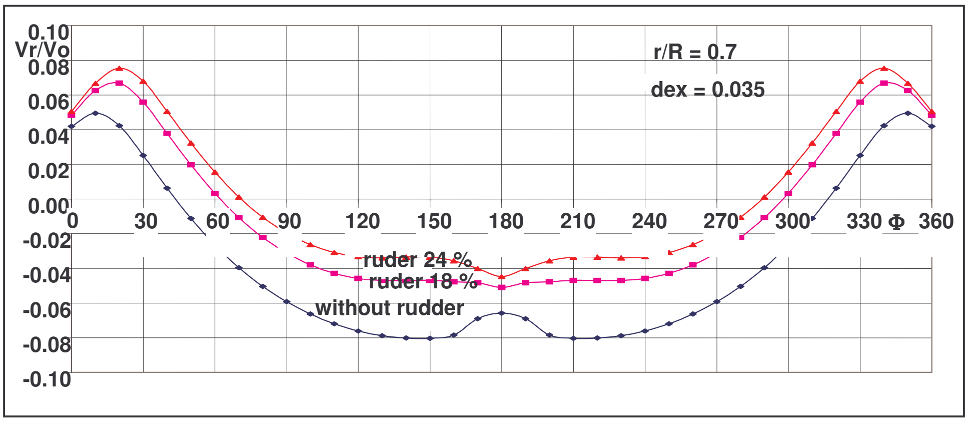

Fig. 13 Radial component of the velocity field with two rudders of different thickness and without rudder

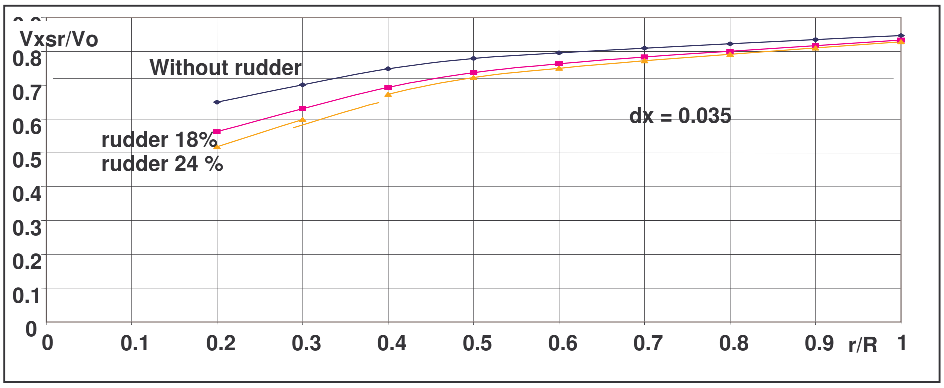

Fig. 14 Circumferential average of the axial velocity component for two rudders of different thickness and without rudder

It may be concluded from the analysis of the above presented results of calculations that:

- the effects of the ship/model scale, propeller operation and rudder presence on the propeller design velocity field are significant and must be accurately determined and properly included in the design development of the ship propulsor and of the entire propulsion system,
- neglecting or inaccurate determination of these effects may lead to erroneous design of the propulsor geometry and to unrealistic propulsive prediction for the ship,
- furthermore, it may lead to erroneous prediction of the cavitation phenomena on the designed propeller, resulting in higher level of unsteady pressure, acoustic emission and fluctuating bearing forces.

The presented procedure of numerical determination of the propeller design velocity field is based on the model scale measurement of the nominal velocity field and on application of numerically developed corrections. These corrections take into account the complete geometry of the actual hull and propeller (optionally also rudder), together with free surface and viscous flow effects. Consequently, they are much more accurate than the traditional semi-empirical corrections. The above presented procedure has been demonstrated to be sufficiently accurate to become an effective design tool for development of the ship propulsors and propulsion systems.

References

[1] Koronowicz T., Szantyr J., Chaja P.: *A Computer System for the Complete Design of Ship Propellers*, Archives of Civil and Mechanical Engineering, Vol. 8 No. 1 pp. 49-60

[2] Koronowicz T., Krzemianowski Z.: *Investigations of influence of screw propeller operation on water flow aound stern part of ship hull*, Polish Maritime Research, No. 1, Vol. 14, January 2007,pp. 3-10

[3] Koronowicz T., Kwapisz L., Wacławczyk T.: *The Velocity Field Prognosis Behind a Ship Hull in Full Scale*, St. Petersburg 2002?

[4] Koronowicz T., Szantyr J., Bugalski T.: *Theoretical Model for Determining the Pressure Field Resulting from Hull Flow and Operation of the Marine Propeller*, Polish Maritime Research, No.3, Vol. 4, September 1997, pp.2-9

[5] Szantyr J.: *A Numerical Method for Analysis of Cavitation on Marine Propellers*, Polish Maritime Research, No.3, Vol. 1, September1994, pp. 3-6

Modelling of Tip Vortex behind a Blade Using Different Turbulence Models and Different RANSE Solvers. Comparison with LDA measurements.

Paweł Dymarski*, Jan Szantyr**, Paweł Flaszyński**, Marek Kraskowski*, Rafał Biernacki**
*Ship Design and Research Centre – CTO S.A., **Gdańsk University of Technology

Introduction

The paper presents preliminary results of a research project related with RANSE modelling of tip vortex induced by propeller blade. The main target of the project is to investigate which turbulence model gives the best predictions of the tip vortex structure and what type of grid should be used in order to obtain accurate results. The paper presents results of computation with the use of different models of turbulence and three different RANSE solvers. In the framework of the project experimental tests have been carried out. The model tests consisted of measurements of velocity field behind a tip of blade with the use of Laser-Doppler Anemometer (LDA) and measurements of lift and drag force.

RANSE methods are widely used for computations of flow around ship hull. Recent years RANSE methods are increasingly used for computation of flow around screw propellers and for advanced computations of flow past hull-propeller-rudder system. Flow around screw propeller is very specific because of presence of strong vorticity which is produced by propeller blades. Numerical modelling of tip vortex structure is usually not simple with finite volume method, because it requires using relatively small control volumes (CV) far behind the blade. The size of CVs should be at least two times smaller than the diameter of vortex core, which is generally relatively small, therefore the grid density should be properly fitted to vortex structures which occur in flow.

In presented work computations were performed on two types of grid:

- initial grid: block structural with about 1.2 million of CV's
- “manually” refined grid (based on the initial) – 1.7 million of CV's for selected cases

Three different solvers have been used: *Fluent*, *Comet* and *Solaga* and six different turbulent models.

Solvers and models of turbulence

Computations has been carried out with the use of three different RANSE codes and 6 models of turbulence. The table 1 shows the matrix of models and solvers, which were used: 1.2M - indicates, that computations on initial grid has been performed, while 1.7M means, that additionally computation on refined grid has been done.

Tab. 1. Matrix of computations

	RANSE solvers:		
Turbulence model:	***Fluent***	***Comet***	***Solaga***
Spalart-Allmaras	1.2M		1.2M
k-epsilon		1.2M	
k-epsilon RNG	1.2M		
k-omega		1.2M	
k-omega SST	1.2M;1.7M	1.2M	
RSM*	1.2M;(1.7M)	-	

* There was a problem to obtain convergent solution with the Reynolds Stress Model. The problem was more significant when solver *Comet* was used, therefore computations with RSM have not been completed.

Geometry of the models

The computations and model tests have been carried out for two models of foil. The shape of these two foils was intentionally very similar to propeller blade. The difference between foils occurs in distribution of angle of attack along span. The first of these two foils was similar to blade with loaded tip “L”, the second one had a geometry of blade with unloaded tip “U”. The span of hydrofoil is 357 mm, the mean chord is 302 mm.

Computations

The size of domain of computations was the same as the size of test section in cavitation tunnel.

The grid was hexahedral and block-structured, Fig 3 a. Number of control volumes of initial grid was about 1.2 million elements, after refining number of CVs was about 1.7 million. The area of refinement was cylindrical, the cylinder axis covered a core of a tip vortex and the diameter of the cylindrical area was 60 mm. Fig 3 b. shows a domain intersection with the area of refinement.

The value of y+ was about 1.7. The following discretization schemes have been used: MUSCL in *Fluent*, CDS blended with UDS in *Comet* and *Solaga*. During computations in *Comet* the blending factor was 0.8 (80% CDS and 20% UDS), however in *Solaga* 65% CDS and 35% UDS has been used. Results of computations are presented at Fig. 4 – 7. Fig. 4 shows maps of longitudinal velocity component, Fig. 5 – vertical component of velocity, finally Fig. 6 and Fig. 7 present comparison between results for computations performed on initial and refined grid.

Figures 4 and 5 show, that results are depended on turbulence model, which was used for computations. Some results, are very close to data from LDA measurements, especially RSM and k-omega MSST in *Fluent* give reliable outcomes, however some models are not suitable for presented issues.

Fig. 1. Models of foils “L” and “U” before painting

Model tests

Models of foils have been made in CTO with the use of CNC machine. Picture 1 shows both models before painting. Model tests has been carried out in CTO's Cavitation Tunnel. Size of the test stand is: 0.8m x 0.8m x 3.0m. Velocity measurements were performed with the use of 2D Laser-Doppler Anemometer. During model tests longitudinal and vertical velocity component was measured. The measurements has been carried out in three planes, which were orthogonal to flow direction and were located 10 mm, 70 mm and 330 mm behind a tip of a blade. The area of measurements was a rectangle 62 mm x 41 mm, the size of mesh was 1mm x 1mm.

Figure 2 shows the test stand and the model during LDA measurements.

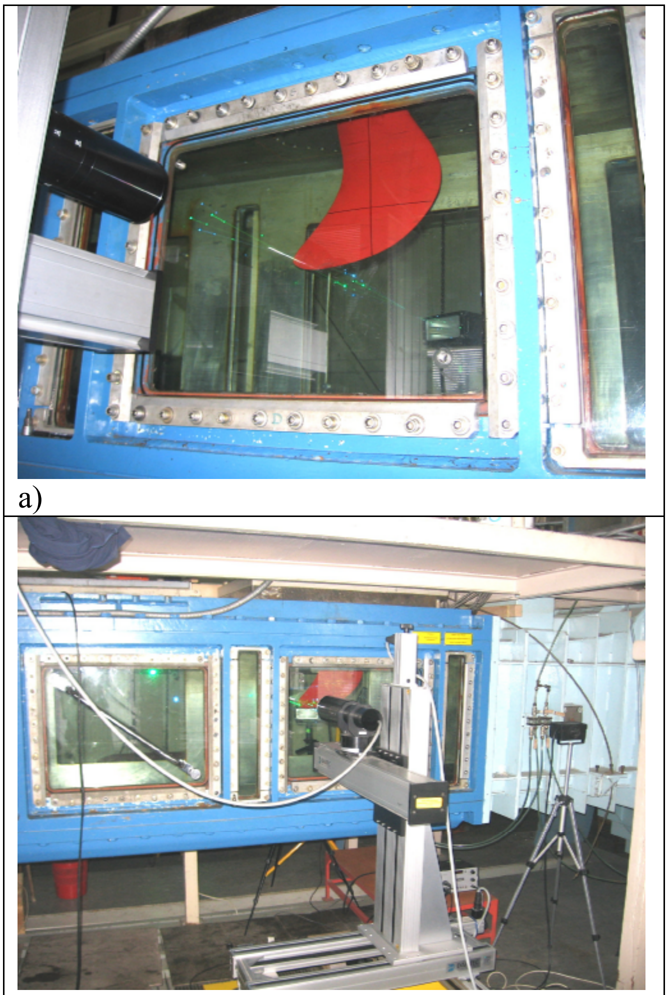

a)

b)

Fig. 2: models of foils a) model tests – LDA velocity measurements, b) test stand: cavitation tunnel in CTO

Summary and conclusions:

The set of computations has been performed for two type of blade with “loaded” and “unloaded” tip for 3 different angles of attack. Calculations have been performed with the use of 6 different models of turbulence and 3 different RANSE Solvers. Same computations have been repeated with the use of refined grid. For each computational case an adequate model test with LDA measurements has been carried out. The best accuracy has been achieved with the use of Reynolds Stress Model and k-omega MSST model (both in *Fluent*). Acceptable results were obtained with standard k-epsilon model (in *Comet*) and Spalart-Allmaras model (*Solaga* and *Fluent*).

Models, which should not be use for modelling of tip vortex phenomenon are:

- k-epsilon RNG in *Fluent*,
- k-omega in *Comet*,

The results obtained from these two models were qualitatively different than results obtained form LDA measurements, they are not presented in this extended abstract, because of size limitations.

For the most promising turbulent models computations on refined mesh (1.7M elements) have been performed. Results obtained on refined grid were slightly better than the initial, but the difference was not significant.

Computations with Reynolds Stress Model were less stable than others, it was difficult to obtain convergent solution for initial grid in *Comet*, part of computational cases performed in *Fluent* on refined grid were not stable.

Acknowledgement

The research presented in this paper has been financially supported by Polish Ministry o Science and Higher Education, Grant No. N504 033 32/2951. The authors would like to express their gratitude for this support.

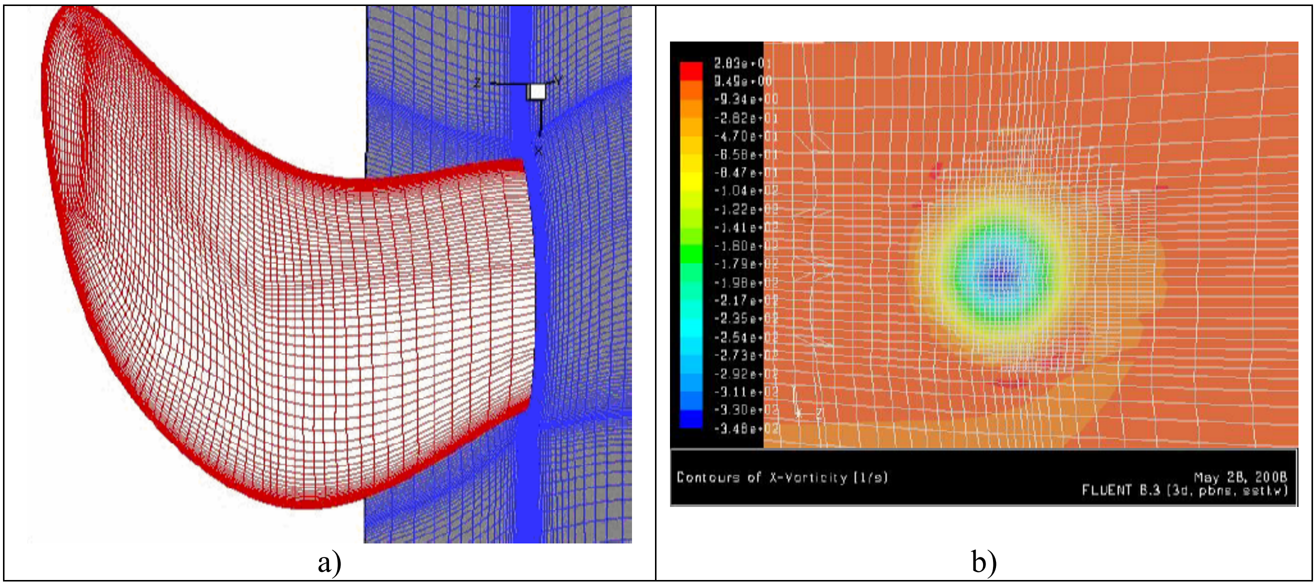

a) b)

Fig 3. a) Grid structure at the foil surface and at wall of domain; b) Grid around a tip vortex after refining.

References:

[1] Wilcox D.C.: *Turbulence Modeling for CFD*. 2^{nd} Edition. DCW Industries, 2002

[2] Ferziger J.H., Peric M.: *Computational Methods for Fluid Dynamics*, 2^{nd} ed., Springer, 1999

[3] *Comet version 2.00 – User Manual*. ICCM Institute of Computational Continuum Mechanics, Hamburg 2001

[4] *Fluent 6.1 User's Guide*. 2003

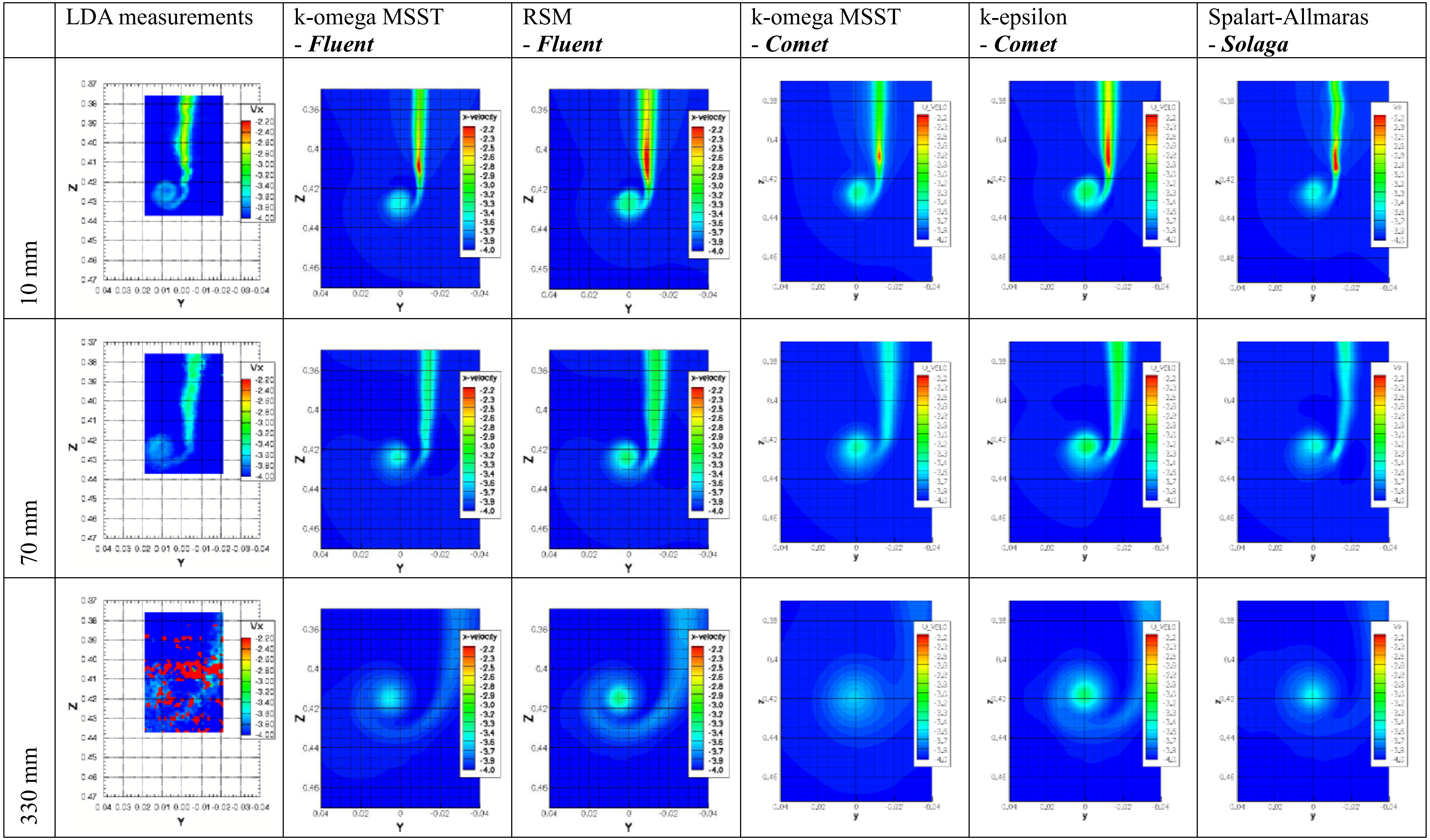

Fig. 4. Longitudinal velocity component: experimental results and RANSE computations for model “L”, alfa=2.5°

	LDA measurements	k-omega MSST - ***Fluent***	RSM - ***Fluent***	k-omega MSST - ***Comet***	k-epsilon - ***Comet***	Spalart-Allmaras - ***Solaga***
10 mm	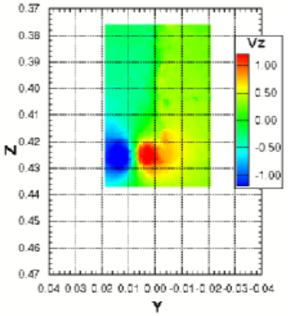	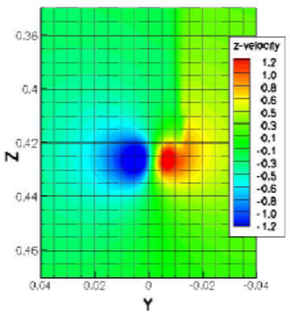	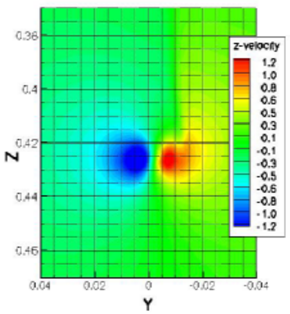	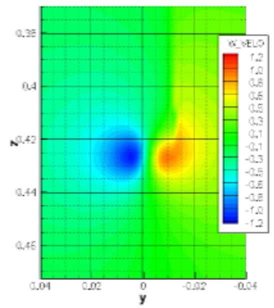	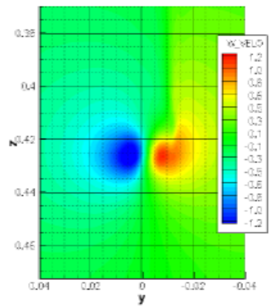	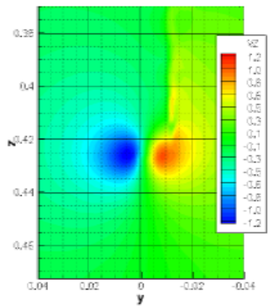
70 mm	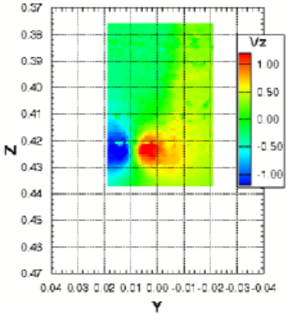	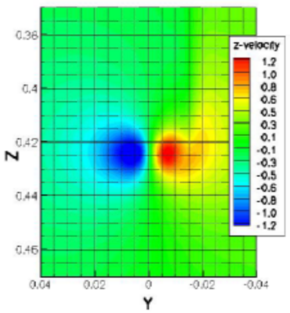	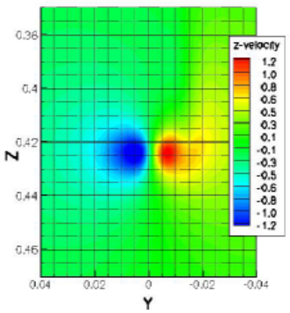	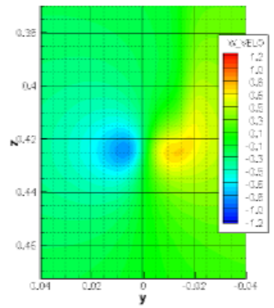	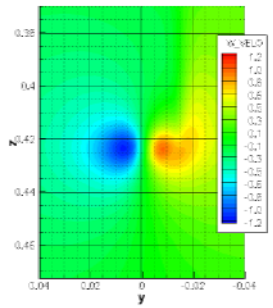	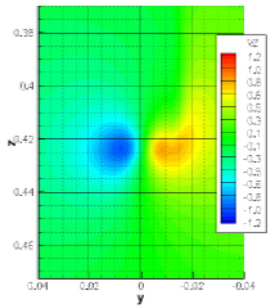
330 mm	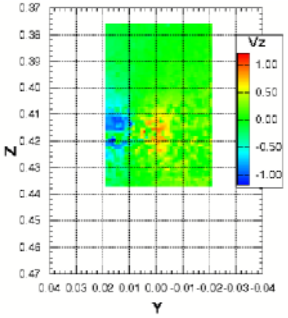	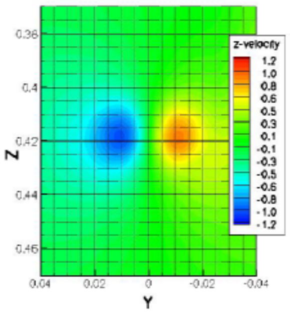	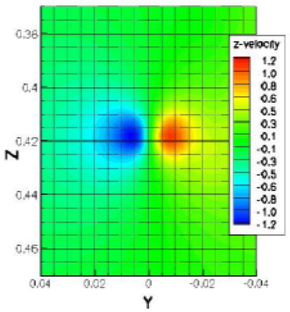	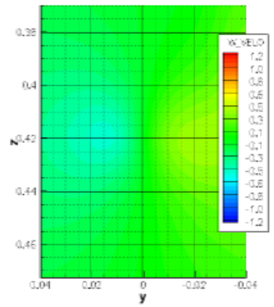	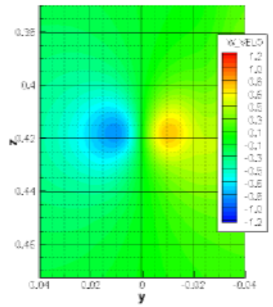	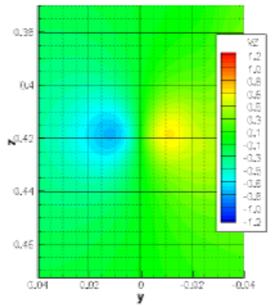

Fig. 5. Vertical velocity component: experimental results and RANSE computations for model “L”, alfa=2.5^{o}

	LDA measurements	k-omega MSST - ***Fluent***, 1.2M CV's	k-omega MSST - ***Fluent***, 1.7M CV's	LDA measurements	k-omega MSST - ***Fluent***, 1.2M CV's	k-omega MSST - ***Fluent***, 1.7M CV's
10 mm	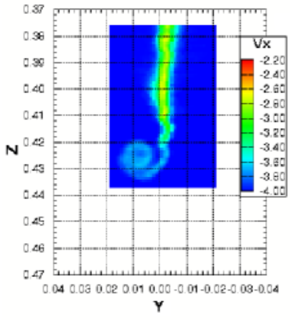	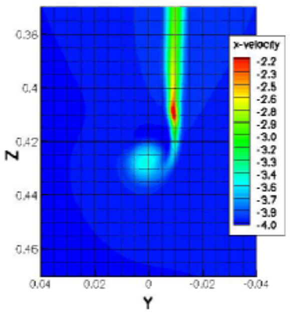	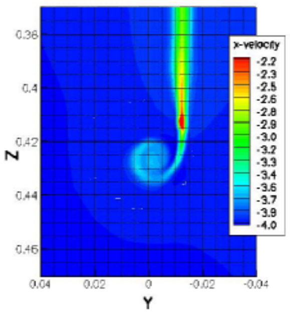	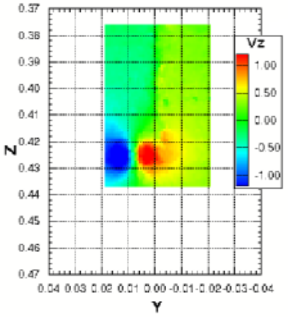	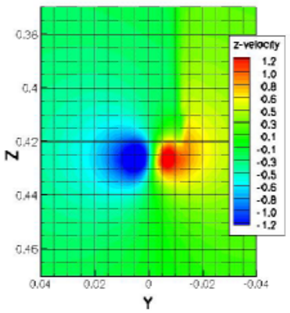	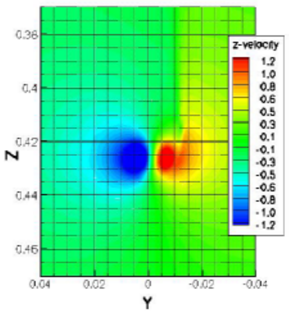
70 mm	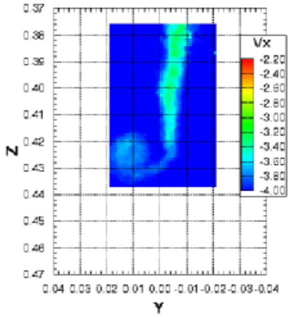	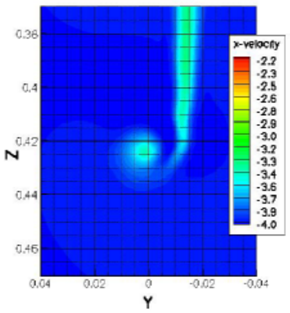	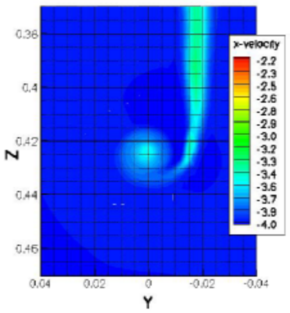	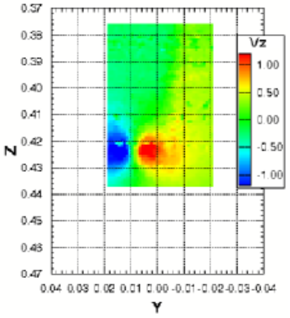	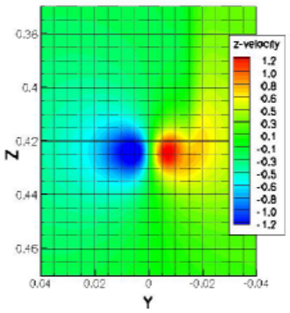	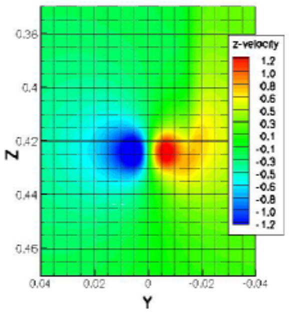
330 mm	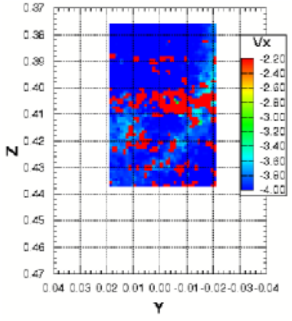	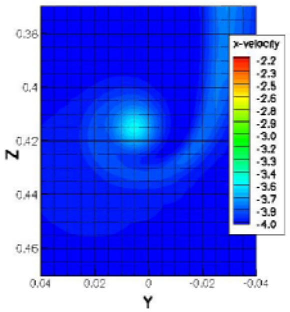	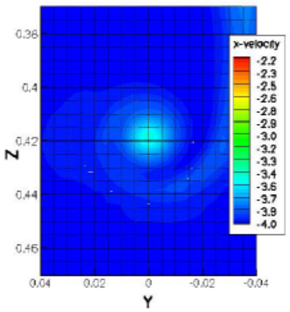	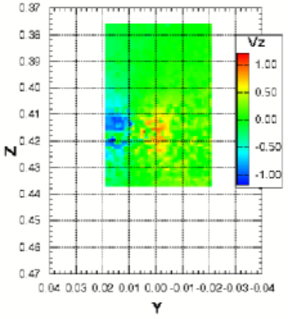	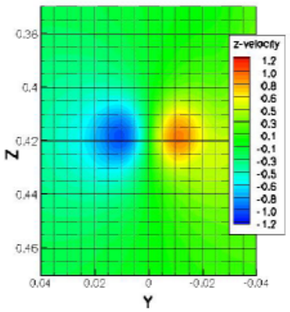	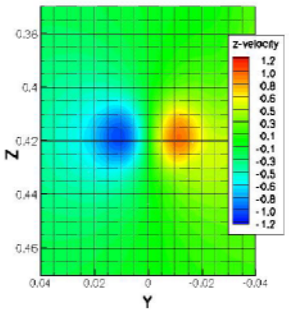

Fig. 6. Longitudinal velocity component: experimental results and RANSE computations on initial grid 1.2M and refined grid 1.7M. Model "L", alfa=2.5^o

Fig. 7. Vertical velocity component: experimental results and RANSE computations on initial grid 1.2M and refined grid 1.7M. Model "L", alfa=2.5^o

RANS computations for wake improving vortex generators

Daniel Schmode (daniel.schmode@gl-group.com)

Introduction

Vibration excitation caused by the propeller are an important issue for the maritime industry. Highly non-equal wake fields in combination with a highly loaded propeller can cause serious vibration problems. If a new vessel suffers from vibration problems, vortex generators (VG) can be a cheap remedy. This paper presents capabilities of RANS computations to assess the effectiveness of VGs. Full and model scale computations using several turbulence models are presented and discussed.

Vortex Generators

Flow control devices are widely used in the aviation and automotive industry. VGs are used on surfaces where flow separation is a potential problem to delay or avoid flow separation. On aircraft they are installed on the leading edges of the wings. They are typically triangular plates, large enough to reach the outer part of the boundary layer. VGs are aligned to have an angle of attack with respect to the local flow.[1]

A vortex generator creates a tip vortex that draws fast flow with high momentum from the outer part of the boundary layer into the inner part. This re-energizing of the inner part of the the boundary layer delays flow separation. Mounted on the suction side of a foil, a VG can avoid flow separations and thus reduce the pressure resistance of the foil. Nevertheless, the VG itself induces a resistance. If this resistance is larger than the resistance reduction due to avoided flow separation, the effectiveness of the whole configuration is not improved.

Vortex Generators as Wake Improving Devices

In the maritime industry, flow control devices are used for wake equalizing purpose. An example is the “Schneekluth“ duct [1]. It was investigated thoroughly by model scale experiments. It proved its effectiveness, but there are still doubts on the effectiveness at full scale. Other concepts were proposed, based on fins that are located directly in front of the propeller (e.g. Grothues spoilers) [1].

Two different concepts of VG application are possible. The first concept can be applied if separation occurs. VGs are mounted directly upstream of the propeller to minimize the separations.

A second concept is discussed here. The VGs are mounted far upstream of the propeller (~12%Lpp). Its vertical position is chosen such, that the core of the vortex passes above the propeller tips (Figure 1). In the diffuser-like aft ship flow the vortex diameter is widening rapidly. In the propeller plane its diameter is approximately half the propeller diameter. In the following coordinate system, x points bow-ward and y points to port. The port-side VG generates a vortex with negative vorticity. Below the core of the vortex, the y-velocity component of the vortex points inward. Thus, it transports high momentum form the outer boundary layer to the inner region (Figure 1). This concept improves the wake even if no flow separation occurs.

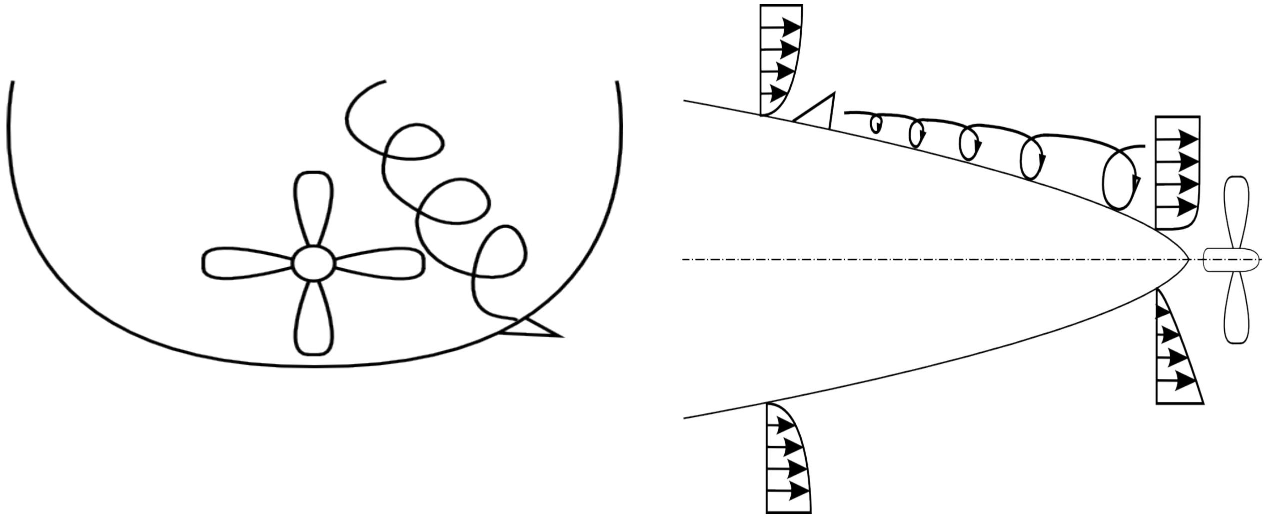

Figure 1: Principle of vortex generator as wake improving device.

Numerical Investigation

A 3500 TEU container vessel sailing at Fn=0.25 was investigated in the HSVA towing tank and in HyCat. The model scale was λ~30. Wake and pressure pulses above the propeller were measured with and without VGs. The pressure pulses were reduced by the VG up to 50% of the plain hull configuration.

Computations were carried out using the RANS solver STARccm+. The automatic grid generation tool ProAM was used to create the unstructured hexahedron based grids. The model scale grid consisted of approximately 2100k cells, while the full scale gird had 3300k cells. Wall functions were used in both cases, and wall boundary layer resolution was adapted to y+ values of approximately 100. The free surface was not modeled. A symmetry boundary condition was used 1m above the still water line instead.

Three turbulence models were compared, namely the SST k-ω, a k-ε based Reynolds-Stress linear pressure strain, and a SST k-ω based detached eddy model. For detailed description of the models, see [2].

Figure 2 shows the x-vorticity. Behind the VG, the vortex is small and strong. It progresses downstream close to the hull surface and passes the propeller above the tips. Towards the stern, the strength of the vortex is decreasing and the diameter increasing.

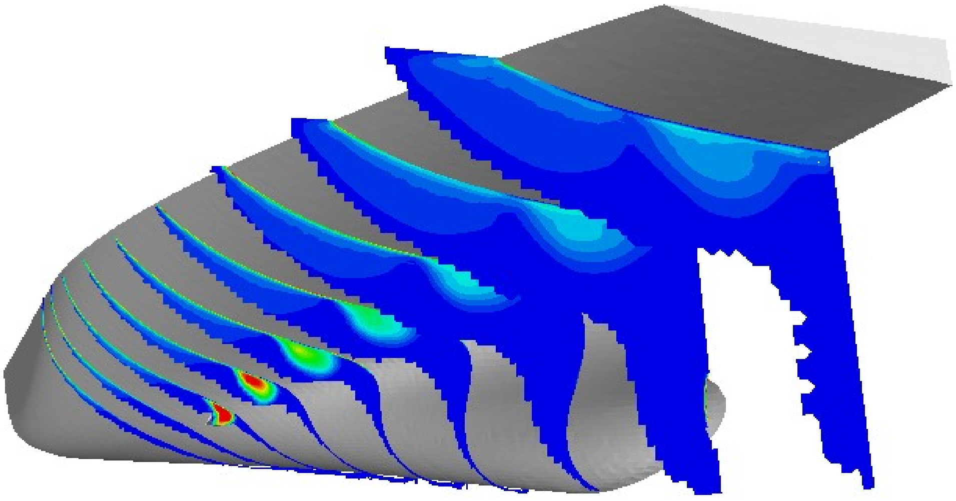

Figure 2: X-vorticity, the vortex core passes above the propeller plane (RSM).

Figure 3 plots the y-velocity component close to the hull. The configuration with VG shows a larger inward directed y-velocity at the section 3 to 5 (from stern to stem). These are caused by the inward velocity component below the vortex core. Above the vortex core, the y-velocities are smaller than in the version with VG.

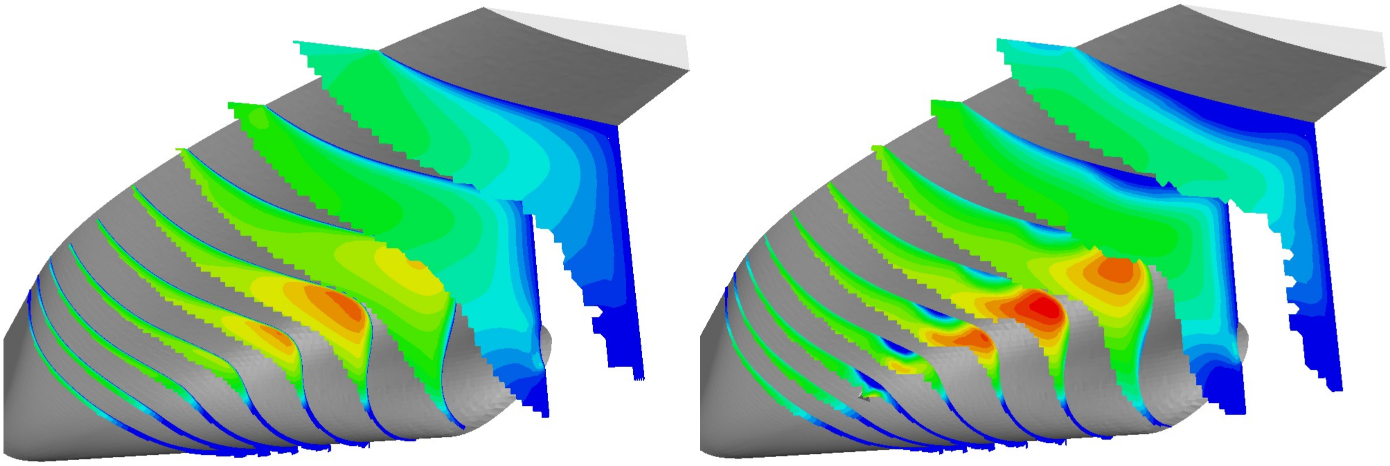

Figure 3: Y-Velocity, left without VG, right with VG (RSM).

Figure 4 plots the x-velocity component. The version with the VGs shows a strong wake behind the VG. This wake passes the propeller plane above the propeller tips. Thus it does not spoil the wake. The larger inward directed y-velocity transports large momentum flow to the inner boundary layer, which causes a less pronounced low velocity peak in the 12 o'clock propeller position.

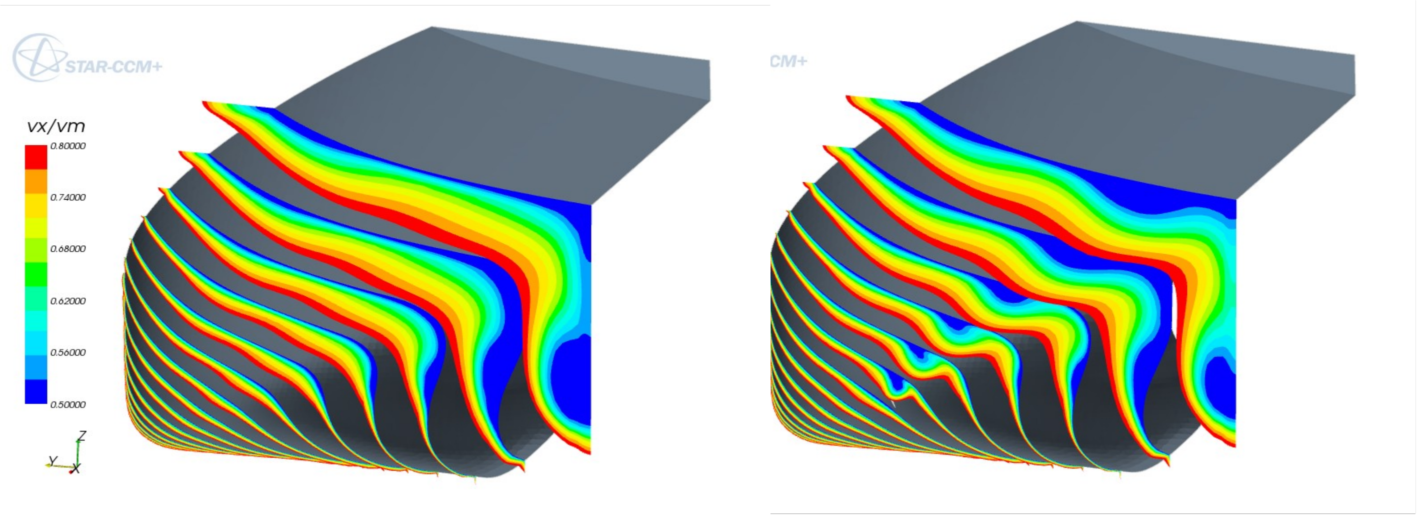

Figure 4: x-Velocity, left without VG, right with VG.

The measured wake is plotted in Figure 5. The VG increases the axial velocity by about 5% in the 12 o'clock position. The computations using RSM (Fig. 6) compare well and shows the same 5% increase. The computations using SST k-ω compare less well on the inner radii, but also reproduce the 5% increase in the 12 o'clock position. Computation using DES model give exactly the same result as the SST k-ω. This may change on denser grids, when the LES terms are activated.

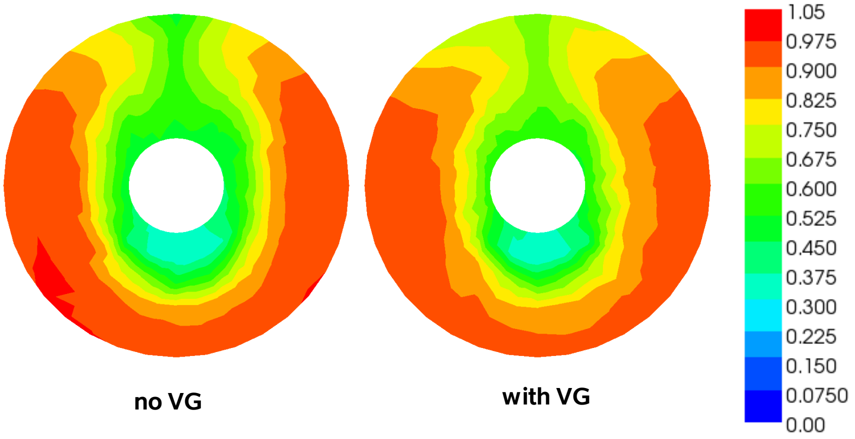

Figure 5: Axial velocity component normalized using ship speed measurement

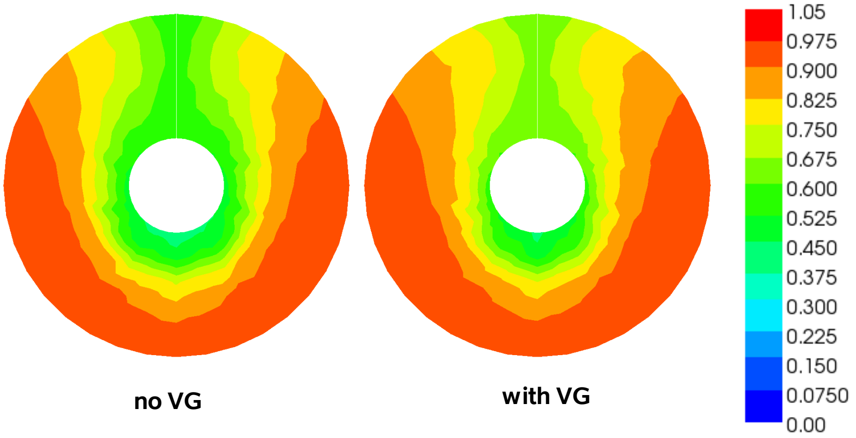

Figure 6: Axial velocity component normalized using ship speed computed with RSM turb. model.

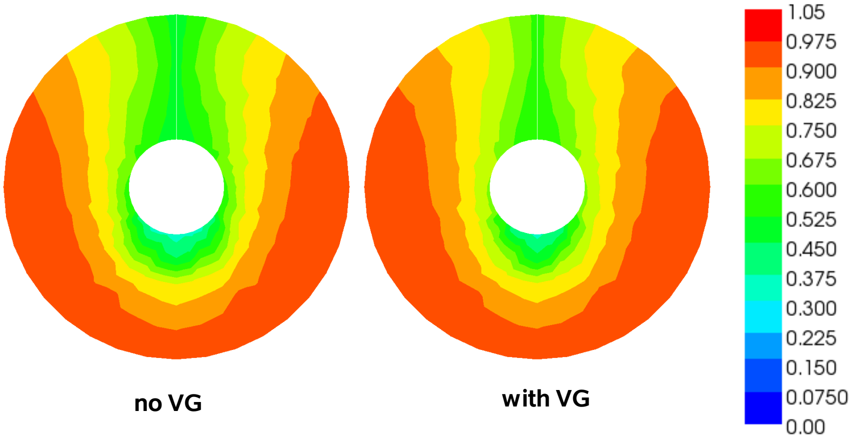

Figure 7: Axial velocity component normalized using ship speed computed with SST-k- ω model.

Instead of a grid refinement study, we only refined the cells between the VG and the propeller along a cylinder that has approximately the diameter of the propeller (Fig. 8). The resulting wake looks similar to the non refined one. We conclude that the grid resolution is sufficient to capture the effect of the vortex on the wake.

Comparing result using SST k-ω and RSM, a difference is evident in the 12 o'clock position. Measurements and the RSM computation show Y-shaped contour lines. These are more I-shaped in the SST computation. Nevertheless, the practical interest concentrates on the magnitude of the velocity peak in the 12 o'clock position, and this is captured using the SST turbulence model. Thus, the model error caused by the turbulence model was sufficiently small for industrial application here.

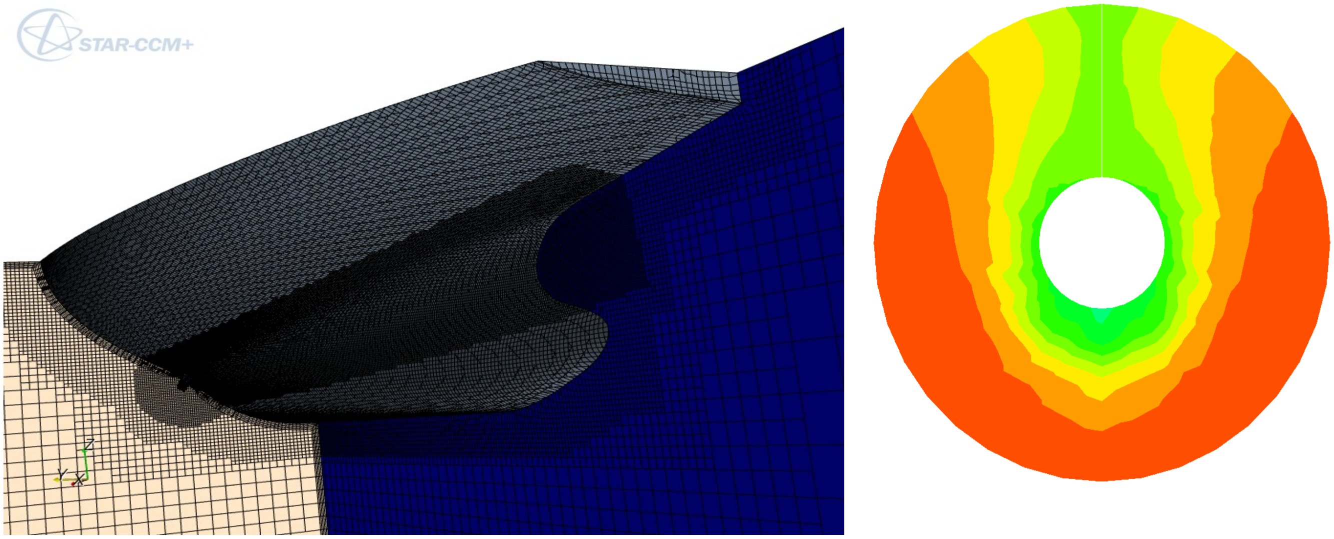

Figure 8: Local refinement behind VG (left), Axial velocity component normalized using ship speed on refined grid with RSM turbulence model (right).

The results of the full scale computation are plotted in Fig. 9. The boundary layer is smaller here, and the low-velocity-peak in the 12o'clock position is also less pronounced. Consequently, the difference between the plain hull and the VG version is also less pronounced, but still evident in the computational results. Assuming that the conclusions drawn from the model scale validation are also valid for the full scale computations, we believe that model and discretization errors in the full scale computation are smaller than the error of the extrapolation methods used to approximate the full scale wake from model scale measurements. Consequently, we believe that RANS computation are a reliable design tool to investigate the effectiveness of wake improving vortex generators.

In addition to the full-scale prediction capability, RANS computations give a deeper insight in the local flow topology. The trace of the vortex core can be visualized, and the optimal positioning of the vortex can be found easily. The angle of the VG can be adjusted according to the local streamline.

Computation times for the model scale case on a current 4-core PC are less than 12h. This fact allows application of RANS as a design tool. Different positions, angles, shapes, and sizes of the VGs can be investigated in a reasonable project time.

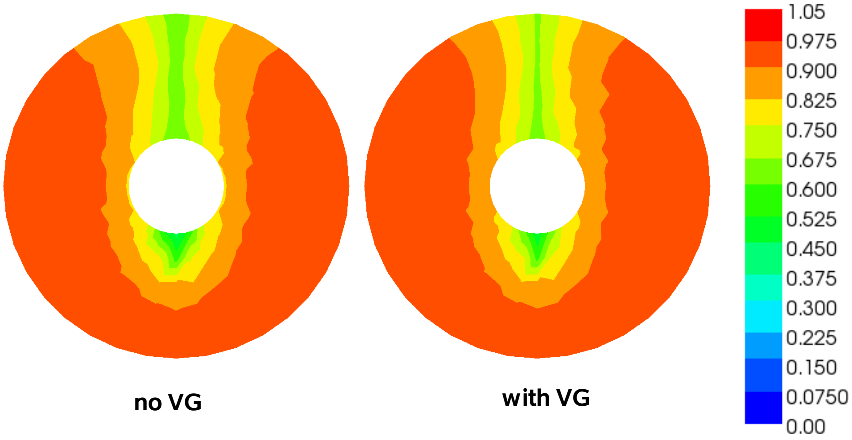

Figure 9: Axial velocity component normalized using ship speed ,full-scale computed with RSM.

Conclusions

The effectiveness of vortex generators as wake improving devices was investigated using RANS computation. The results gave insight into the local flow and confirm the basic principles of the concept of a VG a as wake improving device. Wake computations compared well with model scale measurements. The effect of the VG on the 12 o'clock pressure peak was well captured. Moderate computation times allow industrial application for design and optimization purposes.

References

1. Schneekluth, H. and Bertram, V. (1998). Ship Design for Efficiency and Economy
2. StarCCM+, online documentation

Wake Field Analysis of a Drifting Ship with RANS-CFD-Methods

HENDRIK VORHOELTER, STEFAN KRUEGER, Hamburg University of Technology
hendrik.vorhoelter@tu-harburg.de, krueger@tu-harburg.de
Numerical Towing Tank Symposium, Brest 2008

In the work presented the nominal wake field of a Series60 hull form is investigated in drift motion. The wake is analysed with two different RANS-CFD-codes (FreSCo and COMET). The computational results are compared to each other and to measurements.

1 Motivation

Today, analysis of flow field details around ships and part of ships are part of any design process. Investigations of different propeller designs and propeller-rudder-hull combinations are state-of-the-art. For manoeuvring simulations forces and moments acting on the hull, propeller and rudder are computed for different states of motions. Thus, a propeller inflow not only for the steady straight ahead run of the ship is required. KOSE (see KOSE, 1982) had made a proposal how the effective wake fraction could be corrected in dependence on the lateral velocity in the propeller plane. Unfortunately, this correction is based on the measurement results of only one single screw vessel of the Series60. Therefore, it has to be doubted that this correction is valid for modern hull forms and especially for twin screw vessels. However, modern RANS-CFD methods allow the numerical estimation of a ship's wake in the design process. Therefore, a method shall be developed, which estimates the wake field in manoeuvring simulations.

2 Concept of the Work

As described above RANS-CFD-codes are used for the estimation of a ship's wake field in manoeuvring conditions. In a first step CFD computations are performed with two different RANS-codes on a test case for which measurement results are available. The results are dicussed and compared to each other.

The work is part of an ongoing research on the improvement of manoeuvring simulations at the Institute of Ship Design and Ship Safety at the Hamburg University of Technology. Later on the computed wake fields shall either be used as direct input for propeller and rudder investigations or a ships specific correction of the wake fraction depending of the lateral motion in the propeller plan is developed. This correction would then be applied on the measured or computed wake field for the straight ahead run.

3 Test Case

A Series60 hull form with $c_B = 0.6$ is chosen as test case. The hull form is described by TODD (TODD, 1963). The Series60 form is chosen for two reasons. The first one is, that KOSE developed his effective wake fraction correction on the basis of measurements of a Series60 model also, although this was a $c_B = 0.7$ model (see KOSE, 1982). But the two hull forms are similar (see TODD, 1963). The second reason is, that OLTMANN performed detailed measurements of the model wake field and forces and moments acting on the hull and propeller in drift motions (see OLTMANN, 1974 and 1976). The model with its principal dimensions and the experiments are described in the following.

3.1 Model data

The model data is derived from the original Series60 publication (TODD, 1963). The principle dimensions of the hull form are shown in table 1, the section plan is shown in figure 1.

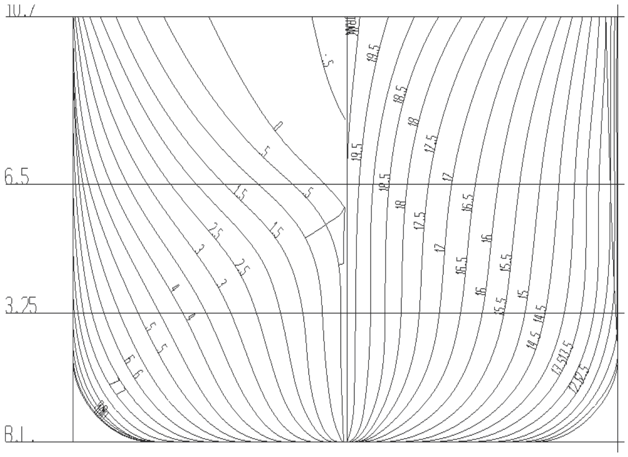

Fig. 1: Section Plan of Series60 with c_B=0.6

Dimension	Value
Length between perpendiculars [m]	121.920
Length over all [m]	126.309
Breadth moulded [m]	16.255
Draft moulded [m]	6.501
Prismatic coefficient C_B [-]	0.600
Longitudinal centre of buoyancy f. A. P.[m]	59.069
Deplacement [t]	8024

Tab. 1: Principle dimensions of Series60 model with c_B=0.6

In the Todd report the hull form is described without stern tube. For the experiments the model must have been fitted with a stern tube. The introduction of a stern tube into the model is also described by Toda (see Toda et al., 1990). But the results of the wake field measurements show that the influence of the stern tube on the wake especially in drift motion is small. Thus, it was decided to model the hull form without stern tube for the present investigations.

3.2 Oltmann's Experiments

Oltmann investigated a model of the Series60 hull form with c_B=0.6 at the Hamburg Ship Model Basin in 1973. The major part of the experiments was the measurement of forces and moments acting on the hull as well as propeller torque and thrust. The scale of the model was $\lambda=26.667$ and the Froude number $Fr=0.300$. This led to a model speed of $v_M=2.01\mathrm{m}/s$. The corresponding model Reynold's number was $Re=8.06\cdot10^6$.

The model was equipped with rudder and propeller and investigated at constant speed and propeller revolutions with different drift and rudder angles. The drift angles were varied from -12° to 12° is steps of 2°. As the thrust and torque variations depending on the drift motion were larger than expected (see Oltmann, 1974) 3D- measurement of the ship's wake field were performed (see Oltmann, 1976). The wake was measured with five-hole Pitot probes in the propeller plane on five concentric circles around the propeller axis. The radii varied between 37% and 125% of the half propeller diameter. The velocity was measured every 10°.

4 Set-up of CFD-Model

For the numerical analysis a CFD-model is set up. The hull form is prepared in the ship design system *E4*. The section plan is shown in figure 1. For the RANS-CFD computations a finite volume mesh is generated with *HEXPRESS*. The computations are performed with the RANS-solvers *FreSCo* and *COMET*. The post-processing was done with *E4* and ParaView.

4.1 Computational Domain and Mesh Generation

The size of the computational domain in length, breadth and hight is four times two times one the ship length. The top of the domain is placed at the free surface which is not modelled in the computation, as the influence of the free surface on the propeller inflow can be neglected.

The domain is meshed with the automatic mesh generator *HEXPRESS* (see Numeca, 2005). *HEXPRESS* generates a fully hexahedral finite volume mesh by subdivision of an initial mesh. The initial mesh, which covers the total domain has a division of 40x20x10 cells. Viscous layer cells are used on the surface of the hull. The thickness of the first layer is adjusted to achieve a y^+-value of 30 on surface of the hull at the aft end. The final mesh has about 1,000,000 cells. The minimum angle inside one cell is 26.1°, whereas in 12 cells an angle is found smaller than 30°.

4.2 Boundary conditions

The top of the domain, which represents the free surface, is treated as symmetry plane. The plane at the front and the port side are treated as inflow with fixed velocity. The velocity components in x and y direction are adjusted to achieve the desired drift angles. The analysis are performed only for positive drift angles different to the model tests. The starboard and aft plane which represent the outflow are treated as pressure boundaries. The bottom is treated as slip wall.

4.3 Applied RANS-CFD solvers

The first RANS-CFD solver, which is used is *COMET* in the version 2.3 (see ICCM, 2001). *COMET* is a validated tool for CFD-analysis in the marine industry. In this work it is used as benchmark for the second RANS-solver FreSCo.

FreSCo is a RANS-solver specially designed for marine purposes and currently under development by HSVA, MARIN and TUHH (see SCHMODE ET AL. 2007a and 2007b).

4.4 RANS-CFD solver settings

As far as possible the same settings are used for both CFD-solvers. The pressure equation is solved with the SIMPLE algorithm, the momentum equations are discretised using flux-blending. The k-ω-SST model is used for the turbulence modelling. The hull surface is treated as non-slip-walls with High-Reynolds-Number wall functions. The computations are performed steady. The solution is iterated until the residuals and the mean forces on the hull are on constant level. If the development of the residuals and forces on the hull is analysed, it can be seen that the residuals become constant but on a rather high level after 700 to 1000 iterations. The friction force becomes steady also. But the pressure force is oscillating. This is probably due to eddy separation at the stern, which leads to a fluctuating flow field.

4.5 Post-processing

The post-processing is done in two steps. At first the flow field is read out at the same read out points which were used in the experiments. Hence, it is possible to compare the measured and computed wake fields directly. Secondly all wake fields are analysed in *E4*. The nominal wake fraction is computed, as well as the mean velocity in the propeller plane in the lateral and vertical direction. The mean velocity is normalised with the model speed. The analysis is not performed on the measured radii, but on seven standard radii from 0.4 to 1.0 of the half propeller diameter in steps of 0.1. Thus, a comparison to other ships is possible.

5 Results

In fig. 5 the wake field, both computed and the measured, for the 0° drift angle case are shown. The colour and contour lines indicate the axial velocity normalised with the model speed. The arrows indicate the velocity in the propeller plane. The measurement is at the left, the *FreSCo* result in the centre and the *COMET* result at the right side. It can be seen that both codes deliver roughly the same result. In the both computations is the boundary layer to thick, although the *FreSCo* boundary layer is thinner. At the twelve o'clock position the isolines are contracted in the measured wake field. This can also be seen in the *COMET* result. The reason for this contraction is not the stern tube, but a vertex which arises in the area of section three to four. The contraction is also observed in not fully converged *FreSCo* computations.

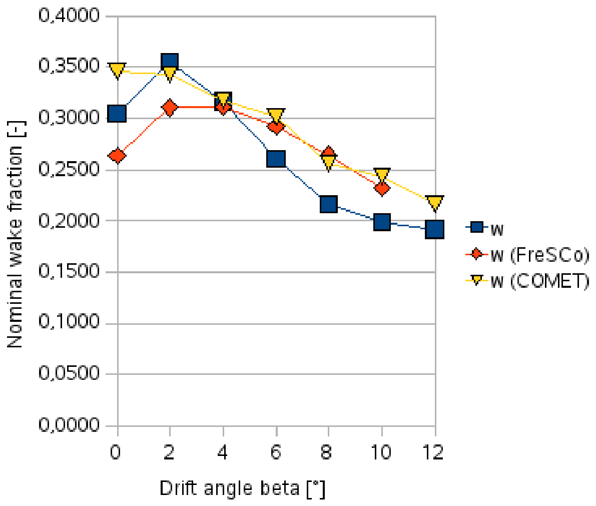

Fig. 2: Nominal wake fraction from measured and computed wake fields

In fig. 2 the nominal wake fraction is shown for the measured and the computed wake field. Both CFD-solvers capture the trend of decreasing wake fraction for increasing drift angle. For drift angles larger than 4° the fraction quite similar. COMET over predicts the wake fraction for the zero drift case, whereas *FreSCo* captures the trend of a decreased wake fraction in the straight ahead condition. Although the wake fraction is under predicted.

In fig. 3 the normalised mean lateral velocity in the wake is shown. The theoretical y-velocity is the lateral undisturbed velocity in y-direction. Both solvers deliver comparable results and the trend is captured.

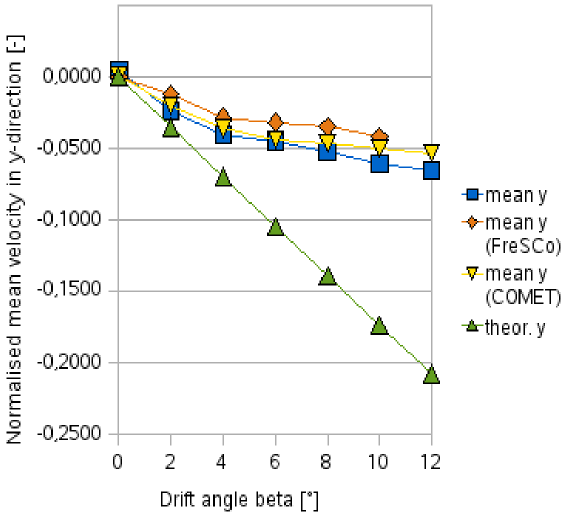

Fig. 3: Mean Velocity in y-direction

In fig. 4 the normalised mean velocity in z-direction for the wake field is shown. Although one would expect larger differences in the vertical velocity due to the negligence of the free surface, the difference between the measurements and computations are small. The trend is captured and both codes deliver similar results.

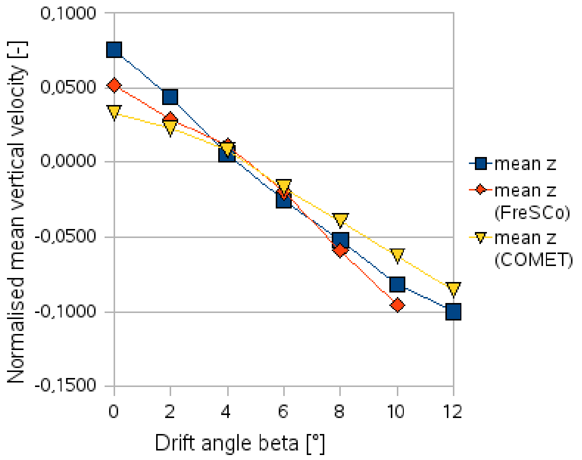

Fig. 4: Mean Velocity in z-direction

In the tables 2 to 4 the detailed results for all computations are shown. In fig. 6 the wake field from the measurements and the FreSCo computations is shown for the drift angles of 0°, 2°, 6° and 10°. It can be seen that the vertex which is arises from the centre skeg is reproduced in the computations. The difference of the boundary layer thickness between the computational result and the measurement decreases with increasing drift angle.

6 Conclusion and Further Work

CFD-results for a Series60 hull form in drift motion were presented for two RANS-CFD solvers (*COMET* and *FreSCo*). The correlation between the two codes is good, although differences in details are observed. The comparison between the CFD and experimental results is encouraging. The main effects, e.g. the large difference between the theoretical and the applied lateral velocity, are captured. But the quantitative comparison, e.g. of the wake fraction, shows that there is a of further work to be done. For example it has to be discussed whether the laminar-turbulent-transition has an influence on the boundary layer thickness and thus the measured and computed wake fields.

7 Bibliography

Kose, K. (1982): On a New Mathematical Model of Maneuvring Motions of a Ship and its Applications. Int. Shipbuilding Progress. 205. Delf

Numeca (2005): HEXPRESS User Manual version 2.2c. Brussels. NUMECA International

Oltmann (1974): Inclined towing test with a series 60 hull model (Schrägschleppversuche mit einem Schiffsmodell der Serie 60), Institut für Schiffbau, Schriftenreihe Schiffbau, Nr. 307, Hamburg (in german)

Oltmann (1976): Wake field measurements with a Series60 model (Nachstrommessungen mit eine Schiffsmodell der Serie 60), Institut für Schiffbau, Schriftenreihe Schiffbau, Nr. 340, Hamburg (in german)

Schmode, D., Rung, T. (2007a): RANS Code Verification Using Method of Manufactured Solution. in proceedings of 10th Numerical Towing Tank Symposium, NuTTS07, Hamburg, Germany

Schmode, D., Wöckner, K., Rung, T. (2007b): Free Surface Modelling in *FreSCo*, Latest Developments. in proceedings of 10th Numerical Towing Tank Symposium, NuTTS07, Hamburg, Germany

Toda, Y., Stern, F., Tanaka, I., Patel, V.C. (1990): Mean-Flow Measurements in the Boundary Layer and Wake of a Series 60 CB=0.6 Model Ship With and Without Propeller. J. of Ship Research, Vol. 34. No. 4. pp. 225-252

Todd, F.D. (1963): Series60, Methodical Experiments with Models of Single-Screw Merchant Ships, David Taylor Model Basign, Report 1712, Washington D.C., USA

8 Annex

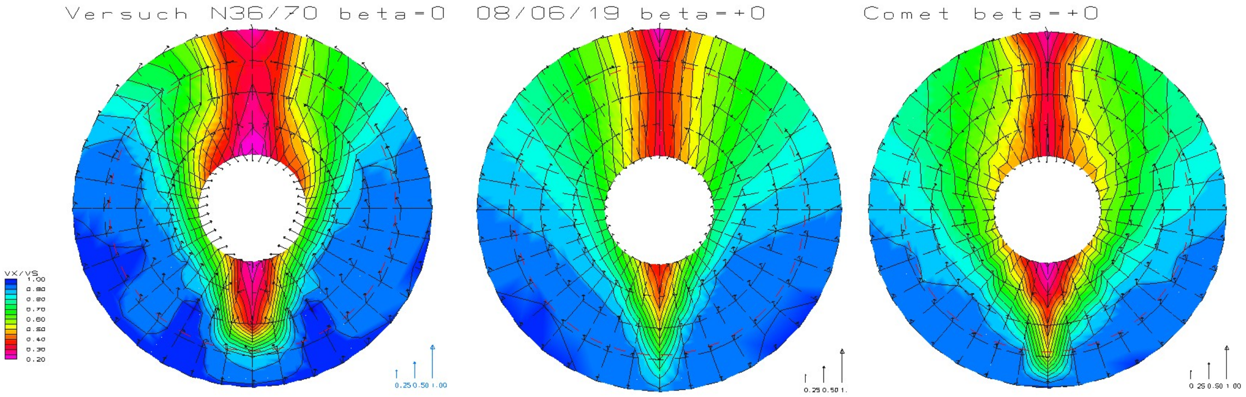

Fig. 5: Comparison between measurement (left), FreSCo (centre) and COMET (right) for β=0°

β [°]	0	2	4	6	8	10	12
w	0,3044	0,3547	0,3162	0,2608	0,2165	0,1989	0,1916
wx	0,3087	0,3578	0,3187	0,2632	0,2197	0,2028	0,1957
mean y	0,0047	-0,0238	-0,0404	-0,0452	-0,0523	-0,0603	-0,0656
mean z	0,0755	0,0443	0,0051	-0,0251	-0,0520	-0,08	-0,0999

Tab. 2: Nominal total wake fraction w, nominal axial wake fraction w_x, mean horizontal velocity y, mean vertical velocity z (normalized with model speed) for drift angles from β=0° to 12° from measurements

β [°]	0	2	4	6	8	10
w (FreSCo)	0,2640	0,3101	0,3115	0,2918	0,2642	0,2319
wx (FreSCo)	0,2646	0,3109	0,3125	0,2931	0,2654	0,2329
mean y (FreSCo)	0,0001	-0,0123	-0,0281	-0,0316	-0,0349	-0,0420
mean z (FreSCo)	0,0521	0,0289	0,0116	-0,0197	-0,0591	-0,0955

Tab. 3: Nominal total wake fraction w, nominal axial wake fraction w_x, mean horizontal velocity y, mean vertical velocity z (normalized with model speed) for drift angles from β=0° to 12° from FreSCo results

β [°]	0	2	4	6	8	10	12
w (COMET)	0,3453	0,3420	0,3174	0,3017	0,2562	0,2430	0,2166
wx (COMET)	0,3459	0,3429	0,3185	0,3030	0,2590	0,2442	0,2177
mean y (COMET)	0,0010	-0,0202	-0,0362	-0,0441	-0,0461	-0,0502	-0,0537
mean z (COMET)	0,0331	0,0227	0,0083	-0,0170	-0,0394	-0,0626	-0,0858

Tab. 4: Nominal total wake fraction w, nominal axial wake fraction w_x, mean horizontal velocity y, mean vertical velocity z (normalized with model speed) for drift angles from β=0° to 12° from COMET results

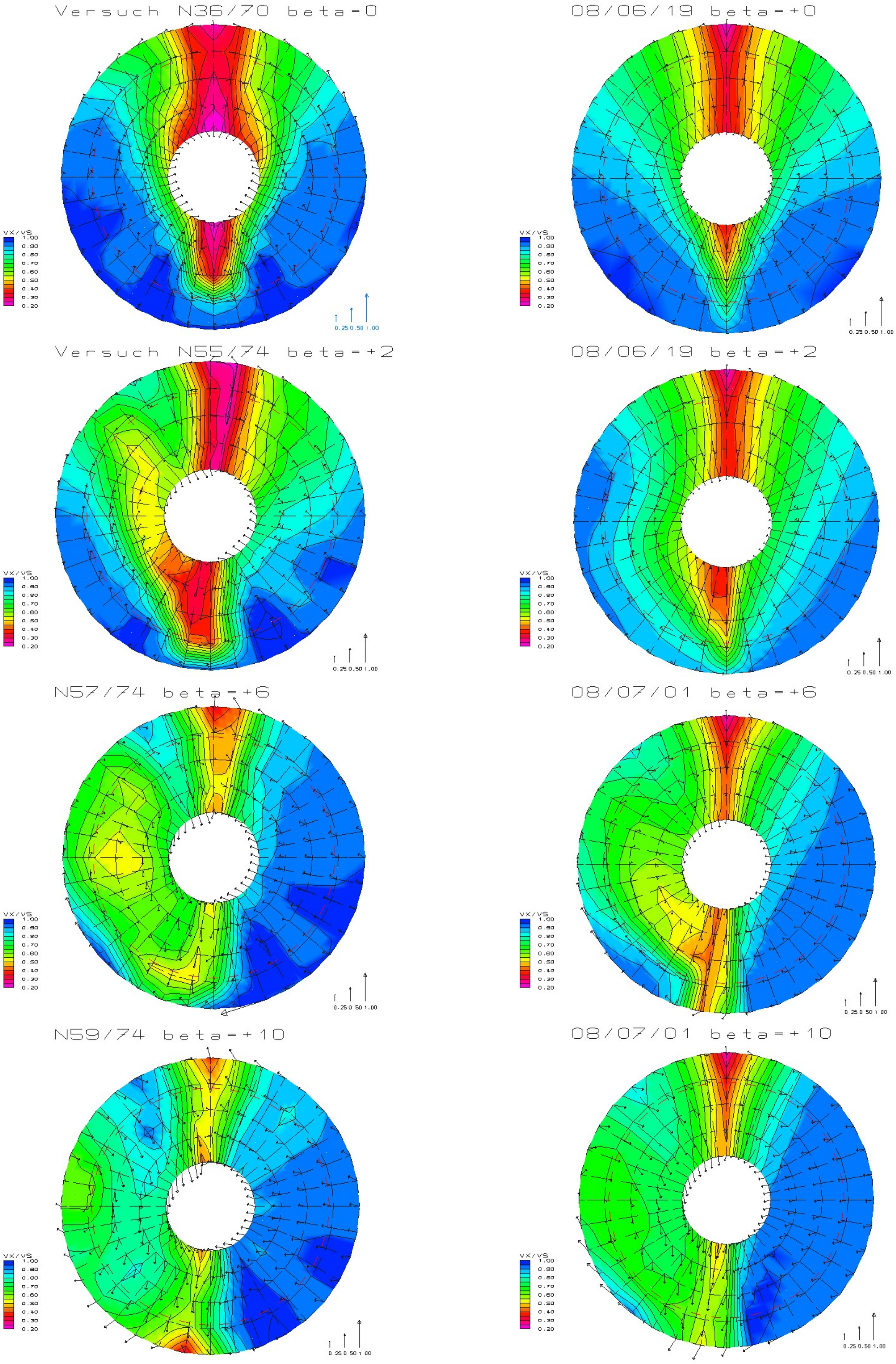

Fig. 6: Measured (left) and computed wake field (right) for drift angles β=0°,β=2°, β=6° and β=10°

The Use of CFD in Modelling Blanketing Effects for Yacht Race Simulations

Thomas Spenkuch[1], Stephen Turnock[1], Sandy Wright[2], Ajit Shenoi[1]

[1] Fluid Structure Interactions Research Group,
[2] Wolfson Unit for Marine Technology and Industrial Aerodynamics
School of Engineering Sciences,
University of Southampton, UK.
Email: {ts305, srt, a.m.wright, r.a.shenoi}@soton.ac.uk

Summary

A detailed examination of the performance of a typical upwind sail rig arrangement was carried out for different heel and yaw angles using a commercial Computational Fluid Dynamics (CFD) solver. Experimental wind tunnel data provided by the Wolfson Unit for Marine Technology and Industrial Aerodynamics were used to validate the calculated CFD results. The computed results demonstrate good agreement and the effect of mesh density on the flow solution is presented. The purpose of this work is to identify the downwind position and track of the resultant sail vortex system. The ability to model correctly this behaviour within a yacht race simulation is critical to identifying the blanketing effect between two yachts.

1 Introduction

The traditional way of quantifying the performance of a sailing yacht is carried out by assessing how fast a yacht will complete a course under given conditions. The Robo-Race simulator which allows both influence of the yacht design and tactical choices of the crew has been developed to capture the behaviour of a fleet of yachts [1, 2]. It is designed to simulate fleet races with *N* Americas Cup Class yachts, where *M* yachts controlled by the computer and *(N-M)* yacht controlled by a real sailor. Different models for the yacht-crew interaction have been designed and implemented for the helmsman and the sail tailers, as well as a 'routing engine' which solves problems of a strategic and a tactical nature, such as collision avoidance and navigation in wind shifts. The simulator Robo-Race is a MATLAB®-Simulink® based tool which is built on the module 'Robo-Yacht' which uses a four degree of freedom 'physics engine' as well as behavioural models for the automatic crew.

As part of a fleet race simulation it is important to be able to capture the interactions between multiple yachts. The upwind sailing performance of a yacht is influenced by the presence of another yacht when the downwind yacht sails in the wind shadow of the upwind yacht. The upwind yacht is said to 'blanket' or 'cover' the downwind yacht. The blanketing effect caused by the upwind yacht's sails has an effect on the flow propagating downwind reducing its magnitude and altering its direction. Existing models such as [3] represents a simple empirical approach to the phenomenon of blanketing and is implemented in the current version of 'Robo-Race' [1, 2]. A potential way of developing a more sophisticated approach is through the application of Computational Fluid Dynamics (CFD) solvers to give detailed information about the complex flow in the wake of a typical sail rig for a range of sailing conditions. CFD flow investigations are often used as part of the design process of high performance sailing yachts. Several methods to simulate the flow around a sailing yacht are available for designers and flow analysts. The most common are the panel or vortex lattice grid codes or CFD calculations based on RANS (Reynolds Averaged Navier-Stokes) equations. Due to the rapid increase in performance and consequent decrease in cost of computers, engineers and designers are increasingly attracted to investment in computational methods. The use of RANS-based CFD analysis of complete sail systems is becoming a key component of elite racing yacht campaigns, such as the America's Cup or the Volvo Ocean Race [4, 5]. For example using a CFD tool, Yoo *et al.* [6] calculated the viscous flow around a sail-like rigid wing, which is similar to main and jib sails of a 30-foot sloop. CFD investigations of full 3D RANS equation calculations for an America's Cup Class (ACC) yacht have been carried out by Graf and Wolf [4] to prove the validity of optima for mast profile geometry derived from 2-D RANS equation simulation results. Collie and Gerritsen [7] made numerous investigations into the challenging turbulent flow past downwind yacht sails and the practical application of CFD to such sails.

The aim of this study is to develop a better method for describing the blanketing effect within a yacht fleet race. This work examines how well CFD predicts the performance of the sails assessed against wind tunnel data. In particular, a detail analysis of the position of the sail wake and its downstream evolution into a concentrated vortex is carried out. The CFD results will be used to provide curve-fits for use in a simple real-time lifting line approach within the wind environment module of 'Robo-Race'.

2 Sloop Rig Model

The Wolfson Unit for Marine Technology and Industrial Aerodynamics evaluated a sailing yacht at the University of Southampton in the low speed section of a wind tunnel (4.6m width by 3.7m height). The model was mounted on a six-component balance attached to a turntable and suspended from the balance in a tank of water [8]. Different sail setups and heel angles were tested. The experimental data obtained from these wind tunnel tests were used to carry out a validation study into the influence of heel upon the performance of a sloop rig (see Figure. 1).

The dimensions for the jib and mainsail surfaces are defined by five sections beginning at the foot (0%) and increasing in steps of 25% up to the top (100%). Each sail section shape is defined by its camber, draft, front and back percentage (see [9] for further information). The angle of the sail towards the mast angle varies for each section to create the span-wise distribution of the sail twist in order to model more realistic sailing conditions. The foot length of the jib and the mainsail are 774 mm and 667 mm respectively. The height of the jib is 1618 mm and the mainsail is 2000 mm high comprising a total sail area A made up of 0.665 m^2 (jib) and 0.720 m^2 (mainsail). Figure.1 shows the sail rig surfaces with a superimposed viscous grid of middle density.

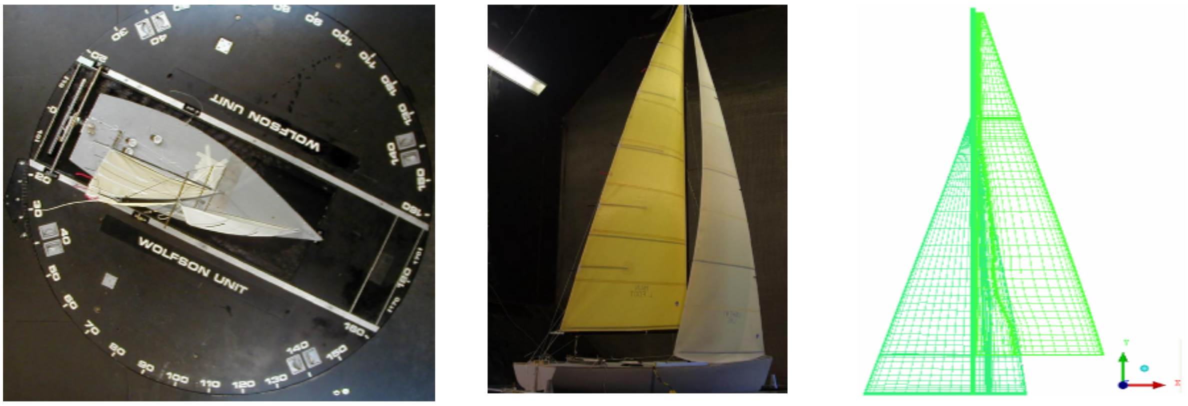

(a) plan view **(b) side view** **(c) surface mesh (medium)**

Figure 1: Views of experimental tests (a, b) and corresponding computational sail rig mesh (c)

The following 3D simulations with different incidence and heel angles are executed to determine the effect of heeled sails. The comparison with the experimental data shows the level of accuracy of the CFD calculations and gives an idea of the accuracy of the viscous wake analysis. The lift and drag coefficients of the sail rig are used for the validation and defined further below (see Equations 1 and 2).

For the viscous sail wake analysis, the criteria of maximum vorticity [10] and minimum pressure [11] are used for the identification of the position of the vortex cores. Six surfaces parallel to the inlet and outlet wall of the wind tunnel are introduced downstream of sail rig beginning at the stern of the yacht and continued by 0.5, 1.5, 3.5, 6 and 9 yacht lengths behind it. On those surfaces the vorticity ω is calculated and defined as the curl of the velocity (see Equation 3):

$$Cl = \frac{Lift}{0.5\rho u_\infty^2 A} \quad (1), \qquad Cd = \frac{Drag}{0.5\rho u_\infty^2 A} \quad (2), \qquad \vec{\omega} = \vec{\nabla} \times \vec{u} \quad (3),$$

where A is the sail area of 1.385 m^2.

3 Initial Investigation and Setup

All meshes and simulations for this study were carried out using the software packages of ANSYS® ICEM CFD 11.0 and ANSYS® CFX 10.0. As stated in [7], the Shear Stress Transport (SST) offers the best performance for the available computational power and is the applied turbulence model for all calculations within this study, whereas the fluid air is set up as an ideal gas.

Wind tunnel tests on 2D impervious sails carried out by Newman and Low [12] were used to investigate three different mesh types (structured, unstructured and hybrid) at four different mesh densities around typical sail sections with the effect on lift, drag, reattachment and separation locations analysed. The similar Reynolds numbers of 1.2×10^5 (Newman and Low) and 1.71×10^5 (Wolfson Unit data) provide confidence that the flow conditions and behaviour are similar. Further 2D investigations using a cut of the sail rig at the height of 5% of the luff of the mainsail were carried out to determine an appropriate mesh technique, a time step value for the unsteady runs and the difference of the steady and unsteady simulation approach. The structured meshes utilised a H-block topology for each sail with features such as clustering at the leading/trailing edges, boundary layer mesh around the sails to ensure a y^+-value of 1 and an O-grid around the mast (see Fig. 2 and 3). Detailed information about this mesh sensitivity study can be found in [9]. A structured 2D mesh of 163,900 cells was found to give an acceptable level of fidelity without requiring a too large 3D mesh. The results of the 2D slice mesh sensitivity study were used to build-a 3D mesh around the jib-mainsail-mast configuration. Supplementary investigations into the boundary layer growth on the wind tunnel working section walls were made to find a method whereby these could be treated with a 'free-slip' condition and yet any axial pressure gradient effects could be captured.

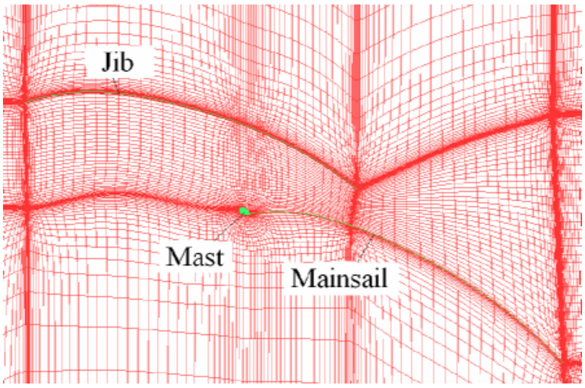

Fig. 2: Smooth structured mesh of middle density

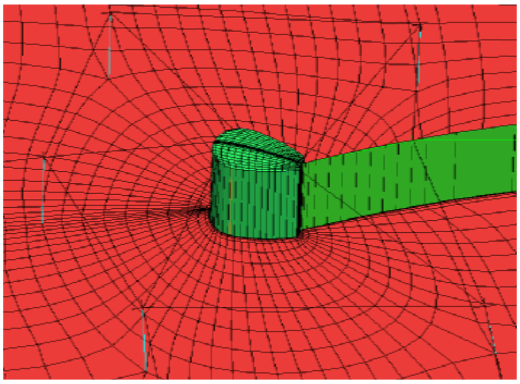

Fig. 3: O-Grid around mast, density: middle

For the 3D simulations three structured meshes were chosen, consisting of the wind tunnel domain including the jib, the mainsail and the mast. The applied block topology offers the opportunity to split the blocks around the sail rig in such a way that an approximation to a rotary disc with split blocks around the rig was created in order to adapt the mesh easily to the actual heel and wind incidence angles. The wind tunnel domain is split in 576 blocks; 6 in x-, 8 in y- and 12 in z-direction. This high amount of blocks arises as the computational domain has to be split 12 times in z-direction to assure that the blocks are correctly associated to the complex twisted sail rig structure. Three structured meshes with the same features as the 2-d meshes described above were created for the grid validation investigation (see Table 1 and Fig. 4).

Table 1: Mesh sensitivity study, individual C_D and C_L for each component and the sum for the complete sail rig. A practical restriction of 4 million cells limited further mesh sensitivity studies with finer meshes.

Grid Density	Number of Cells	Jib		Mainsail		Mast		All	
		C_D	C_L	C_D	C_L	C_D	C_L	C_D	C_L
Coarse	851,469	0.123	0.934	0.209	0.505	0.013	0.028	0.345	1.467
Middle	1,692,787	0.111	0.94	0.207	0.508	0.012	0.035	0.33	1.484
Fine	3,374,461	0.102	0.93	0.21	0.516	0.01	0.036	0.322	1.481

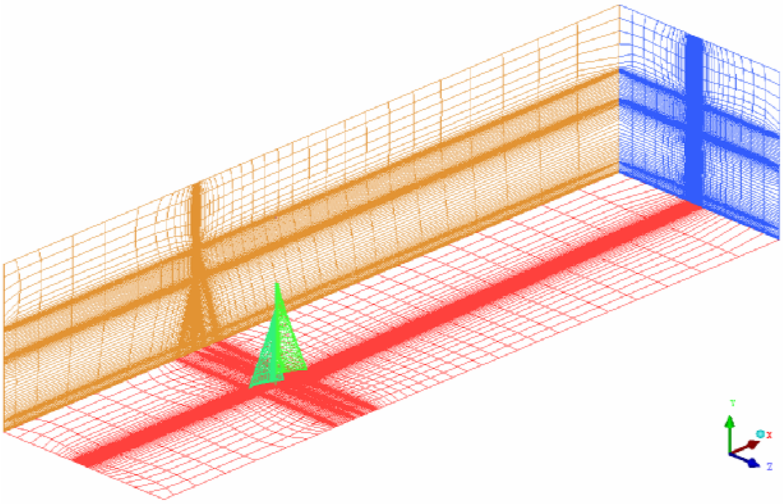

Figure 4: 3-d mesh of middle density with sail rig located 3 mainsail chord lengths behind the inlet and 10 mainsail chord length in front of the outlet

The following boundary conditions are set up:

- velocity inlet at the wind tunnel inlet, pressure outlet at the wind tunnel outlet;
- no-slip wall condition at the jib, mainsail, mast, wind tunnel bottom; and
- free slip wall condition at the wind tunnel ceiling and side walls (the wind tunnel is reduced by the same amount of the boundary layer thickness on these walls in order to apply these saved cells around the sail rig).

The velocity of the flow through the wind tunnel domain was 7 m/s which corresponds to a Reynolds Number of 1.71×10^5. Two different series of runs were carried out to investigate the effect of the heeling angle and the angle of attack (AoA) on sailing performance. These were:

1. to investigate the influence of the angle of attack, the angle of attack varies whereas the heel angle remains constant (AoA varies in values of 23°, 27°, 32° and the heel angle is kept constant at 0°, 30°);
2. to investigating the influence of the heel angle, the heel angle varies whereas the angle of attack remains constant (AoA remains constant at 27° and the heel angle varies in values of 0°, 10°, 20°, 30°).

4 Results and Discussion

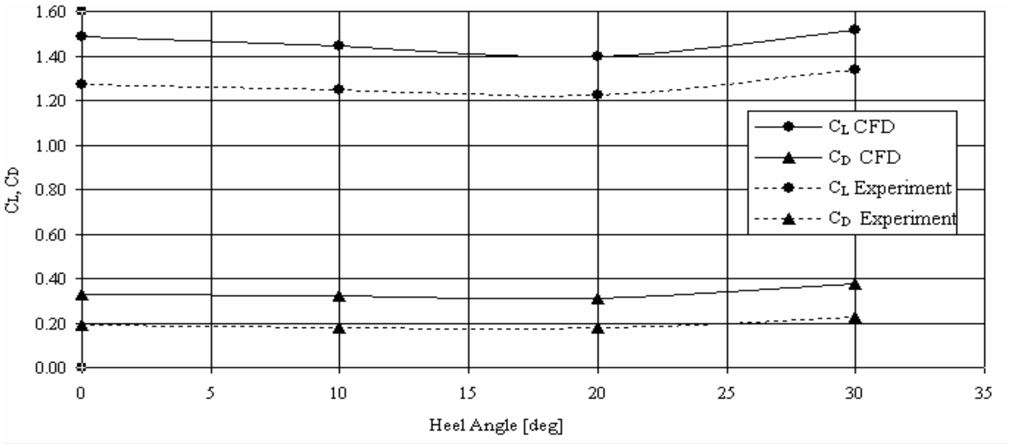

Fig. 5: C_D and C_L for experimental data and CFD results. Different heel angles are investigated where the AoA remains constant at the value of 27deg.

Fig. 5 shows the experimental and CFD results for a varying heel angle where the AoA is kept at a constant 27 deg. It can be seen that C_D and C_L decreases approximately linear to a heel angle of 20 deg and increases for the 30 deg heeled sail rig. Fig. 5 illustrates the same development of the CFD and experimental data as the heel angle increases. It can be seen that CFD is able to captures the special flow behaviour observed during the wind tunnel tests in the Wolfson Unit. Generally, an overprediction of the drag coefficient is observed which can be explained by either: (1) a general overprediction of drag by the SST model or (2) the use of an insufficiently fine mesh of middle density due to the lack of computational power.

Fig. 6 below displays the CFD results with and without hull and the experimental data of the Wolfson Unit. The presented experimental values are obtained by varying the position of the sails whereas the hull and the wind direction remain constant. The best fit lines describe the efficiency of the sail rig height where lines of shallow slope identify greater efficiency than the steep ones as their lift to drag ratio increases.

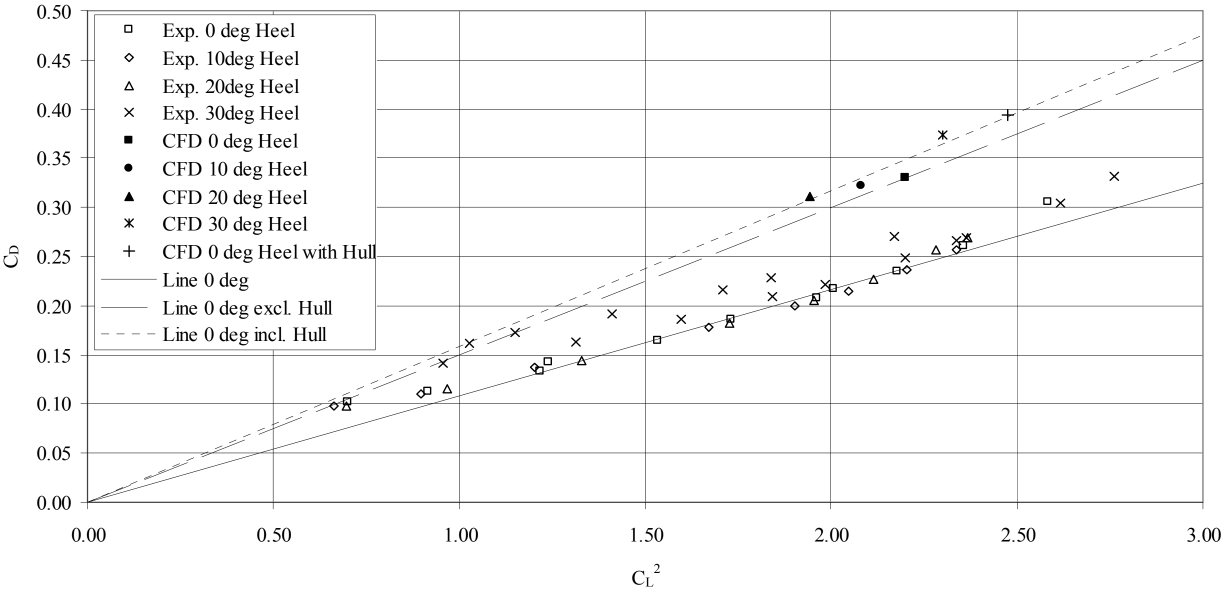

Fig. 6: Experimental and CFD data for 27deg AoA including hull

The added lines in the figure above clearly show a difference between the efficiency of the 0 deg and 30 deg heeled sails for the experimental results as the induced drag efficiency changes for the 30 deg heeled case. The same behaviour is observed for the CFD results as the lines of best fit clearly identify a loss of efficiency for the 30 degrees heel angle compared to the 0 degree heel angle simulation. Furthermore, not only the notable change of the shift in the lines is captured by the CFD calculation, but also the fact that the three data points for 0, 10 and 20 deg cases are comparable as can also be seen from the experimental results. The effect of the hull on the performance of the sailing yacht is also clearly evident. The slope of the corresponding line is steeper than that of those without the hull. This loss of efficiency can be explained considering Fig. 8, where flow 'jump' over the hull is observed. This 'jump' makes the flow less efficient by changing the pressure distribution of the jib and mainsail in an unfavourable way, especially at the foot.

Three main vortices are generated by the sail rig; two smaller ones at the top of the mast and at the end of the foot of the mainsail and a big vortex around the top region of the jib and mainsail. The two smaller vortices decrease in strength rapidly and are almost negligible after 3-4 yacht lengths downstream of the sail rig. Therefore they are not further considered in this study. The major vortex generated from the top region of the jib and mainsail are coalesced after 2 yacht length downstream of the sail rig and plays the dominant role in the resultant sail vortex system (see Figures 7 and 8).

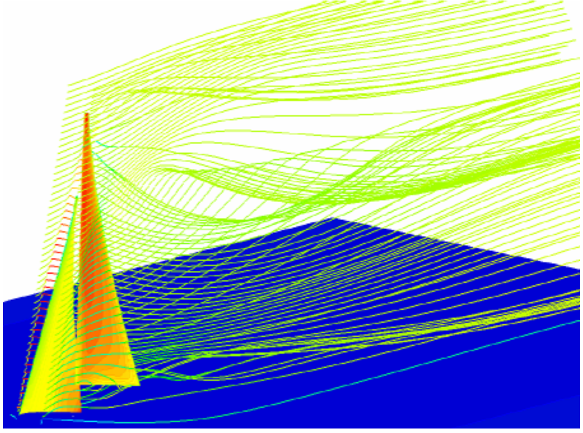

Fig. 7: Local pressure contour on sails and streamlines to identify the vortices in the wake. 27deg AoA and 10 deg heeled sail rig.

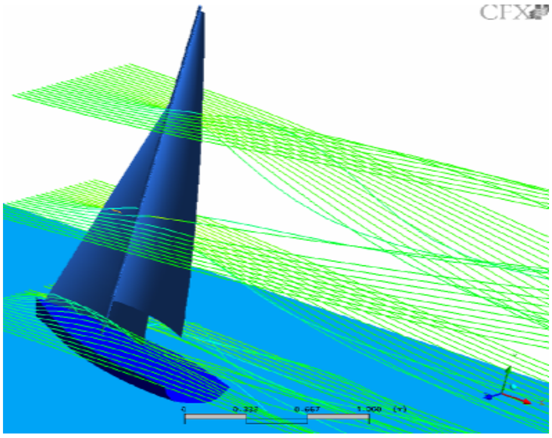

Fig. 8: Streamlines around sailing yacht to show the updated flow behaviour downwind as the flow has to 'jump' over the hull. 27deg AoA and 0 deg heel angle.

Figure 9 below displays the development of the maximal vorticity of the major vortex downstream of the sail rig. It can be observed that the vorticity values have different starting values and decrease exponential. The varying starting values can be explained by the different generated lift which differs according to the actual incidence angle. The steep decrease in vortex strength continues up to the value of 2 yacht lengths downstream and decelerates afterwards. Furthermore, it can be seen that the exponential decrease in vortex strength (vorticity) does not vary much for the different sail rig setups and wind conditions.

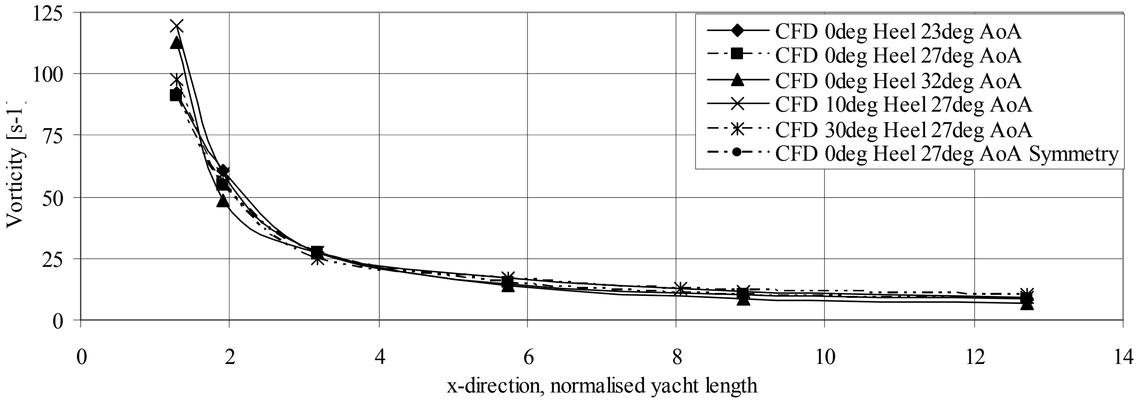

Fig. 9: Development of maximum vorticity downstream of the sail rig, 0 in x-direction describes the bow and 1 the stern of the sailing yacht, CFD results for different heel and incidence angles.

Figure 10 shows the tracks of the vortex cores at different locations downstream of the sail rig. It can be observed that the filaments of the vortex cores start at around 70% of the mainsail height, whereas the highest shed off value is reached at 32deg AoA. Afterwards, the vortex core filaments decrease to a minimum that occurs at around 57% in horizontal and 13% vertical direction for all runs expect for the 30 heeled sail rig setup (60% and 18%, respectively). Subsequently, the vortex cores gain between 3% and 5% in height, whereas the simulation with 32deg AoA achieves the greatest increase. Furthermore, the vortex core of the 30 deg heeled sail rig covers the greatest vertical distance of all sail rig setups. The presents of the side walls of the wind tunnel domain are likely to have a small influence on the filament of the vortex cores that has to be investigated in future. A first step in this direction was carried out by applying the 'symmetric' boundary conditions on the wind tunnel side walls. For this simulation no effect on the vorticity and the position of the vortex cores could be observed (see Figures 9 and 10). To investigate this influence in more detail, further investigations with a bigger wind tunnel domain will be carried in future.

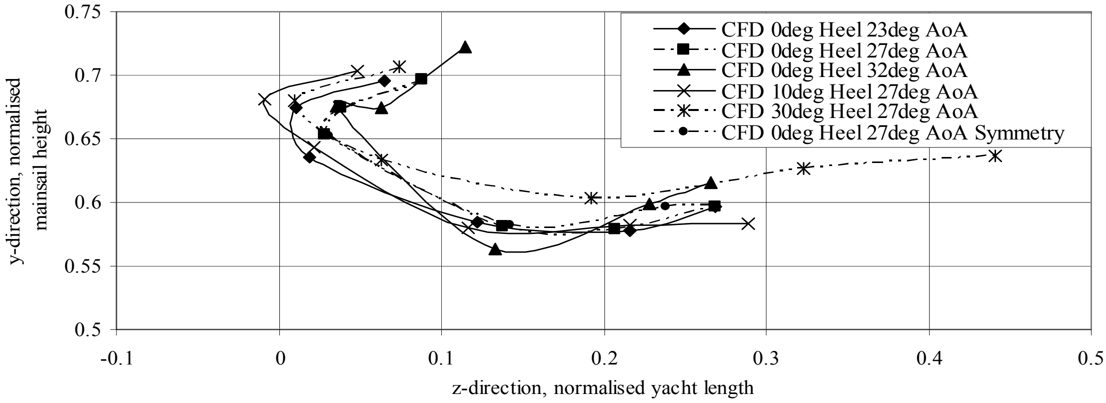

Fig. 10: Tracks of vortex cores within the sail rig wake downstream; the line starting points at around 70% of the normalised mainsail height describe the position of the vortex cores at the stern of the yacht and the line end points express the vortex core position 9 yacht length downstream of the stern; the other 4 points of a vortex core track are calculated at 0.5, 1.5, 3.5, and 6 yacht lengths downstream of the yacht's stern, CFD results for different heel and incidence angles.

5 Conclusion and Future Work

This study clearly demonstrates that the effect of heel angle is captured by the RANS-equations using the SST model. The aim of showing the effect of heel on sail rig performance was achieved and the trends of the computed results show good agreement with experimental data. Moreover, the special flow behaviour for the 30 degrees heeled sail rig is well predicted as the flow around the sails is correctly calculated and the difference between the 20 and 30 degrees heel angle is clearly visible, as also observed by experiment. The only disadvantage is the overprediction of the drag coefficient in the simulations. This can be solved by using more computing power. Furthermore, for a more detailed wake analysis, a Statistical Identification Method such as *VORTFIND* has to be considered for identifying the vortex cores as the used vorticity maxima and pressure minima methods have difficulties in identifying weak vortices in the presence of a shear flow [13]. Nevertheless, the wake examination, especially the vortex analysis, led to important results that can be used for the development of a more detailed model to capture blanketing and covering within a fleet race. Further investigation with a bigger computational domain downwind of the sail rig have to be carried out to determine influences of the side walls of the wind tunnel and the entire affected area by the sail rig.

References:

[1] Scarponi M. 2008 '*Including Human Performance in the Dynamic Model of a Sailing Yacht: A Combined Ship Science – Behavioural Science Approach Towards a Winning Yacht-Sailor Combination', PhD Thesis*, Università di Perugia.

[2] Scarponi, M., Shenoi, R.A., Turnock, S.R., Conti, P. 2007 '*A combined ship science behavioural science approach to create a winning yacht-sailor combination*', SNAME, The 18th Chesapeake Sailing Yacht Symposium, pp. 1-10.

[3] Philpott, A., Henderson S.G., Teirney, D.P. 2004 '*A simulation model for predicting yacht match-race outcomes*', Operations Research, Vol.52 (1), pp. 1-16.

[4] Graf, K., Wolf, E. 2006 '*CFD Investigations and Design Integration for IACC Yachts'*. 2nd High Performance Yacht Design Conference Auckland.

[5] Parolini, N. and Quarteroni, A. 2005 '*Mathematical models and numerical simulations for the America's Cup*', Comput. Methods Appl. Mech. Engineering 194, pp. 1001-1026.

[6] Yoo, J., Kim, J., Park, I., Ahn, H., Van, S. 2006 '*CFD Calculations on the Sail-like Three Dimensional Airfoils',* 2nd High Performance Yacht Design Conference Auckland.

[7] Collie, S., Gerritsen, M. 2006 '*The Challenging Turbulent Flow Past Downwind Yacht Sails and Practical Application of CFD to Them.'* 2nd High Performance Yacht Design Conference Auckland.

[8] Teeters, J., Ranzenbach, R., Prince, M. 2003 '*Changes to Sail Aerodynamics in the IMS Rule'*. The 16th Chesapeake Sailing Yacht Symposium.

[9] Spenkuch, T. 2006 '*Effect of heel on sail rig performance using CFD: a quantified evolution of the ability of CFD to capture this behaviour*', MSc Thesis, University of Southampton, UK.

[10] Lesieur, M,. Begou, P., Comte, P. & Métais, O. 2000 '*Vortex recognition in numerical simulations*'. ERCOFTAC, Bulletin No. 46, pp. 25-28.

[11] Banks, D. & Singer, B. 1995 '*A predictor-corrector technique for visualizing unsteady flow*'. IEEE Transactions Visualization and Computer Graphics 1, pp. 151-163.

[12] Newman, B., Low, H. 1984 '*Two-dimensional impervious sails: experimental results compared with theory'*, Journal of Fluid Mech., Vol. 144, pp. 445-462.

[13] Pemberton, R.J., Turnock, S.R., Dodd, T.J., E. Rogers 2002 *'A Novel Method for Identifying Vortical Structures'*. Journal of Fluids and Structures 16(8), pp. 1051-1057.

Eleventh Numerical Towing Tank Symposium
NuTTS 2008, Brest, France

Improvement to body impact predictions using CFD through analysis of an unsteady boundary layer.

Simon G. Lewis[1], Dominic A. Hudson, Stephen R. Turnock

University of Southampton, University Road,
Southampton, SO17 1BJ, UK

1. Introduction

Small boats are often required to operate at as high a speed as possible. The crew experience repeated shocks and vibration, which can lead to a reduction in their physical and mental performance. Accurate prediction of the motions of high speed craft is an essential element in understanding the response of the crew to a particular design configuration. Previous work has been conducted using a non-linear potential flow model and the use of computational fluid dynamics to model wedge impacts with water (Hudson et al, 2007).

In order to model the flow around complex bodies accurately, the boundary layer must be predicted correctly. The problem of a body impacting water and subsequent settling requires an unsteady boundary layer to be modelled. In order to ensure that this boundary layer is being modelled correctly, the flow along an impulsively started flat plate moving parallel to the flow is investigated. The boundary layer on an impulsively started flat plate is well understood and is also reasonably simple to model using CFD. A commercial Naver-Stokes equations solver is used to carry out the simulation (ANSYS, 2008). The results are used to develop a methodology for generating a mesh capable of boundary layer resolution in this type of flow. A bow section impacting with water is then modelled, using the techniques developed for accurate prediction of the boundary layer.

2. Boundary Layer

A significant amount of work has been carried out on impulsively started boundary layers and the subject is well understood. The initial stage of the development of a boundary layer with time is defined by Rayleigh (1911) for an infinite plate. As the boundary layer reaches a steady state, it is best described by Blasius (1908). The development of the flow from the initial to the steady state is described by Hall (1969) and the empirical data from this model is used for comparison with the CFD (see section 2.2). Initially, the steady state results are analysed, with the results presented in section 2.1.

The mesh has a length of 0.4m, a height of 0.05m and a width of 0.001m. The problem is two dimensional (2D) although the software does not have the option to solve 2D problems and so the computational domain width is one cell thick. A check is carried out to ensure there is no flow in the spanwise direction (i.e. parallel to the leading edge of the plate). The leading edge of the plate is positioned 0.5m downstream from the flow inlet. Three meshes are constructed, each with a different number of cells. Variations between each mesh are given in table I.

Table I: Parameters of each mesh

Number of cells	Distance of first cell from the wall.
5000	$4.0*10^{-3}$ m
50000	$1.8*10^{-4}$ m
90000	$5.0*10^{-5}$m

A timestep of 0.0001s is chosen to ensure that the Courant number remains close to 1 as desired (WS Atkins Consultants, 2003).

---

[1] Email: sgl101@soton.ac.uk

2.1 Prediction of the steady boundary layer

The turbulent boundary layer thickness for a two dimensional infinite flat plate is defined by White (1999) as:

$$\frac{\delta}{x} = \frac{0.16}{\mathrm{Re}_x^{1/7}},$$

where Re_x is the length based Reynolds number of the flow along a flat plate. This is defined as:

$$\mathrm{Re}_x = \frac{Ux}{\nu},$$

where x is the distance from the leading edge of the plate to the point under consideration, U is the free stream velocity and ν is the kinematic viscosity. The wall shear stress is defined by White (1999) as

$$\tau_w = \frac{1}{2}\rho U^2 C_f,$$

where C_f is the coefficient of skin friction, given as

$$C_f = \frac{0.0594}{\mathrm{Re}_x^{0.2}}.$$

A comparison between the theoretical boundary layer thickness and the predicted boundary layer across the plate is presented in Figure 1. The CFD results are given for each of the meshes. Similarly, the wall shear stress across the plate is illustrated in figure 2. The finest mesh (with 90000 cells) produces the most accurate predictions for the boundary layer thickness. The shear stress on the plate wall is under-predicted from the leading edge of the plate to 0.2m downstream.

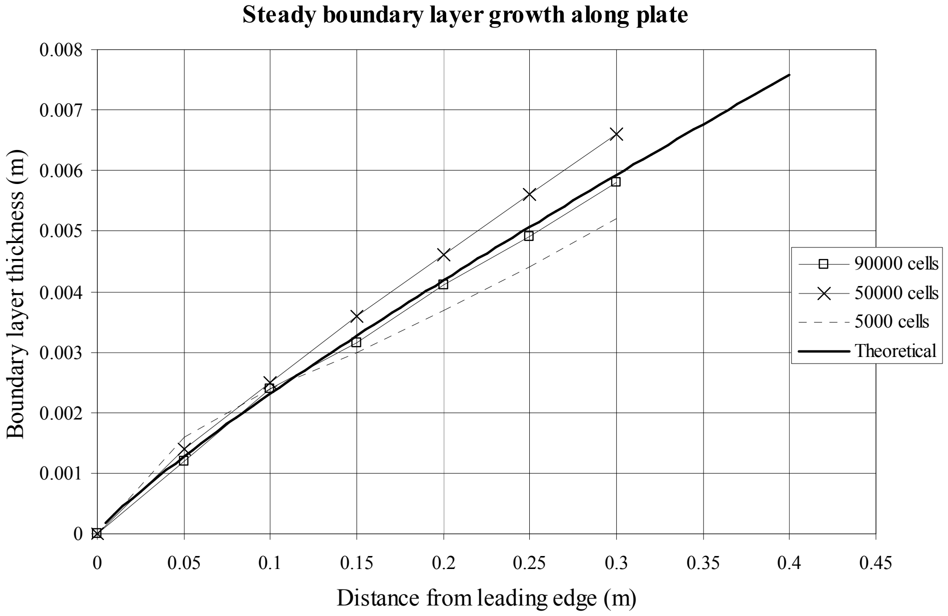

Figure 1: Boundary layer thickness distribution along the plate.

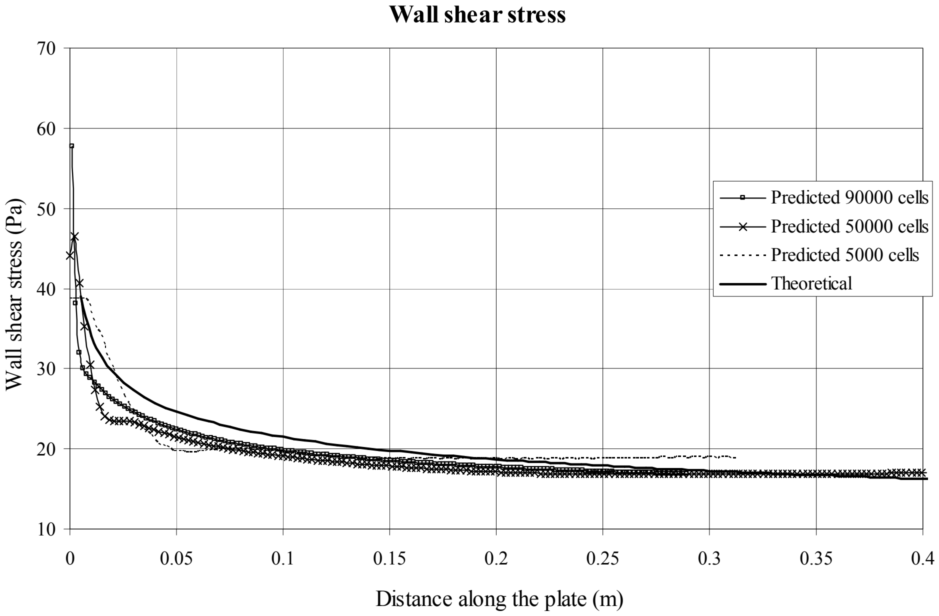

Figure 2: Wall shear stress distribution along the plate.

2.2 Boundary layer on an impulsively started plate

The theory used to solve unsteady boundary layer equations can be found in Hall (1969). Figure 3 presents the unsteady boundary layer growth at two positions on the plate: 0.1m and 0.25m from the leading edge. The boundary layer thickness is non-dimensionalised. The CFD shows a good correlation with the theoretical results.

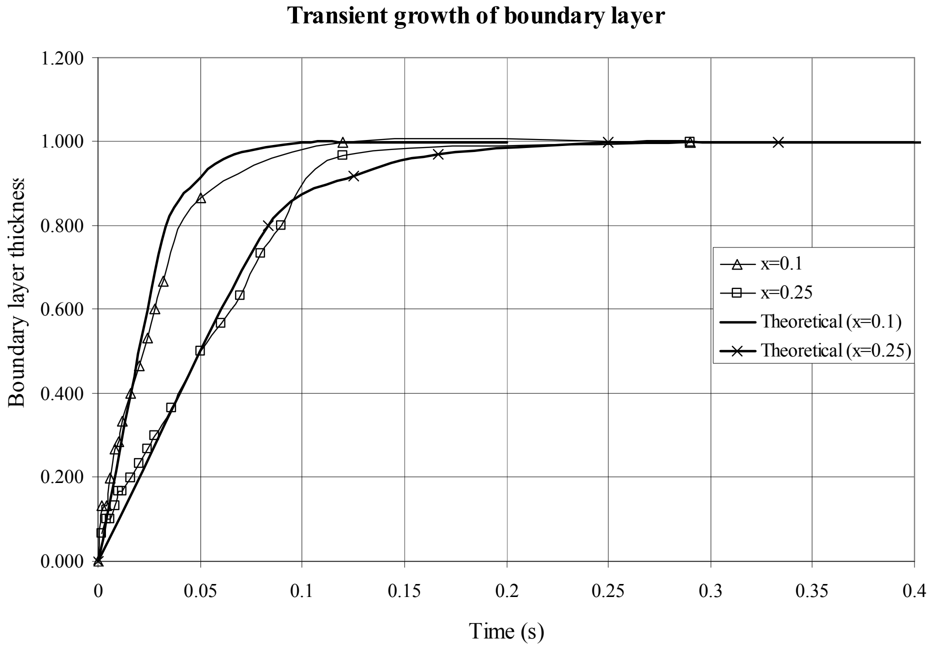

Figure 3: Transient growth of boundary layer at x = 0.1 and 0.25.

Using this data, the same y+ values are used to create the mesh for the hull water entry problem presented in section 3.

3. Ship bow section entry

A ship bow section was dropped from varied heights into a small towing tank at MARINTEK. The tank is 30m long, has a width of 2.5m and a depth of 1m. The bow section, presented in figure 4, has a breadth of 0.32m, a draft of 0.2m and a length of 1m. Table II presents the coordinates of the geometry of the hull section with units in *mm*. The highlighted coordinates represent the position of the 4 pressure transducers. The total weight of the drop rig was 261kg.

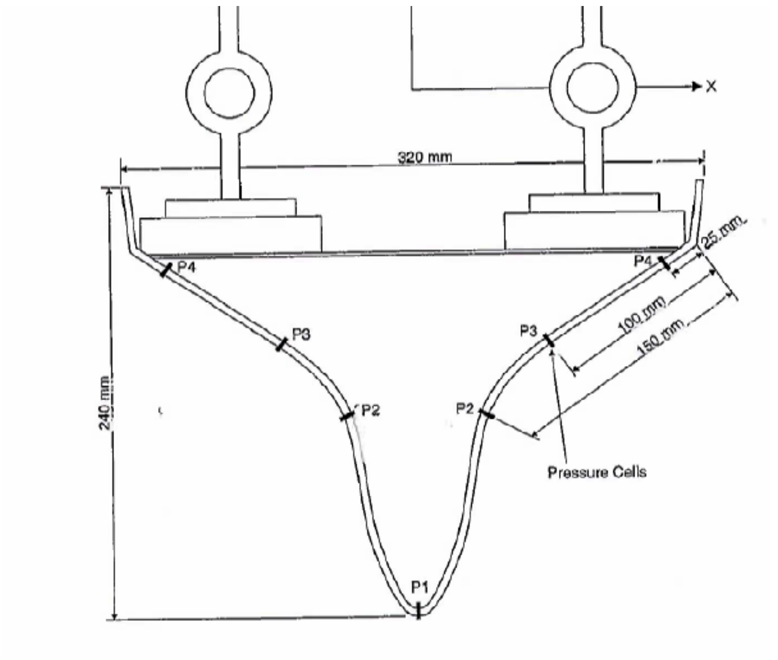

Figure 4: Diagram of ship bow section (Aarsnes, 1996).

Table II: Coordinates of the bow section

x	y
0	**-240**
5	-240
16	-227.9
23.3	-210.6
28.9	-192.3
32.7	-170.4
35.6	-150.3
41.2	**-130.2**
49.5	-113.8
61.3	-102.1
75	**-89.5**
94.1	-76.9
114.2	-64.4
139.7	**-48.3**
156.1	-36.6
160	0

Measurements were taken with a sample rate of 20 kHz in most tests. Data collected during the tests include:

- Force measurements
- Pressure measurements using a pressure cell with a range of 0 – $1.5*10^6$ $N.m^{-2}$. The cell diameter is 3mm.
- Acceleration measured using accelerometer with a range of 0 – 10*g*, with a linear frequency range of 0 – 1kHz.
- Wetted surface measurements using wave gauge tape.

Three meshes of the bow section were created, each with a length of 0.8m and a height of 0.4m. The finest mesh contained 30000 cells, and the first node was situated $2 * 10^{-5}$m from the wall of the bow section (see figure 5). The time step is varied from 0.5ms to 0.05ms. The details of the method for the CFD simulation can be found in Hudson et al (2007).

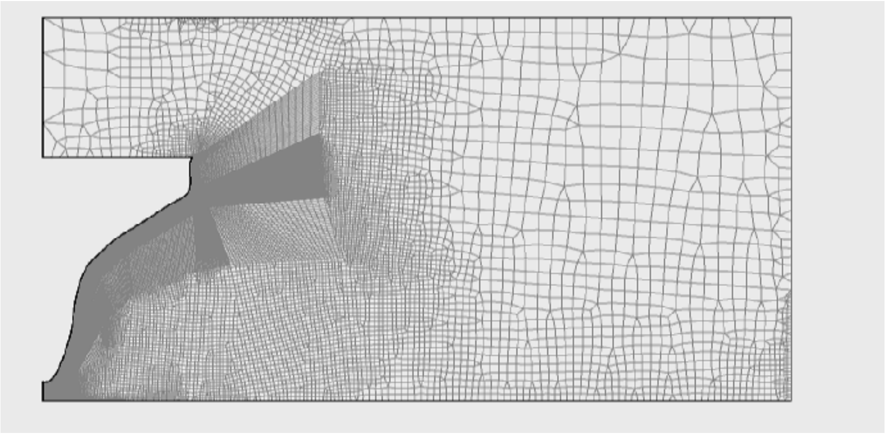

Figure 5: Mesh for the ship bow section.

3.1 Results

Figures 6 and 7 present the results of the pressures predicted at each of the pressure transducers (shown in figure 4). The impact pressures are captured well, although are under predicted by up to 10%. It should be noted that the bow section was decelerated by a spring mechanism after the impact occurred, although information regarding the point at which the spring starts acting is not available. It is therefore assumed that after 0.07 seconds, the acceleration of the wedge is affected by the spring system.

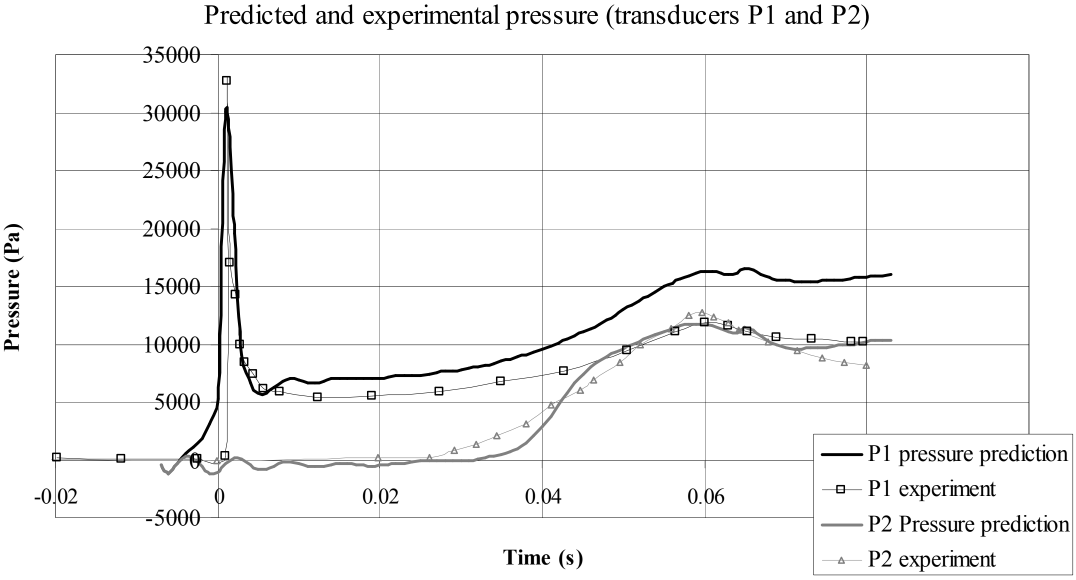

Figure 6: Pressure predictions compared with experimental data from pressure transducers P1 and P2.

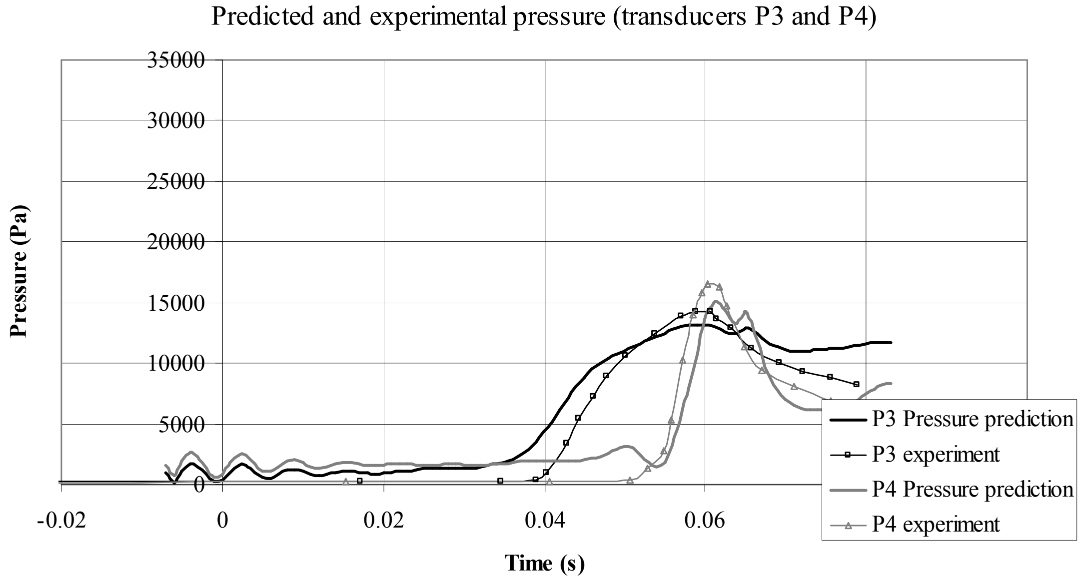

Figure 7: Pressure predictions compared with experimental data from pressure transducers P3 and P4.

4. Conclusions

A computational fluid dynamics method using the Reynold's averaged Navier-Stokes equations is applied to solve the problem of a two-dimensional unsteady flow along a flat plate. The investigation carried out on the unsteady boundary layer on a flat plate provides insight into the most suitable means to model more complex CFD problems. This accurate modelling of an unsteady boundary layer allows improvements in the prediction of a body impacting with water. The results presented demonstrate that such a CFD approach predicts the magnitude and time history of the pressure distribution accurately as compared to available experimental data.

Acknowledgements

This work is part funded by the EU FP6 funded Network of Excellence, MARSTRUCT.

References

Aarsnes J. J., 1996 Drop test with ship sections – effect of roll angle *MARINTEK report number 603834.00.01.*

ANSYS 2008, CFX version 11, user manual available at http://www.kxcad.net/ansys/, last accessed July 2008.

Blasius, H., 1908. Grenzschichten in Flüssigkeiten mit kleiner Reibung, *Z. Math. U. Phys.*, Vol. 56 pp.1-37.

Hall M. G., 1979. The boundary layer over an impulsively started flat plate. *Proceedings of the Royal Society of London. Series A. Mathematical and Physical Sciences*, Vol 310 No. 1502 pp. 401-414.

Rayleigh, Lord, 1911. On the motion of solid bodies through viscous fluid, *Phil. Mag.*, Vol. 21 pp.697-711.

Hudson, D. A., Turnock S. R., Lewis S. G., 2007. Predicting motions of high-speed rigid inflatable boats: Improved wedge impact prediction, *Proceedings of the Ninth International Conference on Fast Sea Transportation FAST2007*, Shanghai, China, September.

White F. M., 1999. Fluid Mechanics Fourth Edition *McGraw Hill.*

WS Atkins Consultants. (2003). 'MARNET best practice guidelines for marine applications of computational fluid dynamics'. Technical report, MARNET.

Simplified models for the estimation of slamming loads on bulbous bows.

Alan TASSIN [1,2], Nicolas JACQUES [1], Alain NEME [1], Jean-Marc LAURENS [1]
tassinal@ensieta.fr, jacqueni@ensieta.fr, nemeal@ensieta.fr, laurenje@ensieta.fr
[1] LBMS - ENSIETA - 2 rue François VERNY, 29806 BREST CEDEX 9
[2] DCNS - Ingénierie des Navires Armés - Dép. Analyse de Structures

Acknowledgement: This work is supported by the French naval group DCNS, which provides the subject and a PhD grant.

1 Introduction

Some bulbous bows are used as sonar domes and are generally made of fibre-reinforced plastic. The largest hydrodynamic loads acting on these composite structures are due to slamming. Therefore, it is an important criterion for the design of these structures. Although it is possible to correctly estimate such loads by numerical models based on the finite volume method or the finite element method (FEM), the associated high computation costs prohibit their use for optimization in a design approach. As a consequence, ship builders are interested in the development of dedicated slamming aid design tools as a complement to common sea keeping software.

Since the 1930s, simplified models (solutions to the Wagner problem) have been proposed for two-dimensional (2D) flows. These models are reliable, especially for blunt sections. In this paper, the 2D Wagner problem is first presented (for an overview see [2], [8]), a semi-analytical solution is described and a three-dimensional strip method is used for the pre-determination of the slamming loads on two different specimens with aspect ratios of common bulbous bows. The results of the strip method are compared to those of a Finite Element Analysis performed with Abaqus/Explicit. The strip method results differ significantly from the 3D FEM results. A 3D analysis of the flow must be considered to study the impact of bulbous bow type structures. As a consequence, solutions based on the 3D Wagner problem should be developed.

2 A semi-analytical tool for the slamming of two-dimensional arbitrary sections

Since Wagner first set down the well known “Wagner problem” that accurately describes the global flow and rationally estimates the slamming force for small dead rise angles, a lot of studies have contributed to extend the model to large dead rise angles, general body shapes and the description of the jet region (see [4], [5], [6], [7]). The 2D Wagner problem is described above and a semi-analytical method to determine the wetted surface for arbitrary body shapes is described in detail. This 2D solution is used to calculate the slamming loads on 3D bodies using a strip method and using the regularised pressure field solution proposed by Zhao & Faltinsen [3].

2.1 The Wagner theory

The Wagner theory is based on a simplification of the impact problem in a coupled problem: the instantaneous fluid flow approximation and the wetted surface evolution. For the sake of convenience, this study is limited to the impact at constant speed V $(V>0)$. The cross-section is assumed to be symmetric about its vertical centreline and is represented by function $h(x)$, which defines the vertical distance between a point of the surface and the section bottom.

The fluid problem is formulated assuming an ideal fluid flow (incompressible, inviscid and irrotational) described by a velocity potential φ. The liquid is initially at rest and gravity effects are neglected. The fluid free surface and the solid geometry are assumed to remain close to their initial state. All the boundary conditions are then linearized and projected on the initial free surface $z=0$ (see Figure 1).

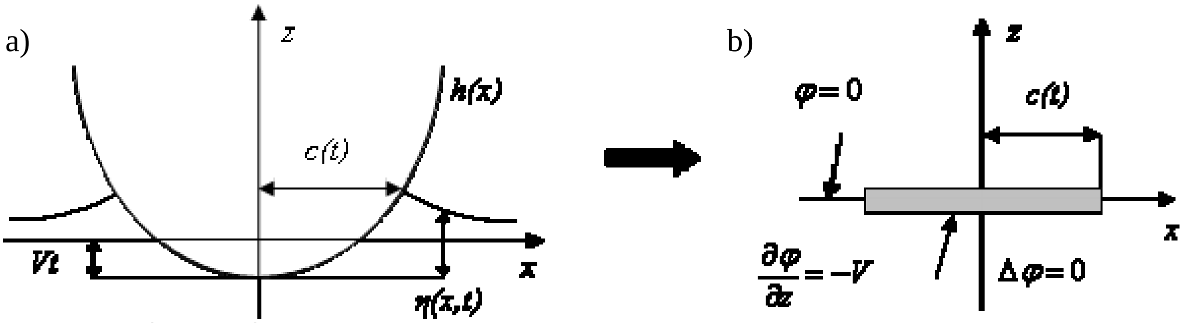

Figure 1 : Definition of the impact problem (a) and its approximation according to the Wagner theory (b).

The velocity potential has to verify the following system of equations:

$$\begin{cases} \Delta\varphi = 0 & & (1) \\ \varphi = 0 & z = 0\,, |x| > c(t) & (2) \\ \dfrac{\partial\varphi}{\partial z} = -V & z = 0\,, |x| < c(t) & (3) \\ \nabla\varphi \to 0 & \sqrt{\mathrm{x}^2 + z^2} \to \infty & (4) \end{cases}$$

This system can be solved analytically by introducing the complex velocity potential and using conformal mapping (see [1]):

$$\varphi = -V\sqrt{c(t)^2 - x^2} \quad \text{on } z = 0^- \text{ and } |\mathrm{x}| < c(t) \qquad (5)$$

The pressure is obtained by the linearized Bernoulli equation:

$$p = -\rho\,\partial\varphi/\partial t\,, \qquad (6)$$

where ρ is the fluid density. At this stage, the wetted surface width *c(t)* is unknown and has to be determined.

2.2 Computation of the width of the wetted surface

From the analytical flow solution, the vertical relative velocity between a point on the free surface and the body is obtained as a function of the wetted surface width *c(t)*:

$$U_r(x,t) = \frac{\partial\varphi}{\partial z} + V = \frac{V|x|}{\sqrt{x^2 - c(t)^2}} \text{ for } |x| > c(t) \qquad (7)$$

The time integration of the free surface relative speed U_r gives the free surface relative elevation $\eta(x,t)$

$$\eta(x,t) = \int_0^t U_r(x,\tau)d\tau = \int_0^t \frac{V|x|}{\sqrt{x^2 - c(\tau)^2}}d\tau \qquad (8)$$

By using the substitution $\gamma = c(\tau)$ in eq. 8 and introducing function μ such as

$$\mu(\gamma) = \frac{Vd\tau}{d\gamma} \quad , \qquad (9)$$

the following expression is obtained for the relative free surface elevation:

$$\eta(x,t) = \int_0^{c(t)} \frac{|x|\mu(\gamma)}{\sqrt{x^2 - \gamma^2}}d\gamma \qquad (10)$$

The width of the wetted surface is the x-coordinate of the intersection point between the free surface and the body, and thus is solution of the following equation:

$$h(c) = \int_0^c \frac{c\mu(\gamma)}{\sqrt{c^2 - \gamma^2}}d\gamma \qquad (11)$$

A closed-form solution can be obtained only for a wedge or a parabola [2]. One way to deal with arbitrary sections is to divide the interval of integration of the right-hand side of Eq.10 into parts as:

$$\int_0^c \frac{c\mu(\gamma)}{\sqrt{c^2-\gamma^2}}d\gamma \quad = \sum_{\mathrm{k=1}}^{\mathrm{N}} \left(\int_{c_{k-1}}^{c_k} \frac{c\mu(\gamma)}{\sqrt{c^2-\gamma^2}}d\gamma \right) \text{, where } \mathrm{c}_0 = 0 \text{ and } \mathrm{c}_\mathrm{N} = \mathrm{c} \qquad (12)$$

Assuming $\mu(\gamma)$ continuous over the interval [c_0 , c_N] and linear over each subinterval [c_{k-1} , c_k], that is $\mu(\gamma) = \mu_{k-1} + \frac{\gamma - c_{k-1}}{c_k - c_{k-1}}(\mu_k - \mu_{k-1})$ for $c_{k-1} < \gamma < c_k$ and where $\mu_k = \mu(c_k)$, eq. 11 then leads to:

$$h(\mathrm{c_i}) \quad = \sum_{\mathrm{k=1}}^{\mathrm{i}} \left(\int_{c_{k-1}}^{c_k} \frac{c_i\mu(\gamma)}{\sqrt{{c_i}^2-\gamma^2}}d\gamma \right) \qquad (13)$$

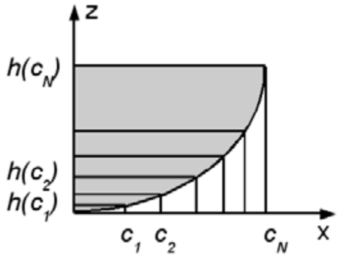

Figure 2 : Body shape discretization.

The right-hand side of eq. 13 can be estimated analytically. Therefore, the coefficient μ_k is obtained from the coefficients already determined ($\mu_j, j = 0$ to k-1) and from $h(c_k)$ (see Figure 2). μ_0 is set to 0 for a body with horizontal tangency at the keel and to $2h(c_1)/\pi c_1$ for a sharp edged body at the keel.

The integration of Eq. 9 allows us to obtain:

$$D_i - D_{i-1} = \int_{c_{i-1}}^{c_i} \mu(\gamma).d\gamma \ , \qquad (14)$$

where D_i denotes the penetration depth at time t_i such as $c(t_i) = c_i$.

$$D_i = \int_0^{t_i} V.dt \qquad (15)$$

2.3 Pressure computation

The classical Wagner solution for the pressure has been improved. Zhao & Faltinsen (see [3]) present a regular solution from the Wagner solution (see [2]) and the local jet solution using matched asymptotic expansions. Eq. 16 below presents the pressure expression for $|x| \le c$:

$$p = \underbrace{\rho V \,\mathrm{c}\frac{\mathrm{dc}}{\mathrm{dt}}(c^2 - x^2)^{-1/2}}_{\text{Wagner term}} \underbrace{- \rho V c\frac{\mathrm{dc}}{\mathrm{dt}}[2c(c-x)]^{-1/2}}_{\text{matching term}} + \underbrace{2\rho\left(\frac{\mathrm{dc}}{\mathrm{dt}}\right)^2 |\tau|^{1/2}\left(1+|\tau|^{1/2}\right)^{-2}}_{\text{jet term}} , \qquad (16)$$

where τ is related to x by:

$$x - c = \frac{\delta}{\pi}(-\ln|\tau| - 4|\tau|^{1/2} - |\tau| + 5) , \qquad (17)$$

and δ is the jet thickness:

$$\delta = \pi V^2 2c\left(4\frac{dc}{dt}\right)^{-2} . \qquad (18)$$

For $|x| \ge c$, the pressure expression is given by the jet term of eq. 16.

Figure 3 shows the slamming load during the impact of a cylinder of radius R. The results obtained by the proposed semi-analytical model are compared to those of a Finite Element Analysis and to the experimental data of Campbell and Weynberg [11]. A good agreement is observed between the different results, which validates the proposed method. The force per unit length F is obtained by integrating the pressure from $x=-2c$ to $x=2c$, neglecting the pressure contribution for $|x| > 2c$.

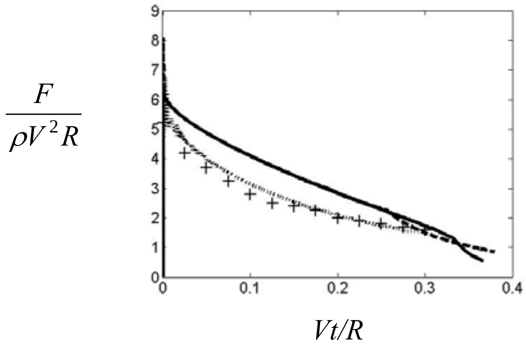

Figure 3: Load coefficient as a function of the penetration ratio for a cylinder. (+) experiments of Campbell and Weynberg [11], (..) FEM with Abaqus/explicit, (--) Semi-analytical with 10 subintervals, (__) Semi-analytical with 50 subintervals

3 Strip method for three-dimensional structures

In this section, a strip method is applied to estimate slamming loads on 3D bodies. The principle is trivial: 2D computations are run on cross sections orthogonal to the principal axis X_1 of the structure. Therefore, the fluid flow in the X_1 direction is neglected (see Figure 4 below).

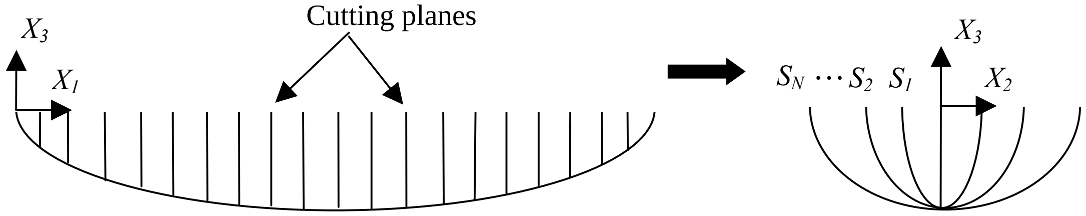

Figure 4: Example of cross-section generation on an elliptic body.

4 Three-dimensional Finite Element Analysis

The Coupled Eulerian-Lagrangian (CEL) capability in the finite element commercial software ABAQUS/Explicit is used to analyse the hydrodynamic impact of three-dimensional bodies. In the CEL approach, an Eulerian multi-material formulation is used to describe the fluid flow, while the structure is modelled within the Lagrangian framework. The Eulerian mesh is fixed in space, and the material can flow through the elements. Besides, each element can contain a mixture of two or more different materials. The Eulerian solver in ABAQUS/Explicit is based on the volume-of-fluid method. In this method, a new variable is added within each element for each material included in the model: the volume fraction of this material. At the end of each time increment, the material interfaces in the Eulerian domain are reconstructed using the volume fraction data. A special fluid structure coupling algorithm enforces the interaction between the Lagrangian structure and the Eulerian materials. This algorithm forces to be transmitted between the Eulerian and Lagrangian meshes, which are superimposed (Figure 5). Therefore, there is no need to use a conforming mesh for the Eulerian domain. However, this domain should be extended beyond the initial water surface in order to capture the strong deformation of the free surface due to slamming (Figure 6). The size of the Eulerian domain is about five times larger than the one of the impacting solid. For the simulation presented in this paper, the meshes contain between 1.7 and 2.3 million elements. A 3 ms simulation has a run time of about 12 hours on a single processor workstation and requires about 8 gigabytes of memory.

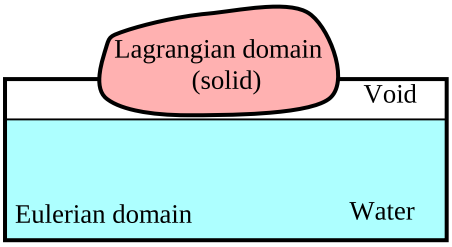

Figure 5 : Schematic representation of the FE model (initial configuration).

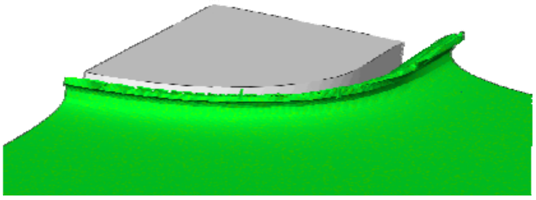

Figure 6: Deformation of the water free surface. By symmetry, only a quarter of specimen I is meshed.

5 Results

The strip method has been applied to two different structures with aspect ratios (Width/Length) of common bulbous bows: a cylinder with a length of 192mm and a radius of 320 mm with two hemispherical extremities of the same radius and a wedge with a length of 192mm and 15° angle with two conical extremities of the same angle. Both specimens are 320mm wide and their total length is 512mm.

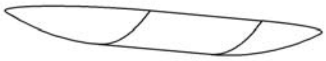

Figure 7: Specimen I: cylinder+sphere

Figure 8: Specimen II: wedge+con

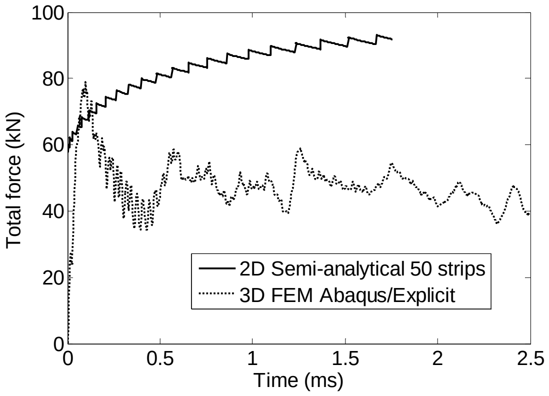

Figure 9 : Total force as a function of time for an impact speed of 12m/s on specimen I.

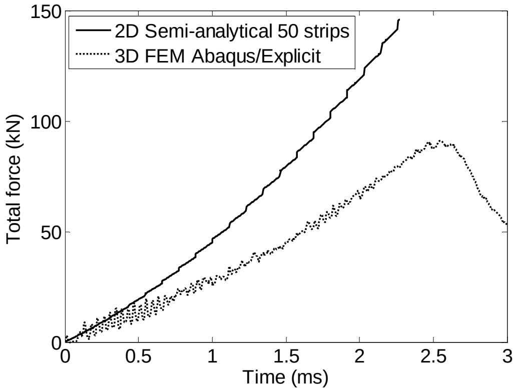

Figure 10 : Total force as a function of time for an impact speed of 12m/s on specimen II.

Figure 9 and Figure 10 compare the performance of the strip method to the 3D FEM results, where 3D FEM is considered as the reference. Significant discrepancies between the results of the strip method and those of the FEM analyses are obtained. The loads predicted by the strip method are significantly greater than the ones obtained with 3D FEM computations. The strip method used for slender bodies, is clearly not reliable for large aspect ratio bodies such as specimens I and II. Indeed, the aspect ratio (Width/Length) of specimens I and II is 0,625. Scolan & Korobkin [9] have studied for an elliptic paraboloid, the influence of the aspect ratio on the Force ratio F_{3D}/ F_{2D}, where F_{3D} and F_{2D} are respectively the slamming loads obtained with a 3D Wagner solution and with a strip method based on a 2D Wagner solution. For an aspect ratio of 0,625, F_{3D}/ F_{2D} is equal to 0,72.

6 Conclusion and perspectives

The aim of this work is to develop a tool for the estimation of slamming loads on combined bulbous bows/sonar domes. For this purpose, a strip method based on the 2D Wagner theory has been developed. 3D FEM computations have also been performed. The results obtained with these two approaches show the limitation of the strip theory in the case of bulbous bow type structures. 3D effects on the flow should be considered. The 3D Wagner problem is non-trivial to solve, but analytical solutions for particular geometries show that the phenomenon is accurately described by this approach (see [9], [10]). Few studies examine the resolution of the 3D Wagner problem for arbitrary body shapes. Therefore, it is an interesting approach to investigate.

Experimental impact tests are currently carried out at constant speed on a dedicated high-speed hydraulic test machine available at ENSIETA. Impact tests on cones have already been conducted (see [12]). 3D specimens will be tested in order to validate the load estimations of 3D simplified models and 3D FEM.

7 References

[1] Newman J.N., Marine Hydrodynamics, MIT Press, 1977

[2] Faltinsen O.M., Hydrodynamics of high-speed marine vehicles, Cambridge University Press, 2005

[3] Zhao R., Faltinsen O.M., Water entry of two-dimensional bodies, J. Fluid Mech., Vol. 246, 1993

[4] Zhao R., Faltinsen O.M., Aarsnes J., Water entry of arbitrary two-dimensional sections with and without flow separation, 21st Symposium on naval hydrodynamics, 1997

[5] Cointe R., Two-dimensional water-solid impact, Journal of offshore mechanics and arctic engineering, Vol. 111, 1989

[6] Cointe R., Armand J.-L., Hydrodynamic impact analysis of a cylinder, Journal of offshore mechanics and arctic engineering, Vol. 109, 1987

[7] Xiaoming Mei, Yuming Liu, Dick K.P. Yue, On the water impact of general two-dimensional sections, Applied ocean Research, 21, 1999

[8] Korobkin A., Analytical models of water impact, Eur. Jnl. Of Applied Mathematics, Vol. 15, pp.821-838, 2004

[9] Scolan Y.-M., Korobkin A., Three-dimensional theory of water impact. Part1: Inverse Wagner problem, J. fluid mech., Vol. 440, 2001

[10] Scolan Y.-M., Korobkin A., Three-dimensional theory of water impact. Part2: Linearized Wagner problem, J. fluid mech., Vol. 549, 2006

[11] Campbell I., Weynberg P., Measurement of parameter affecting slamming, Technology reports center, OT-R-8042:3318-334, 1980

[12] Constantinescu A., Nême A., Jacques N., Rigo P., Finite element simulations and experimental investigations of simple 2D geometries in slamming, ASME 27th, International Conference on Offshore Mechanics and Arctic Engineering, paper 57482, Estoril, Portugal, 2008

Numerical Simulation of Stern Slamming and Whipping

Jan Oberhagemann, Ould El Moctar, Michael Holtmann, Thomas Schellin, Volker Bertram,
Germanischer Lloyd, Hamburg/Germany, volker.bertram@GL-group.com
Daewoong Kim, Daewoo Shipbuilding & Marine Engineering, South Korea, daewoong@dsme.co.kr

Our objective was to assess stern slamming for a modern LNG carrier, Table I, under two loading conditions. Particularly the flat area between propeller shafts, Fig.1, may be subject to stern slamming. Details of the procedure are found in *Oberhagemann et al. (2008).* We took the normal relative velocity between hull and water surface in the stern region as criterion to identify critical situations with respect to severe slamming. A linear GFM seakeeping analysis, based on the wave climate of the North Atlantic according to IACS Recommendation 34, yielded maximum normal relative velocities. Equivalent regular design waves, leading to the same relative velocities, were identified. Based on these regular equivalent design waves, input parameters were defined for the RANSE (Reynolds-averaged Navier Stokes equations) simulations, coupled with the computation of the nonlinear ship motions in these waves. The computed pressures were compared with design pressures according to classification society rules. Slamming loads obtained with the RANSE solver served as boundary conditions for transient finite element (FE) computations.

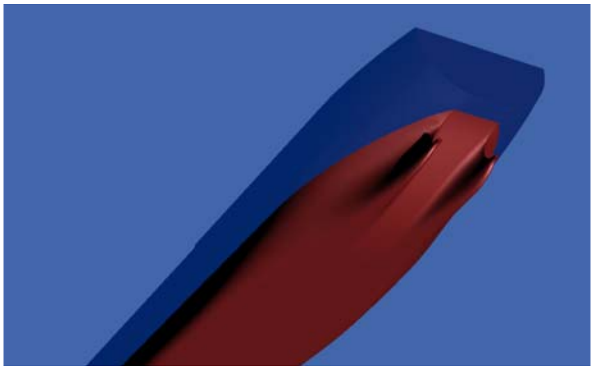

Fig. 1: Stern region of the LNG carrier

Table I: Principal particulars

Length between perpendiculars	303.0 m
Beam at waterline	50.0 m
Design speed	19.5 kn
Draft (ballast condition)	9.4 m
Draft (design condition)	11.7 m
Metacentric height (ballast)	14.0 m
Metacentric height (design)	6.7 m
Longitudinal gyradius (ballast)	75.3 m
Transverse gyradius (design)	16.3 m

To assess effects of hull girder whipping, we performed transient coupled computations that combined fluid dynamics and structural dynamics, *El Moctar et al. (2006).* Only the influence of the transient phenomena of fluid flow on the structure was considered. The influence of structural deformations on the surrounding flow was assumed small and was thus neglected. The commercial RANSE solver COMET computed fluid dynamic pressures, and the finite element software package ANSYS performed the structural analysis. Hydrodynamic forces and moments acting on the ship's hull were converted to nodal forces for the FE model. Mass inertia forces and moments were also added to nodal forces, allowing computations in a ship-fixed coordinate reference frame.

The computational procedure consisted of four steps:

1. A linear GFM code obtains transfer functions of normal relative velocities at previously defined critical areas underneath the ship's stern.
2. A statistical analysis combines these results with user-specified operational restrictions to determine maximum normal relative velocities; then regular design waves for stern slamming are selected leading to these same normal relative velocities.
3. RANSE simulations for the freely moving ship in the selected waves compute slamming pressures.
4. FE code simulates the hull structural response caused by the slamming loads to determine dynamic amplification of hull girder stresses due to whipping.

For the seakeeping analysis, the hull was discretized into 4290 panels. Computations were carried out for ballast and design conditions for 13 encounter angles ($0° \le \mu \le 180°$) at 15° intervals, for 30 wave periods ranging from 5.0 to 18.0 s, and for six ship speeds v_{ship} ranging from 0 kn to 19.5 kn. We assumed that the highest normal relative velocities between water and hull resulted in maximum slamming pressures. Standard spectral techniques together with the linearly computed transfer functions of ship motions were employed to specify regular design waves for stern slamming. At the moment of water entry, maximum relative normal velocities were computed for 20 critical locations underneath the ship's stern region, Fig. 2. Due to symmetry, only the port side was investigated.

Long-term statistical analyses were performed, assuming equal distribution of wave encounter angles for each given loading condition and ship speed. Short-term statistics relied on Pierson-Moskowitz seaway spectra with a cosine squared distribution of wave energy about the primary wave direction. For long-term statistics, frequencies of occurrence of sea states were set according to the IACS Recommendation 34. The applied probability of exceedance was 10^{-8} for 17 years operational time. Multiplication of transfer functions for normal relative velocities with the corresponding maximum wave amplitudes yielded complex response spectra of normal relative velocities. Values of maximum normal relative velocities were always taken at the peak of the response spectra.

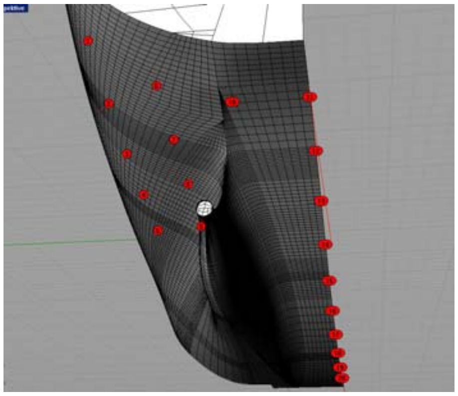

Fig.2: Locations of investigated slamming loads

Table II: Selected design waves

wave	1	2	3
wave amplitude [m]	14.2	14.2	12.2
wave period [s]	13.5	13.5	12.5
encounter angle	0°	15°	180°

A subsequent analysis determined amplitudes of regular design waves for each combination of encounter angle, wave period, and ship speed. Based on operating experience with similar ships, the following restrictions were observed:

- Wave steepness must not exceed 0.156, corresponding to wave height:wave length = 0.1.
- Except at zero forward speed, maximum acceleration on the bridge deck must not exceed the acceleration of gravity.
- Depending on the ratio of forward speed v to design speed v_0, the propeller tip must not emerge for $v > 1/3\ v_0$, or the propeller emergence should not exceed one third of the propeller radius for $v = 1/3\ v_0$. At zero speed, this criterion is invalid.
- Wave heights greater than 15 m are only allowed for ship speeds of less than one-third design speed.
- For critical locations that do not emerge, maximum normal relative velocity is set to zero.

The ballast loading condition always resulted in higher maximum normal relative velocities than the loaded (design) condition, and the zero speed cases always gave higher values than other ship speeds. This was because wave height restrictions depended on ship speed and high relative velocities occurred together with high relative motions, causing parts of the propeller to emerge.

For the RANSE computations, we selected three regular design waves that caused maximum normal relative velocities, all for the ship in ballast condition at zero forward speed, Table II. Sample results are shown for a representative critical location. The RANSE solver not only computed slamming pressures, but also solved the nonlinear ship motion equations by imposing initial and boundary conditions according to the regular design waves.

For each design wave, a volume grid with tetrahedral cells was created. For wave 2, the grid had 1.5 million cells and covered a fluid domain extending two ship lengths aft and three ship lengths forward of the ship's center of gravity, two ship lengths to port and starboard of the centerline, and 200 m above and one ship length below the calm waterline. We refined the grid in the region of the water-air interface and stretched the cells towards the outlet boundaries and in the regions far from the free surface. Boundary faces on the hull surface in the critical stern region had a size ranging from 0.2 to 0.25 m², allowing an accurate representation of the pressure distribution. For wave 1 and wave 3, the grids were similar. However, due to symmetry (stern wave respectively head wave) we modeled only the port side of the hull and the surrounding fluid domain. Thus, the number of grid cells was reduced to about 700000. For wave 3, regions of refined and stretched cells were adjusted to reflect head wave conditions. In each case, about 4000 time steps with a time step size of 0.02 s were computed, corresponding to 80 s of simulation time or about six wave encounter periods.

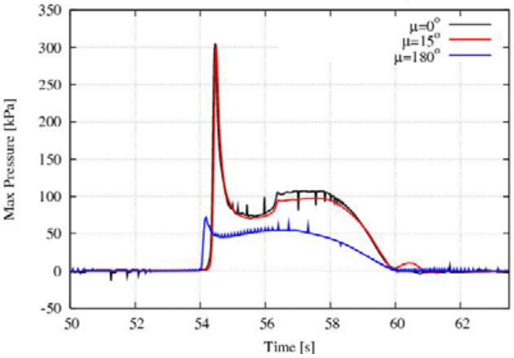

Fig.3: Computed slamming pressure in [kPa] for waves 1 (black), 2 (red), 3 (blue)

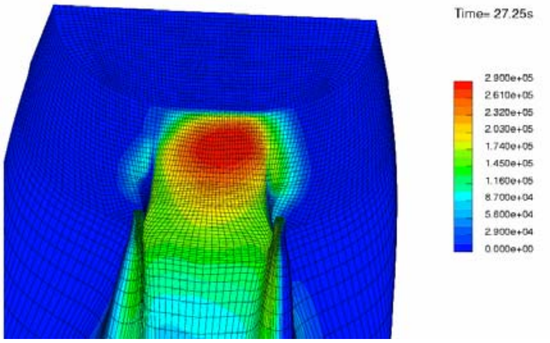

Fig.4: Computed pressure distribution for wave 2 occurring at peak slamming pressure

Fig.4 shows computed time series of slamming pressures. For waves 1 and 2, pressures reach similar peak values of about 305 kPa and the duration of peaks and the slope of the pressure curves after the first peak are similar. Shape and duration of these pressure traces agreed well with full-scale and model test measurements for other ships, indicating that the RANSE simulations captured all relevant physical phenomena, *Schellin et al. (2007).* Although the pressure time history for wave 3 resembles the time histories from waves 1 and 2, pressures were significantly smaller. The peak pressure from wave 3 was only about 25% of the peak pressure from waves 1 and 2. In the computations, stern slamming occurred only between the two propeller axes. The pressure distribution in Fig.4 is typical for the time of peak slamming pressure. Formulas in classification society rules give slamming pressures of 325 kPa for this ship. Rule based slamming loads thus lead to a conservative hull structural design. Furthermore, rule based design pressures refer to quasi-static pressures, whereas computed slamming peak pressures lasted only for a short time.

Whipping analyses were performed, using the hydrodynamic loads obtained by the RANSE computations as transient loads acting on the FE model of the ship structure. The FE model consisted of 263000 elements and considered a total of 575000 nodal degrees of freedom. The mass distribution of the light-ship weight was completed by adding masses of filled and partially filled tanks. Transient FE computations showed that the excitation of the lowest fundamental natural mode contributed most to the additional stresses caused by hull girder vibrations. Of interest were accelerations at the ship's bow and stern, longitudinal stresses at the ship's midship section, and torsional stresses at the one-quarter and three-quarter ship stations. We selected large amplitude waves with periods where the probability of exciting whipping responses of the ship structure was relatively high. These waves caused not only maximum slamming pressures, but also high shear forces, bending moments and, for wave 2, torsional moments acting on the ship's stern section. Slamming loads obtained from RANSE computations were converted to nodal forces for the FE model. Two-dimensional Lewis form hydrodynamic masses were distributed to appropriate shell nodes. A total hydrodynamic mass of 19359 t resulted in the transverse direction and 199024 t in vertical direction.

For wave 1, the simulated time ranged from 22.6 to 36.1 s. Fig.5 shows time histories of vertical accelerations (a_v) at the ship's stern and at the ship's bow. For convenience, the vertical slamming force (F_z) is also plotted. Although the influence of slamming on the acceleration at the bow is significant, it is less than at the stern. High-frequency vibrations were not observed at the bow. The Fourier decomposition of vertical accelerations for both locations, Fig.6, shows the dominance of the two vibration modes of 0.79 and 3.59 Hz at the stern. The second peak at 3.59 Hz almost vanishes at the bow. The effects of the fundamental vibratory hull girder modes with natural frequencies of 0.79 and 3.59 Hz are more pronounced in the stern section, Fig.7. Superposition of ship motion induced vertical accelerations and slamming-induced accelerations, Fig.8, shows the influence of the dynamic contribution to total accelerations. Computed time histories of midship longitudinal stresses in the hull girder, Fig.9, consist of the quasi-static wave-induced bending stress, the dynamic slamming-induced vibratory stresses, and the total longitudinal stress. The maximum value of the dynamic slamming stress is 23% of the maximum value of the quasi-static bending stress. Slamming occurred at the time when the hull girder stress level due to wave bending was low, Fig.10 (left). Therefore, the maximum total longitudinal stress was only slightly larger than the maximum quasi-static longitudinal stress. Fig.10 (right) shows the hull at the moment of maximum longitudinal stresses in the hull girder.

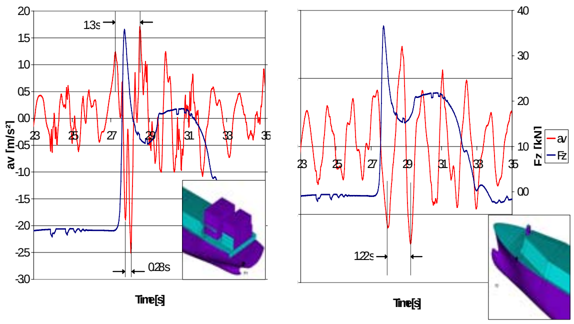

Fig.5: Vertical acceleration (red) in [m/s²] and vertical force (blue) in [kN] at stern (left) and at bow (right) for wave 1

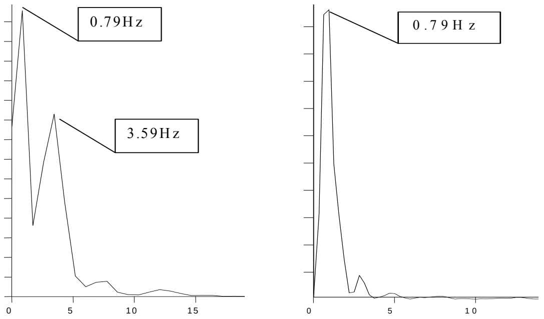

Fig.6: Frequency spectra of vertical acceleration at stern (left) and at bow (right) for wave 1

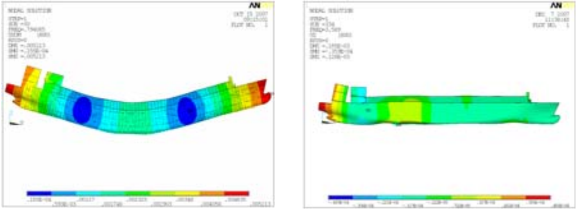

Fig.7: Hull girder modes at natural frequencies 0.79 Hz (left) and 3.59 Hz (right) for wave 1

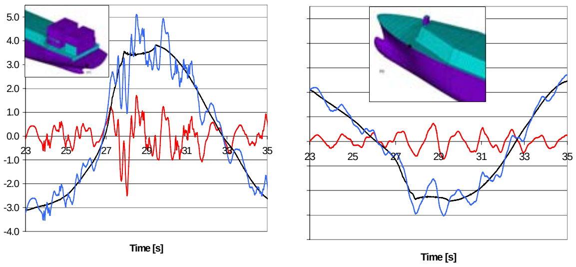

Fig.8: Elastic (red), rigid body (black), and total (blue) vertical acceleration in [m/s²] at stern (left) and at bow (right) for wave 1

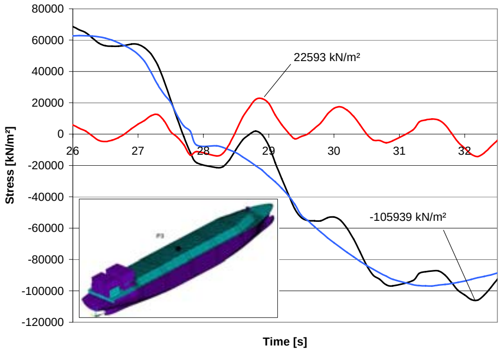

Fig.9: Longitudinal midship quasi-static wave bending stress (blue), slamming stress (red), and total (black) stress in [kN/m²] for wave 1

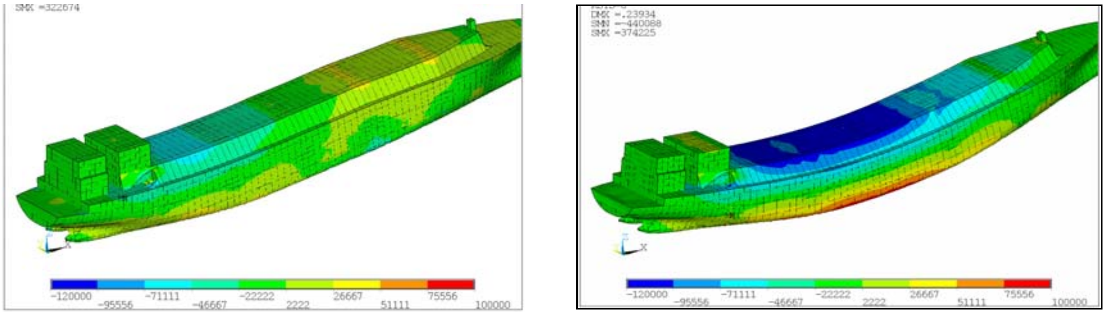

Fig.10: Longitudinal stress distribution in [kN/m²] at time of maximum midship dynamic stress amplification (left) and at time of absolute midship maximum stress (right) for wave 1

For wave 2, the simulated time ranged from 61.5 to 75.0 s. Frequency spectra of computed vertical accelerations also revealed three-node and four-node natural modes of vertical hull bending at 1.41 and 1.81 Hz, respectively. Our results indicated that no torsional or other asymmetric natural modes were excited, although wave 2 (encounter angle μ = 15°) caused a relatively small torsional moment to act at the stern. Computed time series of vertical accelerations, Fig.11 show a larger influence of the slamming-induced dynamic contribution than for wave 1.

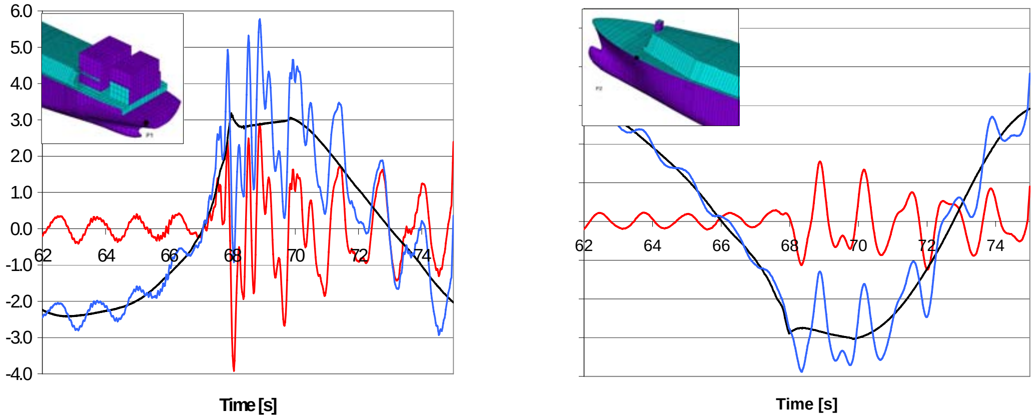

Fig.11: Elastic (red), rigid body (black), and total (blue) vertical acceleration in [m/s²] at stern (left) and at bow (right) for wave 2

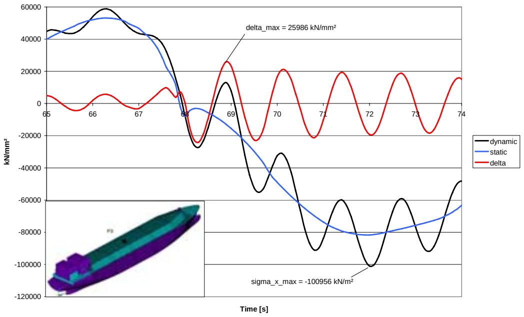

Fig.12: Longitudinal stress at 0.5 L in [kPa], deck, for wave 2

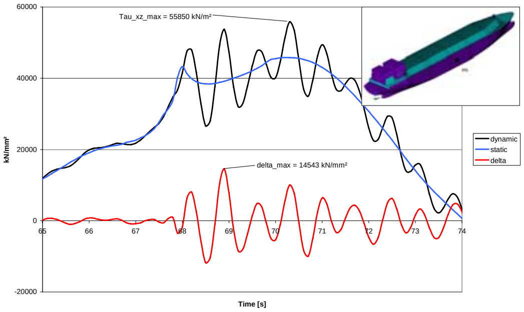

Fig.13: Shear stress at 0.5L in [kPa], hull side, for wave 2

The corresponding stress analysis yielded a maximum slamming-induced dynamic stress 32% larger than the maximum quasi-static wave bending stress, Fig.12. Similarly to the wave 1 case, the slamming event occurred at the instant of time when the total hull girder bending stress was almost zero. For wave 2, we evaluated shear stresses at three stations on one side of the ship. Nevertheless, dynamic effects led to increased total shear stresses of up to 25% at the ship's quarter stations, Fig.13.

For wave 3, slamming pressures were not found to be critical and their effects, therefore, were not separately investigated.

EL MOCTAR, O.; SCHELLIN, T.E.; PRIEBE, T. (2006), *CFD and FE methods to predict wave loads and ship structural response*, 26th Symp. Naval Hydrodynamics, Rome

OBERHAGEMANN, J.; HOLTMANN, M.; EL MOCTAR, O.M.; SCHELLIN, T.E.; KIM, D.W. (2008), *Stern slamming of an LNG carrier,* 27th Int. Conf. on Offshore Mechanics and Arctic Engineering (OMAE), Estoril

SCHELLIN, T.E.; EL MOCTAR, O. (2007), *Numerical prediction of impact-related wave loads on ships*, J. Offshore Mechanics and Arctic Engineering 129/1, pp.39-47